DISS. ETH No. 19730

Kinematics and failure mechanisms of the Randa rock slope instability (Switzerland)

A dissertation submitted to
ETH ZURICH

for the degree of
DOCTOR OF SCIENCE

presented by
VALENTIN SAMUEL GISCHIG
Dipl. Natw., ETH Zurich

born
25 January 1982
citizen of Baltschieder, Valais

accepted on the recommendation of
Prof. Dr. Simon Loew
Dr. Jeffrey R. Moore
Dr. Florian Amann
Dr. Keith F. Evans
Prof. Dr. Erik Eberhardt

2011

Contents

Abstract

The rock slope instability above the village Randa in the southern Swiss Alps is the legacy of two successive rockslides, which occurred in April and May 1991 and released 22 and 7 million m^3 of crystalline rock, respectively. The remaining unstable rock mass currently moves at a rate up to 30 mm/yr and became the subject of a multidisciplinary ETH research project in 2000. Geological mapping, geotechnical characaterization, geophysical imaging, and micro-seismic monitoring were combined to help constrain a structural and kinematic model of the uppermost portion of the instability. This PhD thesis incorporates the outcomes of the two first phases of the project with observations from new remote sensing and monitoring datasets, as well as with numerical modelling. This work attempts to resolve the internal structure and kinematics of the entire unstable rock mass, as well as identify the underlying physical processes responsible for its temporal behaviour.

A set of four ground-based differentially synthetic aperture radar (GB-DInSAR) displacement maps measured from the opposite valley flank revealed the presence of both a basal sliding surface and a lateral release plane bounding the current instability. Further, the displacement pattern showed a transition from toppling near the top of the instability above 2150 m to translational sliding below. New structural information extracted from combined helicopter-based LiDAR DTMs and oblique orthophotos allowed for extending the 3D structural model, previously limited to the accessible uppermost portion of the instability, to the inaccessible 1991 failure surface. Stereographic analysis of large-scale structures with minimum trace lengths of 15 m confirmed that toppling kinematics is dominant above 2150 m, while below sliding along a discontinuous basal rupture surface is more likely. New geodetic measurements at the top of the instability combined with structural data indicated that dislocation across the lateral release plane has a strong opening component and is thus not involved in wedge sliding. The derived kinematic model was further validated in a 2D numerical study using UDEC, which also set the basis for subsequent numerical investigations into the temporal behaviour of the rock mass.

Exploration of different driving mechanisms governing the temporal behaviour of the instability relies on comprehensive analysis of quasi-continuous monitoring data. At Randa, these include fracture displacements measured both at the surface and at depth, as well as relevant additional parameters such as air and rock temperature, meteorological conditions, and borehole water pressure. Within the framework of this study, the monitoring system operational since 2001 was updated with new fiber-optic strain sensors and thermocouple sensor arrays in 2008. Analysis of all monitoring data since 2001 revealed an intriguing annual trend of increased displacement rates after temperatures drop in fall and decreasing rates in spring after snowmelt. This seasonal variation in displacement rate also occurred at depths down to 68 m, and has been measured from a number of different monitoring systems. The behaviour is opposite to that reported for most large landslides, where maximum displacement rates are associated with increased groundwater pressure after snowmelt or heavy rainfall. Here, it is suggested that thermal effects are responsible for the observed seasonal trend, and a conceptual numerical study was performed to investigate transient thermo-mechanical effects. It could be shown that near-surface thermo-elastic strain is transferred to depth of constant temperature (below the thermal active layer) as a result of material elasticity and topography. The associated stress changes, although small in magnitude, can induce slip along discontinuities provided they are at critical stress levels. The previously mentioned numerical model representing the 2D kinematics of the Randa instability was subsequently run in thermo-mechanically coupled

mode using annual temperature cycles as a surface boundary condition. Model results were able to reproduce the observed displacement rates and their seasonal variations, and confirm that thermo-mechanical effects are the dominant driving mechanism at the Randa instability.

In addition to thermo-mechanical effects, other possible forcing factors were explored, namely the role of groundwater pressure, fracture air ventilation, freezing of water in fractures, and regional seismicity. Hydrogeological conditions, identified through mapping the temporal occurrence of surface water seepages, are characterized by a low groundwater table that may only marginally affect the unstable rock mass. While freeze-thaw effects are also considered to be secondary, fracture air ventilation is likely to disturb the temperature field at depth and may thus contribute to thermo-mechanical forcing of instability deformation. Special focus was set on the seismic response of the instability. Triggered dynamic strain measurements recorded across surface tension fractures during a nearby small earthquake, as well as spectral amplification characteristics derived from seismic recordings revealed the significant role of compliant tension fractures on seismic response of the unstable rock mass. Elastic numerical models including only steeply-dipping compliant fractures were able to reasonably explain the strong frequency-dependent amplification measured at Randa. Such seismic site effects are rarely considered for hard rock slope instabilities.

Zusammenfassung

Die Hanginstabilität oberhalb des Dorfes Randa (Wallis) in den südlichen Schweizer Alpen stellt eine Felsmasse dar, welche nach zwei aufeinanderfolgenden Bergstürzen im April und Mai 1991 (22 bzw. 7 Millionen m^3 kristallines Gestein) instabil blieb. Derzeitige Bewegungsraten liegen im Bereich von bis zu 30 mm/Jahr. Die Hanginstabilität wurde im Jahre 2000 Gegenstand eines multidisziplinären Forschungsprojektes der ETH Zürich. Geologische Kartierung, geotechnische Charakterisierung, geophysikalische Bildgebung und mikro-seismische Überwachung wurden kombiniert, um ein strukturelles und kinematisches Modell des obersten Teiles der Instabilität zu konstruieren. Diese Doktorarbeit berücksichtigt die Ergebnisse der ersten zwei Phasen des Projektes, und analysiert diese zusammen mit Beobachtungen aus neuen Fernerkundungs- und Überwachungsdaten sowie mit Hilfe numerischer Simulation. Das Ziel ist die interne Struktur und Kinematik der gesamten instabilen Felsmasse detailliert zu beschreiben und die zugrundeliegenden physikalischen Prozesse, die ursächlich für das zeitliche Verhalten sind, zu identifizieren.

Vier Verschiebungskarten aus terrestrischen differenziellen SAR (GB-DInSAR) Messungen von der gegenüberliegenden Talseite bewiesen die Existenz einer basalen Gleitfläche und einer lateralen Begrenzungfläche, welche die aktuelle Instabilität begrenzen. Das räumliche Verschiebungsmuster liess zudem einen Übergang zwischen zwei unterschiedlichen kinematischen Bewegungstypen erkennen. Der Bewegungsmechanismus oberhalb von 2150 m wurde als Toppling identifiziert, unterhalb herrscht Translationsgleiten vor. Helikopter-basierte LiDAR DHMs und entzerrte Photos ermöglichten die Akquisition von Strukturdaten, insbesondere in der bisher unzugänglichen 1991-er Abbruchsfläche. Damit wurde das 3D Strukturmodell verbessert und auf die gesamte Instabilität ausgeweitet. Eine stereographische Analyse der grossskaligen Diskontinuitäten (Spurlängen grösser als 15 m) bestätigte, dass die Kinematik oberhalb von 2150 m von Toppling dominiert ist, während darunter Gleiten entlang einer basalen Bruchfläche wahrscheinlicher ist. Die Interpretation neuer geodätischer Messungen oberhalb des Anrissbereiches in Kombination mit Bruchorientierungen ergab, dass der Versatz entlang der lateralen Begrenzungsfläche eine beachtliche Öffnungskomponente aufweist. Ausgleiten eines Bruchkeils entlang dieser Bruchzone ist daher kinematisch unwahrscheinlich. Das kinematische Konzept-Modell, welches sich aus diesen Betrachtungen ergab, wurde mit Hilfe numerischer 2D-Modelle validiert. Diese dienten auch als Basis für weiterführende numerische Simulationen im Hinblick auf das zeitliche Verhalten der instabilen Felsmasse.

Untersuchungen bezüglich dem zeitlichen Verhalten der Instabilität beruhen auf einer umfassenden Analyse quasi-kontinuierlicher Messdaten. Diese umfassen Verschiebungen entlang von Brüchen an der Oberfläche und in der Tiefe, sowie weitere relevante Parameter wie Luft- und Felstemperaturen, meteorologische Daten und Wasserdrücke in Bohrlöchern. Im Rahmen dieser Studie wurde im Sommer 2008 das Messsystem, welches 2001 in Betrieb genommen wurde, mit faseroptischen Verformungssensoren und Temperatursensorketten ergänzt. Die Auswertung der gesamten Überwachungsdaten seit 2001 ergab ein konsistentes zeitliches Verschiebungsmuster. Die Verschiebungsraten nehmen mit fallenden Temperaturen zu bzw. nach der Schneeschmelze im Frühling wieder ab. Solche jahreszeitliche Schwankungen traten auch in Tiefen bis zu 68 m auf. Die meisten in der Literatur beschriebenen Hangbewegungen zeigen, dass die maximalen Verschiebungsraten mit erhöhtem Bergwasserdruck nach der Schneeschmelze oder nach Starkniederschlägen in Verbindung gebracht

werden können. Dies steht im Gegensatz zur heutigen Randa-Instabilität. Die Daten zeigen, dass thermische Effekte für den beobachteten Jahresgang der Verschiebungen verantwortlich sind. Daher wurde eine konzeptionelle numerische Studie durchgeführt, welche den Effekt von transienten thermo-mechanisch induzierten Spannungsänderungen auf das Verformungsverhalten idealisierter Felsböschungen untersuchte. Es konnte gezeigt werden, dass oberflächennahe thermo-elastische Dehnungen aufgrund von Materialelastizität und Topographie in Tiefen konstanter Temperatur übertragen werden können (d.h. auch unter die thermisch aktive Schicht). Die damit einhergehenden Spannungsänderungen können trotz niedriger Amplitude Gleiten entlang von Diskontinuitäten induzieren, falls diese einen kritischen Spannungszustand aufweisen. Das zuvor hergeleitete numerische Modell zur Reproduktion und Validierung der 2D-Kinematik der Instabilität, wurde aufgrund obiger Erkenntnisse im thermo-mechanisch gekoppelten Modus gerechnet. Dabei wurden jährliche Temperaturzyklen als Oberflächenrandbedingung verwendet. Die Modellresultate konnten die beobachteten Verschiebungsraten und deren Jahresgang hinreichend reproduzieren, was bestätigt, dass der thermo-mechanische Effekt den dominanten Antriebsmechanismus der Randa-Instabilität darstellen kann.

Zusätzlich zu thermo-mechanischen Effekten wurden weitere mögliche antreibende Faktoren untersucht, wie die Rolle des Bergwasserdruckes, der Luftzirkulation und Frostbildung in Klüften, sowie der Einfluss der regionalen Seismizität. Die hydrogeologischen Gegebenheiten wurden mittels Kartierung des zeitlichen und räumlichen Auftretens von Quellen erfasst. Diese Untersuchungen ergaben, dass ein tiefliegender Bergwasserspiegel existiert, der nur marginal die instabile Felsmasse beeinflussen kann. Frost-Tau-Effekte werden ebenfalls als sekundär beurteilt. Dagegen ist es wahrscheinlich, dass Luftzirkulation in offenen Brüchen das Temperaturfeld tiefreichend stört, wodurch möglicherweise das Deformationsverhalten durch zusätzliche thermo-mechanische Effekte beeinflusst wird. Spezielle Beachtung wurde der seismischen Antwort der Instabilität geschenkt. Während eines kleinen regionalen Erdbebens wurden dynamische Verformungen an einem Zugbruch an der Oberfläche erfasst. Zusammen mit gemessenen spektralen Amplifikationscharakteristiken demonstrieren diese den signifikanten Einfluss von elastisch nachgiebigen Zugbrüchen auf die seismische Antwort einer instabilen Felsmasse. Spektrale Amplifikationsfaktoren von bis zu 10 konnten auf der Grundlage elastischer numerischer Modelle mit steil einfallenden Brüchen geringer Steifigkeit erklärt werden. Solche seismischen Standorteffekte werden bei Instabilitäten in kompetentem Fels selten berücksichtigt.

1. INTRODUCTION

1.1 Study motivation and objectives

Growing population and infrastructure in mountainous areas enhances the importance of accurately assessing natural hazards. Landslides are one of the primary natural hazards in high-relief areas with dense population and infrastructure such as in the Swiss Alps. Successfully coping with landslides requires recognition of hazardous sites, if required, monitoring and application of mitigation measures. Technologies both for recognition and monitoring of landslides have developed towards higher accuracy, better spatial coverage, and more flexible deployment in recent years. For landslide detection and characterization, remote sensing techniques can be applied including satellite- or ground-based radar interferometry (InSAR), as well as high resolution, airborne or terrestrial LiDAR and photogrammetry (e.g. Metternicht et al., 2005; Oppikofer et al., 2011; Strozzi et al., 2010, etc.). Displacement and deformation monitoring (e.g. with GPS, geodetic surveys, InSAR, inclinometer/extensometer surveys, etc.) can help characterizing the displacement field and deriving the kinematic behaviour of an active landslide body. For early warning purposes, automatic monitoring systems are used (e.g. GPS, crack extensometers, inclinometers, fiber-optic strain sensors), which can often be read remotely via wireless communications. Acceleration of movements in monitoring data is commonly used as indicator of impending catastrophic failure (e.g. Crosta and Agliardi, 2003; Voight, 1989). Although this method has led to correct prediction of catastrophic landslides (Ladner et al., 2004; Krähenbühl, 2006), cases are reported for which it was misleading (Kilchenstock, Heim, 1932; Innerkirchen, Gruner, 2001). Correct interpretation of displacement data remains a challenging task, because the underlying physical processes driving rock slope deformation are poorly understood. High-resolution monitoring of the temporal behaviour of instabilities offers new insights into the failure mechanisms of unstable brittle rock slopes in natural settings, and is essential for any attempt to predict catastrophic failure.

In 2000, an interdisciplinary research project was initiated by the Chair of *Engineering Geology* at *ETH Zurich* aimed to understand rockslide processes and mechanisms, and the progressive development of failure surfaces in crystalline rock. In Phases I and II of this project, geological, geophysical, and geotechnical methods were applied at the rock slope instability above the village Randa in southern Switzerland. Various insights into structure and kinematics of the unstable rock mass were gained through this combined approach. Details are given in section 1.5. Together with almost 10 years of monitoring data, a unique dataset is available to study time-dependent failure mechanisms at Randa in great detail.

This study is part of Phase III of the aforementioned research project, and builds on the outcomes of the two preceding phases. The outcomes of this PhD thesis can be summarized in three main themes:

1. Investigations in the two former phases were limited to the uppermost part of the instability, which is accessible for field work. Information from the 1991 failure surfaces, too dangerous and steep for field access, remained sparse. With the help of helicopter-based LiDAR and photogrammetry surveys, the existing structural model has been extended to the entire instability, including both new structural information and the 3D information obtained in the other two phases.
2. Similarly, little information regarding the displacement field of the rock mass was available for the steep 1991 failure surfaces. A set of four GB-DInSAR surveys between 2005 and 2007, as well as new geodetic measurements at the top of the instability yielded new information about the spatial dis-

placement pattern. In combination with the structural model, the kinematic behaviour of the unstable rock mass was determined and further explored with 2D numerical modelling.

3. The monitoring system operational between 2001 and 2008 was upgraded with additional instruments measuring deformation, rock temperature, and meteorological parameters. Analysis of all data revealed that stress changes induced by near-surface annual temperature cycling are the dominant mechanism driving slope deformation at the Randa instability. The kinematic model and further numerical models assisted successful interpretation of monitoring data, and gave useful insights into the mechanisms through which external factors drive time-dependent failure.

1.2 Thesis structure

The thesis consists first of this introductory chapter followed by two main parts. In the introduction, background on time-dependent rock slope failure processes are given (Section 1.3), the study area including the 1991 failure events is described (Section 1.4), and finally the outcomes of previous studies investigating the ongoing Randa rock slope instability are summarized (Section 1.5). In Chapter 2, the multi-component monitoring system deployed at Randa is described in detail, and the main data sets are presented. The two main parts of the thesis that follow include papers that have either already been published or are submitted and in review. The two sections are summarized as:

Part I presents structural and kinematic analysis of the current Randa instability, which also includes information from the inaccessible 1991 failure surfaces. Two papers were published on this topic: The first (Chapter 3) presents interpretation of GB-DInSAR data leading to the identification of large-scale release surfaces, which are essential for further kinematic analysis. The second paper (Chapter 4) presents a thorough kinematic analysis of the unstable rock mass, which integrated data from different remote sensing and monitoring techniques, as well as the results from previous research presented by Willenberg et al. (2008b).

Part II focuses on the temporal behavior of the Randa instability. Chapters 5 and 6 present a study on thermo-mechanical effects on slope stability based on comprehensive analysis of monitoring data and numerical models. In Chapter 7, the role of additional driving factors that may play a role at the Randa instability are explored and discussed, namely water pressure changes, freeze-thaw effects, air ventilation, and seismic loading.

In a final chapter (Chapter 8), a summary of the overall outcomes and conclusion of this study is presented, together with an outlook for further possible research on slope instabilities in brittle rock.

1.3 Time-dependent failure of unstable rock slopes

To understand the temporal behavior of slope instabilities, it is crucial to address time-dependent failure mechanisms acting within the rock mass. These are commonly referred to as *progressive failure mechanisms* in literature, and are in contrast to static rock or fracture mechanical concepts that do not include time as critical parameter. Terzaghi (1962) describes progressive failure as the chain reaction of failure within a rock slope, caused by stress redistribution after loss of cohesion at a certain point. He also mentions that discontinuities in natural settings are limited in persistence and some fracture propagation through intact rock bridges may be required for a rock slope to fail catastrophically. Bjerrum (1967) describes progressive failure in a soil mechanics context. He presents cases of failed over-consolidated clay slopes where the residual shear strength estimated from average gravitational shear stress along the failure plane was significantly lower than the peak shear stress of the same material measured in laboratory tests. He concludes that a flaw at some location in the clay mass must have served as initiation point for a shear surface that progressively propagated through the material due to stress redistribution, and consequently led to failure. Leroueil (2001) points out that stress redistribution after local failure may not necessarily lead to catastrophic failure but can create a new equilibrium state. Progressive failure can then be reactivated by a change of slope geometry, increase of pore pressure, or a decrease of strength through creep, fatigue or weathering. Haefeli (1967) gives examples of progressive, multi-stage failures in snow, soil, rock, and ice. Erismann and Abele (2001) illustrate the concept of progressive failure within brittle rock, which is most applicable for our purposes: Along a rough discontinuity, small changes in the force acting at an interlocking asperity may lead to failure, if it is critically stressed. Subsequent slip and stress redistribution brings other interlocking asperities closer to strength limit, which may then fail in a later stage. In a similar way, fractures can propagate stepwise through intact rock bridges due to small stress changes. Eberhardt et al. (2004) hypothesized that step-wise failure of rock bridges led to the catastrophic failure events at Randa in 1991 and modelled these processes with different numerical approaches.

In this study, progressive failure is understood as the processes of local failure of interlocking asperities along critically stressed planes and fracture propagation through intact rock bridges, which both may be followed by stresses redistribution inside the rock mass. It is a time-dependent process that reveals itself as quasi-continuous movements of the unstable rock mass, and acts until the kinematic and mechanical conditions for catastrophic failure are met.

The underlying mechanisms that drive progressive failure are changes of the driving stress or continuous degradation of the strength properties of the rock mass. Physical processes leading to stress and strength changes within the rock mass are referred to as *preparatory factors* (Gunzburger et al., 2005). They consist of the following:

1. Changing pore water pressure due to heavy rainfall or snowmelt
2. Passing seismic waves
3. Daily or seasonal surface temperature variations
4. Freeze/thaw cycles
5. Changes in slope geometry due to erosion and/or alpine uplift
6. Microscopic damage processes (fatigue, stress corrosion, creep)
7. Chemical weathering, e.g. by infiltrating water
8. Thawing of permafrost

Gunzburger et al. (2005) summarized the effect of these factors on the time-dependent stability state of a slope in a simplified sketch, which is reproduced in Figure 1.1a. Earthquakes, thermal cycling, and slope steepening mainly affect the driving forces within a rock mass. Incremental irreversible deformation induced by these stress changes also reduces the bulk strength, and thus affects the resisting forces. Similarly, water pressure changes can induce reversible stress changes, but may also weaken the rock mass, if incremental damage occurs. Microscopic damage processes, chemical weathering, and thawing of permafrost continuously alter the strength of the rock mass. Also shown are normal/shear stress cross-plots, which illustrate the effect of different mechanisms at a particular location along a pre-existing discontinuity (Figure 1.1b-f). The included Mohr-Coulomb failure envelope represents discontinuity strength with a small amount of cohesion. Water pressure changes lower only the normal stress (decrease of effective stress; Figure 1.1b), while earthquakes (Figure 1.1c), temperature cycling (Figure 1.1d), and changes in slope geometry (Figure 1.1e) alter both the shear and the normal stresses. Microscopic damage processes and weathering lower both cohesion and friction, while thawing of permafrost mainly decreases cohesion, but may also affect friction in an unpredictable way (Figure 1.1f). Figure 1.1 also illustrates that the transition between preparatory and triggering factors is continuous, since some of these processes can act as triggering factors if they occur with exceptional violence or if the slope is already close to failure. Several processes may also act simultaneously on a rock mass, whereas often one primary factor dominates the behavior of an instability. Table 1.1 gives examples of landslides sorted by dominant mechanism acting either as preparatory or triggering factor. Some instances could be mentioned twice as two factors may drive instability, e.g. the Moosfluh landslide in the Aletsch area currently accelerates due to glacier retreat, but also exhibits seasonal variations in displacement rates probably caused by groundwater recharge after snowmelt (Strozzi et al., 2010). Note that examples are also quoted for which no clear trigger could be identified. Such cases are of particular interest, since they may have been subject to long-term, (cyclic) driving mechanisms, which damage the rock mass at small increments until driving and resisting forces equalized.

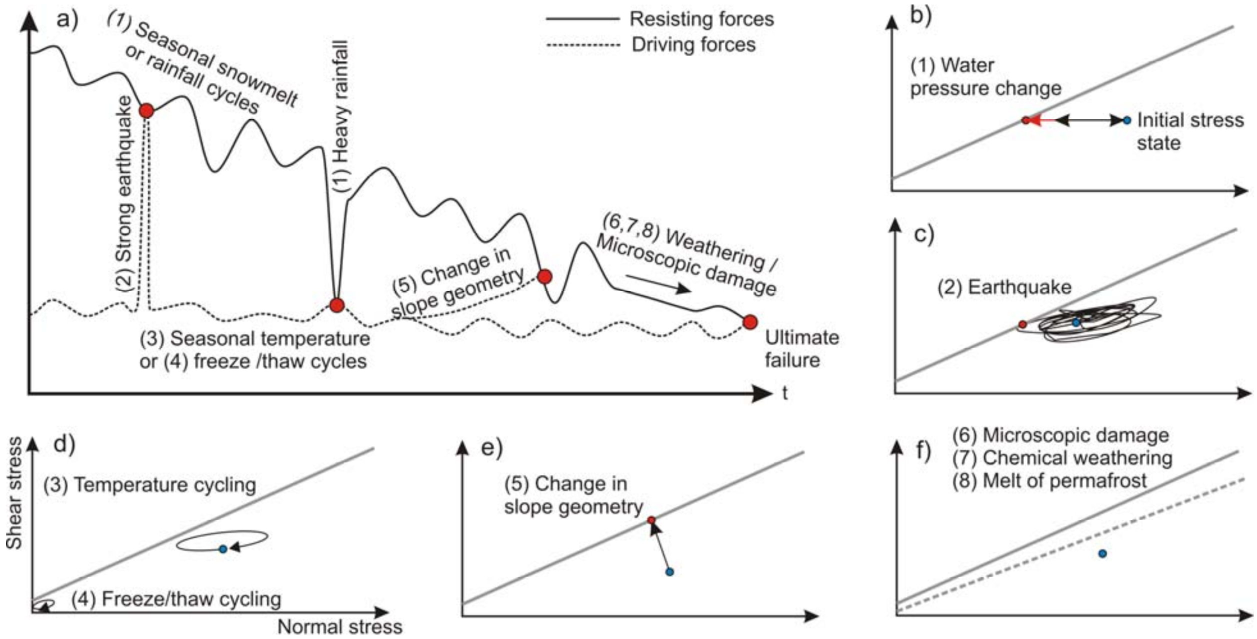

Figure 1.1: a) Temporal evolution of driving and resisting forces in an unstable rock mass subject to different driving factors (after Gunzburger et al., 2005). The sketch refers to the stability of the entire rock mass. Red dots indicate when necessary conditions for failure are met. b – f) Stress state and strength at a single point along a preexisting discontinuity within the unstable rock mass, and the effect of changes in different driving and resisting forces.

Table 1.1: Examples of instabilities or catastrophic failures sorted by their dominant preparatory factors (denoted 'ongoing') or triggering factor (year of failure give). DSGSD means'deep seated gravitational slope deformations'.

Driving factor	Example	Year	Reference
Changing water pressure	Goldau rockslide, CH	1806	Eisbacher and Clague (1984); Heim (1932)
	Ruinon rockslide, Italy	Ongoing	Crosta and Agliardi (2003)
	Aresawa rockslide, Japan	2004 & ongoing	Nishii and Matzuoka (2010)
	Val Pola rockslide, Italy	1987	Crosta et al. (2004)
	Cuolm Da Vi (DSGSD),CH	Ongoing	Amann et al. (2006)
	Campo Vallemaggia (DSGSD), TI, CH	Ongoing	Bonzanigo et al. (2007)
Passing seismic waves	Huascaràn rock avalanche, Peru	1970	Plafker et al. (1971)
	Rawilhorn rockslide after M ≈ 6.5, Sierre, CH	1946	Hunziker (2011)
	Various failures after M = 8.0, Sichuan, China	2008	Yin et al. (2009)
	Various failures after M = 7.2, New Zealand	2003	Hancox et al. (2003)
	Various failures after M = 6.2, Aysén Fjord, Chile	2007	Redfield et al. (2010)
	Various failures after M ≈ 6.5, Matter Valley, CH	1855	Heynen, (2010), Fritsche et al. (2006)
Daily/seasonal temperature variations	Checkerboard Creek rockslide, Canada	Ongoing	Watson et al. (2004)
	Several rockslide sites in Graubünden, CH, (e.g. Val d'Infern).	Ongoing (2006)	Krähenbühl (2004) Krähenbühl (2006)
	Rocher de Valabres rockfall, France	Ongoing	Gunzburger et al. (2005)
	Several rockfall sites in Rio de Janeiro, Brazil	Ongoing	Vargas et al. (2009)
Freeze / thaw cycles and Thawing of permafrost	Hörnligrat rockfall, Matterhorn, CH	2003	Gruber & Haeberli (2007)
	Grabengufer rockfall, Randa, CH	ongoing	-
*Change in slope geometry *man-made **through glacial retreat*	Elm rock avalanche, GL, CH*	1881	Heim (1932)
	Moosfluh Aletsch DSGSD, VS, CH**	Ongoing	Strozzi et al., (2010)
	Eiger rockslide, BE, CH**	2006	Oppikofer et al. (2009)
Chemical weathering	Rufi landslides, CH	1999	Eberhardt et al. (2005)
	Goldau rockslide, SZ, CH	1806	Thuro et al. (2005)
Microscopic damage processes	No direct observations identified		
No obvious trigger	Pandemonium Creek rock avalanche, Canada	1959	Evans et al. (1989)
	Rocher de Valabres rockfall, France	2000	Gunzburger et al. (2005)
	Young River rockslide, New Zealand	2007	Massey et al. (2009)
	Randa rockslides, VS, CH	1991	Schindler et al. (1993)

1.4 Study Site description

1.4.1 Geographical and geological setting

The study site of this thesis is the current Randa rock slope instability, which is located above the village Randa (1400 m a.s.l.) on the western flank of the Matter valley near the popular tourist resort of Zermatt. The current instability is the legacy of two catastrophic rockslides, which occurred in 1991 and formed an 800 m high scarp (described in detail later in this chapter). Following these events, a rock mass extending from 1800 to 2400 m a.s.l. remained unstable behind the 1991 failure surface and currently moves at a rate of ~30 mm/yr (Figure 1.2).

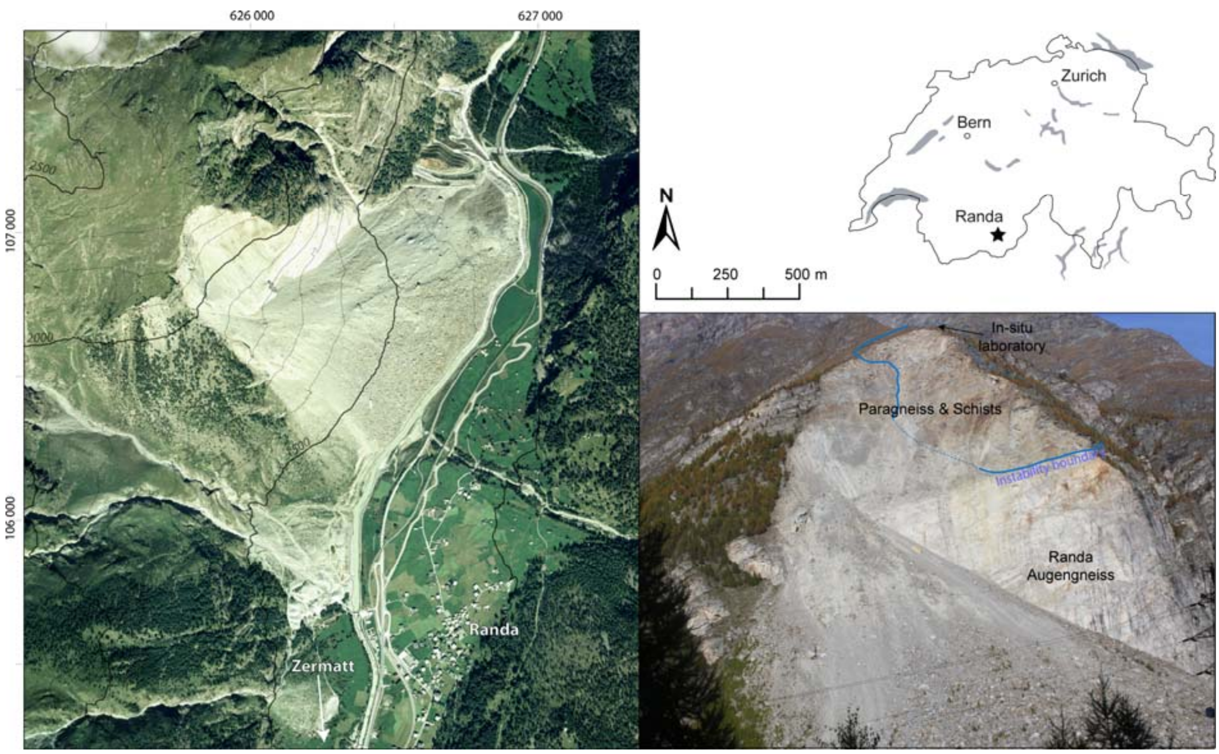

Figure 1.2: Overview map of the Randa rock slide area. Photograph of the 1991 failure scarp showing the two main lithologies and location of the in situ *monitoring system.*

The instability is situated within the Penninic Siviez-Mischabel nappe, a part of the Grand St. Bernard nappe (Figure 1.3a). Two main lithologies dominate our study area, competent orthogneiss overlain by a less competent paragneiss/schist sequence (Figure 1.3b). The orthogneiss is a metamorphosed Permian porphyritic alkaline to subalkaline granitic intrusion; the so-called *Randa-Augengneiss*. The paragneiss, the host rock of the intrusion, is more heterogeneous and contains polycyclic Palaeozoic gneisses, schists, and amphibolites. These rock units are characterized by a persistent foliation dipping into the slope at an angle of about 20°, which in general favours slope stability on the western flank of the Matter Valley. Rock slopes to the north of the Randa rockslide show similar geological characteristics and are mostly stable despite their steepness (Yugsi Molina, 2010). Further details and references on the regional geology can be found in Willenberg (2004) and Yugsi Molina (2010).

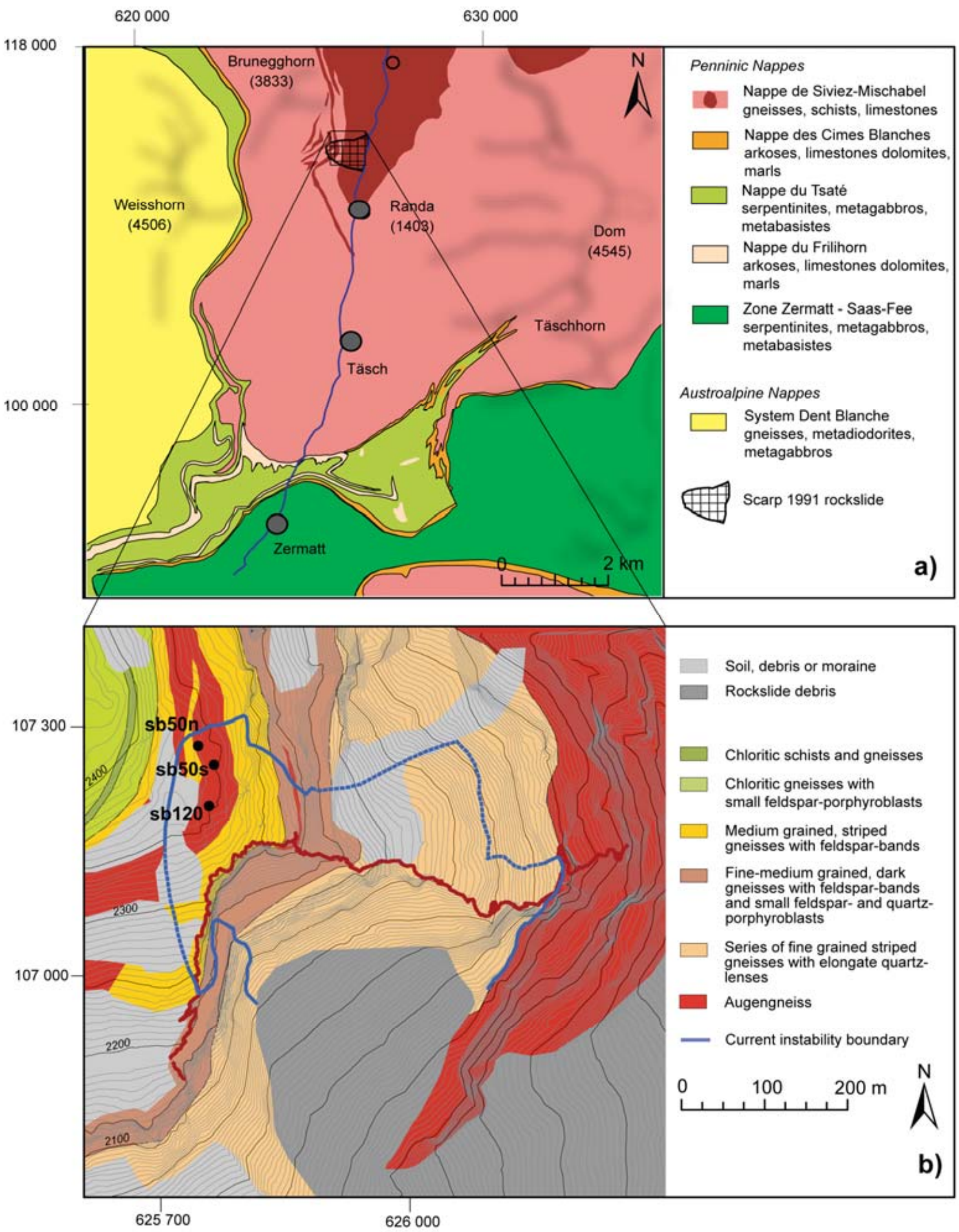

Figure 1.3: a) Overview of tectonic units in the southern Matter valley, b) Detail geological map of the Randa rock slope. Also shown are the locations of three deep boreholes. Both maps were adopted from Willenberg (2004).

1.4.2 The 1991 Randa rockslides

The current Randa instability lies behind the scarp of two large rockslides that occurred over about 3 weeks in 1991 (Figure 1.4). Detailed information about the rockslides is reported by Schindler et al. (1993) and Sartori et al. (2003). The first event on 18 April 1991 released ~22.5 million m^3 of mostly competent orthogneisses from the lower portion of the slope. The second event on 9 May 1991 involved retrogressive failure of about 7 million m^3 of paragneisses and schists. A monitoring system composed of geodetic surveys, automatic extensometer measurements, and seismic monitoring, was installed after the first events, and provided reliable early-warning information before lesser rockslides on 23 April 1991 (~100'000 m^3)

and the second major events of May. Prior to the April failures, strong seepage related to snowmelt was observed at the base of the orthogneiss along a highly persistent discontinuity, which became the failure surface on the 18 April. Between the first and the second events, seepage occurred at the top of the orthogneiss, while shortly before the second event, nearly horizontal jets of water mixed with clay were observed at the upper boundary of the orthogneisses.

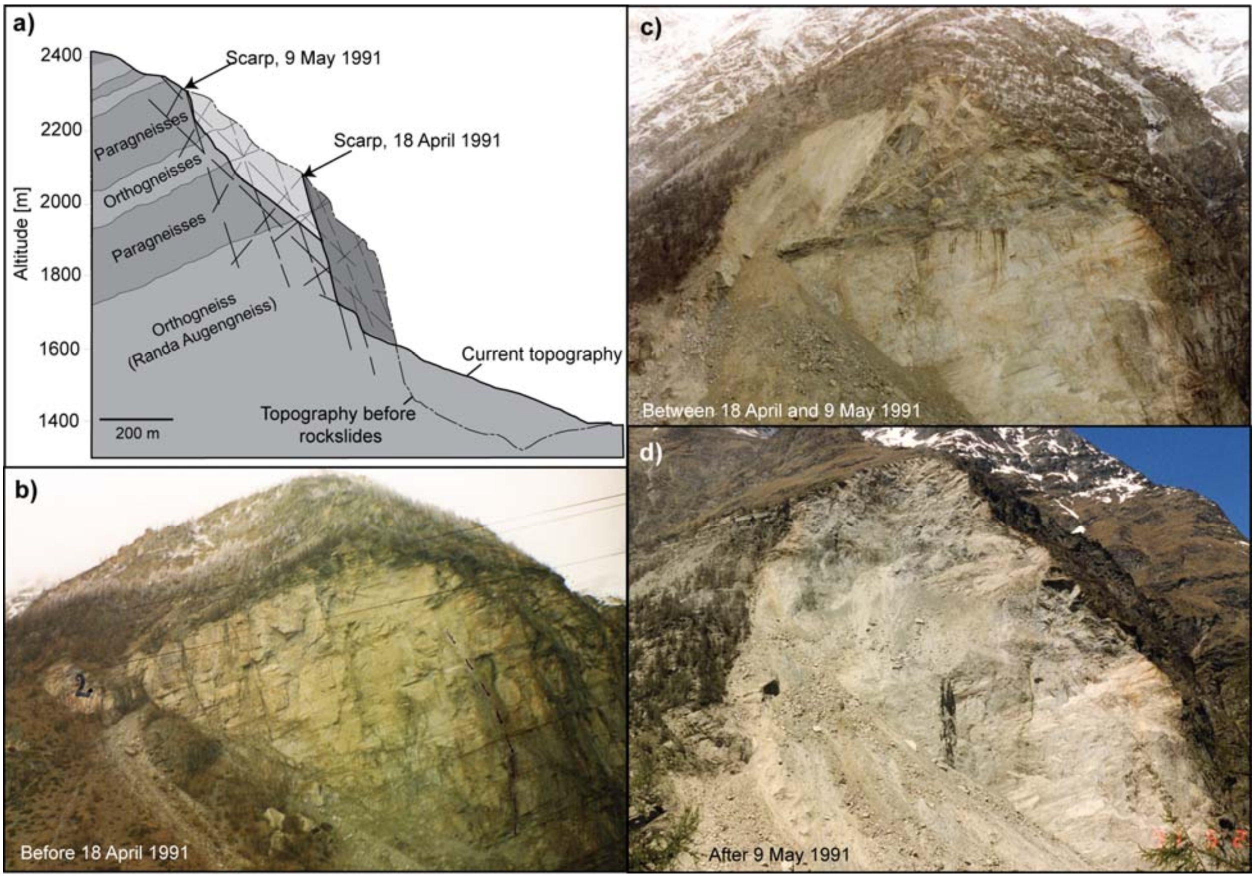

Figure 1.4: a) Profile showing the scarp of the two 1991 rockslides. b-d) Photographs of the slope before, between, and after the two failures. (Photos by J.-D. Roullier).

Detailed reconstruction of the kinematics of both 1991 failures was presented by Sartori et al. (2003). Failure initiated along a 30° dipping highly-persistent discontinuity in the orthogneiss unit close to the valley bottom. It was followed by sequential failure of large prismatic blocks defined by pre-existing discontinuities. Both rockslides were multi-stage events lasting several hours. As a result, the runout distance was much shorter than would be expected from the volume of the failed material (Scheidegger, 1973). Schindler et al. (2003) also mention that the morphology of the debris cone resembles a dry talus rather than a classic rockslide or rock avalanche deposit. Although a small hamlet, important traffic ways, as well as the river was buried, damage caused by the 1991 rockslides could have been much more substantial if the runout distance was greater. Damming of the river, however, resulted in flooding of the upstream village. As preliminary measures, the water needed to be pumped over the blockage and a new riverbed was excavated at the margin of the debris cone. To prevent further flooding, a bypass tunnel was excavated below the rockslide area, which can serve as a spillway in case of further events.

Schindler et al. (1993) also addressed the question of the preparatory and triggering factors leading to the failures. Meteorological data showed that snowmelt was not extraordinary compared to previous years and no extreme rainfall events preceded the failures. Seismological data recorded by the Swiss Seismological Service revealed no significant regional seismic event prior to the failures. The release area is also not located in a permafrost region, which excludes thawing of permafrost from likely triggers. Although no evident trigger could be identified, Schindler et al. (1993) emphasized the possible role of water pressure in combination with clay and sand infill in the cracks in the 1991 failures. Observations of springs within the unstable rock mass prior to failure indicated that the water table was at a maximum due to snowmelt, which likely promoted the impending failures. Schindler et al. (1993) also calculated that the rock mass prior to failure contained 7 – 15% void space, some of which was sandy infill. They hypothesized the role of intense weathering at depth driven by water circulation as long-term strength degradation process. Ongoing weathering would result in widening of cracks further aided by additional debris infill. Further, clay infill could have reduced friction along key discontinuities. Later investigations on weathering within orthogneiss in the bypass tunnel below the rockslide area revealed alteration and precipitation of clay minerals (i.e. smectite; Girod 1999). Thus, reduction of strength along clay-coated discontinuities, in combination with water infiltration, was suggested to be a feasible mechanism for the 1991 rockslides and other instabilities in the Matter Valley (Jaboyedoff et al., 2004b). Sartori et al. (2003) hypothesize that the role of smectites formed through weathering may have played a role in forming an impervious barrier to groundwater flow, which lead to a gradual increase of hydraulic head. They also suggest that gradual strength reduction of the rock mass lead to progressive development of failure planes over a long period. Eberhardt et al. (2004) used numerical models to evaluate the failure evolution through internal strength degradation and sliding plane development. They also emphasize the role of brittle tensile failure before shear failure became possible.

Following the 1991 rockslides, a geodetic network was surveyed periodically to monitor subsequent movement of the remaining unstable rock mass. Maximum displacement rates of 14 mm/yr were detected (Jaboyedoff et al., 2004b), which, after a relaxation phase of about 3-4 years after 1991, have remained more or less constant since 1995. Ischi et al. (1991) estimated the volume of the current instability to be 2.5 – 9 million m^3. Similar to the processes leading to the 1991 failure events, progressive failure is likely to be a process in driving the current movements, which makes the instability an ideal object for studying such phenomena.

1.5 The SNF rockslide project – Phase I, II and III

In 2000, a research project attempting to investigate rock slope progressive failure mechanisms was initiated by the Chair of *Engineering Geology* at ETH Zurich. The PhD thesis present here is part of third and final phase of this multidisciplinary project. The major outcomes of the two first phases are briefly presented in the following sections.

1.5.1 Phase I (June 2000 – May 2002)

The first task within Phase I was to investigate several unstable rock slopes in Switzerland and identify an appropriate site to study progressive failure mechanisms. Randa was found to be an ideal study site, since it consists of massive crystalline rock lacking persistent discontinuities that dip out of the slope, the 1991 rockslide events are well documented, the displacement rates are small, and good accessibility allows extensive geological and geophysical investigations.

After choosing the unstable rock slope in Randa as the project study site, surface geological mapping and fracture characterization was performed in the accessible area of the instability. Futher, the top of the instability was instrumented to capture the spatial and temporal distribution of displacements, pore pressure, and local micro-seismic events. This included drilling of three research boreholes to depths between 50 and 120 m (labelled sb50n, sb50s and sb120), which were used to conduct the following geotechnical investigations:

- Standard borehole logging, i.e. calliper, borehole trajectory, spectral gamma wireline, and optical televiewer logs.
- Periodic measurements of 3D deformation patterns with an inclinometer probe (in all three boreholes) and INCREX extensometer probe (in sb120).
- Continuous displacement measurements with vibrating-wire in-place inclinometers across two fractures in sb120.
- Continuous pore pressure measurements at the bottom of each borehole.

A numerical study of the Randa rockslide events from 1991 was conducted in order to explore the role of deglaciation, internal strength degradation and brittle tensile failure in the evolution of rock slope failure (Eberhardt et al., 2004). It further demonstrated the potential of combining different numerical modelling techniques for understanding progressive failure mechanisms in slopes. They also revealed that high friction angles are required for the pre-failure rock mass to be stable, which points to the presence and importance of intact rock bridges.

1.5.2 Phase II (June 2002 – September 2005)

Phase II of the project was performed in collaboration with the Chair of *Applied and Environmental Geophysics* at ETH Zurich. A 3D geological model of the unstable rock was established by integrating extensive geological mapping with geophysical investigations. 3D-refraction seismic tomography revealed the extent of the unstable rock mass and estimated the percentage of void space within the investigated area to be as much as ~17 % (Heincke et al., 2006b). 3D surface georadar helped identify steeply dipping discontinuities at depth (Heincke et al., 2005; 2006b). With borehole georadar (both cross hole and single hole), various additional discontinuities could be detected that did not daylight at the ground surface (Spillmann et al., 2007a). It was also found that discontinuity persistence at depth can reach 80 m. From the results of all geological data, borehole logs and geophysical investigations, a comprehensive 3D model of the fault system was constructed (Willenberg et al., 2008a).

The opening direction and rate of several discontinuities was measured with both continuous crack extensometers and periodic measurements of benchmark arrays. Surface crack opening, periodic borehole extensometer/inclinometer measurements, as well as geodetic displacement vectors were interpreted in combination with the 3D structural model. Thus, a kinematic model of the unstable rock mass at the top of the instability was derived (Willenberg et al., 2008b). The boundary and internal deformation pattern of the rock mass were found to be mainly controlled by large-scale discontinuities, i.e. pre-existing faults and fracture zones. Shear displacements measured in boreholes were best interpreted to result from block toppling kinematics. A basal sliding surface, as proposed by Sartori et al. (2003) and Jaboyedoff et al. (2004a), was not detected in the deepest borehole. However, the depth of the borehole may have not been sufficient to reach such a surface. All results were limited to the upper 120 m of the instability, while information regarding the extent, structure and kinematics of the unstable rock mass below remained sparse due to inaccessibility. Furthermore, attempts to reproduce the inferred pattern of displacement rates with numerical modelling met with limited success.

A micro-seismic array consisting of 12 three-component geophones was operational at Randa between November 2001 and December 2004. Three geophones were installed at the bottom of each deep borehole, and nine geophones in shallow boreholes at depths up to 5 m. A total of 223 local micro-earthquakes accompanying slope deformation were detected and located with the help of probabilistic location algorithm (Husen et al., 2003). Micro-seismicity tended to be clustered in patches, which correlated with the most active part of the instability and certain active faults. However, some active faults seem to move aseismically. The results were published by Spillmann et al. (2007b).

1.5.3 Phase III (2005 – present)

Phase III of the SNF-funded rockslide research project was performed in collaboration with the Chairs of *Photogrammetry and Remote Sensing* as well as *Geodetic meteorology and engineering geodesy*. It has two main themes. One part involves the objectives and results summarized in this thesis, as outlined in Section 1.2, which include extending the structural and kinematic model to the inaccessible 1991 failure surfaces, as well as investigating the time-dependent behaviour and driving processes of the current instability. The other part is a regional study encompassing the western flank of the Matter Valley between the villages of Randa and St. Niklaus, which has a similar geological and geomorphologic setting as the Randa rock slope. This latter study was performed within the framework of the PhD thesis by Yugsi Molina (2010). A detailed structural analysis based on both field investigations and remote sensing data was performed for the area, and an inventory and classification of rock slope instabilities at different scales was created. It was shown that meso- to macro-scale discontinuities control the occurrence of both smaller rock falls as well as large-scale instabilities. Identified instabilities serve as a basis for various ongoing studies, e.g. regarding the seismic response of rock slope instabilities.

2. MONITORING SYSTEM

2.1 Introduction

Monitoring of displacement, internal deformation, and additional relevant parameters (e.g. groundwater pressure, rock temperature, meteorological conditions, etc.) is essential for understanding kinematics and temporal behavior of an instability. At the Randa instability, geodetic monitoring was initiated by cantonal authorities for long-term surveillance of movements following the 1991 failure events (Jaboyedoff et al., 2004). *In situ* monitoring both at the surface and in boreholes was begun in 2001 within the framework of the ongoing ETH research project. Relevant details of installation, specifications and recorded data from all monitoring components are described by Willenberg et al. (2002, 2004, and 2008b). In 2008, the monitoring system was upgraded with additional instruments and a new local geodetic network, with the goal of investigating the response of the rock slope to thermal effects and seismic loading. In this chapter, all methods and components used in the Randa monitoring scheme are presented.

Figure 2.1 shows an overview of all monitoring components at Randa, while Table 2.1 summarizes relevant details of the systems. The different components are subdivided into two categories: periodic surveys performed at least annually, and components operated by automatic systems recording quasi-continuous data. Periodic monitoring includes geodetic surveying, measurements of benchmark pairs and quadrilaterals, as well as inclinometer and extensometer surveys in the boreholes. Automatic monitoring systems record data measured by meteorological sensors, surface crack extensometers, borehole inclinometers, borehole piezometers, ground temperature sensors, and fiber-optic strain gauges. Also deployed at the site are stand-alone sensors measuring temperature and water pressure. The monitoring system operational between 2001 and 2008 has already been described by Willenberg (2004 and 2008b). For those monitoring components only a short description and an update of new data are presented. Components installed within the framework of this thesis are treated in greater detail in this chapter.

2.2 Periodic surveys

2.2.1 Geodetic measurements

2.2.1.1 Large-scale geodetic network (LSGN)

After the catastrophic failures of 1991, a long-term geodetic monitoring program was initiated by cantonal authorities. It consists of various base stations and reflectors with base-lengths spanning the entire width of the valley (Figure 2.2a). The network was surveyed twice per year between 1996 and 2000, and once per year since 2000. After 2001, the tops of each of the three boreholes were included in the network. Basic distance measurements were performed from two base stations in the valley 2 – 6 times per year. The survey instruments used are Leica type TC5005 total stations (accuracy 1 mm + 1 ppm and 0.1 mgon = 0.4''). The accuracy of the point coordinates within the 3D network is 1.5 – 3 mm horizontally and 4 – 5 mm in height. For the borehole coordinates, accuracies decrease by a factor of two. Absolute distance measurements have accuracy of about 2 – 3 mm. Geodetic surveys were carried out by Aufdenblatten Geomatik, Zermatt.

Displacement vectors resulting from geodetic surveys are presented in Figure 2.2b. Orientations for the borehole tops cannot be considered significant owing to their high location error. Also shown are displacement rates estimated for all 1D reflectors surveyed with simple distance measurements. Time series for five representative points (labeled in Figure 2.2b) are presented in Figure 2.3a. These are referenced to a point located about 250 m behind the instability boundary on stable ground, which partly eliminates errors arising from atmospheric effects. Data demonstrate a long-term linear trend of decreasing distance, except for point 113, which has been stable throughout the entire measurement period. Deviations from the linear trend for the four moving points are shown inFigure 2.3b. Although not significant within the indicated error margins, a slight decrease in the displacement rate can be inferred for all points. Similarly, small annual variations in the displacement rate are visible between 1998 and 2002, for which 3 – 6 repeat measurements were performed per year. Displacements accumulated during this time period are shown in the inset of Figure 2.3a. In summer, these values cannot be considered significant, whereas in winter they are significant at an estimated error of about 2 – 3 mm.

2.2.1.2 Small-scale geodetic network (SSGN)

In 2008 and 2009, a new geodetic network was installed at the top of the instability, with the aim of obtaining greater detail on the spatial displacement pattern, as well as the temporal variation in displacement rate. The network setup is presented in Figure 2.4a. Distances and angles between 3 base-stations and 35 reflectors (Geodata Miniprisms) were measured with a Leica total station (type TPS1201). Details on surveys, data processing, and interpretation of displacement vectors will be described in Chapter 4 (Section 4.4.2) and are not repeated here.

For seven points with significant displacement, and for which a complete set of 11 measurements were available, time series geodetic measurements were assembled and are presented in Figure 2.4b. Although the error is larger than the measured displacement between each time interval, a clear pattern can be observed at all points. Accumulated displacements are only significant in winter, whereas during summer displacements cannot be considered significant at the given error margin. A decrease of displacement rate occurs after snowmelt. Such temporal behavior was also assumed from distance measurements on the LSGN from the valley bottom (Figure 2.3b). The annual displacement pattern will be discussed in detail in Chapter 6.

2.2.2 Benchmark monitoring

2.2.2.1 Benchmark pairs

A series of 14 benchmarks pairs (i.e. rock bolts embedded on either side of a fracture) were installed across a number of different fractures at the instability surface. The distance between each pair was measured by hand with a tape-measure at least once per year. The error of individual measurements was estimated to be 0.5 mm. Figure 2.5a shows the derived fracture opening rates, and Figure 2.5b presents the time series of each measured fracture. Except for fracture q2 and fracture o, the opening rate is nearly linear throughout the measurement period. These fractures were monitored by wire extensometers involving long steel wires with springs and may have larger systematic error than benchmark monitoring (i.e. rock bolt pairs). Estimated long-term opening rates, however, are considered reliable.

2.2.2.2 Benchmark quadrilaterals

To resolve not only the normal but also the parallel component of dislocation across opening fractures, benchmark quadrilateral arrays were installed across four tension fractures. Two rock bolts are embedded on either side of the fracture (making four in total). Distances between each bolt pair is measured with a caliper with accuracy of about 0.2 mm. For data processing, the quadrilaterals are separated into two triangles consisting of a common base-length on one side of the fracture, and one bolt on the other side of the fracture. From the changes of side lengths within each triangle, a displacement vector representing the movement of one block with respect to the other, can be computed with a grid-search algorithm. Comparing the vector for both triangles reveals if both triangles show the same amount of opening, i.e. if the fracture opens non-uniformly at the location of the quadrilaterals. Detailed information on the measurement device, procedure, and processing are described by Willenberg (2004).

Figure 2.5c shows dislocation time series for the four fractures equipped with benchmark quadrilaterals. Figure 2.5d indicates the direction of movement relative to the fracture orientation. Fractures open at a rate of 1.9 – 3.5 mm/yr. All dislocation vectors show a slight deviation from the normal to the fracture and thus all have a small component of shearing combined with opening. The two vectors resolved from both triangles did not differ significantly for any of the fractures. Combined interpretation of fracture opening rates, opening directions, and geodetic vectors will be presented in Chapter 4.

2.2.3 Inclinometer and extensometer surveys

Inclinometer surveys within all boreholes were performed annually between 2001 and 2008. In borehole sb120, complementary extensometer surveys were carried out on the same dates. Inclinometer surveys measure a change in inclination with respect to the first survey resulting from dislocation between the two ends of the probe. Multiplying the inclination change by the base-length of the probe (0.61 m in our case), displacement of the lower end of the instrument with respect to the upper one can be obtained. Two horizontal components are measured along two perpendicular grooved slots carved into the inclinometer casing, which lead the inclinometer guiding wheels. The extensometer (INCREX probe) measures changes in distance between the lower and the upper end of the probe (base-length of 1 m), with positive values denoting extension. Data can be presented both as incremental or cumulative displacements. Incremental, horizontal inclinometer displacements have an accuracy varying between 0.21 mm (for 0° inclination) to 0.75 mm (for 15° inclination). Vertical displacement measurements from the extensometer have accuracy of 0.01 mm. For a cumulative representation of displacements, the incremental errors sum and can become substantial. Thus, error propagation has to be carefully assessed and can only be estimated conclusively if the bottom of the borehole is known to be in stable ground, and accurate measurements of the borehole top are available. At Randa, errors in cumulative inclinometer data were investigated in detail by Willenberg (2004 and 2008b) following the suggestions by Mikkelsen (2003). This includes correction for torsion of the inclinometer grooves at depth, mismatch of depth scales between the first and repeat surveys, as well as errors introduced through misalignment of the sensors within the probe. The cumulative data presented here follow recommendations regarding these errors suggested by Willenberg et al. (2008b). Corrections for torsion error and depth mismatch were applied, while the error for sensor misalignment cannot be estimated conclusively. Sensor misalignment, however, can produce substantial errors in cumulative displacement patterns, which likely also exist in the datasets presented here.

Both incremental and cumulative displacements measured in borehole sb120 are presented in Figure 2.6. The figure also includes additional inclinometer surveys from 2007 and 2008 and an extensometer survey from 2007, which were not yet presented by Willenberg et al. (2008b). Further shown are the orientations of the grooves within the inclinometer casing. Patterns of horizontal displacement show distinct displacement concentrated across active discontinuities. The block below the discontinuity moves relative to the upper block into the main direction of instability movement (~135°). Axial shortening is measured across the same discontinuities. Such behavior is best interpreted as normal faulting across discontinuities dipping into the slope. In between these discontinuities, small negative displacements systematically increasing with time indicate block rotation towards the main direction of movements. The overall pattern was interpreted as block toppling, as shown in the conceptual kinematic model by Willenberg et al. (2008b) and included in Figure 3.11. This same behavior can also be deduced from the cumulative displacement patterns. Despite careful consideration of all errors sources, it remained inconclusive whether borehole sb120 reaches stable ground. A basal sliding surface as detected by GB-DInSAR data (see following chapter) would lie below the bottom of the borehole if it is planar, but may intersect the borehole if it is stepped. Thus, from the findings of the two following chapters no final conclusion can be drawn as well. The small displacement magnitudes and the accuracy of the measurements limited by uncorrected errors (sensor misalignment error) prevent more detailed interpretation of the cumulative displacement patterns.

Figure 2.7 and Figure 2.8 show displacement patterns within boreholes sb50n and sb50s, respectively. In sb50n, the last repeat measurement in 2008 shows a pattern that deviates strongly from the other years. It was not possible to determine the reason for this anomalous behavior, but it is most likely caused by erroneous handling of the instrument during the survey. Overall patterns measured in both boreholes confirm the rock mass behavior deduced from borehole sb120. Displacements are best interpreted as toppling of stiff blocks. A complete kinematic interpretation of borehole deformations is presented in Willenberg et al. (2008b).

Due to strong borehole deformations in borehole sb120, extensometer measurements became problematic, since the 1 m INCREX probe became stuck in a narrowed section at 5 m depth. Thus, no extensometer survey was conducted in 2008. Since the borehole became inaccessible for further deformation surveys, a new instrumentation final solution was planed for this borehole. This enabled installation of fiber-optic strain sensors, which were fully embedded in grout (see Section 2.3.9).

2.3 Automatic monitoring system

2.3.1 Data acquisition systems

Two independent automatic monitoring systems are deployed at the study site. 1) All vibrating-wire sensors, meteorological sensors, and thermocouples are read every 30 min by a Campbell Scientific CR-10X datalogger, and data are transferred via dial-up mobile network connection. 2) A total of 11 fiber-optic strain sensors are controlled by a recording unit and a local PC installed at the site. Data are transferred via wireless internet connection from the PC. Both monitoring systems are powered by solar panels. A detailed sketch showing all monitoring components is presented in Figure 2.9.

Vibrating-wire sensors (i.e. three borehole piezometers, two in-place inclinometers, and two crack extensometers) were installed between 2001 and 2004 (Willenberg, 2004). In 2008 and 2009, a group of meteorological sensors (relative humidity, air temperature, barometric pressure, and a rain gauge), and two thermocouple arrays were added. A multiplexer (type AM16/32B from Campbell Scientific) was required for sequential reading of 14 thermocouples. Similarly, a multiplexer (type MultiMux from Canary Systems) was used to sequentially read all vibrating-wire sensors. The in-place inclinometer previously positioned at 68 m was repositioned to 12 m depth during installation of the fiber-optic strain sensors in borehole sb120. Another inclinometer was operational at a depth of 85 m within borehole sb120 between 2004 and 2008. However, that sensor measured strong daily signals correlated with battery voltage and unstable noise levels on one axis. The inclinometer was assumed to be malfunctioning and removed in 2009.

A fiber-optic strain system was installed in summer 2008. The sensors consist of optical fiber cable serving as a waveguide for broadband laser pulses. The sensing portion consists of an etched section of the waveguide with alternating refraction indices (so-called fiber Bragg gratings). Depending on the length of these sections, a certain wavelength is enhanced through constructive interference and reflected back to the optic interrogator (Micron Optics SM130) and processing unit (Micron Optics SP130). The system as provided by Smartec SA is branded 'MuST'. It operates at a sampling frequency of 100 Hz. Recordings have a repeatability of 0.5 $\mu\varepsilon$ (which may be further increased by averaging), and stability better than 2 $\mu\varepsilon$. Data are recorded on a PC, and the system is configured to store data both in a triggered and an averaging mode. A fully-sampled 30 s time series is recorded if strain exceeds a certain threshold above the average; otherwise a five minutes mean from the circular buffer is stored. Sensors were installed across active fractures at 38, 40, and 68 m depth in borehole sb120, as well as across fractures Z9 and Z10 (note that Z9 and Z10 correspond to benchmarks q2 and x2 in Figure 2.5, respectively). In the borehole, three identical sensor chains were installed with three sensors located at each monitoring depth. Each of the three sensor chains is read in serial mode. Two chains are actively measured to ensure redundant data at each depth. The third chain was installed as back-up, if one of the other two sensor chains fails. This was the case after July 2010, when the two lower sensors (at 40 and 68 m depth) along one chain did not return the laser signal. It was assumed that shearing along a connection point at 40 m destroyed the optical fiber. The third chain was then activated and has produced meaningful data since then. Details of the installation and first measurements were presented by Moore et al. (2010).

2.3.2 Meteorological parameters

Meteorological sensors became operational in October 2008 (Figure 2.10). Mean annual air temperature estimated from fitting a sinusoidal curve with a one year period to air temperature data is ~1.9 °C. The maximum temperature measured since installation was 21 °C, the minimum value was -19 °C.

A rain gauge was installed in June 2009. The rain gauge bucket is not heated, so winter time precipitation cannot be measured. Also apparent rainfall events during snowmelt may reflect melting of snow collected within the bucket rather then true rain events. The cumulative measured rainfall was 210 mm between June and November 2008 and 310 mm in summer 2009. The mean precipitation in the Matter valley is about 500 mm.

Snow height is not measured at the Randa site. Presented data are taken from the two closest SLF meteo stations: 'Triftchumme' lies at 2750 m elevation about 9 km south of Randa close to Zermatt, while 'Stelligletscher' is at 2910 m about 6 km north of Randa above St. Niklaus. These data give important information on first snowfall, major snowfall events, and regarding the onset of snowmelt. However, the snow height at our study site may be significantly different. During winter field visits the snowpack at Randa was found to be strongly affected by wind transport and highly spatially variable.

2.3.3 Crack extensometers

Fracture opening time series for fractures Z9 and Z10 are presented in Figure 2.11a. Both fractures show a constant long-term opening rate between 2003 and 2010 of about 2 mm/yr. The same rates were obtained from benchmark monitoring. Both fractures also show a superimposed seasonal pattern, with closure during summer and opening in winter. The seasonal pattern is more emphasized at Z10, since the instrument is snow-free during most of the winter. In contrast, Z9 is covered by thick snow in winter, which insulates the rock from temperature fluctuations. Thus, opening rates in winter are characterized by a very low noise level and are nearly linear. Similarly, winter temperature data recorded by the instrument's built-in sensors show extended periods when temperatures at Z9 are close to zero and temperatures at Z10 are negative (Figure 2.11b). During summer, temperatures measured at both fractures mimic each other well. The seasonal displacement pattern marked by high rates in winter and lower or negative rates in summer is related to thermal effects. The trend can be explained by thermal expansion and contraction of the fracture walls. Such effects are discussed in detail in Chapter 5 and 6. Note that time series in Figure 2.11 are all filtered with a 3-days low-pass filter.

2.3.4 In-place inclinometers

In 2004, two in-place inclinometers were installed in borehole sb120 across actively deforming fractures detected with periodic inclinometer/extensometer surveys. The instruments are emplaced in a special inclinometer casing with grooved channels holding the guiding wheels of the probe. Two sensors measure inclination along two perpendicular axes. Multiplying the change in inclination by the probe base-length of 1.87 m gives the displacement of one end of the instrument with respect to the other. Also included in each probe is a thermistor for temperature correction.

Displacement time series from the two different depths are presented in Figure 2.12. Both displacements from the two axes (Figure 2.12a, b), as well as the magnitude of the displacement vector (Figure 2.12c) are shown. Positive displacements denote movement of the lower block with respect to the upper block in the direction indicated with a sketch of the inclinometer casing. All displacement time series show an annual trend. Acceleration of displacement occurs in late Fall around the time of first snowfall, while deceleration occurs after snowmelt. To illustrate this trend, time series in Figure 2.12c are colored blue if the air temperature is below 0 °C and red otherwise (before 2008 the temperature at fracture Z10 was taken as an approximation). We suggest, that this annual pattern is related to rock temperature changes and further explore this hypothesis in Chapter 5 with combined analysis of all monitoring data.

Displacement orientations for both depths are presented in Figure 2.13. Time series for both axes were filtered with a 5-days low-pass filter, and resampled every 10 (at 68 m) or 5 days (at 12 m). Displacement data are colored blue if the air temperature is negative and red when it is positive (similar as in Figure 2.12c). Also shown is the strike of the monitored fractured as derived from optical televiewer logs (Willenberg et al., 2008a). Slight annual changes in displacement direction occur at both depths, however this is more pronounced at 12 m. The displacement direction at 12 m turns towards the south (azimuth of 167°) during summer and then towards the east (azimuth of 133°) during winter. Such seasonal patterns in displacement direction can only be understood as a combination of both the primary driving mechanism leading to seasonally-variable displacement rates, as well as the complex kinematics of the rock mass.

The temperature at 68 m depth was constant at 4.0 ± 0.2 °C (Figure 2.12d). At 12 m depth, a small annual temperature signal of about 0.6 °C amplitude is superimposed on a mean value of about 4.3 °C. The temperature maximum occurs in January, the minimum in July/August. Displacement time series change only marginally if correction for these slight temperature changes is applied.

2.3.5 Piezometers

A single piezometer with embedded thermistor is installed at the bottom of each of the three boreholes. The instruments are placed below a slotted section of the borehole casing that is filled with sand, thus ensuring free movement of water from the rock mass (Willenberg, 2004). Piezometric pressure at 120 m in borehole sb120 and at 50 m in sb50s is presented in Figure 2.14a, along with the barometric pressure since 2008. Since 2005, borehole sb120 has shown pressure variations correlating with barometric pressure and a mean pressure corresponding to air pressure at an altitude of 2230 m. No lag or attenuation of the pressure signals at depth with respect to barometric pressure can be observed, which points to high pneumatic permeability of the rock mass (see inset figure). In contrast, the measured pressure in borehole sb50s corresponds to 3 – 4 m of water column. The pressure increases within a few days during snowmelt and slowly decays over the rest of the year. Minor, fast pressure increases occur after heavy rainfall events. During times of pressure maxima, fluctuations correlate with barometric pressure. In contrast, during times of pressure decay the signals are strongly attenuated compared to barometric pressure.

The piezometer at 50 m depth in borehole sb50n appears to be malfunctioning, since it typically measures unreasonably high or low values. Only during a few short periods does the sensor measure data that correlates with that from sb120 and barometric pressure. An example time period during which the sensor produced several intervals of presumably meaningful data is shown in the inset of Figure 2.14. Erroneous data (i.e. pressure values below 500 kPa or pressure changes of more than 20 kPa per sampling interval) are cut from this time series. Although the data mimic the pressure recorded in borehole sb120 and the barometric pressure well, the values consistently lie below the other two pressure measurements. Pressure data may also suffer from an offset in addition to the suggested malfunction. However, observed correlation with barometric pressure and pressure of the dry borehole sb120 suggests that borehole sb50n may also be dry.

Temperatures measured at the bottom of each borehole are presented in Figure 2.14b. Mean temperatures are 4.2, 3.5, and 3.1 °C in sb120, sb50s, and sb50n, respectively. While temperatures in sb120 and sb50s are constant throughout the entire monitoring period, a small annual temperature signal of about 0.3 °C amplitude is found in borehole sb50n. This annual signal is discussed in more detail by Moore et al. (2011, in preparation) and in Chapter 7.

2.3.6 Error signals in Vibrating-Wire sensor data

Daily signals were detected in all time series vibrating-wire (VW) sensor data, although these were small in amplitude. We shortly present and discuss these signals here, since they set a limitation on data interpretation on a daily basis. Figure 2.15 presents a typical portion of 10 days of VW sensor data from Randa. Also included is the voltage of the datalogger battery that is charged by a solar panel. The battery voltage shows a typical daily signal with high voltage during charging in the day and lower voltage at night. Both the inclinometer and the piezometer data show a daily signal, which can be seen to strongly correlate with battery voltage. Note that temperature at these two sensors is constant. The crack extensometer temperature was also constant during this time period, since the sensor was covered by a thick, insulating snowpack. A small daily noise signal can also be observed, which is not as pronounced as in the other time series. The daily signal amplitudes are all below the level of accuracy given by the sensor manufacturer. We assume these are controlled by the datalogger electronics, and caution that such daily signals should not be interpreted as real signals.

2.3.7 Ground temperature

Rock and soil temperature profiles are measured with two independent vertical arrays of thermocouples. The array in rock consists of nine thermocouples grouted in a 4 m deep borehole at depths of 0, 0.02, 0.08, 0.16, 0.32, 0.5, 1, 2, and 4 m. Soil temperatures are measured with an array of 0.5 m depth consisting of four thermocouples buried into soil about 5 m away from the rock temperature borehole (depths: 0.02, 0.16, 0.32, 0.5 m). Another thermocouple was drilled 50 mm into a small sub-vertical rock face that is not covered with snow in winter, to measure rock surface temperature that is more representative of conditions on the 1991 failure surface.

Thermocouples are passive sensors. They rely on a voltage difference developed at the sensing junction, where two metals with different electric properties are connected. Voltage is a linear function of temperature (within the measurement range). However, the voltage as read by the multiplexer does not correspond to an absolute temperature, since additional voltage develops at the ports where the thermocouple wires are connected to the multiplexer. Since this voltage is also dependent on the multiplexer temperature, an independent thermistor measuring temperature of the multiplexer is required as a reference. According to the manufacturer, a local temperature gradient within the multiplexer can result in slightly erroneous temperature readings (Campbell Scientific, 2008). Minimizing such effects requires careful insulation from ambient temperature fluctuations. In our case, this was achieved with an additional cover packed with insulating material around the multiplexer box.

Rock and soil temperatures as a function of time and depth are presented in Figure 2.16a and b. Time series were filtered with a 3-day low-pass filter. Rock temperatures at 4 m depth vary between ~2.5 and 9.5 °C. Although the sensor location is covered with snow in winter, negative temperatures penetrate up to 1.2 m depth at maximum. In soil, on the other hand, negative temperatures penetrate only to about 0.4 m depth. Figure 2.16c compares surface temperatures of rock, soil, and the steep rock face with ambient air temperature measured at the site. The highest summer temperatures are measured at the rock face. In winter, the highest temperatures are measured beneath snow cover on the soil surface.

A 10 days portion of daily temperature signals are presented in Figure 2.17a and b. Temperatures from the steep rock face generally have similar amplitudes as the top of the rock borehole. The onset of warming in the morning, however, is earlier due to the rock face's easterly aspect. Soil temperatures at depth show a much stronger attenuation of the surface temperature signal as compared to similar depths in rock, revealing the insulating effect of soil cover. As shown in Figure 2.17c, small daily signals are also recorded at depths of 1, 2, and 4 m, where no daily signal should be measureable. Also shown is the temperature of the reference sensor in the multiplexer box. Daily maximum and minimum temperatures correlate with strongest heating and cooling of the reference sensor. During strongest temperature changes within the box, the strongest gradients across the multiplexer can be expected. Such an imbalance between the measured reference temperature and the real value at the thermocouple ports results in small erroneous temperature signals. The induced signals at depth have amplitudes of about 0.5 °C. Thus, daily temperature signals with amplitudes of this order are not interpretable.

From the temperature time series measured at different depths *in situ,* thermal properties of the various media can be estimated. The 1D-heat equation including time-dependent heat conduction, is given by:

$$\frac{\partial T}{\partial t} = \alpha \frac{\partial^2 T}{\partial z^2}, \qquad (2.1)$$

where z is depth [m] and α is the thermal diffusivity [m^2/s] (Guegen and Palciauskas, 1994). The reaction of a harmonic temperature disturbance at depth z_o can be derived from this equation and expressed as:

$$T(z,t) = T_o(z_o) \cdot e^{-k(z-z_o)} \cdot \sin(\frac{2\pi t}{\tau} - k(z - z_0)), \qquad (2.2)$$

Here T_o is the amplitude of the temperature wave at z_o, and τ the period of the harmonic wave. The constant k depends on the period τ and thermal diffusivity α as:

$$k = \sqrt{\frac{\pi}{\alpha\tau}}, \qquad (2.3)$$

To estimate the thermal diffusivity from *in situ* measurements, we fit a sinusoidal temperature history with a one year period to the measured time series. Through this first-order approach, we obtained an estimate of the mean annual temperature, the amplitude of the annual signal, as well as the phase lag at different depths with respect to the surface temperature history. The results of these estimates are presented in Figure 2.18. According to Equation (2.2), the amplitude $T_o(z)$ at depth z is predicted from the temperature amplitude T_o at the surface as:

$$T_0(z) = T_o \cdot e^{-kz}, \qquad (2.4)$$

or on a logarithmic scale,

$$\ln(T_0(z)) = \ln(T_o) - kz, \qquad (2.5)$$

Similarly, the phase lag $\Delta\varphi(z)$ is:

$$\Delta\varphi = -kz, \qquad (2.6)$$

Thus, applying linear regression to the logarithms of the amplitude and the phase lag estimates in Figure 2.18b and c, an average thermal diffusivity of both rock and soil can be obtained. Resulting thermal diffusivity for rock is 2.16E-6 m^2/s derived from amplitude and 1.97E-6 m^2/s derived from phase lag. The thermal diffusivity of soil is one order of magnitude lower: 2.8E-7 m^2/s (amplitude) or 2.3e-7 m^2/s (phase lag).

2.3.8 Stand-alone temperature loggers

For additional distributed temperature measurements, several stand-along temperature data loggers were deployed at the site. Three UTL sensors (Universal Temperature Loggers, Geotest AG) were used to record temperature in an open fracture showing winter time air ventilation. The temperature sensors are embedded in a water proof casing, which is equipped with long-lived battery and storage allowing for data recording of up to 2 years (at a sampling rate of 15 min).

For additional borehole temperature measurements, including both long-term monitoring and borehole profiling, 'Keller Druck' sensors (type DCX-22) were used. The sensors, although built to record pressure, also include temperature sensors. These temperature sensors, however, were found to be offset and needed to be calibrated in an ice-water bath to obtain accurate absolute temperature data.

Data recorded with UTL and Keller sensors are presented by Moore et al. (2011) and in Chapter 7 dealing with convective temperature disturbances in the rock mass at Randa.

2.3.9 Fiber-optic strain sensors

Sections 2.3.2 to 2.3.7 above describe vibrating-wire sensors as well as sensors measuring complementary parameters that are read by a Campbell Scientific CR-10X datalogger. An independent strain monitoring system, namely a fiber-optic sensor system, was installed in 2008, and is described in the following. The objective of installing this system was to record dynamic strain measurements during earthquakes. Further, long-term strain time series with a sampling rate of 5 minutes were recorded, providing additional measurements of temporal deformation behavior within and at the surface of the unstable rock mass. First results of strain recordings were presented by Moore et al. (2010). Here, we present up to date fiber-optic strain time series. Dynamic records triggered during a small nearby earthquake in May 2010 are presented in Chapter 7.

Data from fiber-optic crack extensometers are shown in Figure 2.19a and b, along with the complementary data measured by neighboring VW extensometers. The time series from both sensor types mimic each other well. Due to the limited measurement range of the fiber-optic sensors, the sensor string has to be re-tensioned each year. After overly destressing the sensor at fracture Z9 in September 2009, fiber-optic data deviated from VW data for a short period. After about one month, however, fracture opening had sufficiently retightened the sensor that it worked properly again. Generally, the fiber-optic sensors have a much lower noise level than VW extensometers, which allows more detailed interpretation. Similar to VW sensors, FO signals must be corrected for temperature induced strain, which does not reflect real rock mass deformation. Daily signals that remain in the time series after temperature correction are, however, still not considered reliable and may result from inaccurate temperature correction or strong temperature gradients on the sensor. Interpretation of daily signals is thus problematic and is only possible during times of constant temperature at fracture Z9 (i.e. when the sensor is covered by thick snow).

Data measured in the borehole at three depths are presented in Figure 2.19d to e. All sensors measure shortening caused by the vertical component of normal faulting dislocation along the monitored discontinuities. Moore et al. (2010) mention that a period of increased shortening rates occurred during the first 100 days after installation, which likely resulted from drying shrinkage of the grout. Here, we only present data from January 2009 to avoid this transient accommodation time. Data from both sensor chains are shown for each depth. In July 2010, sensor chain B stopped working and the reserve chain R was activated. The sensors at each depth show similar long-term behavior with similar rates, and a seasonal pattern showing higher deformation rates in winter and slower rates in summer. This confirms the seasonal pattern observed in inclinometer data.

Superimposed on the long-term strain trend are transient signals that are characterized by abrupt periods of extension followed by a period of an increased shortening rate that eventually decays back to the long-term value. Often these transient extensions occur simultaneously on both sensors, sometimes however only on one sensor. A few of these transient signals were sufficiently large to trigger 100 Hz recordings (see Moore et al., 2010; Figure 5 for an example). The origin of these transient signals remains unresolved to date. Slip of the sensor anchors on the steel wire, to which the sensors were initially attached, cannot serve as explanation, since this would result in rapid shortening instead of extension. One possible explanation could be breaking up and shearing of the grout around the sensors resulting in localized dilation. However, such signals may also reflect the real rock mass kinematics. Besides slow normal faulting and opening along these discontinuities, short-term behavior may start with abrupt downward movement of the lower block producing extension, followed by slower downward movement of the upper block seen as shortening. Another possible explanation is intermitted activation of sliding on nearby discontinuities. In Figure 2.19c to e, the cumulative number of recorded transient signals is shown. Note that only transient signals recorded on both coincident sensors (from the identical chains) were considered, while additional signals recorded by only one sensor were discounted. Especially at 68 m depth, it can be seen that transient signals occur predominantly during winter, i.e. at times of enhanced deformation.

Table 2.1: Summary of all monitoring methods applied at the Randa instability.

Method / Instrument type	Number	Since	Sampling period	Accuracy
Periodic surveys				
Geodetic networks:				
Large-scale network (total station TC5005)	7 3D + 20 1D reflectors	1996	1 year	~2 – 6 mm
Small-scale network (total station TPS 1201)	35 1D reflec-tors	2008-2009	~1 month	~2 – 3 mm
***Benchmark pairs**:*				
Rock bolts & tape-measure	12	2001	~0.5 year	0.5 mm
Benchmark quadrilaterals:				
Rock bolts & modified caliper	4	2002/2003	~0.5 year	0.3 – 0.5 mm
Inclinometer:				0.21 mm (0° tilt)
Servo-accelerometer	1	2001	0.5 – 1 year	0.75 mm (15° tilt)
Extensometer:				0.01 mm
Induction-coil transducer	1	2001	0.5 – 1 year	
Automatic monitoring system				
Meteorological sensors:				
Relative humidity (HMP45C*)	1 each	2008	30 min	2 – 3 %
Air temperature (HMP45C*)		2008		0.2 – 0.4 °C
Barom. pressure (CS100*)		2008		0.5 – 2.0 hPa
Rain gauge (ARG100*)		2009		?
Crack extensometers:			6 min (2001 – 2004)	
Vibrating Wire	2	2001	1 hr (2004 – 2008)	0.15 mm
(Geokon model 4420)			30 min (2008 – pres.)	
In-place inclinometer:			6 min (2001 – 2004)	
Vibrating Wire	1 – 2	2003	1 hr (2004 – 2008)	0.09 mm
(Geokon model 6300)			30 min (2008 – pres.)	
Piezometer:			6 min (2001 – 2004)	
Vibrating Wire	3	2001	1 hr (2004 – 2008)	1.75 – 3.5 hPa/°C
(Geokon model 4500)			30 min (2008 – pres.)	
Ground temperature sensors:				
Thermocouples (105E*)	14	2008/2009	30 min	0.5 °C
Temperature dataloggers:				
UTL dataloggers	3	2008-2010	15 min	0.1 °C
Keller druck sensors	2		30 min	0.5 °C
Dynamic strain sensors	3x3 in bore-hole		0.01 s (triggered mode)	Resolution: 0.5 με
Fiber-optic sensors	2 on surface	2008	5 min (averaging mode)	Accuracy: 2 με

** Campbell Scientific Sensors*

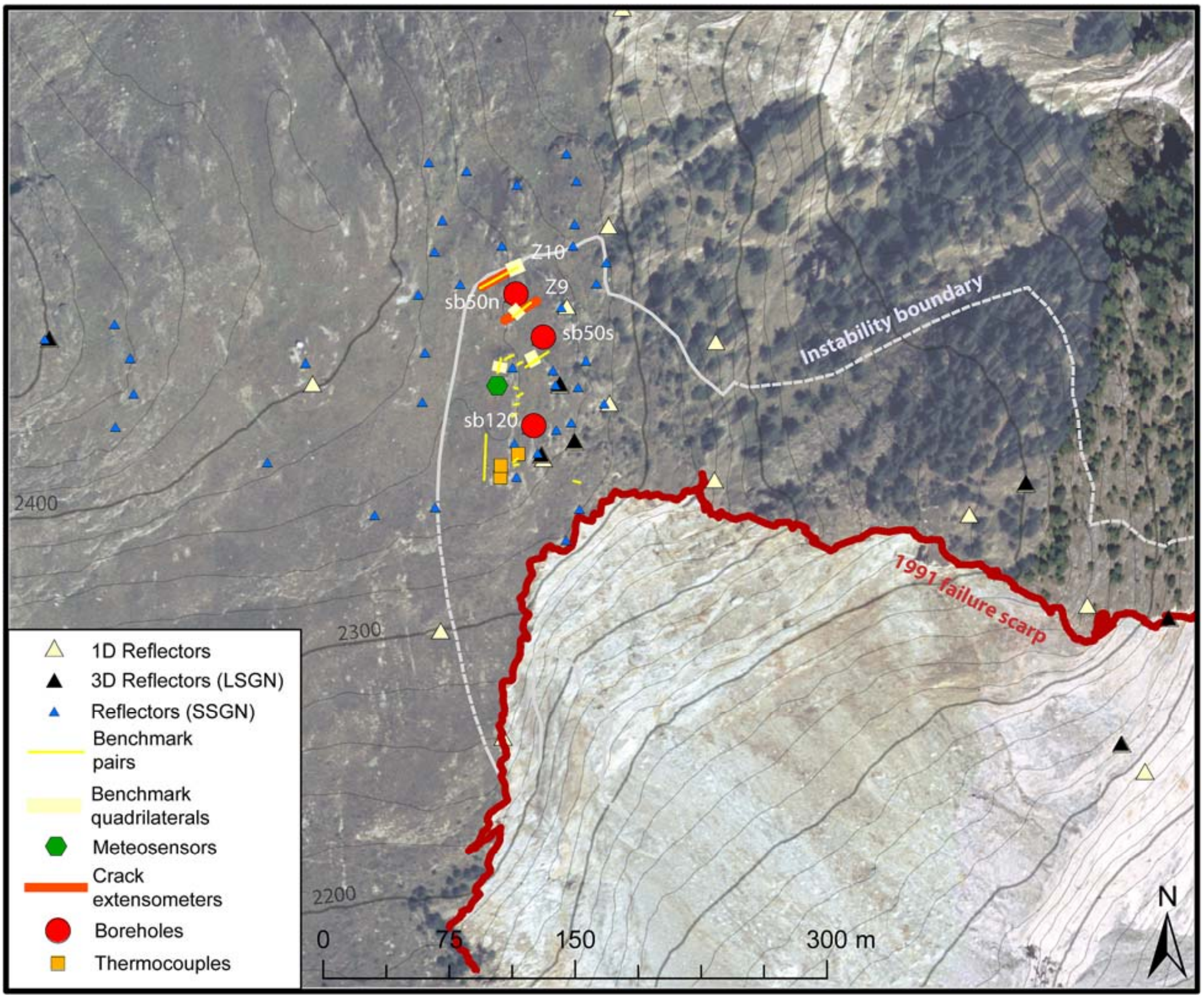

Figure 2.1: Summery overview of monitoring systems at the Randa instability, including geodetic surveys of a small-scale network (SSGN) and a large-scale network (LSGN), manual measurements of benchmark pairs and quadrilaterals, as well as various sensors at the surface and in boreholes measured automatically.

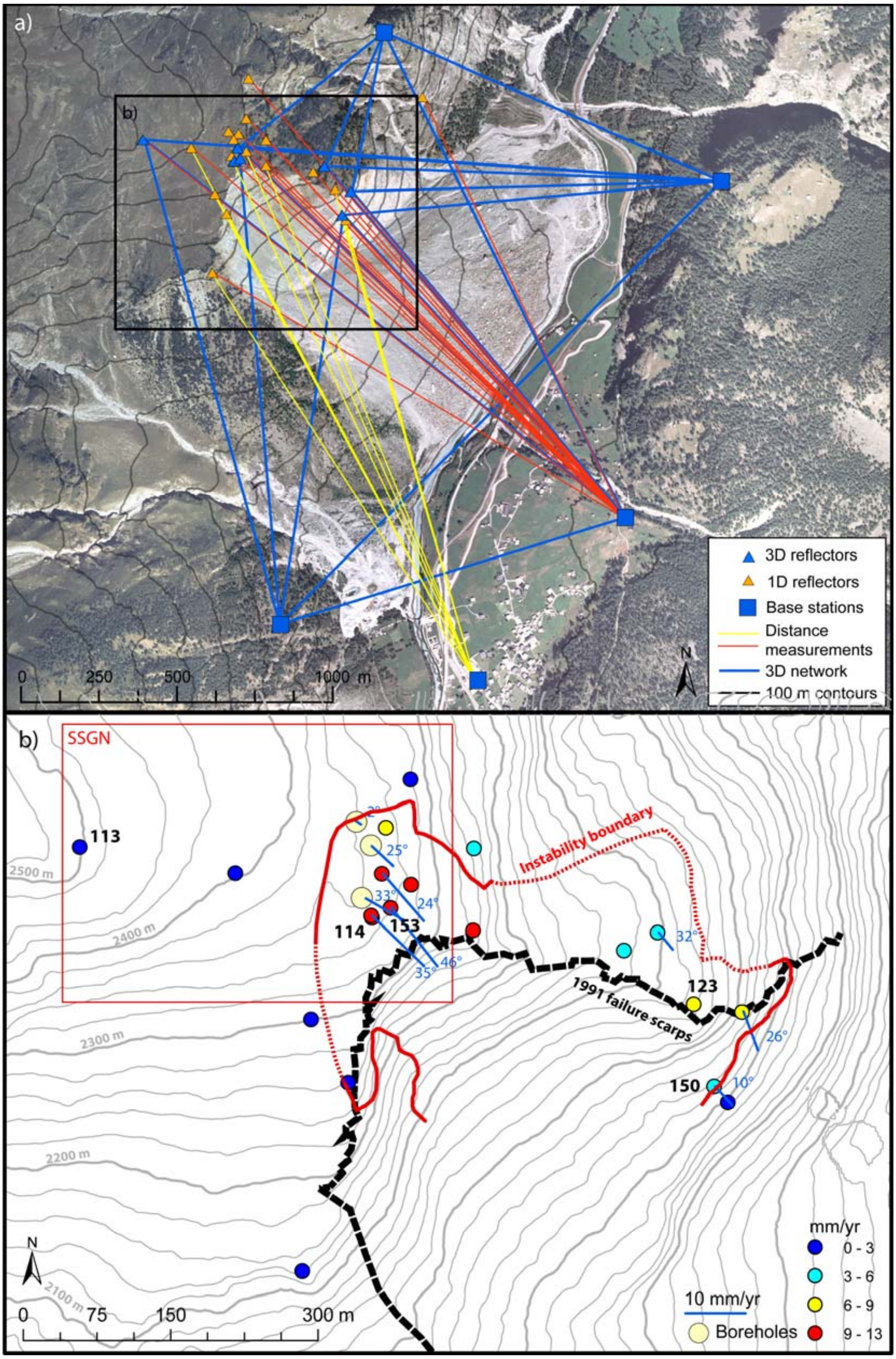

Figure 2.2: a) Network setup for the large-scale geodetic network, including different measurement baselines. b) Results of both 3D geodetic surveys (vectors) and basic distance measurements (color-scaled points; see legend). For vectors, a reference length is given in the legend, while the plunge angle is indicated. Time series for labeled points 113, 114, 123, 150, and 153 are shown in Figure 2.3a.

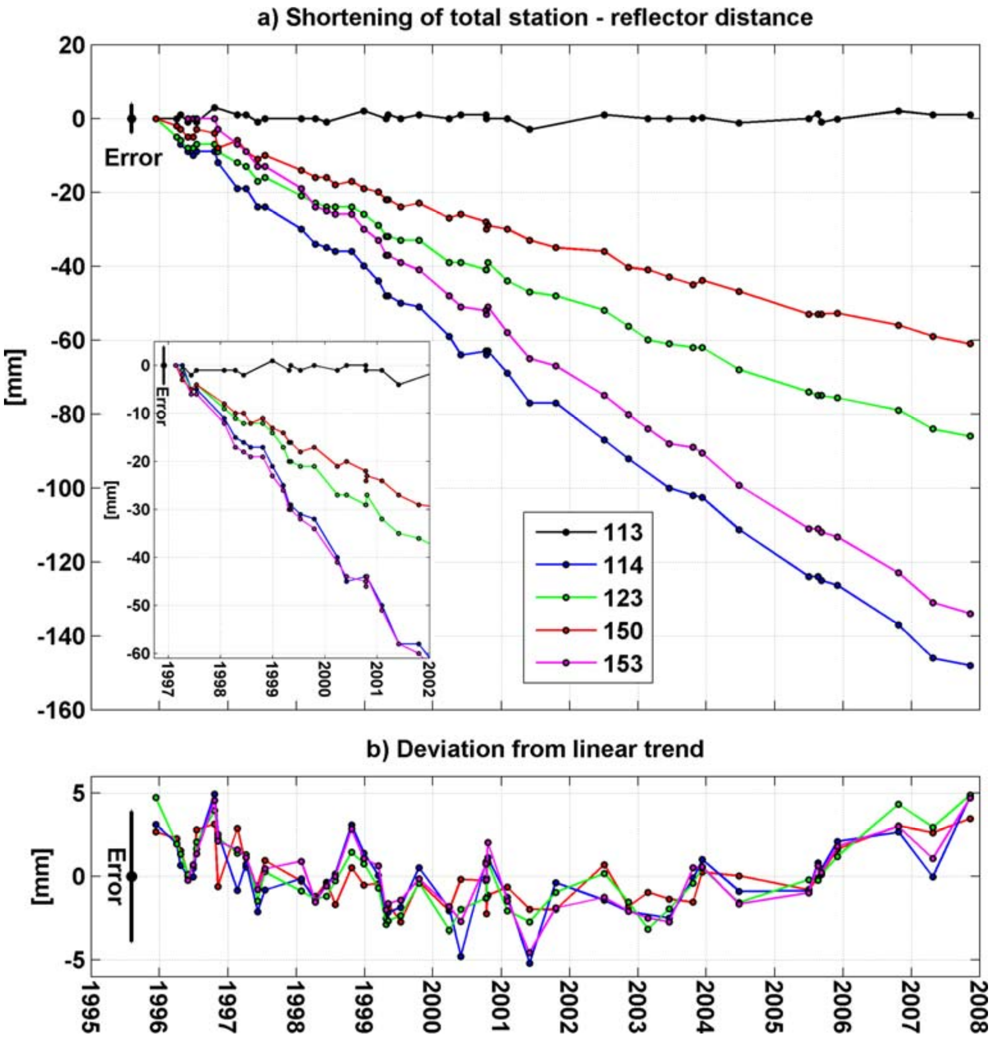

Figure 2.3: a) Time series of five representative points for which only distance measurements are available, showing the long-term displacement of the instability. Displacements are all referenced to a stable point 250 m behind the instability. Inset figure shows a detail of the time period between 1997 and 2002 when 3 – 6 measurements per year were preformed, and which shows slight annual changes in the measured displacement rate. b) Time series of the four moving points in a) with the linear trend removed.

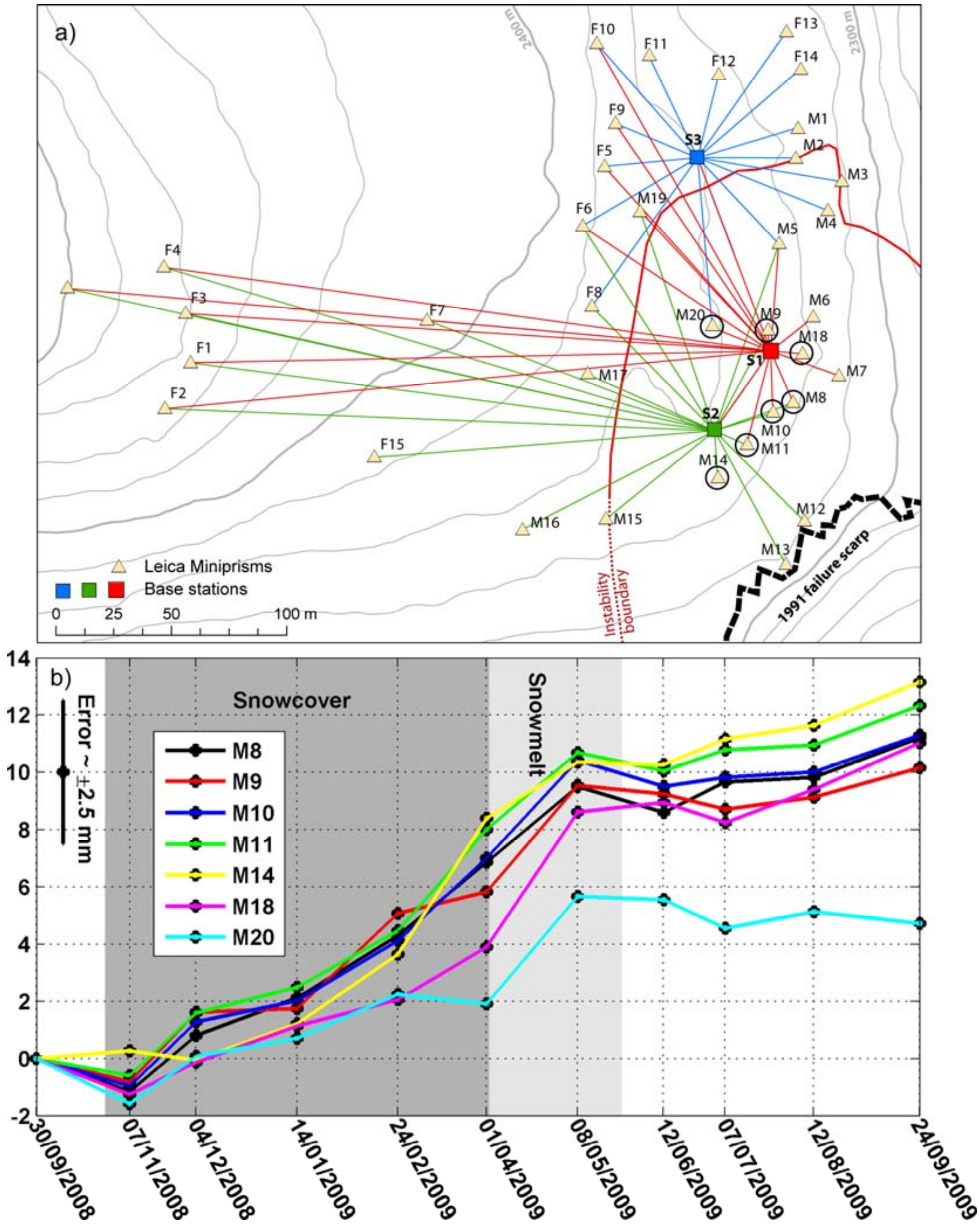

Figure 2.4: a) Network setup of the small-scale geodetic network installed at the top of the instability. Fixed points (labeled F) and monitoring points (labeled M) were measured from three base stations (labeled S). b) Time series for the seven points circled in a). Also shown is the estimated error for individual measurements. A change of displacement rates can be deduced with higher rates in winter and smaller rates in summer.

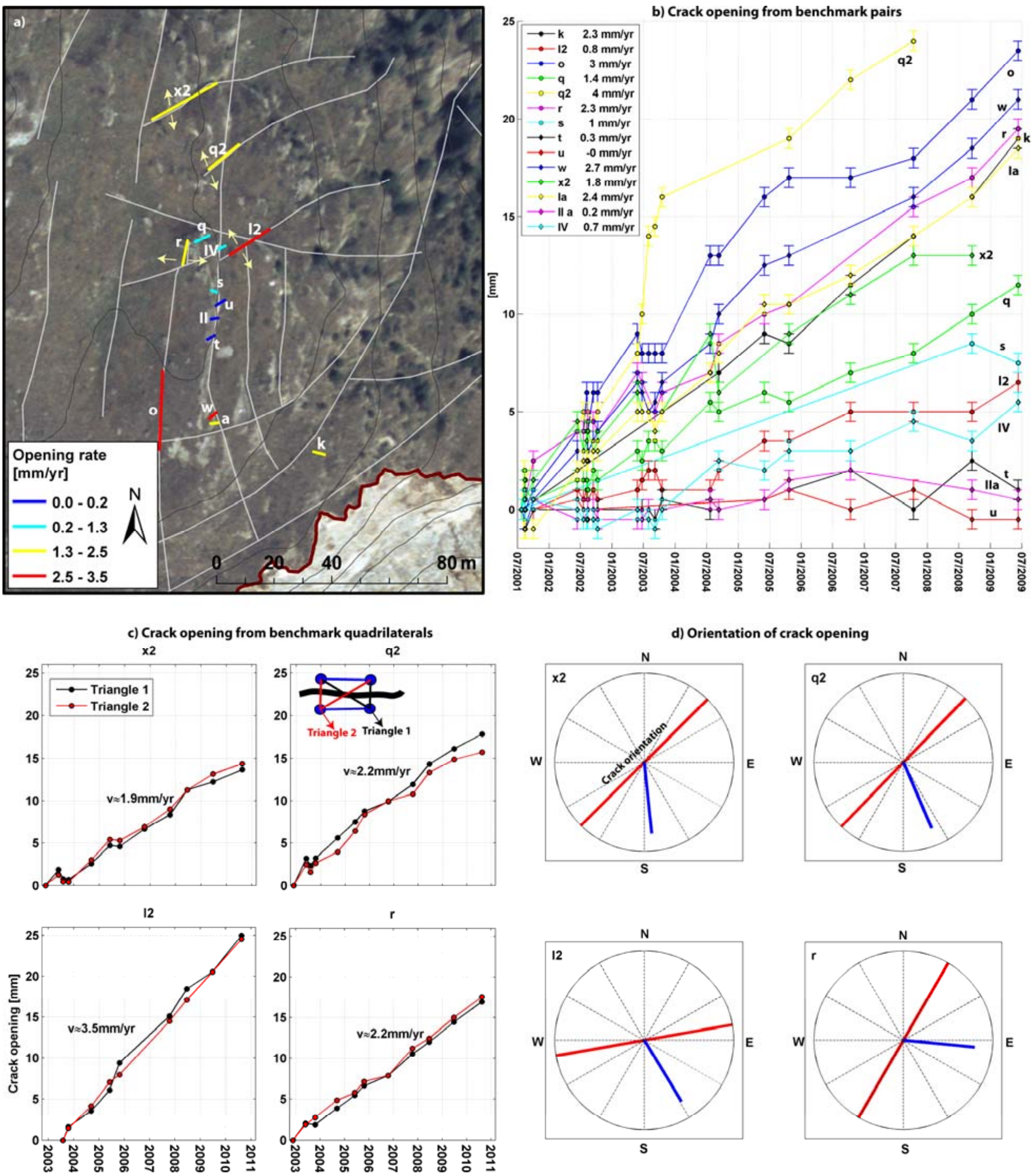

Figure 2.5: a) Locations and rates of benchmark pairs and quadrilaterals (vectors). b) Time series of all manually measured fracture openings. c) Time series of benchmark quadrilateral displacements. Displacements from both triangles do not differ significantly. d) Directions of fracture opening derived from benchmark quadrilaterals.

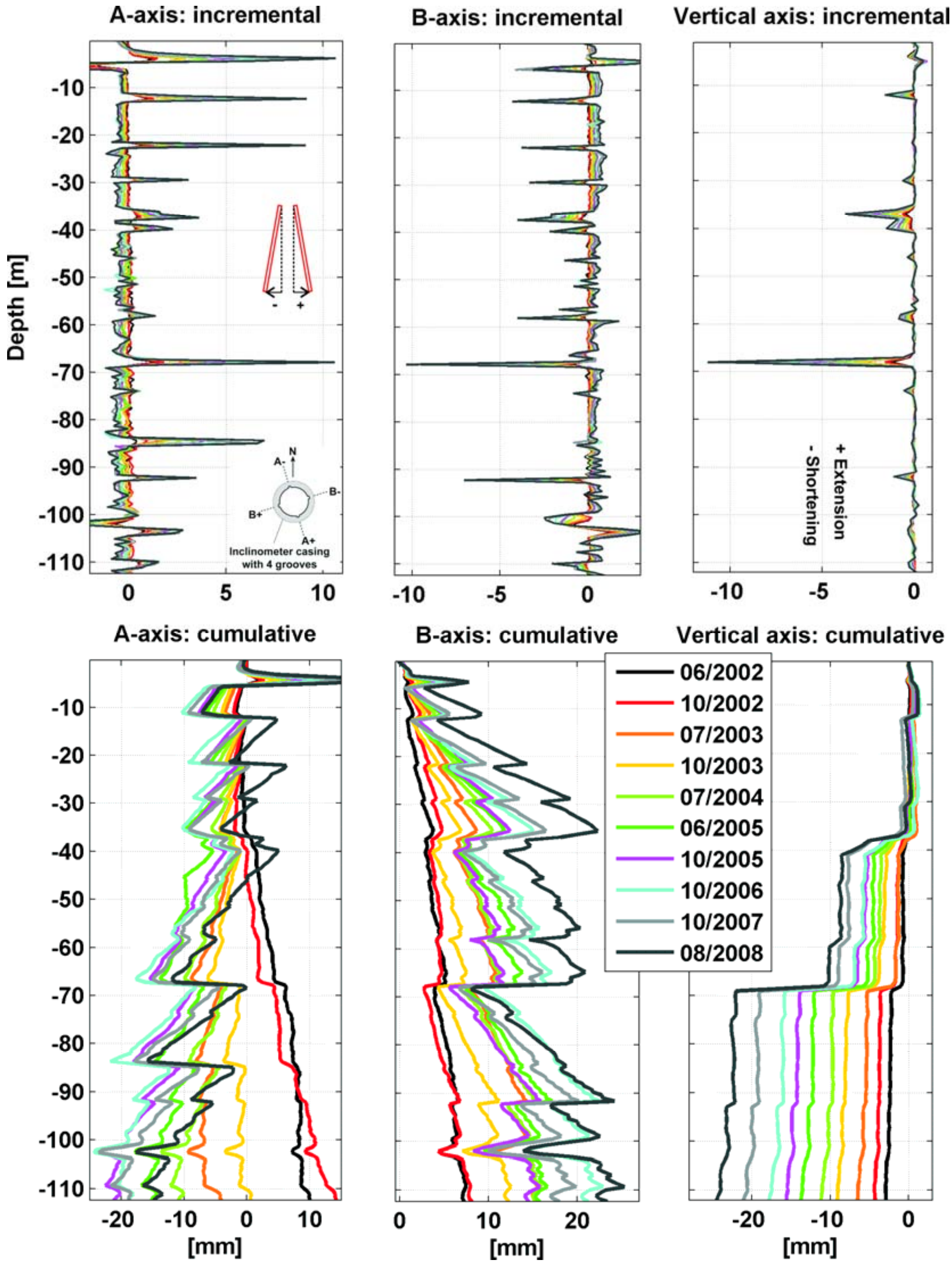

Figure 2.6: Incremental and cumulative displacement patterns derived from all inclinometer and extensometer surveys in borehole sb120. For significance of cumulative displacement patterns see Willenberg et al. (2008b).

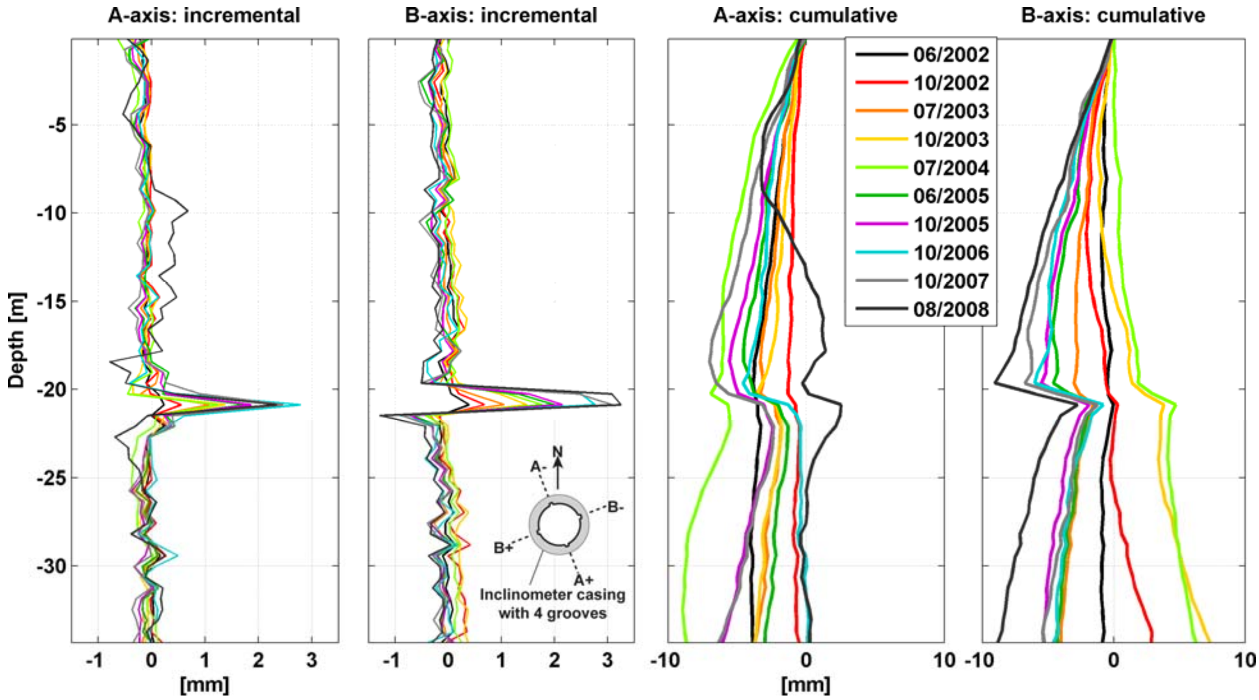

Figure 2.7: Incremental and cumulative displacement patterns from all inclinometer surveys in sb50n.

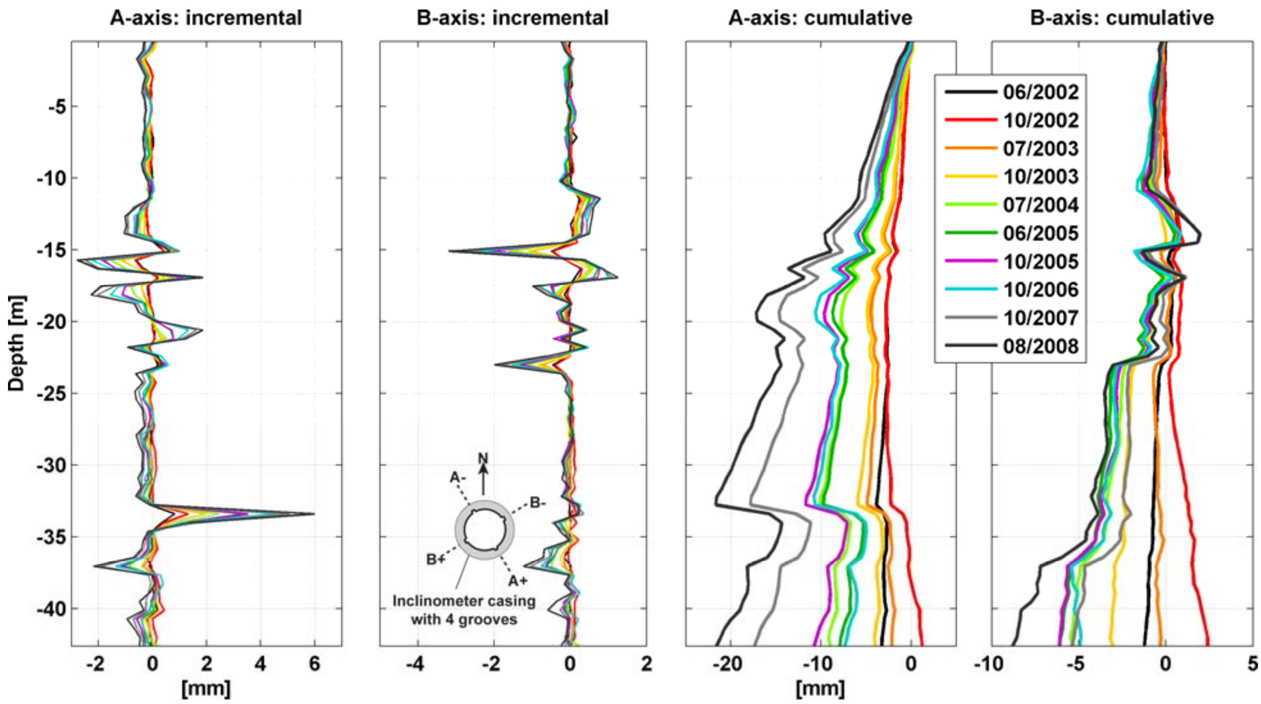

Figure 2.8: Incremental and cumulative displacement patterns from all inclinometer surveys in sb50s.

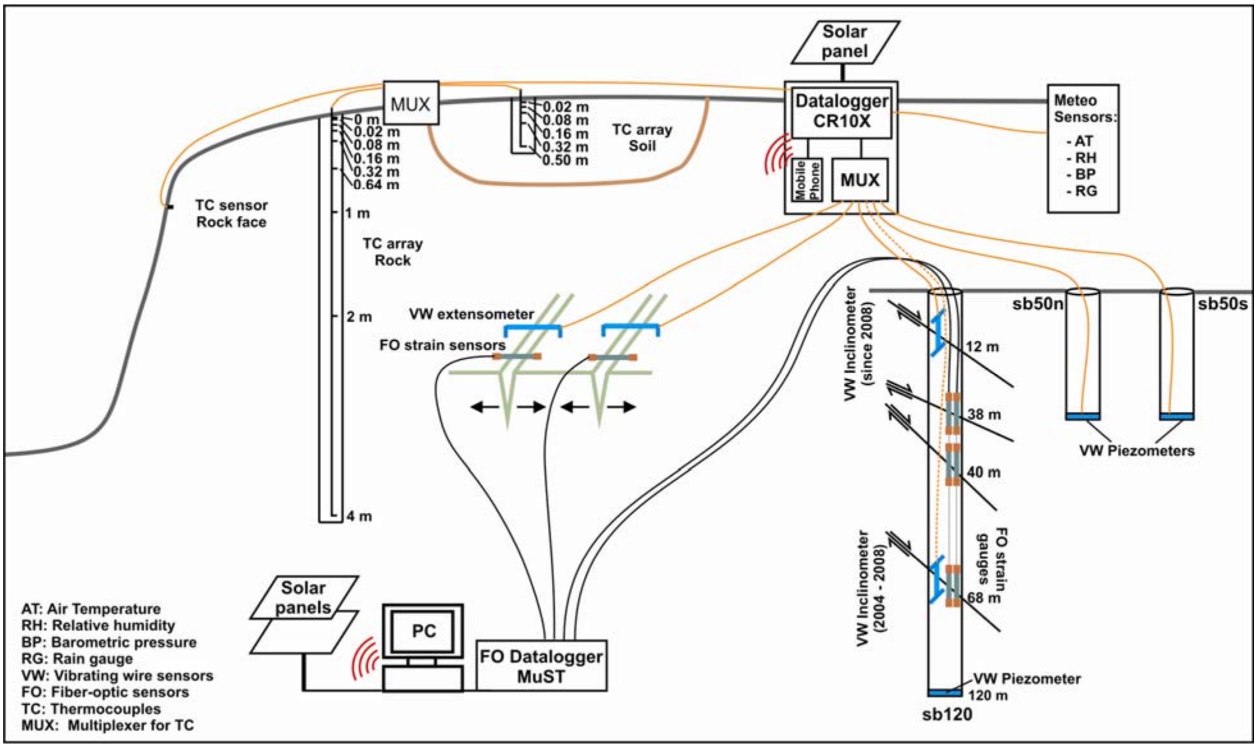

Figure 2.9: Schematic overview of all automatic monitoring system components.

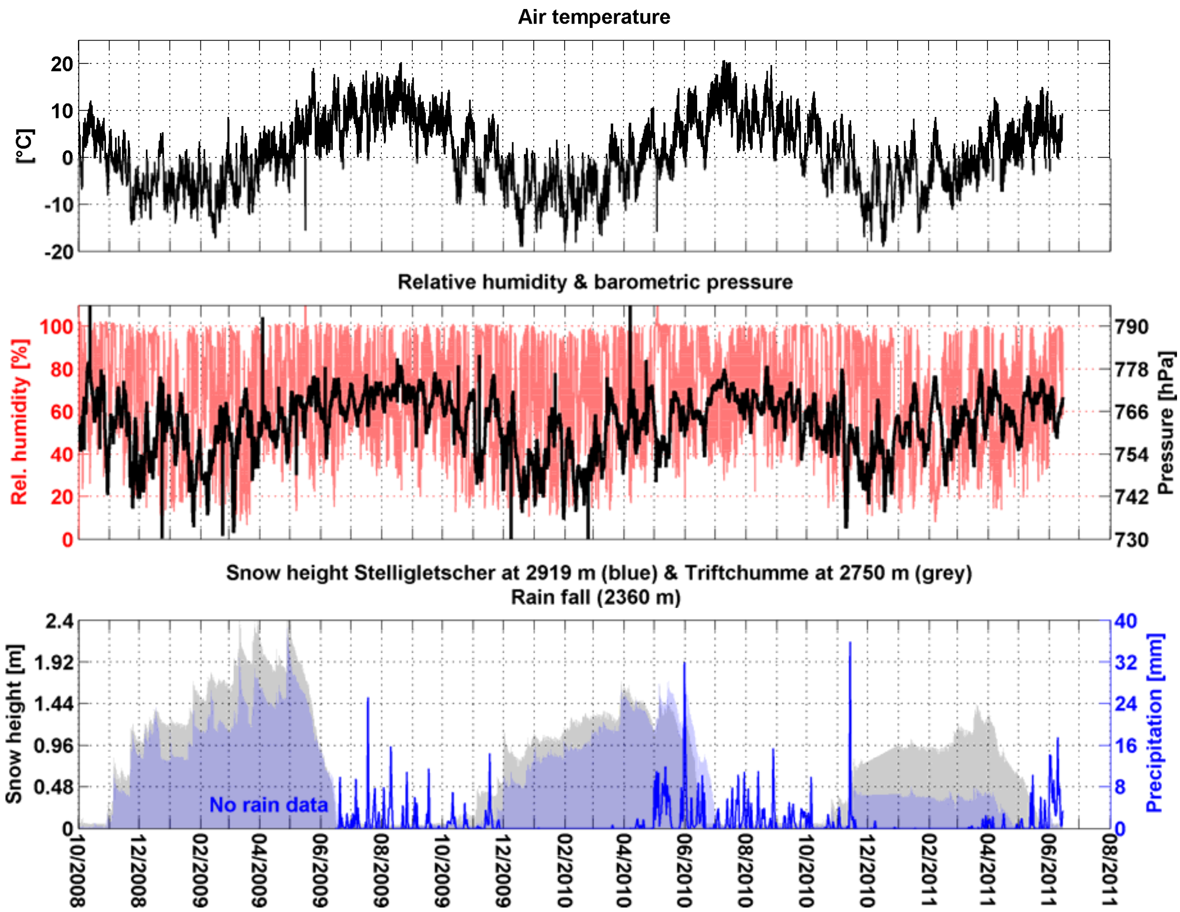

Figure 2.10: Meteorological parameters recorded since 2008 at the Randa instability. Snow heights are measured 9 km south and 6 km north of Randa at two SLF stations (SLF-Data © 2011, SLF). Rain data have been recorded since June 2009.

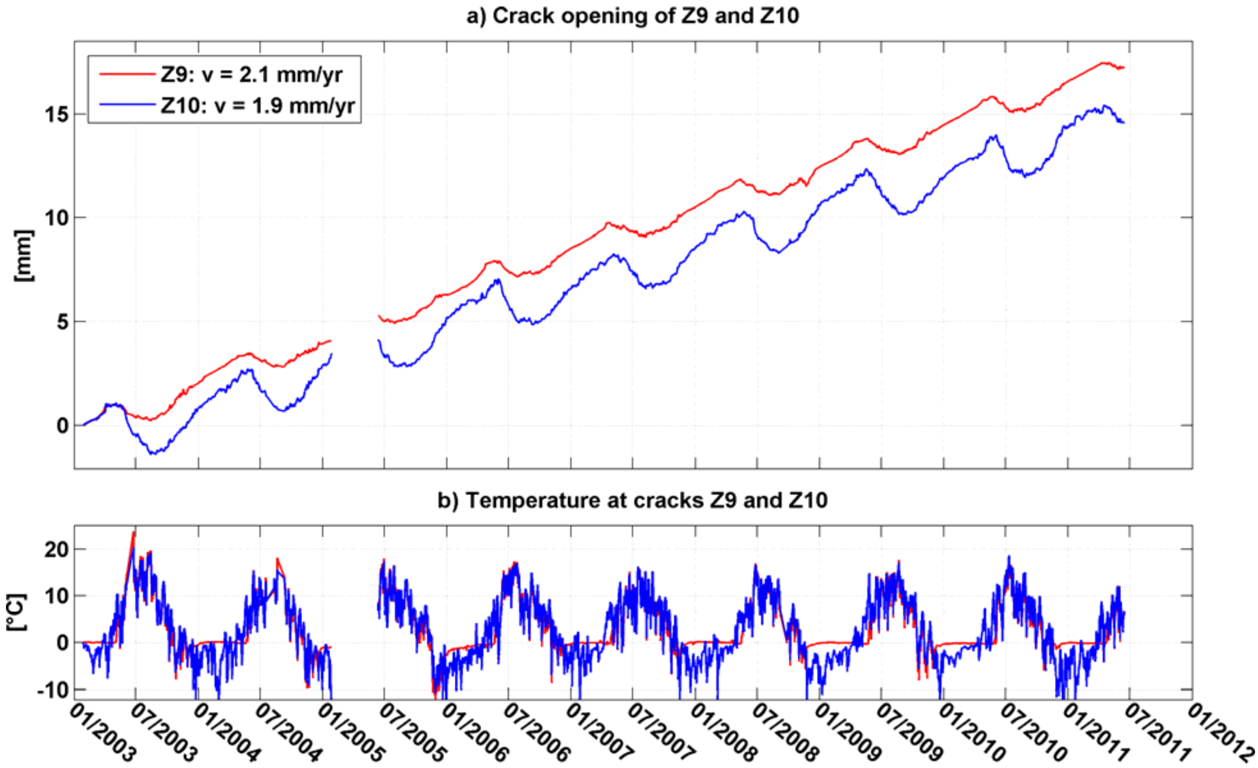

Figure 2.11: a) Crack extensometer data recorded since 2003 across fractures Z9 and Z10 (see Figure 2.1). b) Temperature recorded by internal thermistors within in the instruments.

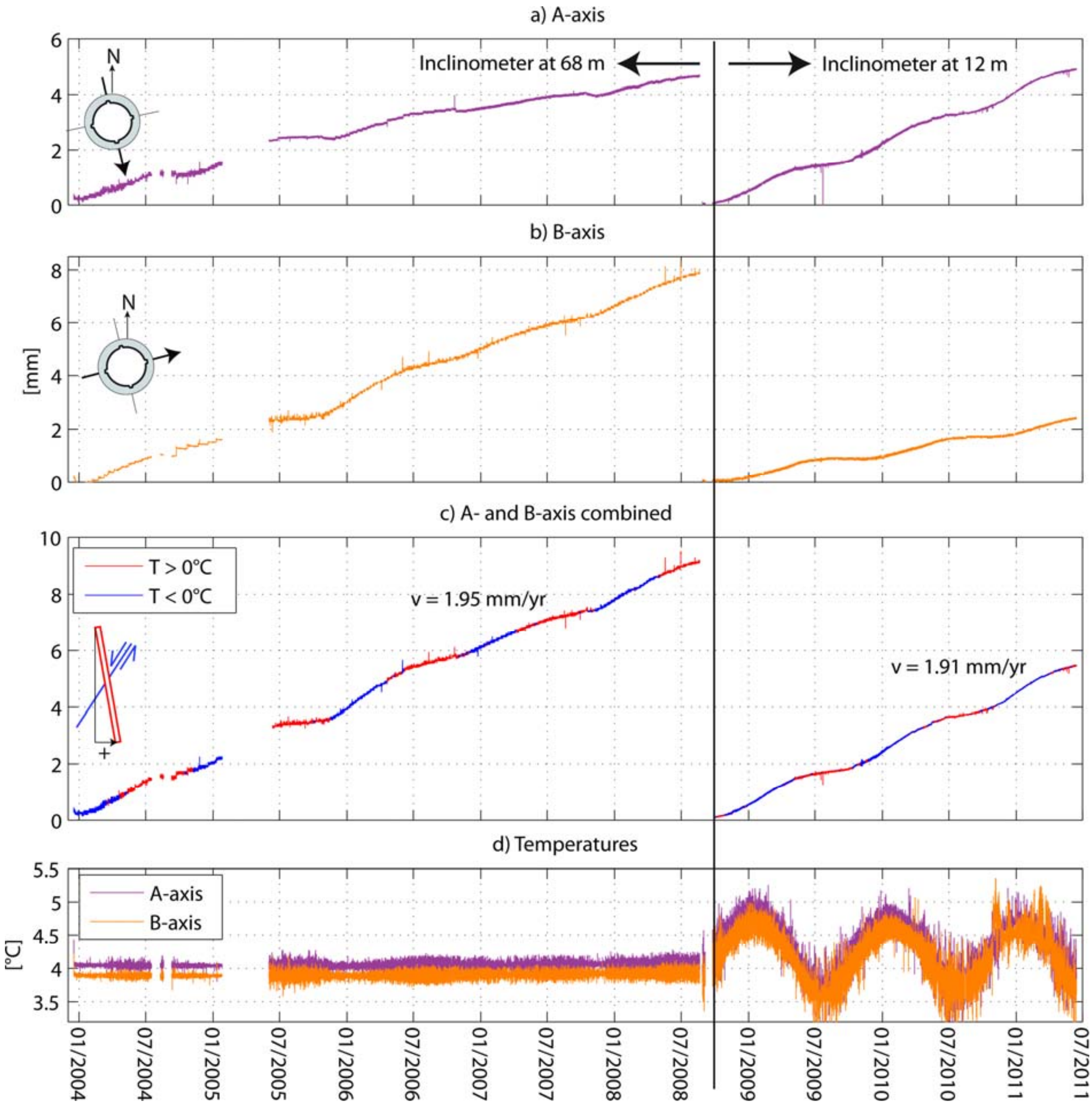

Figure 2.12: In-place inclinometer data from 68 m (2004 – 2008) and 12 m (2008 – present) depth. a) Axis A. b) Axis B. Positive values indicate movements of the lower block with respect to the upper block into the direction indicated. c) Magnitude of the displacement vector defined by both the A- and the B- axes, colored according to air temperatures at the surface. d) Temperatures recorded by the built-in sensors of both inclinometer axes. Temperatures at 68 m are constant, while at 12 m a slight annual signal was measured.

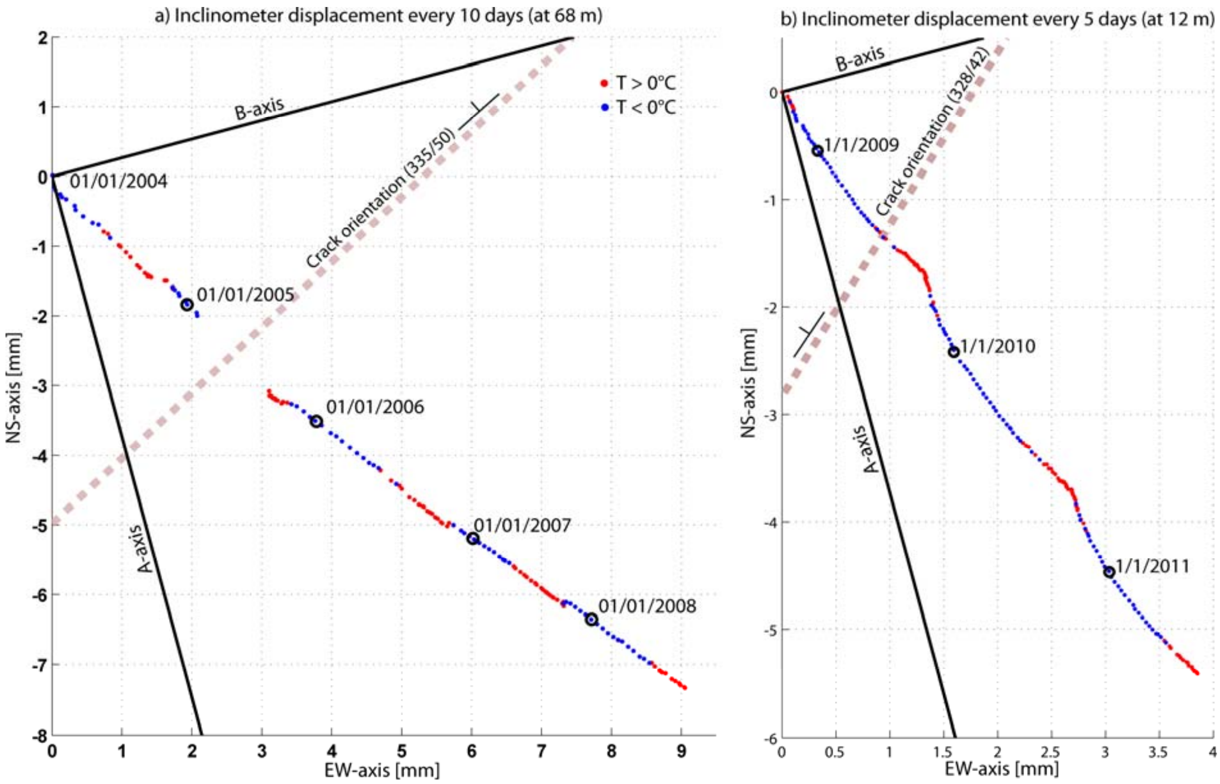

Figure 2.13: Inclinometer data from both axes in a plan view. These data have been filtered with a 3-days low-pass filter and interpolated to one sample every 5 or 10 days. Data points are colored according to air temperatures measured at the surface. a) At 68 m depth. b) At 12 m depth, where a slight change in displacement direction can be observed over the course of a year.

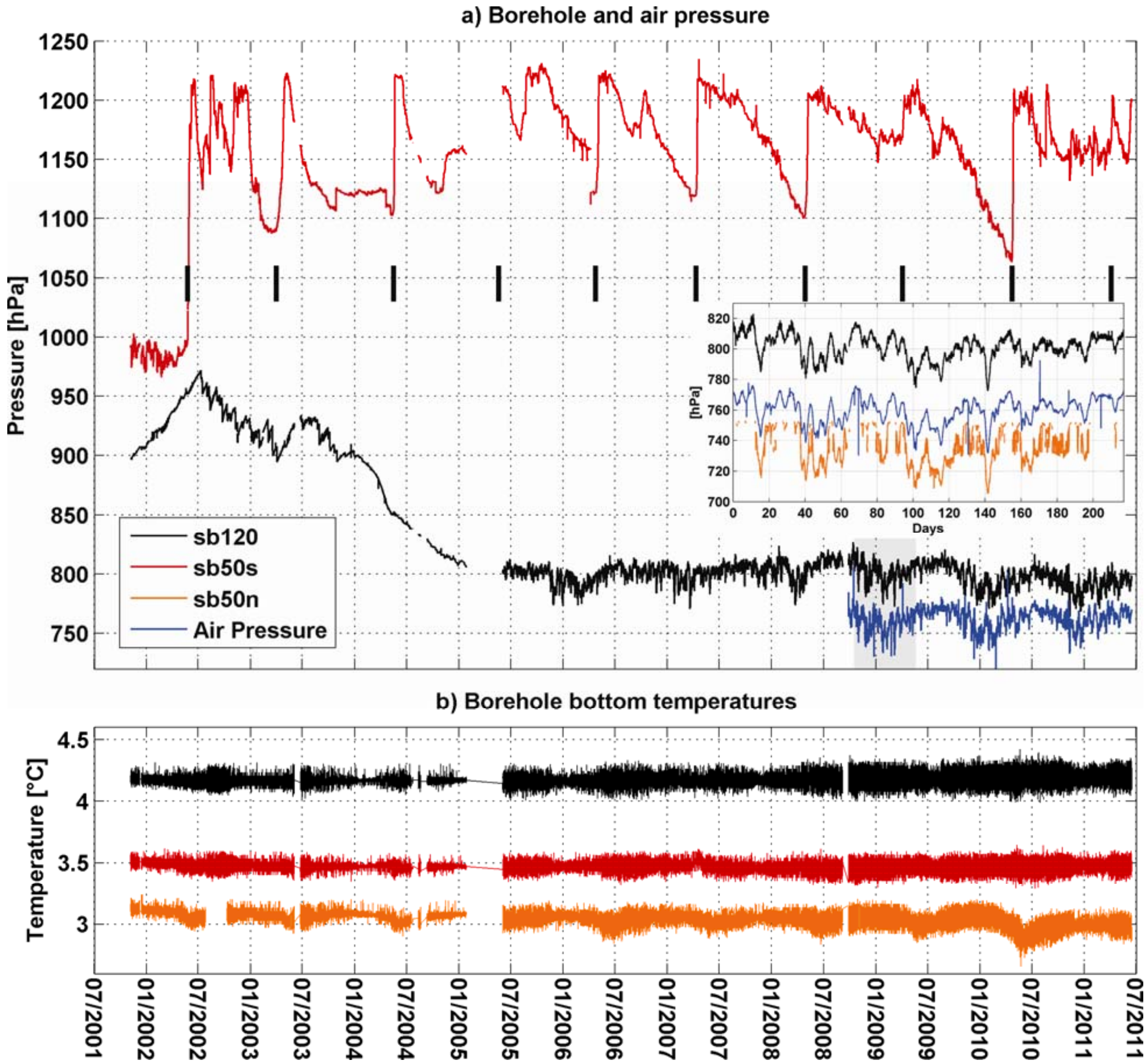

Figure 2.14: a) Piezometric pressure recorded at the bottom of boreholes sb120 and sb50s. The inset figure also shows pieces of meaningful data recorded in sb50n, which otherwise showed predominantly erroneous data (time period corresponds to grey shaded area). Pressure measured in sb120 and sb50n correlate with air pressure. Borehole sb50s shows a water pressure signal, which abruptly increases each year during snowmelt. b) Temperatures measured by thermistors embedded in the piezometric sensors.

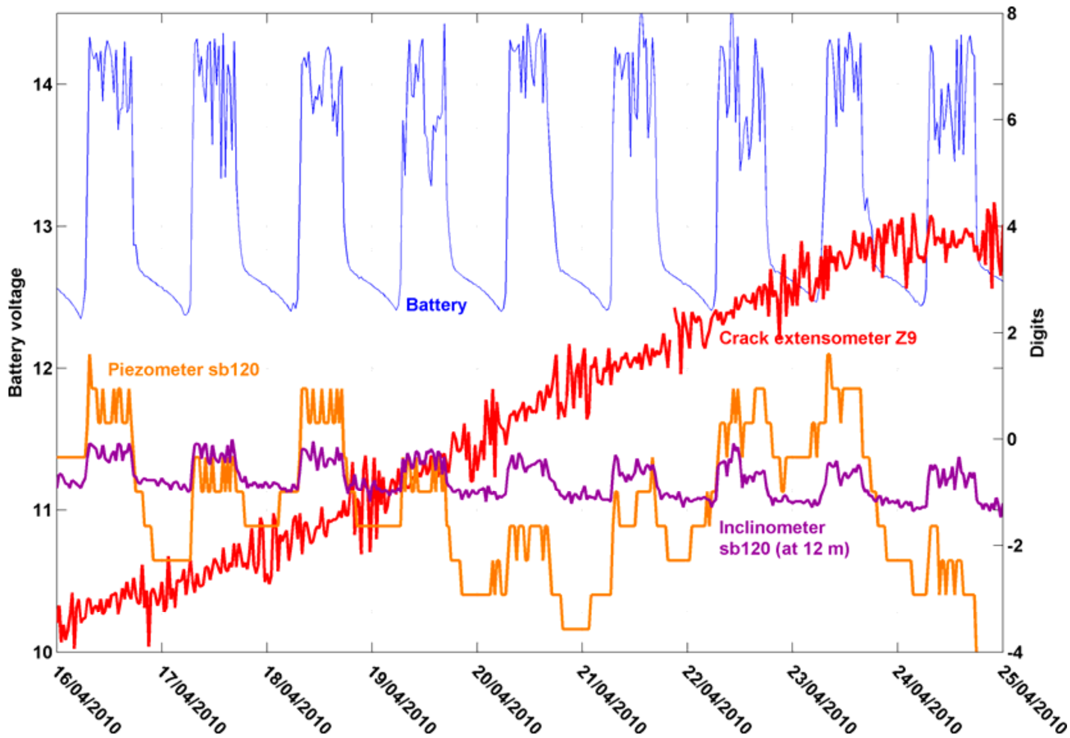

Figure 2.15: Daily noise patterns recorded with vibrating wire sensors. Especially the inclinometer and piezometer show daily signals strongly correlated with datalogger battery voltage.

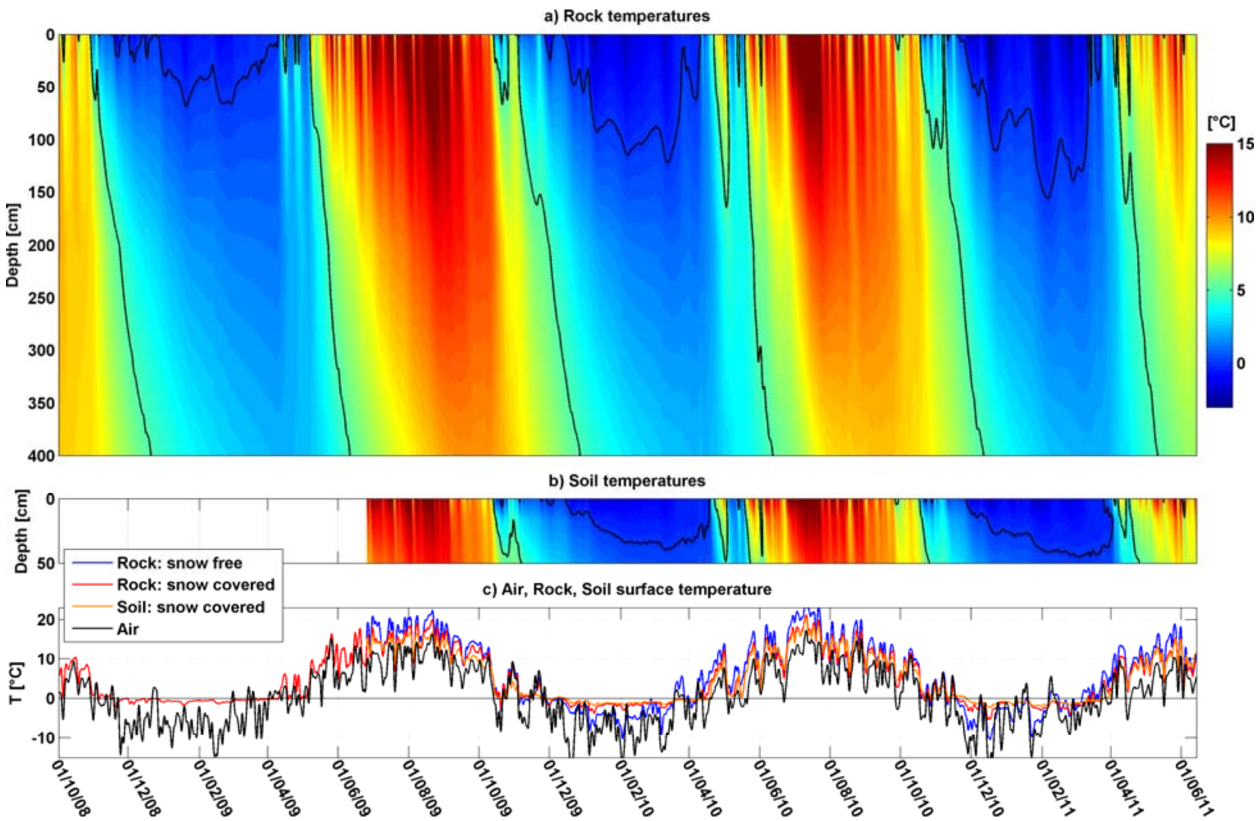

Figure 2.16: a) Rock and b) and soil temperature profiles as a function of depth and time; data are filtered with a 3-days low-pass filter. c) Temperatures of air, soil surface, rock surface and the steep rock face, also filtered with a 3-day low-pass filter. These data are used to derive thermal transport properties (Figure 2.18).

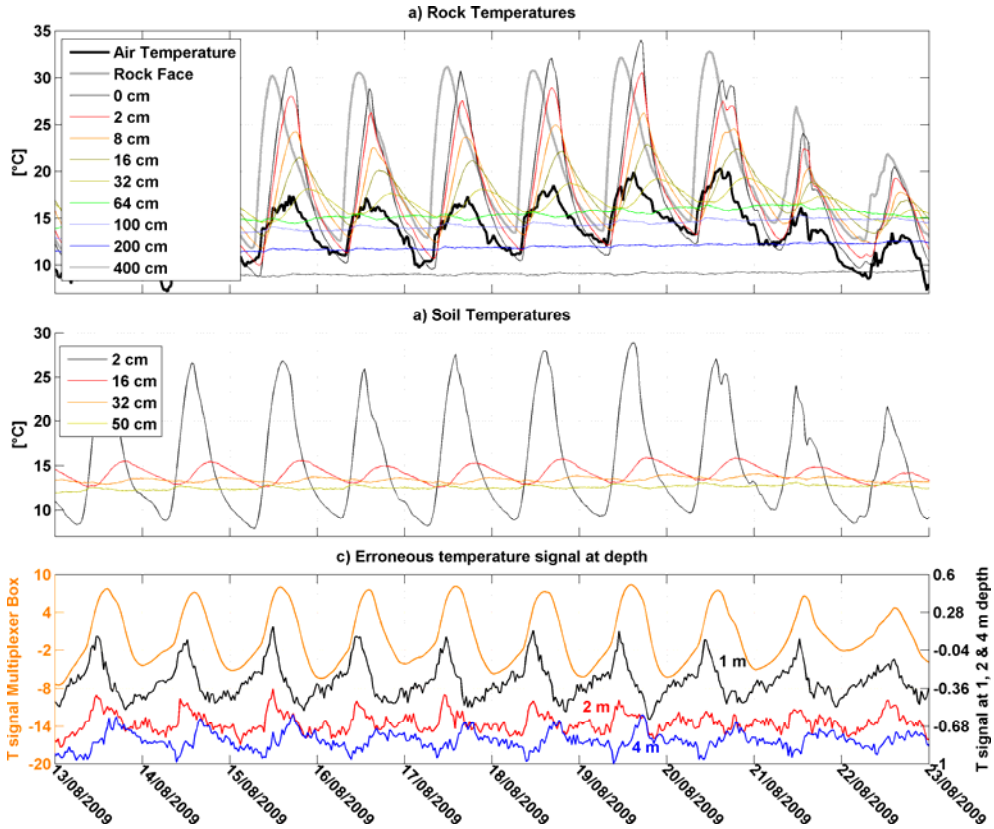

Figure 2.17: a) 10-days section of unfiltered rock temperature data highlighting the daily temperature evolution at depth. b) Daily temperature fluctuations in soil. c) Daily temperature signals at 1, 2, and 4 m depth related to strong temperature fluctuations in the multiplexer box. Note that only temperature variations are highlighted in this figure, while absolute temperatures were shifted for optimal display.

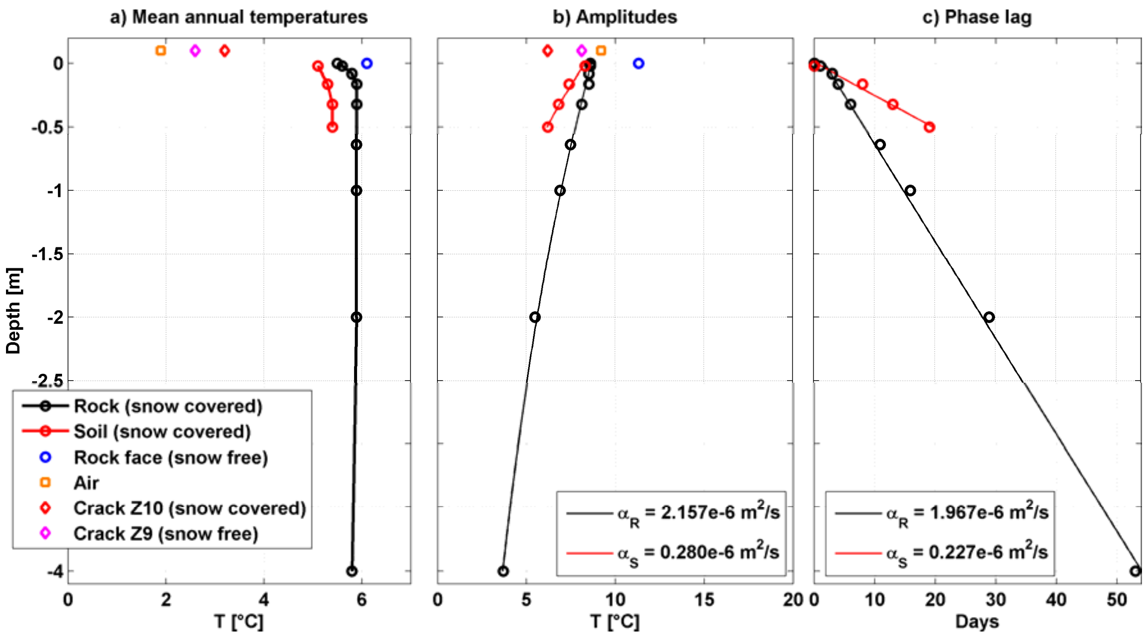

Figure 2.18: Parameters derived from fitting sinusoidal temperature functions to data in Figure 2.16. a) Mean annual temperature estimates. b) Amplitude of the best fit sinusoidal functions. For rock and soil temperatures, thermal diffusivities α_R and α_S were derived from the decay of amplitude with depth. c) Phase shift of the best fit sinusoidal function with respect to surface temperature. Similar to b) the data were used to derive thermal diffusivity values shown in the inset.

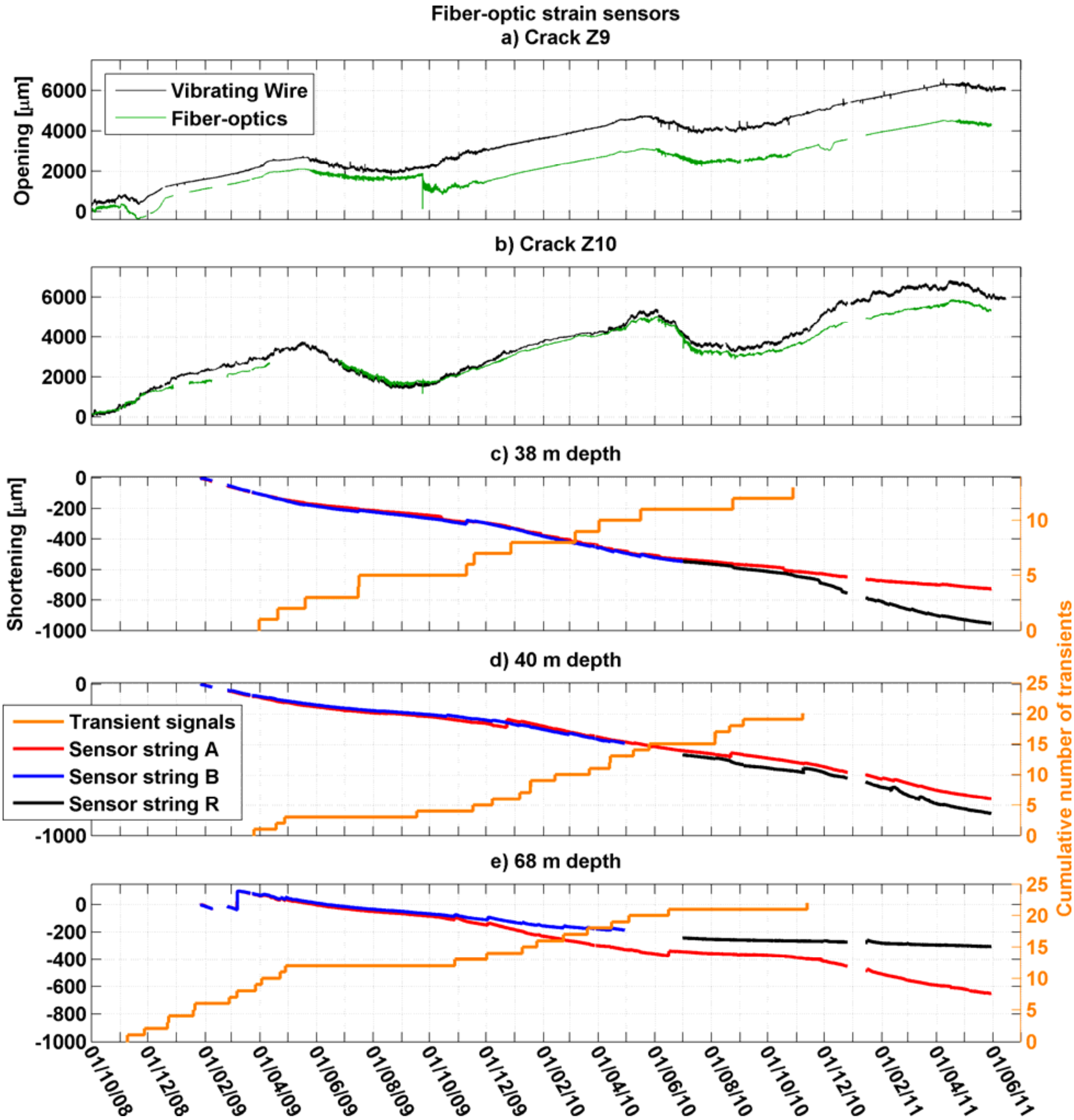

Figure 2.19: Fiber-optic data from surface tension fractures and from three different depths in borehole sb120. a) Fracture Z9, also showing data from the vibrating-wire sensor for comparison. The time series mimic each other well. b) Same for fracture Z10. c) Borehole data from 38 m depth showing vertical shortening across discontinuities dislocating with normal faulting shear sense. Also included are cumulative counts of transient events, which are typically characterized by short-term elongation, followed by increased rates of shortening. Only transient events that occurred on both sensor strings simultaneously are counted. Transient events are only counted until November 2010. d) Same as above for 40 m, and e) 68 m depth.

PART I

Structure and kinematics of the current Randa instability

3. IDENTIFICATION OF ACTIVE RELEASE PLANES USING GROUND-BASED DIFFERENTIAL INSAR AT THE RANDA ROCK SLOPE INSTABILITY, SWITZERLAND

Gischig, V., Loew, S., Kos, A., Moore, J.R., Raetzo, H. and Lemy, F.

Published in *Natural Hazards and Earth System Sciences*, 9, 2027-2038

4 December 2009

Abstract: Five ground-based differential interferometric synthetic aperture radar (GB-DInSAR) surveys were conducted between 2005 and 2007 at the rock slope instability at Randa, Switzerland. Resultant displacement maps revealed, for the first time, the presence of an active basal rupture zone and a lateral release surface daylighting on the exposed 1991 failure scarp. Structures correlated with the boundaries of interferometric displacement domains were confirmed using a helicopter-based LiDAR DTM and oblique aerial photography. Former investigations at the site failed to conclusively detect these active release surfaces essential for kinematic and hazard analysis of the instability, although their existence had been hypothesized. The determination of the basal and lateral release planes also allowed a more accurate estimate of the currently unstable volume of 5.7±1.5 million m^3. The displacement patterns reveal that two different kinematic behaviors dominate the instability, i.e. toppling above 2200m and translational failure below. In the toppling part of the instability the areas with the highest GB-DInSAR displacements correspond to areas of enhanced micro-seismic activity. The observation of only few strongly active discontinuities daylighting on the 1991 failure surface points to a rather uniform movement in the lower portion of the instability, while most of the slip occurs along the basal rupture plane. Comparison of GB-DInSAR displacements with mapped discontinuities revealed correlations between displacement patterns and active structures, although spatial offsets occur as a result of the effective resolution of GB-DInSAR. Similarly, comparisons with measurements from total station surveys generally showed good agreement. Discrepancies arose in several cases due to local movement of blocks, the size of which could not be resolved using GB-DInSAR.

3.1 The Randa rockslope instability

In the spring of 1991 two large rockslides occurred above the village of Randa in the Matter Valley (southern Swiss Alps). Within a three week period, a total volume of 30 million m^3 of rock was released. The resulting talus cone dammed the river and formed a lake, which flooded the nearby village (Schindler et al., 1993). The kinematics and mechanisms of the 1991 events were studied by Sartori et al. (2003) and Eberhardt et al. (2004). One legacy of these failures was the formation of an 800 m high scarp, behind which an estimated 3–9 million m^3 (Ischi et al., 1991) of rock remains unstable. In 1995, a geodetic network, consisting of seven 3-D reflectors and eighteen 1-D reflectors located in the crown and along the edge of the scarp, was setup to monitor rock mass displacements (Jaboyedoff et al., 2004). The kinematics of the current instability was investigated in a research project begun in 2001, which included field mapping and borehole logging (Willenberg et al., 2008a), geophysical imaging of the 3-D extent of discontinuities (Heincke et al., 2005 and 2006; Spillmann et al., 2007a), monitoring of micro-seismic activity associated with rock mass deformation (Spillmann et al., 2007b), as well as surface crack and borehole monitoring (Willenberg et al., 2008b). Displacements resolved from total station measurements were used to approximate the extents of the moving mass. However, due to their sparse distribution, large uncertainties remained. The deformation pattern was interpreted as block toppling in the upper part of the instability (Loew et al., 2007). A basal rupture surface was postulated by Jaboyedoff et al. (2004) by interpreting geodetic data and later by Willenberg et al. (2008b). However, it could not be detected with geophysical imaging or within a 120m deep borehole. All previous investigations were limited to the accessible area at the top of the instability, whereas large portions of the currently unstable rock mass could not be studied due to the inaccessibility of the nearly 800m high cliff face. Inspection of photographs of the 1991 failure surface could not conclusively prove the existence of a basal rupture plane or other active structures that may outcrop on the scarp, since the pattern of faults and joints is too complex and no *in situ* monitoring is available to confirm movements.

In this manuscript we present data from five ground-based differential InSAR (GB-DInSAR) surveys carried out between September 2005 and September 2007. We first describe relevant technical details about the technique, the surveys at Randa and the processing of the data. Displacement maps obtained from these surveys are then interpreted towards the observation of active large-scale release structures bounding the instability, which have remained undetected by previous investigations. The datasets are also compared to the structural map by Willenberg et al. (2008a) and to results from complementary geodetic surveys and microseismic monitoring. Observations are discussed in terms of their implications for kinematics of the rock slope instability, as well as with regards to the spatial and temporal resolution limitations of the technique.

3.2 Ground-based differential radar interferometry

3.2.1 The GB-DInSAR technique

Ground-based synthetic aperture radar interferometry is an established, reliable method for spatial displacement monitoring of rock slopes (e.g. Tarchi et al. 2003a, b; Lingua et al., 2008), and is especially valuable when inaccessibility prohibits the application of other traditional monitoring techniques. For ground-based systems, the synthetic aperture radar (SAR) method relies on linear translation of an antennatransmitter pair to create a synthetic aperture (i.e. an antenna length in the range of 2.0–2.7 m). A series of observations are combined in post-processing as if they had been made simultaneously using a large antenna, providing the resolution in azimuth (Tarchi et al., 2003a, b). The resulting SAR image is a map of complex numbers containing both the amplitude and the phase of the radar signals reflected by the target. The range resolution cell size of such images is inversely proportional to the frequency bandwidth of the system, whereas the azimuthal resolution is inversely proportional to the synthetic aperture length. Two subsequent SAR images can be combined to create an interferogram (i.e. a GB-DInSAR image) by extracting the phase difference 1' between the two acquisitions from the complex values of each resolution cell. The corresponding displacement (Δs) is then obtained as:

$$\Delta s = \frac{\Delta\varphi}{4\pi}\lambda\,, \tag{2.1}$$

where λ is the wavelength of the signals. An important property of the GB-DInSAR method is the ambiguity of the phase differences, which can only vary between ±π. Thus, displacements smaller or larger than ±λ/4 result in apparent values between ±λ/4 differing from the real value by a multiple of the full wavelength. This effect is called phase wrapping and is important for interpretation of GB-DInSAR displacement maps. The reliability of GB-DInSAR data is controlled by both the reflectivity of the ground and temporal decorrelation between acquisitions. Reflectivity of a surface determines the strength of the signal reflected back to the receiver by the target, i.e. the reflected power. It is generally low for densely vegetated areas and smooth targets not perpendicular to the line-of-sight (LOS). Decorrelation results from strong movements within a resolution cell between two acquisitions, e.g. due to unstable debris cover or differential displacements. A measure of the strength of decorrelation is the signal coherence from two subsequent acquisitions, which is defined as:

$$\gamma = \frac{E[ms^*]}{\sqrt{E[m]^2 E[s]^2}}\,, \tag{2.2}$$

where m and s are the complex numbers of two acquisitions for one particular resolution cell, [*] denotes complex conjugate, and E signifies the expectation value. The signal coherence is a number between 0 and 1 and is a measure of the similarity of the transmitted and the received signal. In an interferogram, unreliable data can be masked by setting a threshold for both reflected power and coherence. Further processing steps are commonly performed on GB-DInSAR images, e.g. multi-look filtering (Lee et al., 1994) and other filters, which often lower the theoretical spatial resolution of the system since neighboring cells are no longer independent.

3.2.2 GB-DInSAR data acquisition and processing at the Randa instability

The 1991 failure surface of the Randa rock slope instability is well suited for application of GB-DInSAR due to the absence of vegetation and the possibility to align the radar such that the LOS is sub-parallel to the rock mass displacements. Between 2005 and 2007, five GB-DInSAR measurements were conducted by Ellegi Srl (Milano, Italy) using their GB-DInSAR system called LiSA. The LiSA base station was located at 1560m a.s.l. on the valley wall opposite the 1991 failure scarp. System specifications and acquisition parameters for these radar surveys are summarized in Table 3.1, while campaign dates and time intervals are shown in Table 3.2. Methods employed in processing radar images are described by Fortuny and Sieber (1994) and Tarchi et al. (2003a, b), while some relevant points concerning the Randa datasets are described here. Since Ellegi Srl also processed the Randa data using their proprietary methods, we can only give a basic description of the processing steps.

To exclude unreliable phase measurements, the thresholds for coherence and reflected power given in Table 3.1 were used. The radar data were gridded on a regular 2x2m Cartesian grid (Leva et al., 2003), which is smaller than the theoretical resolution of the system (1.9x4–6.5 m, Table 3.1). This interpolation is used to prevent aliasing during later processing, but also means that the images cannot be interpreted on the level of single pixels. A proprietary multi-look filter was used to help reduce phase noise due to the speckle effect (Lee et al., 1994), i.e. a number of independent views of the scene were averaged to smooth the grainy character of nonaveraged views. Other proprietary post-processing steps, the details of which are not available to the authors, involve filters running over 7x7 pixels in the case of the Randa acquisitions. Thus, the resulting images have an effective resolution of 14x14 m. Values of single pixels are therefore not independent of their neighboring pixels, and thus differential displacement patterns can only be interpreted if they are consistent over a distance greater than the effective resolution. Finally, the images were overlain on a hill-shaded DTM with resolution of 0.5 m, which was derived from helicopter-based LiDAR data (acquired by Helimap Systems SA).

3.3 Results

3.3.1 Displacement maps

GB-DInSAR image maps showing displacements between September and November 2005 (59 days), as well as between November 2005 and October 2006 (316 days) are presented in Figure 3.1. The color scale shows displacements from –4.4 to +4.4mm corresponding to ± $\lambda/4$ of the radar. Negative values (red to yellow) show displacement along the LOS towards the observer, positive values (light blue to blue) away from the observer, and turquoise values represent zero displacement. An overview of the GB-DInSAR scene including the base station position, the line-of-sight, as well as the locations of detail figures described later is given in Figure 3.2 (displacement image between October 2006 and June 2007; 248 days). All displacement maps reveal a similar overall pattern. In the talus at the bottom of the images (region (a) in Figure 3.1), measured displacements suffer from decorrelation and phase wrapping (displacements $>\lambda/4$). Displacements on image B (59 days interval), however, show a consistent pattern interpreted as consolidation of the debris cone (Figure 3.3). On the same image, an elongated decorrelation pattern close to the steep orthogneiss cliff on the debris cone correlates with active debris flow channels. The steep orthogneiss cliff just above the talus (region b) is stable throughout all measurements. Above this stable cliff is a sharp transition to unstable rock (region d), which is best observed on image C (316 days interval). In region (d), displacements are relatively uniform over a large area. Slightly higher displacements in this region result in phase wrapping on image C, i.e. sudden transitions between negative (red) and positive (blue) displacements. To the south of region (d), a large portion of the 1991 scarp is covered with debris (region c). Decorrelation due to debris movement limits interpretation in this area. Region (e) delineates a portion of the scarp which is primarily stable, although some blocks moving towards the scarp edge can be seen. Above region (d) and to the north of the stable region (e), displacements increase towards the top of the scarp (region f). Here, the greatest displacements were measured. The transition from the uniformly moving region (d) to region (f) occurs at about 2200 m. This transition is clearly visible on image B, whereas image C suffers from phase wrapping. Above region (f), some data gaps occur in grassy areas due to decorrelation and shadowing. In the upper part of the images (region g) extended stable areas are found.

3.3.2 Release planes identified on GB-DInSAR displacement maps

The lower boundary of the unstable rock mass can be identified by a sharp transition from 0mm displacement (region b) to 4mm displacement (region d) on image C in Figure 3.1 (enlarged in Figure 3.4). The magnitude of the displacement rate and the location of the transition are consistent across all images. The location of this transition corresponds to the trace of the boundary between the two primary lithologies on the rock slope: strongly fractured paragneiss and schist overlaying more competent orthogneiss. However, the lithological boundary is sub-parallel to foliation and dips into the slope at roughly 20°. Water discharge is often observed along this boundary after snow melt and heavy rainfall. This structure can also be identified on high resolution aerial photographs (Figure 3.4). The transition between the stable cliff and the instability above is characterized by a sharp increase in displacement over one pixel, or by decorrelation across 2–3 pixels. Bearing in mind that the original range resolution before interpolation is about 2m wide, this decorrelation pattern can be interpreted as differential displacement causing loss of coherence. This indicates that deformation is concentrated at the base of the instability within one resolution cell, or a narrow zone only a few meters wide. GB-DInSAR displacement maps also indicate that the transition zone has a minimum length of 150–200 m. We interpret this feature as the basal rupture zone of the instability. The southern boundary of the instability can also be identified on the GB-DInSAR displacement maps (Figure 3.5). It is characterized by a sub-vertical, sharp transition between 0 mm displacement in the south (region (e) in Figure 3.1) and a displacement pattern in the north that shows increasing displacements from 4 to 12mm to the top of scarp (region (f) in Figure 3.1). Note that the apparent positive values result from phase wrapping. High resolution photographs and the LiDAR DTM show that this lateral boundary coincides with a fault surface oriented 095°/70°, containing striations that dip towards the valley. The surface also corresponds to a lateral release plane from the 1991 rockslides. According to the displacement maps, the stratum underlying the fault is stable although some isolated toppling blocks near the scarp can be identified. To the north, the overlying unstable stratum is composed of blocky and highly fractured rock. The intersection of this plane with the ground surface shows that it matches well with steeply dipping, NS-striking faults mapped by Willenberg et al. (2008a). We conclude that this fault corresponds to the southern release plane of the current instability.

3.3.3 Active structures within the instability

A more detailed analysis of deformation patterns within the instability was carried out in order to identify additional active structures critical for kinematic analysis, as well as to explore the resolution limits of the GB-DInSAR technique in structural analyses. The GB-DInSAR displacement maps were first overlain with a map of large-scale discontinuities (faults and fracture zones) obtained from extensive field investigations in the accessible part of the 1991 rockslide crown (Willenberg et al., 2008a; Figure 3.6). The discontinuities are drawn in black if there are corresponding displacement patterns noted on the GB-DInSAR maps (such as steps in the displacement or elongated patterns of decorrelation) and in grey otherwise. In case of correlation between GB-DInSAR displacement patterns and mapped discontinuities, the alignment is usually not perfect but often offset by a few pixels (Figure 3.6). Mostly discontinuities which belong to a set striking nearly perpendicular to the LOS of the GB-DInSAR show correlation. This is expected since such discontinuities usually have the largest differential displacement component along the LOS. The opening rates of discontinuities Z1 and Z9 have been monitored with periodic hand measurements over the last 7 years, and are 3.5 mm/yr and 2.3 mm/yr, respectively. Opening rates for these discontinuities were also estimated from the GB-DInSAR data by extracting displacements from both sides of the cracks from all time intervals. The time series' derived reveal opening rates of 2.7±0.6 mm/yr for Z1 and 1.9±0.6 mm/yr for Z9, which are slightly lower than the opening rates from field measurements. Such discrepancies can be expected since the direction of relative displacement across these discontinuities deviates from the LOS of GB-DInSAR.

The GB-DInSAR displacement maps were also overlain with structures mapped on the 0.5m LiDAR DTM from the inaccessible 1991 scarp surfaces in order to identify previously unmapped active discontinuities within the unstable rock mass. Figure 3.7 shows structures within the 1991 failure surface that correlate with GB-DInSAR displacement patterns in black, while structures not correlating with displacement patterns are shown in grey. Two local toppling instabilities superimposed on the large-scale unstable rock mass could be identified in photographs (inset in Figure 3.7). In addition to the lateral release surface and the basal rupture plane, only a few structures within the unstable portion of the 1991 failure surface were found to correlate with GB-DInSAR displacement patterns. Furthermore, the differential displacement along these structures is small with the exception of the local toppling instabilities. Thus, the large-scale movement of the rock mass is mainly controlled by the basal and the lateral release planes. Especially in the lower portion of the instability only little internal deformation/shearing occurs along large-scale discontinuities.

3.3.4 Comparison of GB-DInSAR displacements with geodetic displacement measurements

Since 1996, displacements of seven 3-D retro-reflectors were measured by surveying a geodetic network with a total station once or twice per year (Willenberg et al., 2008b; Jaboyedoff et al., 2004). The resultant vectors have an azimuth of 135–140°, which is sub-parallel to the LOS of the GB-DInSAR. Another 18 points were surveyed using a total station positioned on a monument close to the GB-DInSAR base station resulting in a similar LOS. The total station surveys and the radar surveys were performed at times less than 50 days from each other. Displacement time series were derived from the five GB-DInSAR measurements at the locations of the geodetic reflectors by summing the displacements between each time interval. Figure 3.8 shows the time series for both GB-DInSAR and geodetic measurements, as well as the locations of these points on an unwrapped (i.e. phase wrapping removed) displacement map between the 2nd and 3rd repeat measurements (248 days interval). The error bars are 2.5 mm for the geodetic measurements and 1 mm for each GB-DInSAR repeat measurement. The latter error sums for each subsequent measurement. Comparison of the time series from both methods shows good agreement in most cases. However, in some instances GB-DInSAR shows lower velocities than the total station measurements (points 110, 130, and 151; Figure 3.8), the average of these rate discrepancies is around 3 mm/yr. Time series were also derived for points showing greater displacement than all geodetic points (red colors in the unwrapped Figure 3.8). They show maximum velocities of about 20 mm/yr, which is greater than those measured with the 3-D geodetic network (~14 mm/yr).

3.3.5 Comparison with micro-seismic activity

Between 2002 and 2004, a seismic array consisting of 3 borehole geophones and 9 surface geophones recorded microseismic activity originating within the instability (Spillmann et al. 2007b). A probabilistic location algorithm taking into account a 3-D seismic velocity model was applied to the 223 events recorded by the array. The result of this procedure is a probabilistic density function (PDF) map, which shows areas of enhanced seismic activity (Figure 3.9a). Willenberg et al. (2008b) pointed out that the seismic activity is generally distributed within the assumed instability boundaries, and that patches of high seismic activity tend to occur along mapped faults and fracture zones. The distribution of seismic activity partially correlates with the GB-DInSAR displacements map (Figure 3.9b). The patches of high seismicity lie mostly within the mapped instability boundary as derived from GB-DInSAR. Furthermore, the areas with the highest displacement rates at the edge and top of the scarp correlate with an extended zone of enhanced seismic activity, which implies that the high displacements are accompanied by strong internal deformation and shearing. The areas of low seismicity below correspond to the more uniformly moving areas on the GB-DInSAR maps (Figure 3.1, region d). However, this region cannot be conclusively mapped as a low activity area, since the recorded seismicity may be adversely affected by high seismic attenuation within the strongly fractured rock mass.

3.4 Discussion

3.4.1 Spatial resolution

The spatial resolution of GB-DInSAR displacement maps is not only a function of the theoretical system resolution, but also influenced by post-processing filtering methods. Resolution is lowered by these filters as the signals are smeared over a few resolution cells (Tarchi et al., 2003a). Measured displacements are therefore representative of an extended area resulting in an effective resolution lower than the theoretical resolution given by the system properties (in our case 14x14 m instead of 1.94–6.5 m), and objects with high reflectivity contribute more to the measured values.

A comparison of mapped discontinuities and the GB-DInSAR displacements (Figure 3.6) shows that many discontinuities correlate with GB-DInSAR displacement patterns, although deviations of a few pixels occur. Opening rates across two discontinuities derived from GB-DInSAR are somewhat lower than field measurements. Such discrepancies can be caused by displacements oblique to the LOS and post-processing filters smearing displacements over a 14x14 m area, although small errors in geo-referencing of the GB-DInSAR images can also introduce further discrepancies. Within the scarp created by the 1991 failures, only a few discontinuities were found to correlate with strong differential displacements on the GB-DInSAR maps. Limited resolution is a possible explanation for this observation, since sharp changes in the displacement pattern may be smoothed through filtering. However, it remains unknown whether such sharp differential displacement patterns are absent within the scarp due to filtering or because the real displacement field within the lower part of the current instability is continuous rather than localized along active structures. Continuous deformations could result from large-scale basal sliding, where large portions of the rock mass move at similar rates.

Resolution limitations can also explain discrepancies between displacement rates derived from GB-DInSAR and geodetic measurements. When a geodetic reflector moves at a different rate than the surrounding area because it is installed on a locally unstable block, the GB-DInSAR and geodetic measurements may not show the same displacements. Points 110, 130, and 151 (Figure 3.8) show higher velocities for the total station than for the radar measurements, which likely results from blocks that move locally faster than the surrounding rock mass. An example is displayed in Figure 3.10 for point 110. Such observations illustrate the spatial resolution limitations of GB-DInSAR, which are important to acknowledge in any attempt to interpret displacement patterns on a scale close to the effective resolution of the system. Differential displacements along active fractures can only be interpreted properly if their spatial extent and displacement difference is large enough to not be affected by resolution limits and filtering effects.

3.4.2 Temporal resolution

GB-DInSAR surveys at the slowly moving Randa rockslide showed that phase wrapping occurs when the time interval between repeat surveys was longer than about 100 days. This value may change with variable deformation rates expected throughout the year. Phase unwrapping simplifies interpretation but introduces error and loss of data coverage (Figure 3.8). For kinematic analysis it is essential to detect structural boundaries, such as a basal rupture zone, which requires a time interval sufficient to accumulate measurable deformation. Therefore, a trade-off exists between time intervals short enough to avoid phase wrapping and decorrelation, and long intervals that allow important structures to become distinguishable. Ideally, one would choose shorter time intervals and more repeat measurements. However, this is expensive in terms of both labor and cost. In our study, just four interferograms were available over a total period of 2 years. Nonetheless, individual images representing both short and long intervals provide complementary information.

3.4.3 Volume calculation

Using the identified release planes, combined with mapped structures and the LiDAR DTM, we were able to define likely boundaries of the unstable rock mass at the Randa rockslide. We estimated the total volume to be 5.7±1.5 million m^3, which lies within the range given by Ischi et al. (1991). An orientation of 095/70 was used for the lateral release plane, while an orientation of 135/40 for the basal shear zone was found to best match the trace observed with GB-DInSAR. This orientation also matches the orientation of the basal failure surface of the second 1991 event (Sartori et al., 2003) and the azimuth of geodetic displacement vectors. For the back boundary to the north-west a nearly vertical plane as given by Willenberg et al. (2008a) was assumed. The northern boundary of the instability remains uncertain since it lies in a partly shadowed and vegetated area with unreliable GB-DInSAR data. Two scenarios for the northern boundary were used to delineate the rock mass: 1. the uninterrupted trace of the basal rupture zone daylighting to the north, or 2. a plane dipping steeply to the south and cutting the basal rupture surface at depth. The volume estimates for both scenarios differed by 0.6 million m^3 for these two scenarios and were averaged for the final number.

3.4.4 Implications for kinematics

A preliminary analysis of the kinematics of the current instability can be deduced from displacement patterns. A 2-D conceptual model of the kinematics of the instability is displayed in Figure 3.11, which combines results from both Willenberg et al. (2008b) and this study. The block toppling mechanism suggested for the top of the instability is confirmed by the GB-DInSAR images, which show a gradual increase of displacements from 4.4 mm to about 12 mm over a vertical distance of ~150 m towards the top edge of the scarp (region (f) in Figure 3.1 and Figure 3.4). As shown on the micro-seismic activity maps by Spillmann et al. (2007b) in Figure 3.9, internal deformation and shearing within this region are strongest, where the displacements rates are highest. This may be interpreted as slip along discontinuities separating toppling columns. Below the top of the scarp, a large area showing nearly uniform displacements (region (d) in Figure 3.1C) suggests different kinematic behavior for the lower portion of the instability. This rather uniformly moving area has a displacement magnitude similar to that just above the basal rupture zone. Within this area only few sharp changes in the displacement field are found, as demonstrated in Figure 3.7. Possibly only a few discontinuities are active within lower parts of the instability, whereas most of the deformation is localized along the basal rupture plane. We interpret this displacement pattern as translational movement on a planar or stepped shear surface, as hypothesized by Willenberg et al. (2008b), Jaboyedoff et al. (2004), and Sartori et al. (2003). The transition between toppling and translational failure occurs at a sharp change of the slope angle in the 1991 failure scarp from about 80° at the top to about 60° below. The displacement rate on the basal rupture surface is estimated to be ~4.4 mm/yr. Some small-scale displacement patterns deviating from this uniform rate in this region are interpreted as superimposed secondary instabilities as shown in Figure 3.7.

3.5 Conclusions

Displacements associated with a large-scale basal rupture zone and lateral release zone bounding the current instability at the Randa rockslide were detected using GB-DInSAR. Structures associated with these displacements were confirmed with high resolution aerial photographs and a helicopter-based LiDAR DTM. The basal rupture zone is a highly persistent, narrow structure daylighting at the boundary between orthogneiss overlain by fractured paragneiss. Previous borehole surveys failed to intersect the basal rupture surface due to insufficient depth. The lateral release surface in the south was identified as a striated and steeply dipping fault, which can be regarded as the continuation of a lateral release surface from the 1991 rockslides. Both of these bounding structures outcrop on the inaccessible 1991 failure scarp and were not conclusively detected by previous investigations. The volume of the current instability was estimated to be 5.7±1.5 million m^3, and the area of the instability with maximum displacement rate (up to ~20 mm/yr) was identified. Displacement patterns confirm block toppling in the upper part of the instability accompanied by microseismic activity suggesting some degree of internal deformation/shearing of the rock mass. The lower portion of the instability exhibits little differential displacement along discontinuities except for the basal rupture plane. Translational failure is thus suggested for lower regions of the instability as opposed to toppling at the top of the instability.

Many of the large discontinuities previously mapped within the accessible area at the top of the instability showed good correlation with displacement patterns on GB-DInSAR maps. In two cases, we could directly compare crack opening rates measured by hand and by GB-DInSAR, with good results. Comparison of GB-DInSAR displacements with total station measurements showed good agreement for most reflector points. However, three points showed higher velocities than measured with GB-DInSAR, which is likely due to local block movements. Such discrepancies also occur in the comparison of mapped structures with displacement patterns. They illustrate the influence of data filtering on the effective resolution of GB-DInSAR. For detailed interpretation of displacement patterns, such spatial resolution limitations of GB-DInSAR must be considered.

Acknowledgements: GB-DInSAR surveys were performed by Ellegi Srl (Milano, Italy) using the GB-DInSAR LiSA system and LiSALab software; Carlo Rivolta provided technical support. GB-DInSAR measurements were financed by the Federal Office for the Environment, Switzerland. Geodetic measurements were conducted by Klaus Aufdenblatten (Zermatt, Switzerland) and directed by CREALP (Centre de Recherches sur l'Environnement Alpin, Switzerland). Helimap Systems SA (Switzerland) performed the helicopter-based LiDAR survey. We thank Michel Jaboyedoff (University of Lausanne) and an anonymous reviewer for useful comments. This project was funded by the Swiss National Science Foundation (Project No. 2100-059238.99).

Table 3.1: Acquisition parameters for the GB-DInSAR surveys.

Target distance	1.3 - 2 km
Range resolution	1.9 m
Minimal azimuthal resolution	4 m
Maximum azimuthal resolution	6.5 m
Synthetic aperture length	2.7 m
Frequency range	17.10 – 17.18 GHz
Coherence and power (reflectivity) threshold	0.65 and -50 dB

Table 3.2: Dates of the GB-DInSAR surveys and time intervals to the previous survey.

Survey	**Date**	**Time to previous survey**
Reference	22 Sept. 2005	
1st repeat (image B)	20 Nov. 2005	59 days
2nd repeat (image C)	3 Oct. 2006	316 days
3rd repeat (Figure 3.8)	7 June 2007	248 days
4th repeat	26 Sept. 2007	111 days

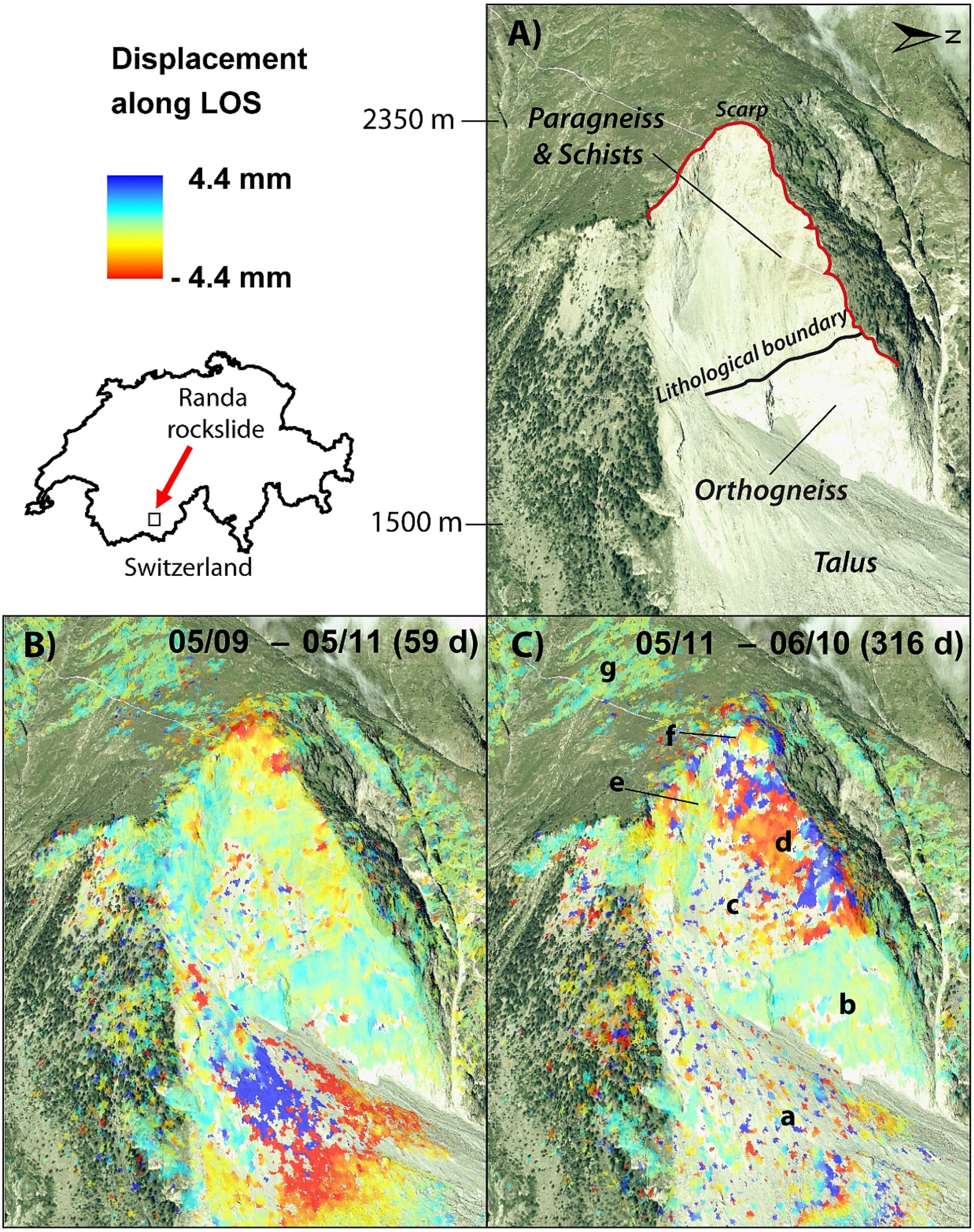

Figure 3.1: (A) Orthophoto draped on DTM. The overview scene is the view of an observer at about 2000m looking approximately towards NW. (B) GB-DInSAR displacement map derived from the 1st repeat with respect to the reference survey. (C) Displacement map from the 2nd with respect to the 1st repeat survey. Dates (yy/mm) of the surveys, as well as the number of days between successive surveys are shown.

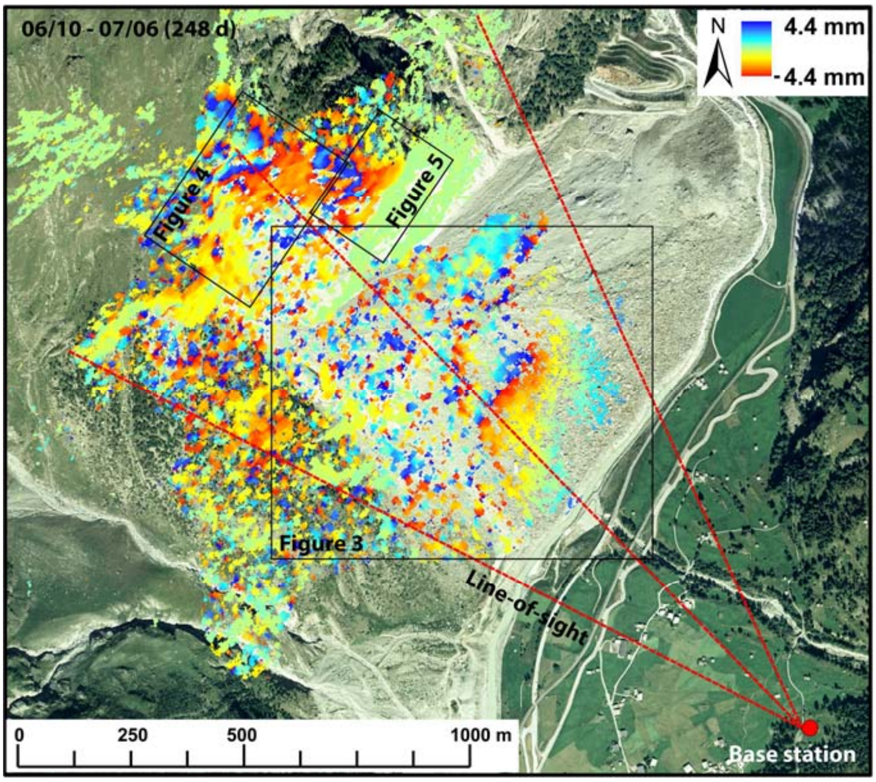

Figure 3.2: Overview map showing the locations of Figure 3.3, Figure 3.4 and Figure 3.5 overlain on an orthoimage. GB-DInSAR displacement map is derived from the 3rd with respect to the 2nd repeat survey (248 days). Also shown is the line-of-sight and location of the base-station on the opposite valley flank.

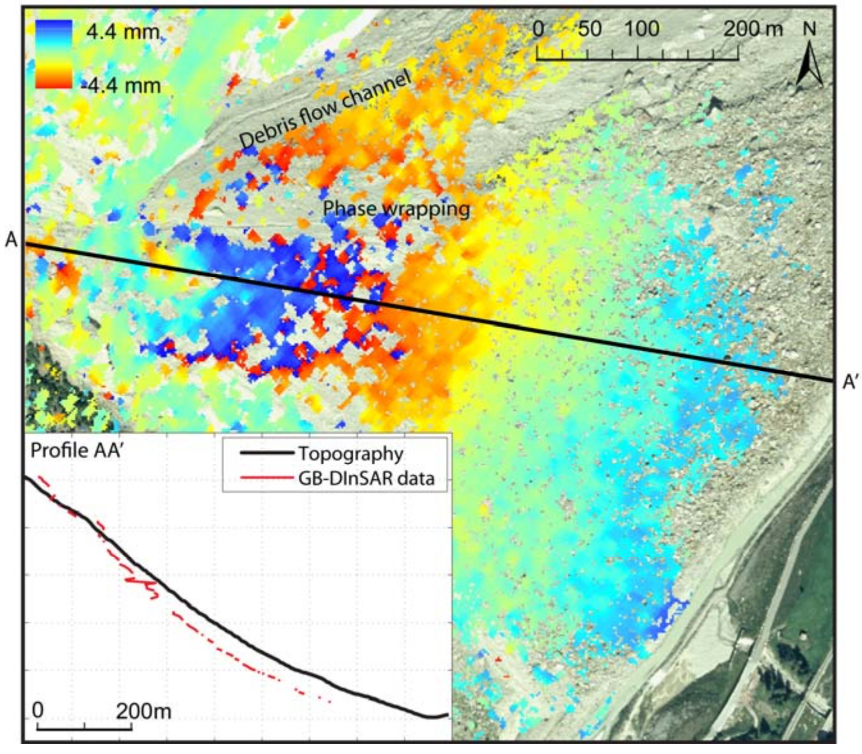

Figure 3.3: 59 days interval GB-DInSAR image showing consolidation of the debris cone. The abrupt change from negative (red) to positive (blue) values is caused by phase wrapping. For profile AA' the GB-DInSAR values were phase unwrapped and presented as a 10 000 times exaggerated change in topography (red line). See Figure 3.2 for location of this detail figure.

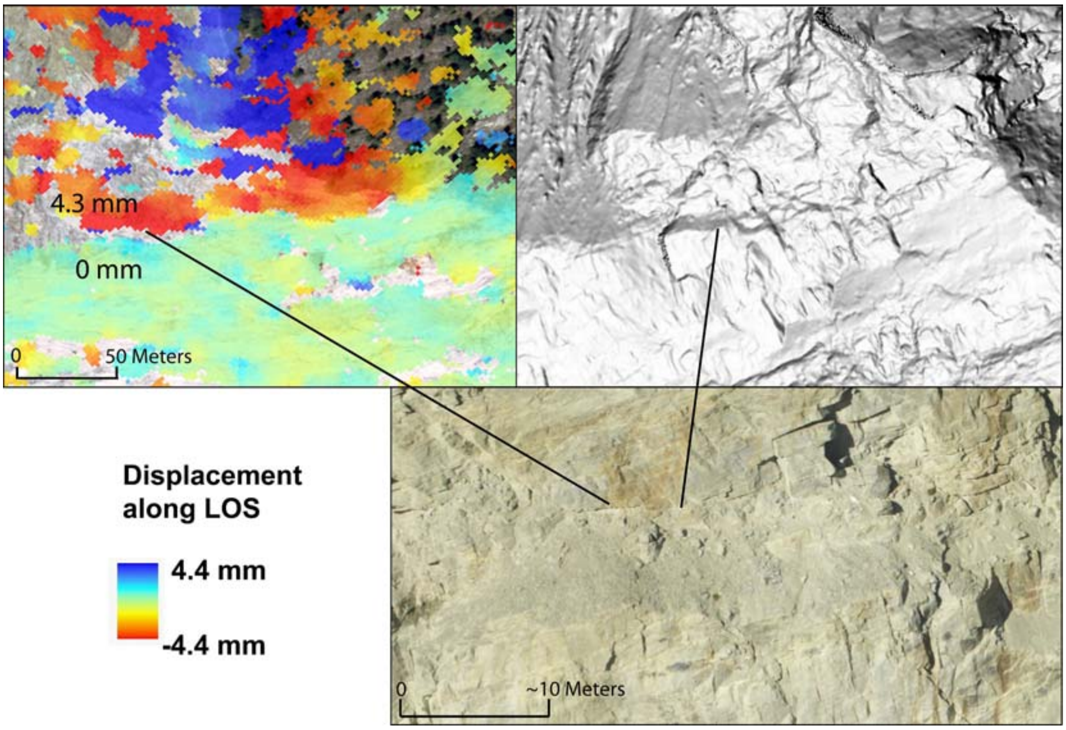

Figure 3.4: Oblique aerial view of GB-DInSAR displacement map (316 days interval; top left), shaded DEM from helicopter-based LiDAR (50 cm resolution; top right), and high resolution photo (pixel size ~2–3 cm; bottom right) showing the basal rupture zone. The displacement pattern indicates an abrupt change from 0 to ~4.3 mm along LOS. This zone coincides with a lithological boundary on the rock face. Location is shown in Figure 3.2.

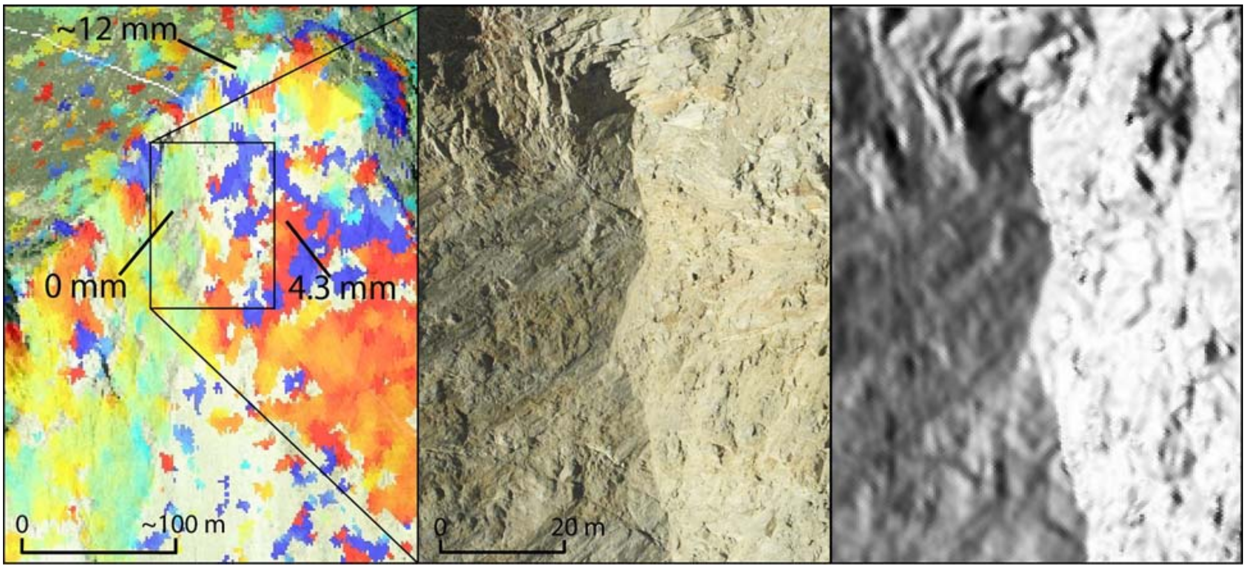

Figure 3.5: GB-DInSAR displacement map (left), high resolution photo (middle), and shaded LiDAR DTM of the lateral release surface (oblique aerial view). This structure can be identified by the transition from 0mm displacement on the left to more than 4 mm on the right. The unstable part on the right suffers from phase wrapping. On the photo and DTM, this transition can be seen as a wedge structure with a striated, smooth plane on the left and highly fractured rock on the right. The color scale for the GB-DInSAR image is the same as in Figure 3.1. Location is shown in Figure 3.2.

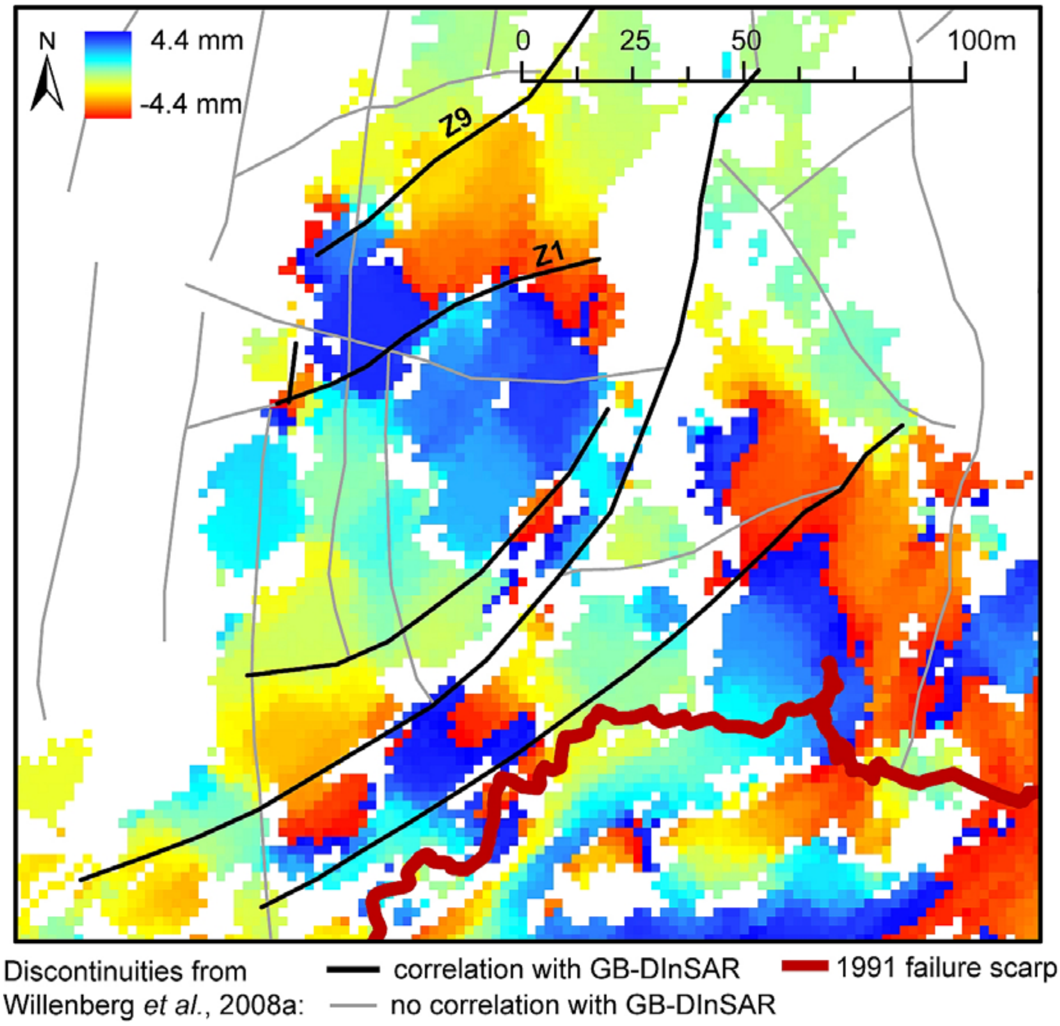

Figure 3.6: Discontinuities mapped by Willenberg et al. (2008a) overlain on the GB-DInSAR displacement map representing 248 days of displacement. Although the displacement map is strongly affected by phase wrapping, some patterns clearly correlate with mapped discontinuities. For the discontinuities Z1 and Z9 opening rates were estimated using the GB-DInSAR displacements and compared to opening rates measured by hand. The GB-DInSAR derived opening rates gave similar but slightly lower values.

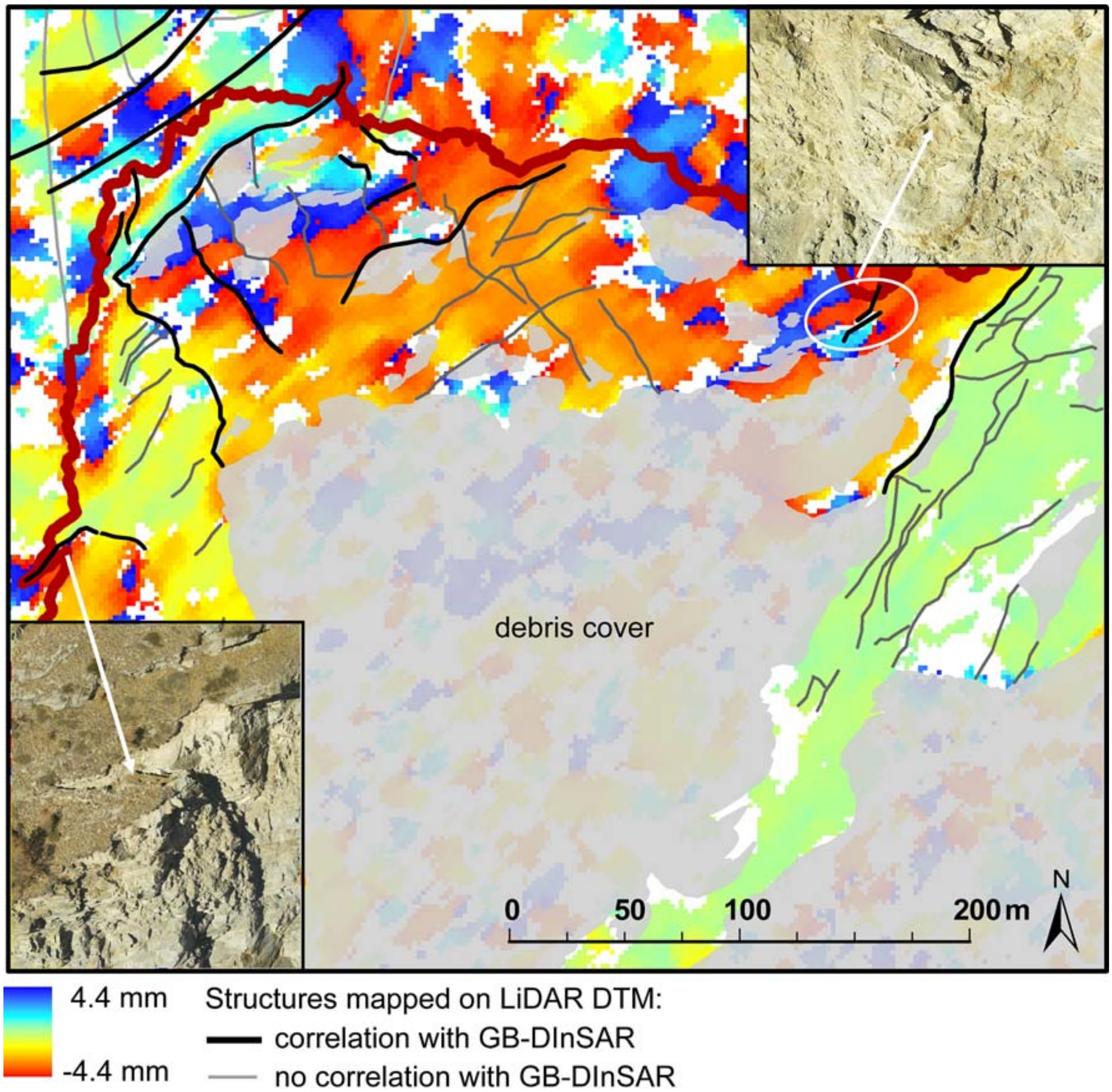

Figure 3.7: The 248 days GB-DInSAR displacement map overlain by discontinuities mapped on the LiDAR DTM. Areas covered by debris are shaded in grey. Two local toppling instabilities could be identified and are highlighted in the inset photographs.

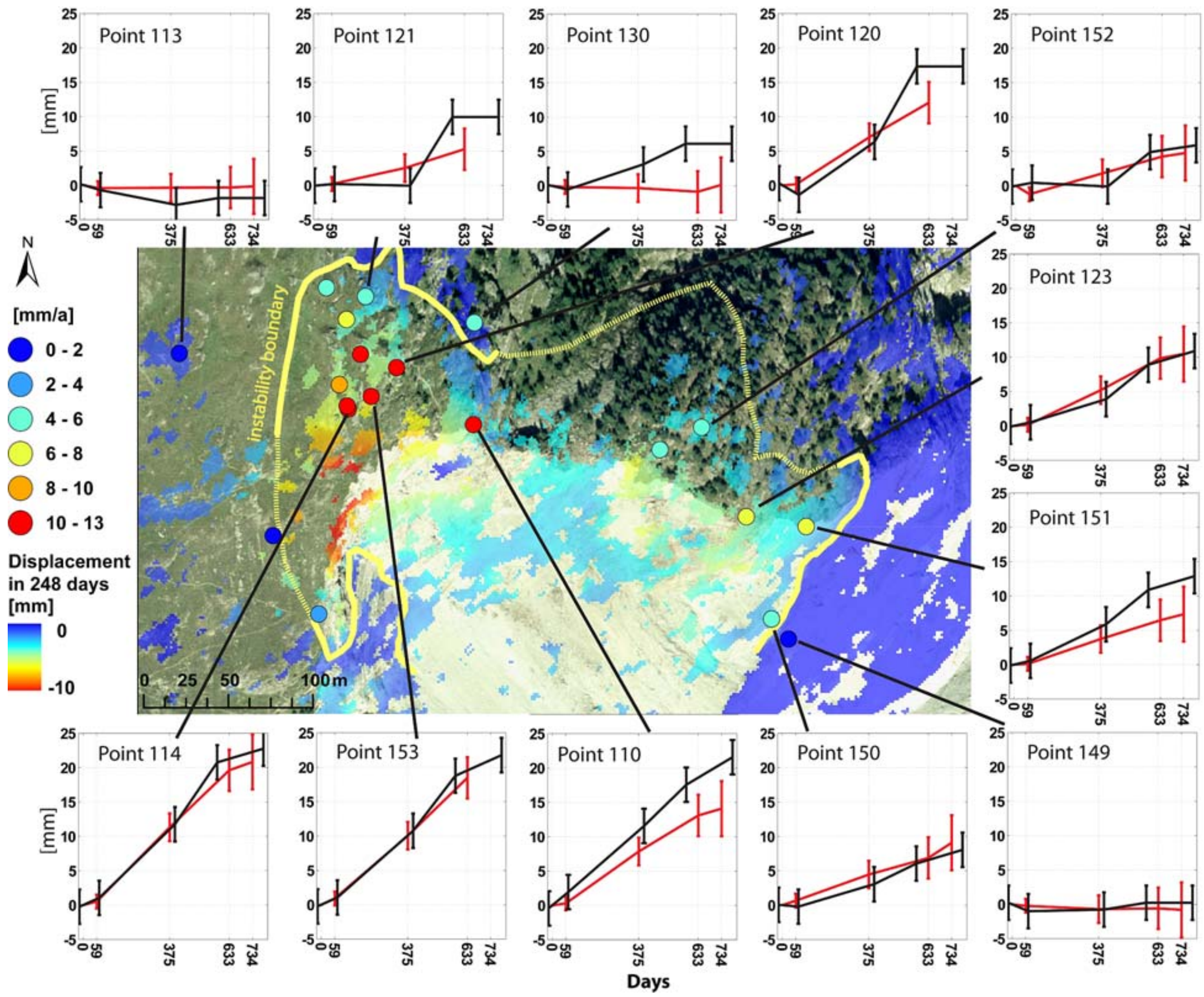

Figure 3.8: Comparison of geodetic distance measurements with GB-DInSAR displacements. Time series derived from GB-DInSAR data at the locations of the reflectors are shown in red, geodetic time series are shown in black. Locations of the reflectors are displayed together with an unwrapped displacement map between the 3rd and the 2nd repeat survey (248 days). The yellow line shows the boundary of the instability derived from GB-DInSAR; dashed portions are uncertain.

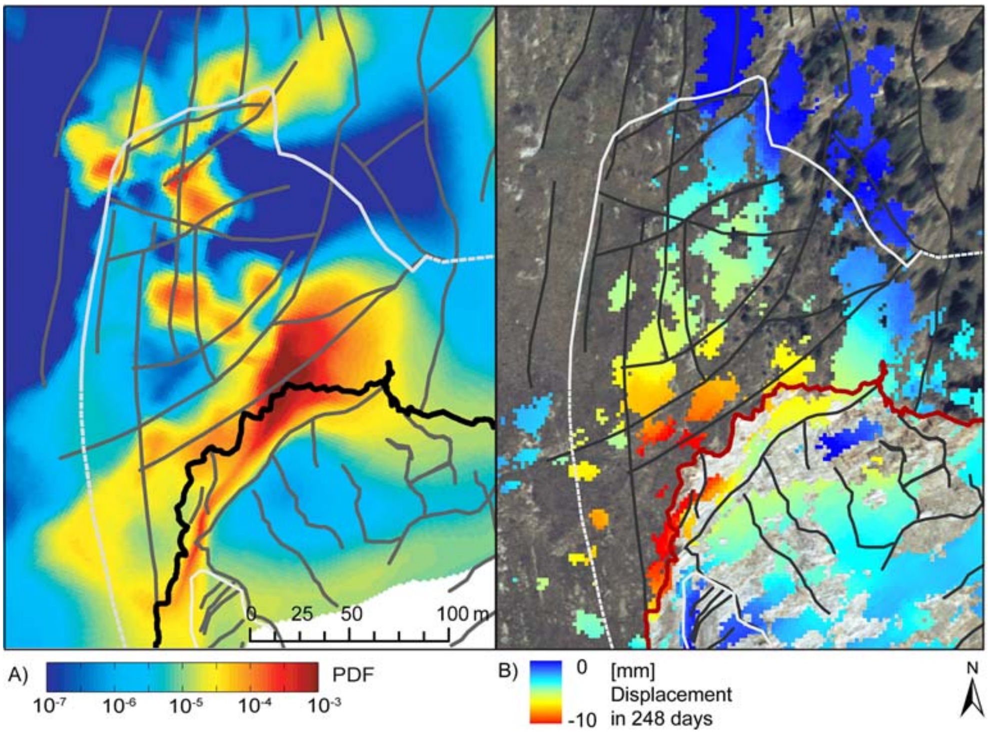

Figure 3.9: (A) Micro-seismic activity map. The locations of 223 microseismic events recorded between 2002 and 2004 are represented as cumulative probabilistic density functions (PDF). High PDF values correspond to high micro-seismic activity. The values are representative for a surface at 15m vertically below the topographic surface. (B) Unwrapped GB-DInSAR images as in Figure 3.8. Both images include the boundary of the instability as derived from GB-DInSAR as well as the discontinuity map from Willenberg et al. (2008a).

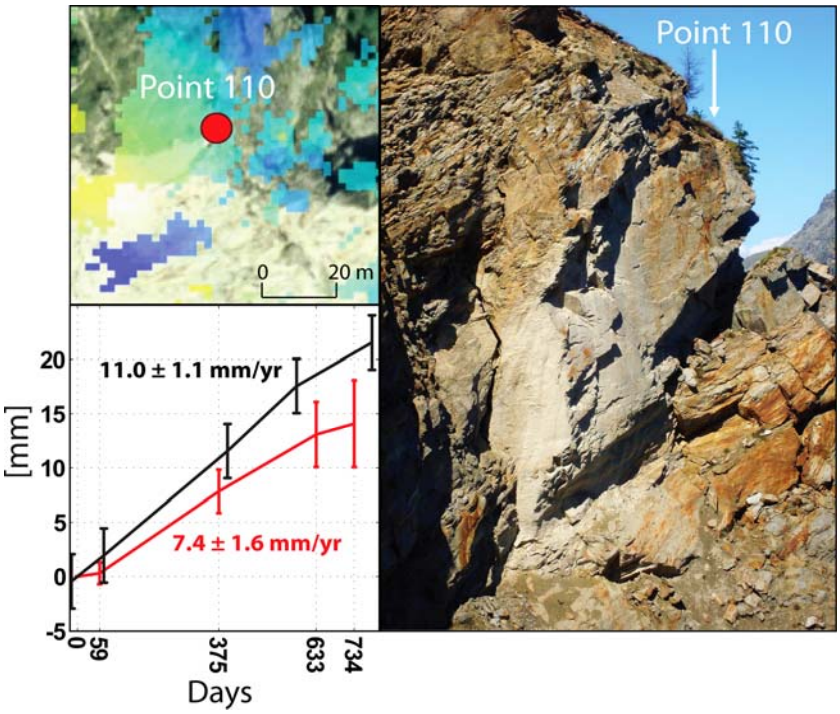

Figure 3.10: Example of a geodetic point for which distance measurements (black line) yielded significantly higher velocities than those extracted from GB-DInSAR (red line). The reflector sits on a block bounded by large open cracks. Due to the size of the block its movements cannot be resolved with GB-DInSAR.

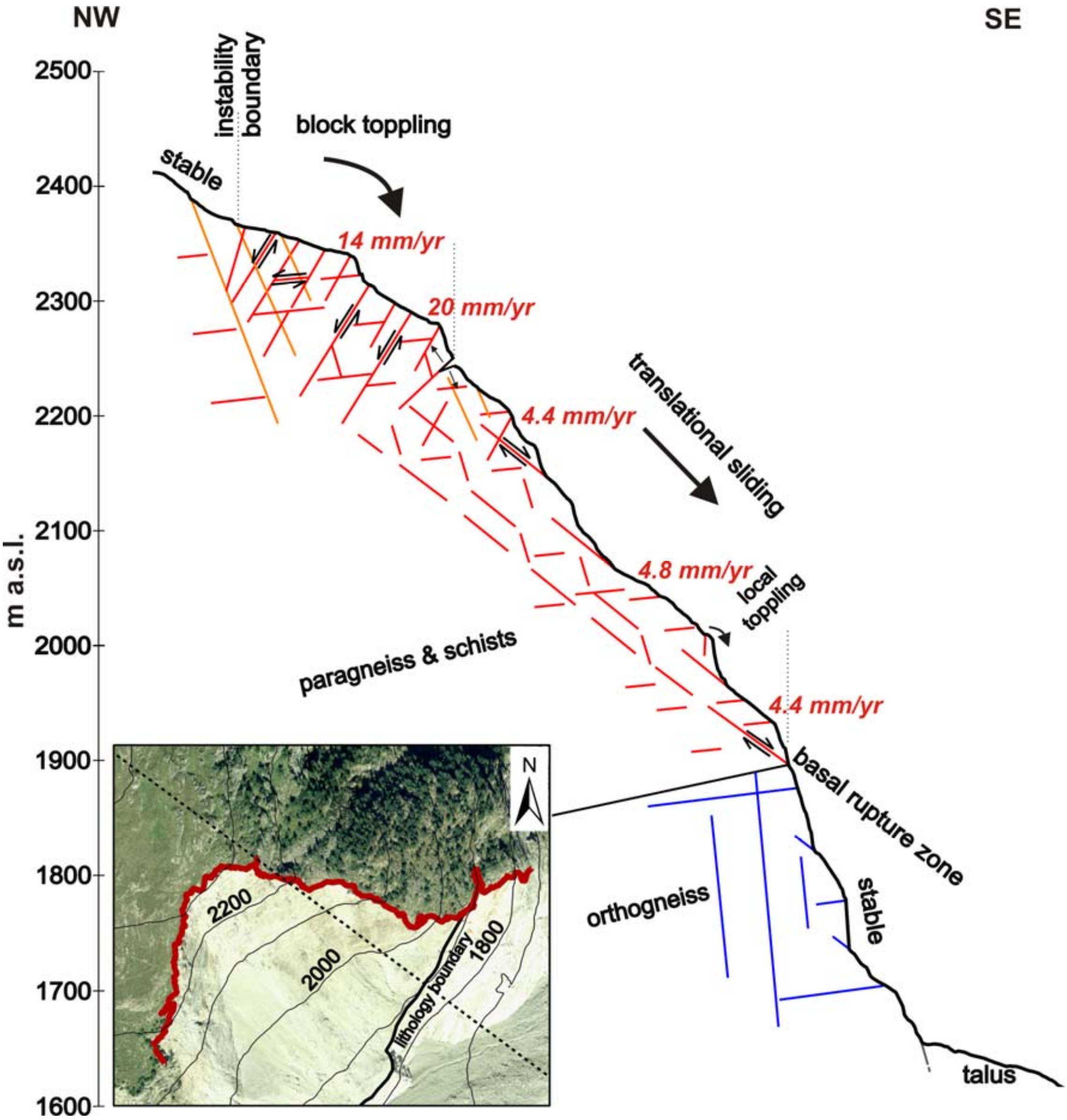

Figure 3.11: Conceptual 2-D kinematic model of the instability. Both the results from Willenberg et al. (2008b) and from this study are included. The velocities indicated are the displacement rates derived from GB-DInSAR.

4. COMPOSITE ROCK SLOPE KINEMATICS AT THE CURRENT RANDA INSTABILITY, SWITZERLAND, BASED ON REMOTE SENSING AND NUMERICAL MODELING

Gischig, V., Amann, F., Moore, J.R., Loew, S., Eisenbeiss, H. and Stempfhuber, W.

Published in *Engineering Geology*, 118, 37-53

29 November 2010

Abstract: Kinematic analysis of slope instabilities in brittle rock is crucial for understanding the reaction of the rock mass to external forcing factors. In steep terrain, inaccessibility often limits collection of relevant data and remote sensing techniques must be applied. This is the case at the current Randa rock slope instability in southern Switzerland, where a total volume of about 5–6 million m^3 moves at a rate of up to 30 mm/yr. A large portion of the unstable rock mass is exposed in an 800 m high inaccessible cliff; the main scarp of the May 1991 rock slope failure. Between 2005 and 2007, a comprehensive suite of remote sensing techniques, including photogrammetry, LiDAR, and GB-DInSAR, was combined with 3D geodetic measurements to characterize the rock mass structure and displacement patterns. Photogrammetry and LiDAR data were measured simultaneously from a helicopter using a system allowing for oblique view angles, which provided optimal observations of the steep rock cliff. We used these datasets to map large-scale structures and extract their orientation and minimum persistence, as well as to characterize the 1991 failure scarp. The northern part of the May 1991 failure surface shows a transition from stepped planar sliding at the base, to failed rock bridges in the center, to tensile failure close to the vertical head scarp. Kinematic analysis of the discontinuity sets in the currently moving rock mass shows that both toppling and translational sliding are feasible failure mechanisms. Toppling is more likely for steep faces above 2200 m, whereas translational failure is more likely in the lower portion of the instability. Interpretation of GB-DInSAR displacement maps revealed similar kinematic behavior, and also allowed identification of a basal rupture zone and lateral release plane bounding the instability. Displacement vectors derived from geodetic surveying provided new insights into the 3D kinematic behavior of the instability. All information extracted from different data sets were integrated in a conceptual model, which was then investigated with 2D numerical simulation using the discontinuum code UDEC. The numerical models were able to reproduce the hypothesized kinematic behavior well.

4.1 Introduction

Hazard assessment and analysis of failure mechanisms for an unstable rock slope require detailed knowledge of the kinematic behavior of the rock mass (e.g. Goodman and Kieffer, 2000). Reconstructions of catastrophic failure events have shown that rock mass kinematics not only controls stability, but can also influence run-out distance; e.g. Sitar et al. (2005) showed for the Vajont landslide that a greater number of kinematic degrees of freedom prior to failure ultimately resulted in higher run-out velocity. Kinematic analyses of rock slopes take into account discontinuity properties, such as orientation, persistence, strength, large- and small-scale roughness, in addition to the geometry of the rock slope (e.g. Goodman, 1989; Wyllie and Mah, 2004). Measuring and characterizing such discontinuity properties have become standard practice in rock mechanics, and many tools for analysis and statistical description of structural data are available (Goodman, 1989; Priest, 1993; Jing and Stephansson, 2007; Tran, 2007). However, in the case of steep rock slopes in alpine terrain, limited accessibility for field investigations presents a major problem, since outcrops yielding most information are often too steep or dangerous to investigate *in situ*.

Remote sensing techniques, such as laser scanning and photogrammetry, have proven to be appropriate tools for characterizing the structure of rock masses (e.g. Lemy and Hadjigeorgiou, 2003; Buckley et al., 2008; Oppikofer et al., 2009; Sturzenegger and Stead 2009). Recent developments have led to helicopter-based systems that integrate both laser scanning and photogrammetry, operated manually (Vallet and Skaloud, 2004) or via remote control (Eisenbeiss, 2008). Due to the advantage of flexibility in selecting the range and view angle according to site requirements, such instruments are ideal for rock slope characterization in steep, inaccessible terrain.

An essential prerequisite for complete kinematic analysis is the spatial displacement field of the moving rock mass. Traditional methods relying on *in situ* monitoring systems, such as geodetic measurements extensometers and inclinometers, or manual benchmark monitoring, are often not applicable in steep terrain. Satellite-based interferometric SAR can be applied to detect and quantify landslide movement (e.g. Singhroy, 1995; Metternicht et al., 2005; Colesanti and Wasowski, 2006; Osmundsen et al., 2009; Strozzi et al., 2010) but is not capable of resolving the internal kinematics of rock slope instabilities. The latest developments in radar interferometry for landslide applications include radar systems adapted for terrestrial deployment (Tarchi et al., 2003a, b; Werner et al., 2008). These ground-based systems (e.g. GB-DInSAR) operate with high resolution and accuracy and are able to provide detailed landslide displacement maps over large inaccessible areas. However, radar can only detect displacements along the line-of-sight (LOS) of the instrument, while displacement vectors remain unknown. Combining GB-DInSAR with geodetic surveying of 3D reflector networks can overcome this shortcoming and allow for comprehensive description of the displacement field.

Once a kinematic model of the rock slope has been created through analysis of both structural and displacement data, it can be verified with numerical modeling using distinct element codes such as UDEC and 3DEC (Itasca, 2008a,b). These simulations are able to reproduce kinematic behavior based on appropriate input of rock mechanical properties and detailed structural data (e.g. Starfield and Cundall, 1988; Bhasin and Kaynia, 2004; Kveldsvik et al., 2008). Although such models remain conceptual to some degree, they can provide important insights into processes acting within the rock mass.

In this study, we integrate remote sensing (LiDAR, photogrammetry, and GB-DInSAR), geodetic measurements, and numerical modeling for a complete structural and kinematic analysis of the currently unstable rock slope at Randa, Switzerland. This instability has been the subject of numerous investigations over the last ten years, which aimed to explore rock mass structure, kinematics, and mechanisms of progressive failure. However, a major portion of the instability is an 800 m high, steep and inaccessible scarp (resulting from the 1991 failures) where *in situ* measurements are impossible. Most investigations in the past were limited to the accessible uppermost potion of the instability, whereas information from the 1991 failure surface remained sparse and was based mostly on interpretation of photographs (Sartori et al., 2003). We first describe the Randa rock slope instability and previous research performed at the site focusing on outcomes relevant for this study. The second section treats acquisition, processing, and analysis of photogrammetry and LiDAR data, and presents structural information extracted from these data sets. In the third part, we analyze the displacement field obtained from GB-DInSAR and geodetic measurements, with emphasis on differential displacement patterns important for 3D kinematics. Finally, a conceptual kinematic model including both the results from Willenberg et al. (2008a,b) and this study is presented and verified with numerical simulation.

4.2 The Randa rock slope instabilities

The current Randa rock slope instability is the legacy of two catastrophic rockslides that occurred in April and May, 1991 (Figure 4.1). A total amount of 30 million m^3 of crystalline rock failed in two events within three weeks. During the first event on 18 April 1991, 22.5 million m^3 of competent orthogneisses failed, which was followed by a retrogressive failure of 7 million m^3 of paragneisses and schists on 9 May 1991 (Sartori et al., 2003). The debris cone blocked traffic corridors and dammed the Vispa River, which caused flooding of the upstream village of Randa. As described by Schindler et al. (1993), the failed volumes would suggest a longer run-out distance when compared to other rockslide events (Scheidegger, 1973), implying that the damage could have been much more substantial. The shorter run-out can be explained by the fact that each of the major failures took place over several hours and was composed of many smaller events. Detailed analysis of the kinematics of these failures was described by Sartori et al. (2003). No triggering mechanisms were definitively identified. It is most likely that the formation of persistent release planes took place through slow, progressive failure of intact rock bridges over a long period preceding the catastrophic events (Eberhardt et al., 2004).

Geodetic monitoring initiated after 1991 (with repeat measurements once or twice per year) revealed that the rock mass in the crown behind the May 1991 scarp moves at average rates up to 14 mm/yr (Jaboyedoff et al., 2004). In 2000, an *in situ* laboratory was established at the top of the instability within the framework of a long-term multidisciplinary research project (Loew et al., 2007). The main objectives of these investigations are: (1) to obtain a comprehensive 3D description of the rock mass structure and kinematic behavior, and (2) to study the driving mechanisms and temporal evolution of rock mass deformation and progressive failure. In 2005, a first 3D model of the major rock mass structures was created by combining data from geological mapping, deep borehole logging, and geophysical imaging (Heincke et al., 2005; Heincke et al., 2006; Spillmann et al., 2007; Willenberg et al., 2008a). Large-scale discontinuities (i.e. faults and fracture zones with trace lengths of several tens of meters) mapped at the surface could be detected in surface georadar and borehole single-hole radar data. Seismic refraction tomography in the 1991 crown area delineated a region with lower rock mass quality, interpreted as highly broken and dilated rock. Thus, a reliable 3D structural model including the subsurface extent, orientation, and minimum persistence of major discontinuities became available for the uppermost 120 m of the instability, whereas for the lower parts of the 800 m high cliff only assumptions could be made. None of the identified fault sets were oriented parallel to the basal rupture surface of the May 1991 failure, however, the existence of such a plane below the currently unstable rock mass was suspected (Sartori et al., 2003, Jaboyedoff et al., 2004, Willenberg et al., 2008b).

To create a kinematic model of the instability, the structural model was combined with displacement data from the surface (i.e. geodetic data, crack extensometers and benchmarks), as well as from inclinometer and extensometer measurements in three deep boreholes (Willenberg et al., 2008b). Significant differential displacements in both shearing and opening mode occur along persistent large-scale discontinuities, which divide the rock mass into rigid blocks with side lengths on the order of 5 to 30 m. The complex borehole displacement patterns observed in the crown area are best explained by block toppling. Nevertheless, shearing along a basal rupture zone could not be excluded, since the 120m deep borehole may not have reached stable ground.

4.3 Structural analysis from helicopter-based oblique LiDAR and photogrammetry data

4.3.1 LiDAR and photogrammetry data acquisition and processing

In order to improve our understanding of the active rock mass structure below the 1991 crown, the 800 m high Randa cliff (Figure 4.1) was surveyed in November 2007 using the Helimap system (Helimap System SA, Switzerland), which combines laser scanning and oblique optical imagery (Vallet and Skaloud, 2004; Vallet, 2007). The system uses a Riegl LMS-Q240i-60 laser scanner and a Hasselblad H1 camera that are both attached to a manned helicopter. A GPS antenna and inertial system provide position and orientation during data acquisition (accuracy on the order of 1 – 10 cm). Data were acquired by flying along nineteen horizontal flight lines parallel to each other at different altitudes, and at an average distance from the rock cliff of about 200 m. Raw processing of the LiDAR data was completed by Helimap System SA (Skaloud et al., 2005; Vallet, 2007). For further analysis in ArcGIS, the 3D LiDAR point cloud needed to be rasterized. With the original XYZ-dataset this causes strong distortions and occlusions in steep and overhanging areas. Thus, the points were rotated such that the raster optimally displays the 1991 failure surface. For processing the oblique aerial photographs, both GPS measurements as well as ground control points (GCP) measured with geodetic surveys were used for higher accuracy (Eisenbeiss, 2009). The orientation of the images was then rotated similar to the LiDAR data and undistorted using the corresponding LiDAR DTM. Thus, a set of orthoimages with an oblique view angle was obtained, which could be used for detailed structural analysis of the rock faces in ArcGIS.

4.3.2 Structural analysis

Both orthoimages and the hill-shaded DTM were used as complementary information to map linear and planar features in ArcGIS. From the delineated polylines and polygons, XYZ-data were extracted and rotated back into the original coordinate frame. Orientations were then determined by fitting a plane through the data. We applied the orthogonal-distance regression method, which attempts to minimize the normal distance of each point to the plane (Björck, 1996). For polygons, the orientations were generally considered reliable since points are optimally distributed along a plane. In contrast, polylines often had a collinear point distribution resulting in inaccurate orientation estimates. Based on careful visual inspection of each polyline along with the fitted plane, we decided if the point distribution was sufficient for a reliable orientation. For some critical structures, we imported planes with assumed orientations into ArcGIS and intersected them with the DTM. By attempting to match the intersection trace of the plane and the DTM with the measured polyline, we could decide whether the assumed orientation was reliable. Reliability was thus assessed for each polyline orientation individually, and unreliable orientations were discarded from the dataset used in later analyses.

For the structural analysis, we treat two structural compartments of the failure surface separately: (1) the Randa orthogneiss forming the lower part of the instability up to about 1900 m a.s.l., and (2) the paragneiss and mica-schist sequence overlaying the orthogneiss (Figure 4.2). Willenberg et al. (2008a) distinguishes large-scale structures (faults and fractures zones) from small-scale fractures by their trace length of several tens of meters. Since resolution of our remote sensing data only allows systematic investigation of structures with extents greater than 15 m, we focus only on large scale structures in accordance with the analysis of Willenberg et al. (2008a). Characterization of structures as faults and fracture zones, or as brittle, brittle-ductile, and ductile features, is somewhat unreliable in our analysis, since orthoimages cannot provide sufficient detail on the architecture of individual structures. We therefore prefer to use the general term *large-scale discontinuities* for all mapped structures.

4.3.3 Results

In the following section, we present structural data obtained through analysis of DTMs and orthoimages. Figure 4.2 shows an overview of the mapped large-scale discontinuities. Figure 4.3a and c present these data in stereographic projection. Sets were distinguished by two criteria: (1) orientation clustering in stereographic projection, and (2) geometrical interactions of individual structures observed during mapping.

For both orthogneiss and paragneiss units, the data sets were compared to those of Willenberg et al. (2008a) and Sartori et al. (2003) (Figure 4.3b and d). The three large-scale systematic discontinuity sets described by Willenberg et al. (2008a) are labeled F1, F2, and F3, and were obtained by geological and geophysical mapping in the uppermost portion of the instability. Sartori et al. (2003) presented seven discontinuity sets (S, J2–J6, J6•) mapped on vertical view aerial photos and DTMs from before, between, and after the 1991 failure events. In our new investigation the set was found within the paragneiss only, whereas F1 and F3 also occurred in the orthogneiss. Note that only a few representative F1 discontinuities – which are parallel to foliation – were mapped in the paragneiss, since the orientation of this set was already described in previous studies. In general, our data match the previously identified discontinuity sets, although some differences in orientation to the sets described by Sartori et al. (2003) occur. For the present study, the sets are labeled consistently with Willenberg et al. (2008a) as shown in Figure 4.3. Discontinuity properties are summarized in Table 4.1. Note that spacing, curvature and surface conditions are difficult to determine from remote sensing data. Only for sets F1, F2, and F3 are direct field observations available. Thus, the properties given in Table 4.1 are rough interpretations.

The mapped discontinuity sets can be summarized as follows:

- F1 (mean dip direction/dip: 240°/20°) contains faults subparallel to foliation and exists in both the para- and orthogneiss. The spacing of the mapped faults is in the range of 5 to 20 m.
- F2 (355°/60°) corresponds to a set dipping steeply into the slope and has a high scatter in orientation. Most open tension cracks at the top of the current instability belong to this set, and they can

also be clearly identified in the 1991 failure scarp. The traces are usually not straight but show long wavelength curvature (wavelength on the order of ~20 m). The spacing of the mapped faults is about 5 to 25 m on average. Minimum trace length is greater than 200 m.

- F3 is characterized by brittle fracture zones rather than single fault planes. Individual fractures of these zones have spacings on the order of decimeters and exhibit smooth surfaces with some signs of weathering. The fracture zones themselves are complex but have a clear morphologic expression forming benches on the scale of 5 to 20 m wide. The trace length can reach up to 200 m. F3p (095°/70°) and F3o (070°/75°) differ in orientation but are both sub-vertical, highly-persistent sets that intersect set F5o at an angle of about 60°.
- F4 occurs in both the paragneiss (F4p: 160°/45°) and orthogneiss (F4o: 135°/60°), and was not identified as a set during investigations at the top of the instability by Willenberg et al. (2008a). These discontinuities are clearly visible in the lower part of the May 1991 head scarp and form stepped surfaces (Figure 4.4). In the paragneiss, the dip directions have large scatter. F4 discontinuities have trace length of at least 200 m.
- F5p (125°/65°) contains shorter discontinuities with lengths up to 30 m in the paragneiss. They connect F4 planes, are often curved, and have irregular surfaces (Figure 4.4). F5o (125°/80°) is the subvertical set forming the steep rock faces of the orthogneiss cliff. F5o discontinuities are more persistent (~150 m) and connect set F4o which dips out of the slope.
- F6 (030°/40°) only occurs within the paragneiss close to its boundary with the underlying orthogneiss. Only about 10 mapped discontinuities belong to this set. The longest trace length measured is about 80 m, however the discontinuity set is parallel to a large tectonic fault in the orthogneiss, which acted as a basal failure plane for the first 1991 rockslide and is now buried below debris (Sartori et al., 2003).

These discontinuity sets also played a key role in forming the May 1991 failure surface, which has a wedge-type geometry bounded by F3 and F4/F5 discontinuities (Figure 4.4 and Figure 4.5 cross-section B). Set F3 forms the large (>200 m) fault structure in the south of the head scarp (Figure 4.2 and Figure 4.4). The rupture plane of the May 1991 failure, with orientation of 135°/40°, belongs to set F4. Above the May 1991 basal rupture surface, the surface morphology exhibits a transition from smooth sliding planes at the base, to sliding planes alterating with irregular subvertical steps, to a region with predominantly irregular surfaces, finally to a subvertical head scarp (Figure 4.4). The large scatter of set F4 in the paragneiss (Figure 4.3a) results from a SE to SSE rotation of the dip direction towards the northern end of the scarp, forming a curved rupture surface in the middle paragneiss portion (Figure 4.5 cross-section C). The steps connecting the individual F4 planes (smooth surfaces) in the lower part of the May 1991 rupture plane are formed by F5 discontinuities (irregular surfaces). Their rough, irregular morphology and large scatter in orientation suggest they are broken intact rock bridges that were destroyed prior to or during the 1991 events through tensile failure (Figure 4.4). Thus, we suggest that the May 1991 failure is characterized by shear failure at the base and tensile failure at the top separated by a transition area in between. In the transition area both tensile and shear failure occurred, which formed a stepped failure surface.

4.4 Displacement field of the unstable rock mass

4.4.1 Ground-based radar interferometry (GB-DInSAR)

Between 2005 and 2007, five GB-DInSAR surveys were performed at the Randa rockslide. The resulting displacement maps covering four subsequent time intervals provided essential information on the large-scale kinematics of the current instability (Figure 4.6). A complete interpretation and discussion of these data is given by Gischig et al. (2009). The displacement data revealed the existence of two major release planes bounding the instability (Figure 4.5). A basal shear surface daylighting at the contact with the Randa orthogneiss forms the lower boundary of the current instability. Its orientation was estimated to be 135°/40°, which matches the F4 orientation of the basal rupture surface of the May 1991 failure. A rather uniform displacement pattern above the basal rupture surface indicates translational failure along a planar or moderately stepped rupture plane, which may be the dominant kinematic mode in the lower part of the instability. The southern boundary consists of a large, steeply-dipping fault oriented 095°/70° which acts as a lateral release plane (as it did for the May 1991 failure). At the top of the head scarp, displacements increase to their highest value. The displacement pattern in the crown area is best interpreted as block toppling, as previously suggested by Willenberg et al. (2008b). The GB-DInSAR data thus revealed that two distinct kinematic failure modes exist at the Randa instability separated by an abrupt change in slope angle at 2200 m: toppling occurs in the nearly vertical cliffs above 2200 m and translational sliding below.

4.4.2 Geodetic measurements

4.4.2.1 Large-scale geodetic network (LSGN)

Surveyors have monitored the Randa instability since 1995 by measuring a geodetic network once or twice per year with a total station (Klaus Aufdenblatten Geomatik, Zermatt). The base lengths of this network range from 1300 to 2000 m and cross the entire valley. The results were presented by Jaboyedoff et al. (2004) and are reproduced in Figure 4.7a. Displacement vectors are available for a total of seven 3D reflectors. Another 18 reflectors, for which only distance measurements from the opposite valley flank are available, helped delineate the lateral extent of the current instability. The three deep boreholes at the top of the instability were also included in the network and measured at the same interval after 2001. Displacement rates deduced from these data range from 2 to 14 mm/yr and show consistent long-term values. The average direction of movement has a trend of about 135° and plunge angle around 25 to 35° (extreme values of 10° and 46° are also observed).

4.4.2.2 Small-scale geodetic network (SSGN)

In September 2008, a new local geodetic network was installed at the crown of the instability and surveyed monthly over the following year. The benefit of these new geodetic measurements is twofold: (1) Only a few displacement vectors at the top of the instability were previously available giving only sparse information about the 3D displacement pattern. A denser network with smaller base lengths can provide more accurate and complete information regarding the relative direction of block movements. (2) Seasonal variations in the displacement rate could be measured by choosing time intervals between repeat measurements of about one month throughout a full annual cycle. As this work concentrates on rock slope kinematics, we will discuss only the displacement direction rather than temporal changes in displacement rate. The latter topic will be the subject of a future publication.

4.4.2.3 SSGN: network design

The layout of the SSGN is presented in Figure 4.7b. In contrast to the LSGN, the measurement base length varies from 10 to 270 m resulting in higher accuracy. Angle and distance measurements were performed using a Leica total station (type TPS1201) and retro-reflector targets (Geodata Miniprisms) attached to rock. Commonly in 3D monitoring applications, a number of base stations are set within a stable area, and the monitoring points measured from different locations to obtain optimal spatial coverage for resolution of displacement vectors. Due to strong topographic occlusions and avalanche risk in winter, it was not possible to place the total station on stable ground and have a sufficient number of monitoring points visible. Instead, three base stations were chosen within the unstable area, and various fixed points located on adjacent stable ground were measured. The locations of the base stations relative to the fixed points were thus computed and additional monitoring points were located relative to the base stations. A total of 14 fixed points, as well as 20 monitoring points (labeled F or M, respectively in Figure 4.7b) were measured from three base stations (S1, S2, and S3). The choice of fixed point locations was based on site inspection and the location of the instability boundary (Figure 4.7b). In total, 11 repeat measurements were carried out within 359 days.

4.4.2.4 SSGN: processing

The first step in geodetic data processing for each repeat survey included application of standard adjustment theory (LTOP; Swisstopo, 2009). Coordinates for each point were thus obtained, which were locally adjusted relative to each other. Displacements between two repeat surveys were computed by applying a coordinate transformation (seven parameter 3D-Helmert transformation; Niemeier, 2002), which attempts to optimally overlay the fixed points of each repeat survey with the ones from the first survey. The advantage of this strategy is the possibility to detect unstable fixed points due to local block movements, which could otherwise be erroneously assumed stable. Mean displacement vectors were then computed by fitting a line through the 3D coordinates of all subsequent repeat surveys for each point using optimal distance regression.

4.4.2.5 SSGN: results

SSGN survey results are presented in Figure 4.8. Resolved displacement orientations generally have an accuracy ranging from 5° to 15°. Smaller errors occur for larger displacements, since orientations are better determined if the point locations of subsequent surveys span a longer distance along a line (maximum error is ~20° for the smallest significant velocity). The velocity accuracy is about 3 mm/yr. In the fixed point group, only point F8 showed movements after a few repeat surveys indicating that the prism was installed on a locally unstable block. It was consequently removed from the fixed point group and assigned to the monitoring group in final data processing. Some monitoring points remained stable, which helped determine the location of the instability boundary in greater detail, especially the southern and northern extents. In general, the instability boundary postulated during previous investigations was confirmed. The measured displacement rates were in good agreement with rates obtained from LSGN surveys for points located close to LSGN reflectors. Near the northern boundary of the instability, displacement rates range from 2 to 6 mm/yr. In the south, displacement rates are around 12 mm/yr and exhibit little spatial variation. At the 1991 headscarp, two points show displacements greater than 30 mm/yr. The trend of displacement vectors varied between 125° and 147° and plunge angles between 25° and 35°. Plunge angles out of this range occur primarily for slowly moving points, for which directions are more uncertain.

4.5 Kinematic analysis of the current rock slope instability

4.5.1 Extent of the unstable rock mass

The current instability at Randa shows a complex 3D geometry with a presumably stepped basal rupture surface daylighting at the lithological boundary, a steeply-dipping persistent lateral release plane in the south, and a ridge-type topographic surface. Figure 4.5 displays this rock mass geometry in a series of vertical cross-sections perpendicular to the direction of movement. Also shown is a map of the vertical extent of the rock mass body as bounded by the lateral release plane, a planar basal rupture surface, and the discontinuity limiting the instability to the north. Using these release planes in combination with the LiDAR DTM, we were able to estimate the volume of the unstable rock mass to be ~6 million m^3 (Gischig et al. 2009). This volume represents the maximum possible extent of the current instability, since the basal rupture surface may be stepped instead of planar and the boundaries in the north-west are uncertain. Internally, the unstable rock mass is dissected into rigid blocks with variable geometries and local displacements.

4.5.2 Kinematic analysis of structural data

4.5.2.1 Stereographic analysis

In a first attempt to understand the kinematics of the unstable rock mass, we apply stereographic analysis techniques (as described by Wyllie and Mah, 2004) to our structural data. This method assumes that all discontinuities are cohesionless, dry and fully persistent, and the blocks rigid. Lateral constraints and stresses on the blocks are not considered. For these reasons the method does not allow deduction of the true kinematic behavior inside the unstable rock mass, but simply indicates what kinematic modes are possible for a given slope angle. For analyzing toppling and sliding in stereographic projection, the limiting elements are the slope orientation, the dip angle of discontinuities, and their friction angle (Figure 4.9). In agreement with Goodman (1989), we assumed that toppling is only possible when the poles of discontinuities controlling toppling have azimuths deviating less than 30° from the slope dip direction. A further geometrical constraint for toppling is that the ratio of the base length (b) to the height (h) lies below the tangent of the dip angle (α), i.e.: $b/h < \tan(\alpha)$ (Goodman and Bray, 1976). Similar to toppling, an envelope deviating 20° from the slope dip direction was included for sliding (Wyllie and Mah, 2004). Wedge sliding is possible if the intersection line of two planes plunges at an angle lower than the slope angle and greater than the friction angle (Markland, 1972). A refinement by Hocking (1974), however, indicates that sliding along one of the two intersection planes occurs if the dip direction of this plane lies between the trend of the intersection line and the dip direction of the slope.

In our analysis, friction angles of 30°–35° are assumed (Figure 4.9). Toppling, planar sliding, and wedge sliding were analyzed for two different slope orientations: the first oriented 140°/75° represents the uppermost portion of the scarp above 2200 m (slope angle 1), and the second oriented 155°/55° is the mean slope orientation of the lower portion of the paragneiss and schist units between 1900 and 2200 m (slope angle 2, Figure 4.9). Orientations representing the northwest dipping slopes in the north of the instability are not considered here, since they are not kinematically compatible with the observed displacement directions.

4.5.2.2 Toppling and planar/stepped planar sliding

For the steeper slope angle 1 in the upper portion of the instability, both translational sliding along F4 and F5 discontinuities (rarely mapped in this area), as well as block toppling with slip along F2 discontinuities was found to be possible (Figure 4.9a). Borehole radar measurements showed that F2 discontinuities have a subsurface extent of >85 m (Spillmann et al., 2007; Willenberg et al., 2008a). With a spacing of 20 m, the geometrical requirement (b/h) is fulfilled for all discontinuities dipping less than 76° into the slope. Thus, toppling is a feasible kinematic mode for slope angle 1. Block toppling was previously deduced for this part of the instability from borehole deformation measurements (Willenberg et al., 2008b) and was also identified from GB-DInSAR measurements (Gischig et al., 2009).

For the more moderate slope angle 2 in the lower part of the instability, fewer large-scale discontinuities lie within the range of kinematic feasibility for sliding and toppling (Figure 4.9b). Sliding is still possible for all large-scale discontinuities with dip angle lower than 55°, including the basal rupture surface. However, the number of large-scale discontinuities, for which toppling is possible, is reduced to 7 (out of 24 measured F2 discontinuities) compared to 20 for slope angle 1. The dip angles of these discontinuities lie between 75 - 89°, which requires a low b/h ratio (<0.25) for toppling to occur. Thus, sliding along F4 discontinuities with dip angles of 40° to 55° is more likely to be the dominant kinematic mode in this area.

We conclude that two kinematic modes may be acting simultaneously within the current instability, and the change in slope angle at about 2200 m corresponds to the boundary of two kinematically different regions. Such a change in kinematic mode was also suggested previously from analysis of GB-DInSAR displacement maps (Gischig et al., 2009). Slope angles used in our analyses are mean values for the two regions in 1991 scarp. Steeper slope angles exist locally within the rugged topography. Therefore, toppling is also feasible in the lower part of the paragneiss but would create local instabilities superimposed on the global sliding instability.

Note, that for both slope angles, sliding and toppling is not possible for the pervasive and highly persistent set F3 (oriented 095°/70°). However, this set could form a wedge with F4 and F5 discontinuities or simply act as lateral release structures for both sliding and toppling. We explore these possibilities in the following section. Set F6 is not considered relevant for the current kinematics. This set is parallel to the highly-persistent fault that acted as a basal release structure of the first 1991 failure. However, only a few large-scale discontinuities belonging to this set were found in the current instability and their orientation prevents an active role in both sliding and toppling for the given slope angles.

4.5.2.3 Wedge sliding

Wedge sliding analysis was performed for combinations of sets F3, F4, and F5. Figure 4.10 shows the intersection lines of set F3 and F4 (I_{3-4}), as well as F3 and F5 (I_{3-5}). Wedge failure along I_{3-4} is possible for both slope angles considered. The dip direction, however, lies between the plunge of I_{3-4} and the slope dip direction of both slope orientations. Thus, sliding along F4 discontinuities instead of sliding along both F3 and F4 discontinuities occurs (Hocking, 1974). The intersection line I_{3-5} of the wedge formed by F3 and F5 plunges at an angle of about 65° and has a trend greater than the dip directions of both F3 and F5. Sliding along this intersection is only possible for slope angle 1. However, the wedge is highly asymmetric and thus considered an unrealistic failure mode for this slope. We conclude that F3 discontinuities do not form wedges but rather act as lateral release planes for sliding along F4 and the basal rupture surface. Furthermore, the direction of movement cannot be explained with wedge sliding involving F3 discontinuities, but is best explained by sliding only along the basal rupture surface. Sliding along F3 discontinuities is unlikely, instead dislocation in opening mode may be expected. If we attempt to analyze toppling and sliding in a 2D representation of the instability, it is sufficient to display the sets relevant for only these modes. Although the F3 set does not determine the dominant kinematics at the current Randa instability, it provides important kinematic freedom for failure to occur. Thus for 3D analysis, F3 discontinuities are critical. However, the lateral release surface bounds the unstable rock mass only in the upper portion of the instability (see cross-sections in Figure 4.5). In the lower region, the instability displays a ridge-type topography and encounters no lateral constraint from F3 discontinuities.

4.5.3 Kinematic interpretation of geodetic displacement data

In Figure 4.11a, SSGN displacement vectors are overlain on the discontinuity map and shown together with opening rates of the monitored cracks. Most cracks were monitored manually by measuring the distance between benchmarks, however for four cracks, benchmark quadrilateral arrays were installed that also provided the direction of relative displacements (Willenberg et al., 2008b). Also shown in Figure 4.11a are the plunge angles of the displacement vectors. Three compartments of different displacement vectors can be distinguished (Figure 4.11b). At the back boundary of the instability, two cracks show opening at rates of 2 and 2.3 mm/yr. Geodetic measurements reveal 2 to 6 mm/yr movement in this region at a trend of about 130°. Separated from this region by a crack opening at 3.5 mm/yr, a uniformly-moving compartment can be identified. The movement rates in this zone are about 12 mm/yr and the displacement orientation is 135°/30° on average. A third compartment is evidenced by the two vectors close to the failure scarp, which show high rates of movement around 32 mm/yr at an orientation of 147°/30°. These displacement vectors have rotated slightly to the south compared to the adjacent compartment. Measured orientations of crack opening deviate from the geodetic vectors, and trend 150° to 180° for the three large-scale discontinuities at the back of the instability belonging to the F2 set. One discontinuity (F3 set) shows opening oriented EW.

From both the geodetic displacement vectors and orientations of crack opening (Figure 4.11), we conclude that opening normal to F2 discontinuities is insufficient to explain the observed movement directions. Figure 4.12 compares the orientations of displacement vectors with the poles of F2 discontinuities mapped at the top of the instability. The vectors trend southeast while from the trends of the discontinuity poles, a stronger southern orientation is expected. The directions of crack opening, however, match well with the trends of F2 poles. The orientation of set F3 confirms that wedge sliding along F3 discontinuities is unlikely, since it would require that the displacement vectors group along the great circle representing set F3. Instead, some amount of crack opening along F3 discontinuities in the western portion of the instability is also necessary to accommodate deformation. Stereographic wedge sliding analysis has already suggested such opening dislocation along F3 discontinuities.

Although trends of the displacement vectors deviate from that expected for toppling along F2 discontinuities, their plunge angles match well. The orientations of F2 discontinuities suggest that displacement vector plunge angles of 10° to 35° are expected for toppling. Also included in Figure 4.12 is the basal rupture surface (135°/40°). Most resolved displacement vectors show plunge angles lower than 40° as expected for translational sliding along the basal rupture surface, confirming that toppling is the dominant mechanism at the top of the instability. The trends of the vectors, however, match well with the dip direction of the basal rupture surface. We conclude that the trend of the displacement vectors is strongly influenced by a component of sliding along the basal rupture surface, while the plunge is determined by toppling at the top of the instability.

4.6 Numerical investigation of 2D kinematics

4.6.1 Universal Distinct Element Code (UDEC)

Numerical modeling of the kinematics of hard-rock slopes requires representing the geometry and strength properties of a large number of discontinuities separating intact blocks. The distinct element method applied in the commercial 2D software UDEC (Cundall and Hart, 1992; Itasca, 2008b) has proven to be a powerful tool for analyzing the behavior of a discontinuous rock mass. Many successful applications in rock slope stability problems are reported (e.g. Bhasin and Kaynia, 2004; Amann, 2006; Kveldsvik et al., 2008). The method allows for intersecting a continuum material with cracks, thus creating blocks that are deformable and able to move individually. Formation of new contacts between blocks, as well as loss of contact between separating blocks, is also accounted for. The blocks themselves are treated with finite difference discretization. Thus, a full set of constitutive relationships and strength properties for discontinuities, as well as the elastic properties for intact blocks are required as input parameters.

4.6.2 Geometry

We first constructed a 2D conceptual model from the combined kinematic analysis of structural data and displacement patterns (Figure 4.13a), which was then used to create the representative geometry in UDEC (Figure 4.13b). Note that in Figure 4.13b only the relevant portion of the model is presented, while the full model extent was larger such that boundary effects are minimized. Discontinuities with dip directions deviating more than 30° from the trend of the profile line were not represented in the 2D profile, with acknowledgment that we will not be able to reproduce all details of the observed kinematics. Especially for set F3 we argue that this set creates lateral release surfaces but has no kinematic relevance for sliding or toppling in a 2D model. F4 and F5 discontinuities were only included below 2200 m, since no large-scale discontinuities from these sets were encountered in the boreholes at the top of the instability (Willenberg et al., 2008a). Not all large-scale discontinuities are shown as fully-persistent in Figure 4.13a, indicating that they may be separated by intact rock bridges. For implementation in UDEC, such discontinuities were created as fully-persistent faults and the presence of intact rock bridges accounted for by assigning increased effective cohesion and frictional strength properties corresponding to a given percentage of rock bridges (Jennings, 1970). Thus, the manner in which the failure surface steps through the rock mass is calculated and no kinematic possibilities are suppressed by setting rock bridges deterministically. The spacing of F1, F2, and F4 discontinuities was set to 20 m, while the spacing of F5 was 15 m. Single large-scale discontinuities for which the location and orientation were known from field mapping were explicitly added to the model.

4.6.3 Material properties

The following constitutive laws were applied: (1) perfect elasticity for intact rock blocks, and (2) Mohr–Coulomb slip with residual strength for discontinuities (i.e. brittle–plastic behavior). The elastic properties (Young's modulus, E, and Poisson's ratio, ν) of the blocks between the large-scale discontinuities were estimated from intact rock properties measured in laboratory experiments (Willenberg, 2004) and by applying the Geological Strength Index (GSI; Hoek et al., 2002). Willenberg (2004) also performed scan line surveys of small-scale fracture networks in the paragneiss and schist and found average joint spacings of 0.5–2.5 m. Resulting block sizes are on the order of 0.1 to 10 m^3 for fully persistent joints and larger for limited persistence. Note that these surveys focused on small-scale discontinuities (i.e. trace length less than 5–10 m) as opposed to the large-scale discontinuities discussed in this work and explicitly included in UDEC. Joint conditions can be described as smooth to rough with stained surfaces and minor weathering. Following the recommendations of Cai et al. (2004), we chose an average GSI value in the range of 65±5 for the paragneiss and schists (Table 4.2). The block sizes within the orthogneiss unit are somewhat larger, thus, a GSI value of 75±5 was chosen. Intact rock properties estimated from laboratory experiments and rock mass properties are summarized in Table 4.2.

Intact rock bridges along large-scale discontinuities were modeled indirectly by assigning higher initial strength properties to discontinuities as described by Jennings (1970). Thus, strength properties (namely friction angle, cohesion, and tensile strength) are calculated from a combination of discontinuity and intact rock properties. The respective contributions of discontinuity and intact rock strength correspond to an assumed percentage of intact rock bridges along the discontinuity. For discontinuities without intact rock bridges a peak friction angle of 30° and peak cohesion of 0.1 MPa was assumed. Residual friction was set to 27° and residual cohesion to 0.02 MPa (F1 and F2) and 0.03 MPa (F4 and F5). The strength properties for each discontinuity set are shown in Table 4.3. The different percentages of rock bridges (i.e. the effective strength properties) were chosen by attempting to fit the observed displacement and deformation patterns as well as the deduced kinematic behavior. However, higher percentages for F4 and F5 were chosen in accordance with observations on the LiDAR DTM.

4.6.4 Modeling strategy

To analyze the kinematic behavior of the Randa rock slope instability, we used a model designed to reproduce the observed extent, depth, relative displacement patterns, displacement dip angles, and dislocation along large-scale discontinuities. The model was obtained by calculating a force-equilibrium state following removal of material by the 1991 rockslides. Stress conditions were initiated by applying an *in situ* stress ratio of k_o=0.6 (Kastrup et al., 2004) to a block with the upper boundary at an altitude of 2800 m. In a first step, the block was excavated to the pre-1991 failure topography, leaving the discontinuity strength at high values to prevent failure. Then, discontinuity strength values were set to those given in Table 4.3, and a new force-equilibrium state was calculated. Thus, some amount of discontinuity failure due to *in situ* stress conditions and topographic stress redistribution is simulated. Finally, the failed rock mass of the April and May 1991 events was removed and a debris cone at the toe of the slope added. The simulated displacement field could then be compared to observations from GB-DInSAR data, geodetic monitoring, borehole inclinometer data, and with the postulated kinematic behavior.

4.6.5 Numerical model results

The final model at force equilibrium showing the accumulated displacement field following removal of the 1991 rockslide material is presented in Figure 4.14. Discontinuities that have reached their strength limit and thus failed are shown as black traces. Results show that the previously suggested kinematic model was reproduced well: between 1850 and 2100 m, the rock mass slides uniformly along a basal plane daylighting just above the orthogneiss/paragneiss contact. Few F1 and F2 discontinuities have failed and dislocation is limited to just one F4 discontinuity. Above 2100 m, a transition to toppling occurs with a few F5 discontinuities having reached strength limit, and above 2200 m toppling is the dominant kinematic mode. Most F2 and many F1 discontinuities have failed and exhibit left-lateral shear, often accompanied by an opening component, which is in accordance with borehole deformation data (Willenberg et al., 2008a). The maximum displacement is about 0.75 m, which lies in the range expected for relaxation following the 1991 failures. An estimate of the true cumulative displacement since 1991 can be derived by summing the observed opening of cracks at the top of the instability. The result indicates a maximum displacement value of about 1.5 m, which is on the same order of magnitude as the modeled value. The percentage of intact rock bridges used for this model is 30% and 45% for set F4 and F5, respectively, while for sets F1 and F2 only 8% and 14% rock bridges was assumed (Table 4.3).

Figure 4.15a shows comparison between modeled displacements along the chosen profile and those measured with GB-DInSAR. Note that the absolute displacement values of both methods are not directly comparable, since the modeling results show displacements accumulated during calculation of force-equilibrium, while GB-DInSAR displacements are representative for the time interval of 316 days between two subsequent surveys. Thus, displacements from both methods were normalized, in order to compare the internal displacement patterns. The comparison shows that the numerical model is able to adequately reproduce the measured displacement pattern. The modeled boundaries of the instability lie within about 20 m of the observed boundaries, and the greatest displacements occur between 400 and 550 m along the profile for both measured and modeled cases. Modeled displacements then decrease and reach a uniform value after about 700 m profile distance. Here, GB-DInSAR data exhibit some deviations towards greater displacements, which may be explained by local toppling blocks at the ground surface superimposed on the larger sliding mass. However, such discrepancies may also arise due to our 2D representation of 3D rock mass behavior.

The plunge of the displacement vectors resolved for geodetic monitoring points at distances no more than 50 m from the profile are compared to those simulated with UDEC in Figure 4.15b. The modeled plunge angles range from 5° to 40° within the unstable area. The spatial pattern of measured plunge angles ranging from 7° to 45° at the top of the instability could generally be reproduced. The single monitoring point at the bottom of the instability showing a plunge angle of less than 10° could not be reproduced in UDEC.

Modeled displacements were also extracted along a vertical profile corresponding to the location of borehole sb120, for which periodic inclinometer and extensometer measurements are available (Figure 4.13b, Figure 4.15c and d). The modeled displacements exhibit a pattern typical for toppling as derived from borehole measurements. Although the exact locations of large displacements may not always match between the measured and modeled vertical profiles, the general patterns and thus kinematics agree well.

4.6.6 Discussion of numerical models

Numerical model results showed that the kinematic failure modes derived from analysis of structural data and displacement patterns are reasonable. However, we acknowledge that these models remain simplified and conceptual, limited by knowledge of the input parameters and subsurface structure (Starfield and Cundall, 1988). Not only is the model a simplified 2D representation, but parameters such as the *in situ* stress ratio (k_o), percentage of intact rock bridges, and elastic properties are estimated. We therefore conducted sensitivity analyses aimed at exploring the influence of the most critical input parameters on the modeled kinematic behavior. Parameters such as elastic modulus, discontinuity spacing and strength, joint stiffness, and k_o were varied between ±25% of the mean values used for the model in Figure 4.14. The outcomes and key results are described here in a qualitative manner.

The choice of elastic modulus has little influence on the model results, where slightly smaller displacements are predicted for stiffer blocks. Discontinuity spacing also has little influence on the modeled kinematic behavior, but displacements increase at smaller spacings. For increasing discontinuity strength, displacements decrease as expected. While the kinematics do not change dramatically for changing the strength of sets F4 and F5, decreasing the strength of sets F1 and F2 significantly promotes toppling. Based on a numerical study, Sjöberg (2000) also showed that toppling is favored over sliding with decreasing strength of toppling discontinuities. Choosing a percentage of rock bridges below 8% for set F2 results in toppling also in the lower regions of the instability. Changing joint normal and shear stiffness does not significantly affect the model outcomes. Note that also the location of discontinuity sets first order control on the instability extent or kinematics; e.g. the location where the lowest F4 disconitnuity daylights defines the depth reach of the instability. Although strong constraints are introduced by choosing discontinuity locations, we stress that this largely follows the outcomes of the structural analysis. The choice of k_o (varied between 0.5 and 0.8 in our analysis) mainly affects the depth and longitudinal extent of the instability, but also the relative extent of toppling and sliding areas. Similar modeling results were shown for the Cuolm Da Vi landslide in central Switzerland (Amann, 2006). We assume that both the initial overburden and erosional history of the valley play an important role in determining the instability kinematics (Eberhardt et al., 2004). Higher initial overburden and subsequent exhumation results in higher k_o (Kulhawy et al., 1989), whereas the erosional history controls the amount of damage accumulated within the rock mass due to stress redistribution (Lorig and Varona, 2000). These effects could be modeled by setting the upper boundary of the block at higher altitudes and by introducing a step-wise excavation sequence corresponding to glacial erosion. However, both processes are largely unknown and thus most problematic to accurately account for. In this study, we prefer not modeling these effects explicitly, but rather to choose appropriate k_o and strength parameters of the discontinuities.

The percentages of rock bridges used in the presented model were chosen to optimally reproduce the observed displacement pattern and kinematic modes (Table 4.3). Thus, detailed interpretation of the relative values of discontinuity strengths is inappropriate. However, we note that similar for all calculated models, the strength of sets F4 and F5 was always significantly higher than sets F1 and F2. We conclude that to reproduce the observed rock mass behavior it is required that F4 and F5 discontinuities are not fully persistent and contain a certain amount of intact rock bridges, which must break prior to catastrophic failure (Eberhardt et al., 2004). In contrast, the strengths of sets F1 and F2 need to be much lower to allow toppling to occur. Higher percentages of rock bridges for sets F4 and F5 were also assumed from observations of the LiDAR DTM (Figure 4.2 and Figure 4.4).

Although we argue that 2D analysis is able to represent the primary kinematics of the instability well, further 3D investigations using 3DEC (Itasca, 2008a) could provide additional insights into the kinematic behavior. Including 3D topography into the model would provide a more realistic estimate of the gravitational stress field and allow for additional kinematic degrees of freedom. The role of set F3, and other discontinuity sets so far neglected in UDEC, could be further explored. However, accurate estimates of elastic properties, discontinuity strength and *in situ* stress remain problematic and thus model interpretation in 3D would still be limited. Furthermore, computation time required for a sound 3DEC analysis increases dramatically compared to UDEC. Since our numerical modeling is also aimed at exploring external forcing factors and the temporal behavior of the instability in future studies, we consider 2D models appropriate.

4.7 Summary and conclusions

This study has revealed new and important insights into the kinematics of the current Randa rock slope instability. Previous investigations yielded detailed information about the internal structure and kinematics of the unstable rock mass, however these were limited to the accessible upper portion of the instability. Applying new remote sensing techniques, supplementary geodetic measurements, and numerical modeling in a complementary way allowed us to extend the kinematic model by Willenberg et al. (2008b) to the entire slope instability, including inaccessible areas. We present a 2D numerical model that supports the existence of two different kinematic modes as suggested from comprehensive data analysis. Further information regarding 3D kinematics was obtained, although not investigated with numerical models. In the following, we summarize the most important findings of our study:

- The rupture surface in the northern part of the May 1991 failure scarp shows a transition from planar and stepped planar sliding surfaces at the base, to failed rock bridges in the center, to tensile failure close to the vertical head scarp (Figure 4.4). Discontinuity sets F4 and F5 were identified forming the stepped portion of the May 1991 failure surface.
- Kinematic analysis of the discontinuity sets in the currently moving rock mass derived from LiDAR and photogrammetry data shows that toppling (along discontinuity set F2) and translational sliding (along sets F4 and F5) are feasible failure modes. Toppling is the dominant mode above ~2200 m as previously determined by Willenberg et al. (2008b). Translational sliding becomes more likely below 2200 m. The highly pervasive discontinuity set F3, which includes the current lateral release plane, is unlikely to participate in wedge sliding with sets F4 and F5. Thus, 2D analysis is justified, although the effect of set F3 acting as lateral release structures can only be explored in 3D.
- GB-DInSAR displacement patterns revealed both the basal rupture surface and lateral release plane of the instability. The existence of two compartments with different kinematic modes was concluded from interpretation of displacement maps (Gischig et al., 2009).
- 3D displacement vectors derived from geodetic measurements at the top of the instability revealed a relatively uniform orientation of movements and three compartments with distinct displacement rates. Plunge angles generally lie in the range between 25° and 35°, typical for toppling along F2 discontinuities dipping into the slope at 50° to 70°. Resolved trends reveal that both opening and shearing occur along the F3 set at the top of the instability. Thus, F3 discontinuities cannot be involved in wedge sliding, which confirms their role in simply providing kinematic free-

dom as lateral release structures. However, 3D displacement vectors are still only available for accessible areas and not for large regions of the 1991 failure scarp.

- Numerical models confirmed the suggested kinematic model in 2D. Displacement patterns both at the surface and from the 120 m deep borehole could be reproduced. The existence of two kinematic modes is largely independent on the chosen input parameters, although changes in the relative extent of toppling and sliding zones can result. However, due to the 3D character of the problem and somewhat limited knowledge of accurate input parameters, the numerical results should only be regarded as a conceptual representation of the true kinematics. Certain features of the instability can only be investigated with 3D modeling, for example the role of the pervasive set F3 so far neglected in our 2D representation. Although our data reveal only sliding and toppling for the current instability, including the full 3D topography could allow for more kinematic degrees of freedom modifying these failure modes. Furthermore, we acknowledge that stress conditions and the internal damage state following the 1991 events could be spatially variable due to the 3D nature of the slope. However, these also strongly depend on the initial overburden, deglaciation sequence, and assumed k_o, which are each difficult to quantify.

In addition to the new information obtained for the Randa instability, our study has illustrated the necessity of using deterministic 3D structural models for reliably resolving kinematics of an unstable rock mass. Furthermore, we demonstrated the potential and also the importance of combining a number of different approaches for understanding rock slope kinematics. Any model derived from one single geophysical measurement carries a certain ambiguity, and only by applying several complementary methods can a model be created for conclusive interpretation. For example, structural analysis of LiDAR and photogrammetry data only allows deriving possible kinematic failure modes, whereas the location of major release planes and instability boundaries can only be assumed. GB-DInSAR data can provide this missing information, but kinematic modes could only be resolved in combination with other structural data. Remote sensing and geophysical techniques are continuously developing towards higher accuracy and resolution, as well as greater flexibility. Therefore, integrated studies of rock slope instabilities will become increasingly accessible and lead to more profound understanding of slope failure processes in the future.

Acknowledgements

LiDAR and photogrammetry surveys were performed by Helimap Systems SA (Switzerland). Annual geodetic surveying of the largescale network was conducted by Klaus Aufdenblatten (Zermatt, Switzerland) and directed by CREALP (Centre de Recherches sur l'Environnement Alpin, Switzerland). Ellegi Srl (Milano, Italy) performed GB-DInSAR measurements and data processing. Geodetic measurements were preformed by the group for Geodetic Metrology and Engineering Geodesy at ETH Zurich (Prof. Dr. H. Ingensand). Freddy Xavier Yugsi Molina prepared orthoimages for map views in ArcGIS. We thank to Kerry Leith and Keith F. Evans for helpful comments and discussions. We also thank an anonymous reviewer and Prof. M. Jaboyedoff for constructive comments. This project was funded by the Swiss National Science Foundation (Project No. 2100-059238.99).

Table 4.1: Summary of discontinuity properties for all sets. The indices p and o indicate paragneiss/schists and orthogneiss, respectively. Only for the sets F1, F2, and F3p were field observations available (Willenberg et al., 2008a). For all other sets, type and surface conditions were assumed from observations on photographs.

Set	Type	Dip / Dip direction	Max. trace length [m]	Spacing [m]	Surface conditions
F1	Brittle-ductile	240°/20°	150	5–20	weathered, slickensides
F2	Brittle, brittle-ductile	355°/60°	> 200	5–20	rough, slightly weathered
F3p	Fracture zones	095°/70°	> 200	5–25	smooth, fine grained infills
F3o	Fracture zones	070°/75°	> 200	-	fine grained infills, slickensides
F4p	Basal shears	160°/45°	> 200	-	rough, corroded
F4o	Basal shears	135°/60°	> 200	-	rough
F5p	Failed rock bridges	125°/65°	30	-	very rough
F5o	Failed rock bridges	125°/80°	150	-	very rough
F6	Brittle (?)	030°/40°	80	-	-

Table 4.2: Intact rock and rock mass properties as implemented in UDEC. Intact rock properties (i.e. elastic properties, UCS, friction and cohesion) were estimated from laboratory tests (Willenberg, 2004). Rock mass properties were then determined using the Geological Strength Index (GSI; Hoek et al., 2002).

	Orthogneiss	**Paragneiss**
Intact rock		
Density (kg/m³)	2640	2700
Young's modulus (GPa)	32	21
Poisson's ratio	0.21	0.2
UCS (MPa)	97	69
Friction angle	55°	41°
Cohesion (MPa)	15.3	14.4°
Rock mass (elastic blocks)		
GSI	75	65
Young's modulus (GPa)	26	14

Table 4.3: Discontinuity properties for the Mohr-Coulomb brittle-plastic constitutive law with residual strength used in UDEC. Initial strength values were derived from a mixture of intact rock and discontinuity properties as suggested by Jennings (1970), resulting in apparent strength properties. For discontinuities without any intact rock bridges, a peak friction angle of 30° and cohesion of 0.1 MPa was assumed.

	Orthogneiss	Paragneiss			
Discontinuities		**F1**	**F2**	**F4**	**F5**
Intact rock bridges	60 %	8 %	14 %	30 %	45 %
Apparent friction angle	46°	31.0°	31.7°	33.6°	35.3°
Apparent cohesion (MPa)	8.3	1.2	2.1	4.4	6.5
Apparent tensile strength (Mpa)	5.2	0.6	1.0	2.1	3.1
Dilation angle	5°	5°	5°	5°	5°
Residual friction angle	27°	27°	27°	27°	27°
Residual cohesion (MPa)	0.05	0.02	0.02	0.03	0.03
Residual tensile strength (MPa)	0	0	0	0	0
Joint normal stiffness (GPa/m)	10	10	10	10	10
Joint shear stiffness (GPa/m)	5	5	5	5	5

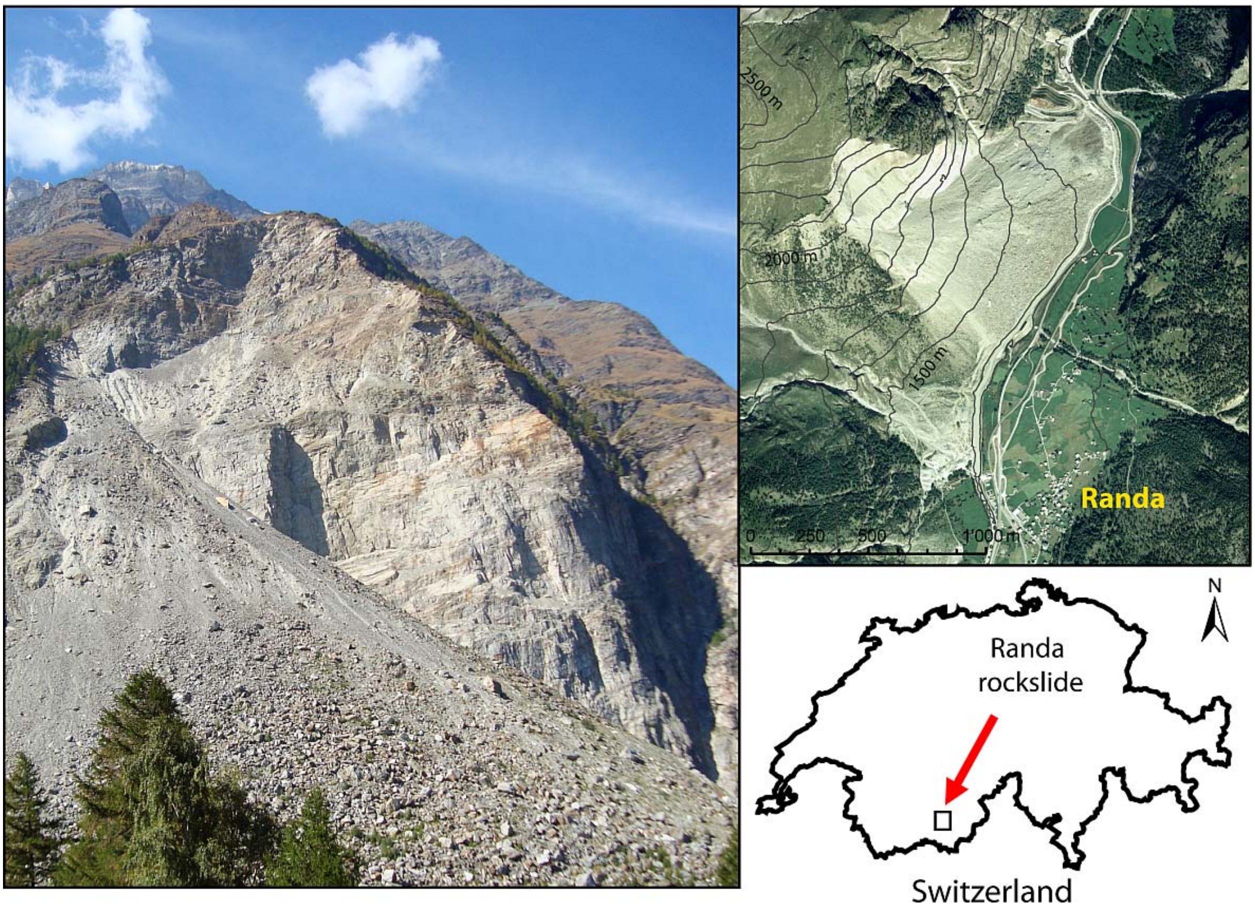

Figure 4.1: Photo and map overview of the Randa rock slope instability and 1991 failure scarp.

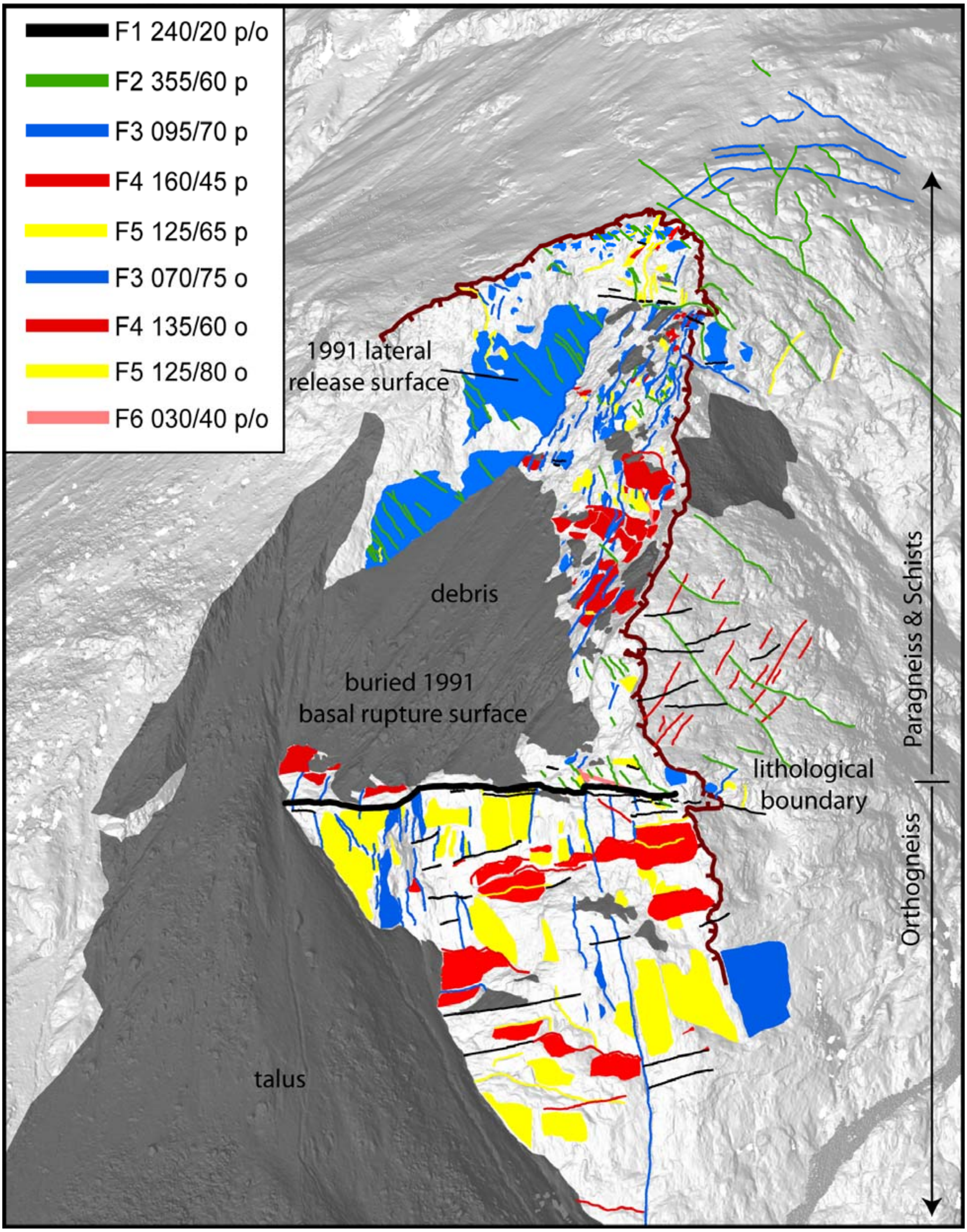

Figure 4.2: Results from structural mapping using LiDAR raster data and undistorted images. Structures are colored according to their assigned set (see inset). Regions shaded in dark grey are areas covered by debris. The indices p and o stand for paragneiss/schists and orthogneiss, respectively.

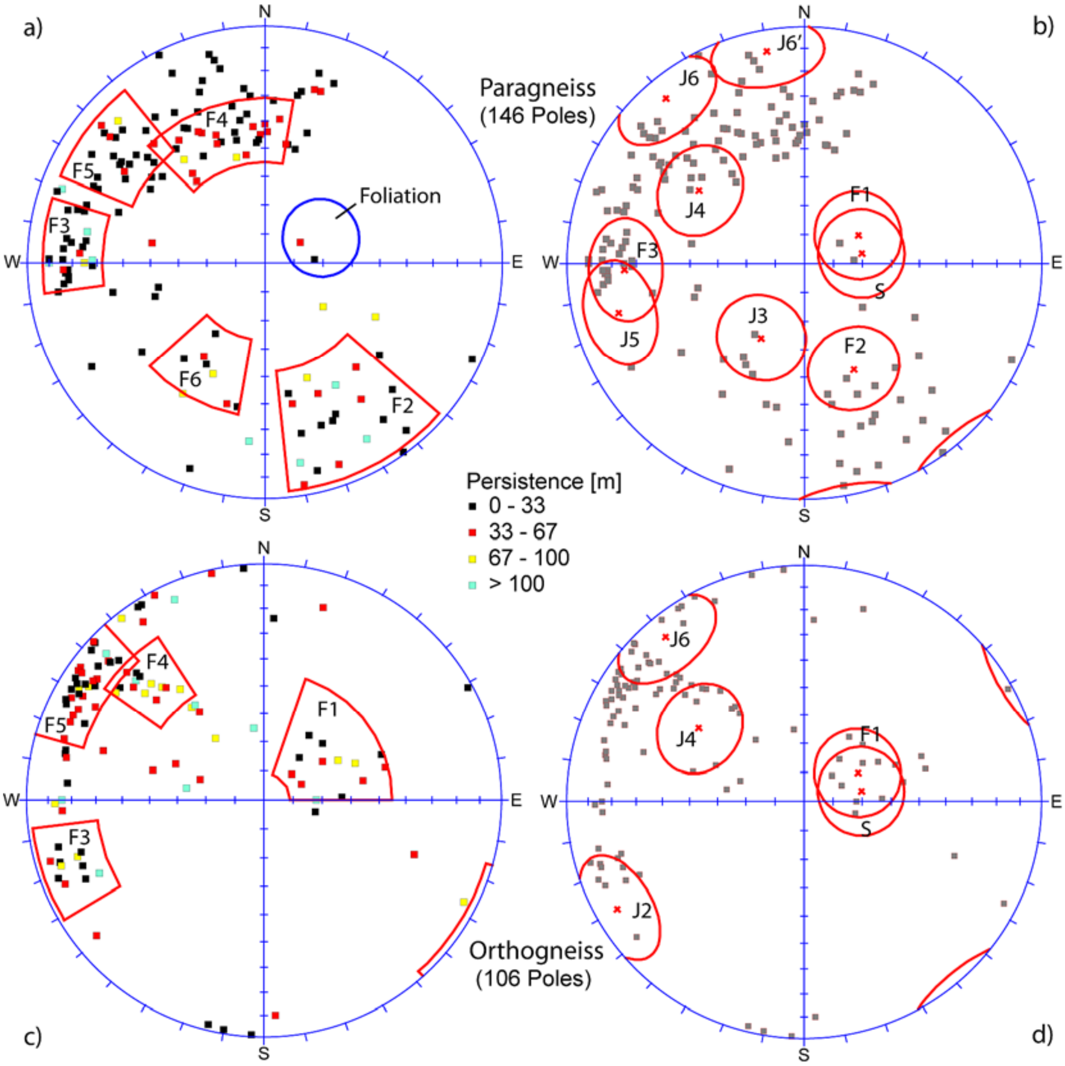

Figure 4.3: Orientations of large-scale discontinuities shown in Figure 4.2 represented in stereographic projection (lower hemisphere). a) Large-scale discontinuities mapped in the paragneisses and schist units (above 1900 m). Assignment to different sets is based on visual criteria and orientation. b) Sets from Sartori et al. (2003): J2-J6, and sets from Willenberg et al. (2008a): F1-F3, are included for comparison. c) Large-scale discontinuities mapped in the orthogneiss (below 1900 m). d) Comparison with former studies as in b).

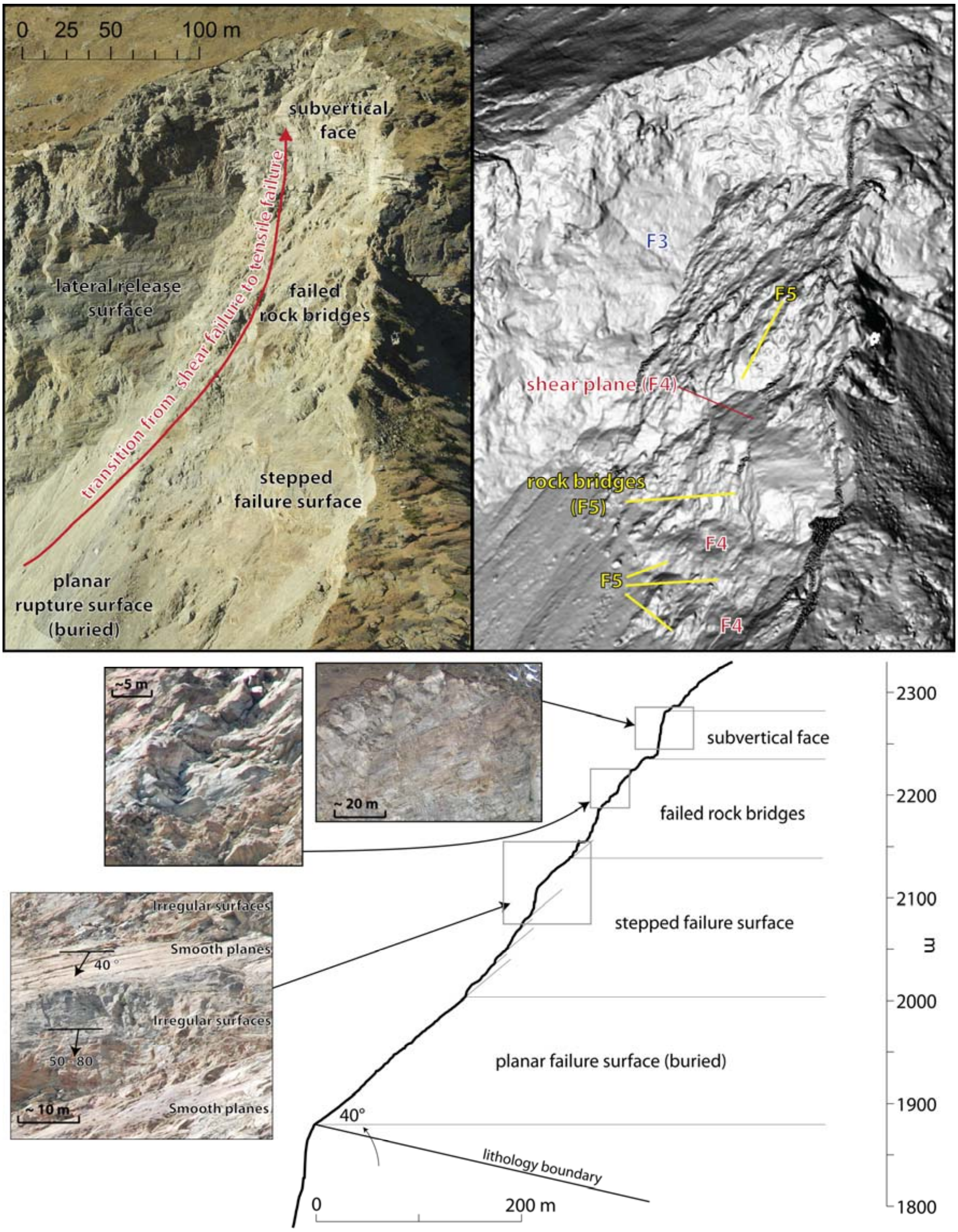

Figure 4.4: Orthophoto and shaded LiDAR DTM in the rotated coordinate system optimally displaying the May 1991 failure surface. The lateral release plane belonging to the set F3 exhibits a smooth surface. The basal rupture surface (135°/40°) in the lower left corner is buried by debris. Above, shear planes (smooth surfaces; set F4) are connected by F5 discontinuities (irregular surfaces), which are interpreted as intact rock bridges that have failed in tension. The rock mass above this stepped surface is strongly fractured with strongly irregular surfaces, which is again interpreted as fractured rock bridges. The subvertical face at the top was likely formed by predominantly tensile failure. Also shown is a profile, which illustrates the transition from shear to tensile failure. It also includes detail photographs of smooth planes (shear planes), irregular surfaces (tensile failure), and the subvertical face at the top of the scarp.

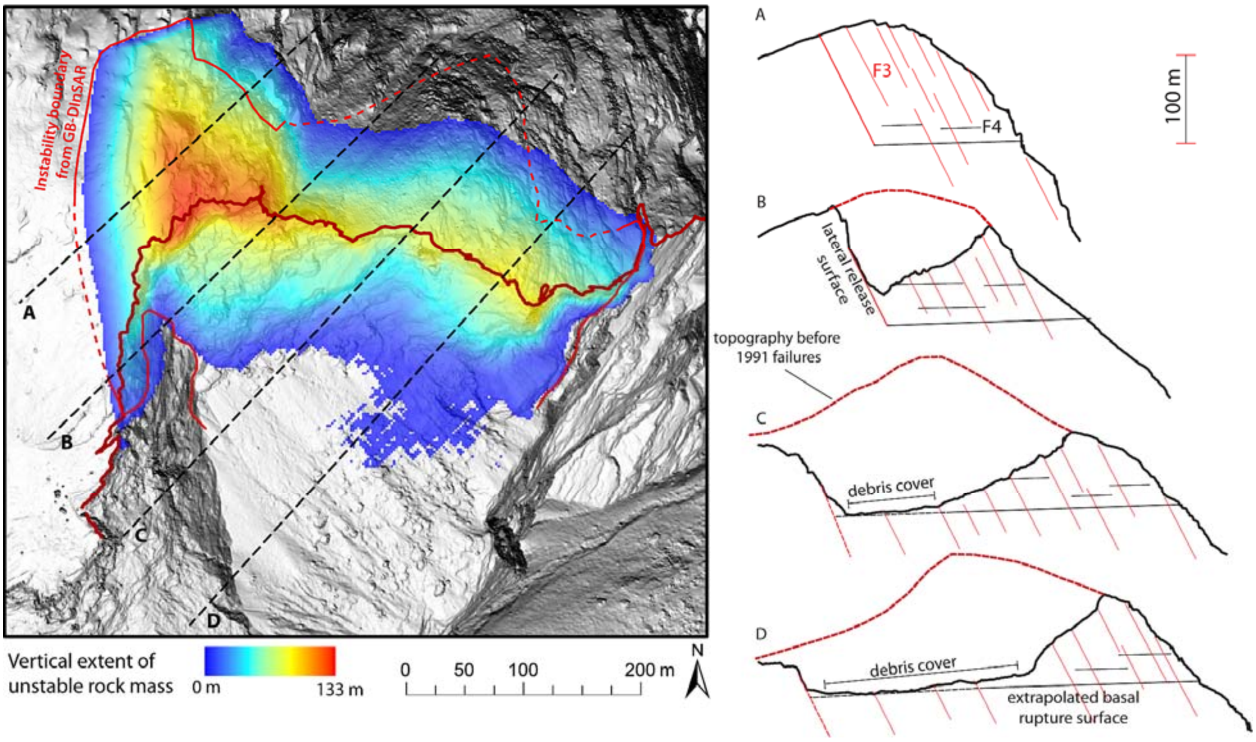

Figure 4.5: Map of the vertical extent of the rock volume bounded by a planar basal rupture surface, the lateral release plane, and the discontinuity limiting the instability to the north. The boundary of this volume matches well with the boundary derived from GB-DInSAR data. Strong deviations occur in the northwest, where GB-DInSAR data are uncertain and structures in addition to the basal rupture surface may define the instability boundary. Four vertical cross-sections through the rock volume display the 3D geometry of the current instability, as well as the rock mass that failed in May 1991. In lower portions of the current instability, the rock mass has a ridge-type geometry, whereas in higher areas the rock mass is additionally bounded by the lateral release surface.

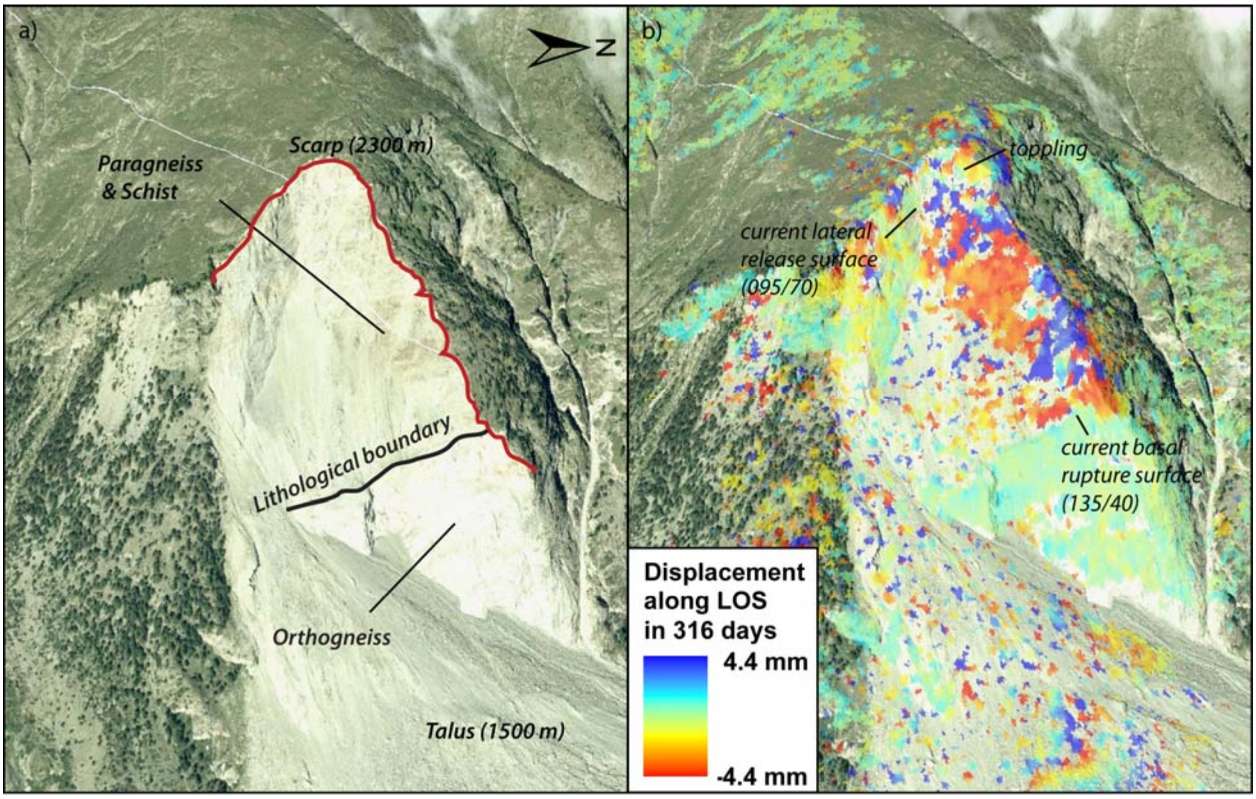

Figure 4.6: a) Orthoimage draped onto a DTM showing an overview of the 1991 failure scarp. b) GB-DInSAR displacement map; displacements towards the observer (i.e. in the line-of-sight, LOS) are negative (red) and away from the observer positive (blue). Note that apparent positive displacements (blue) within the instability may be a result of phase wrapping. Such artifacts are common for InSAR techniques, and occur if the accumulated displacement exceeds λ/4 of the radar wavelength (4.37 mm in our case). For details on GB-DInSAR measurements at the Randa instability see Gischig et al. (2009).

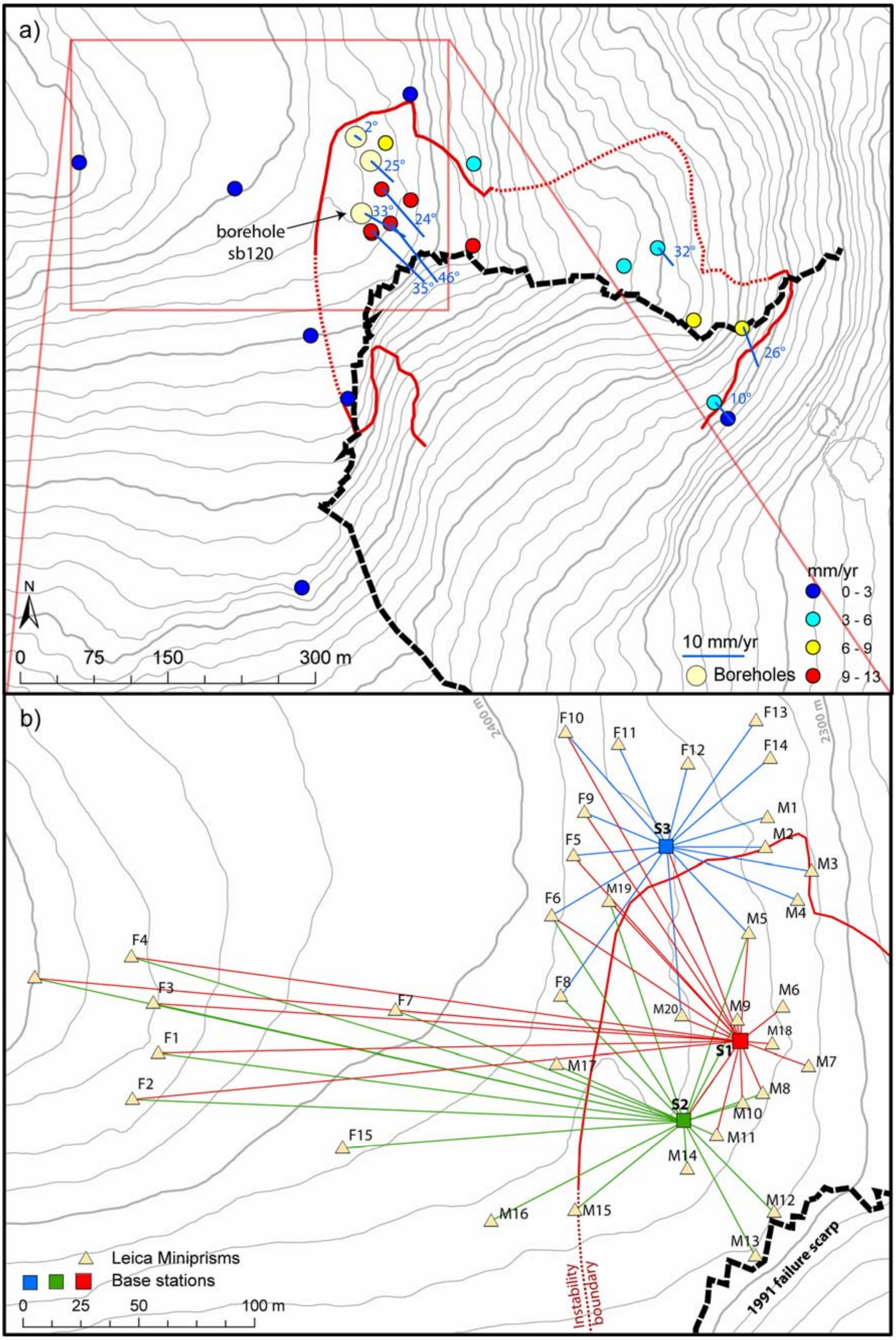

Figure 4.7: a) Results from the LSGN including data back to 1995. Plunge angles of the displacement vectors are indicated. Also shown is the extent of the SSGN. b) Layout of the SSGN: 15 fixed points (F) and 20 monitoring points (M) were measured from three base stations (S1-S3).

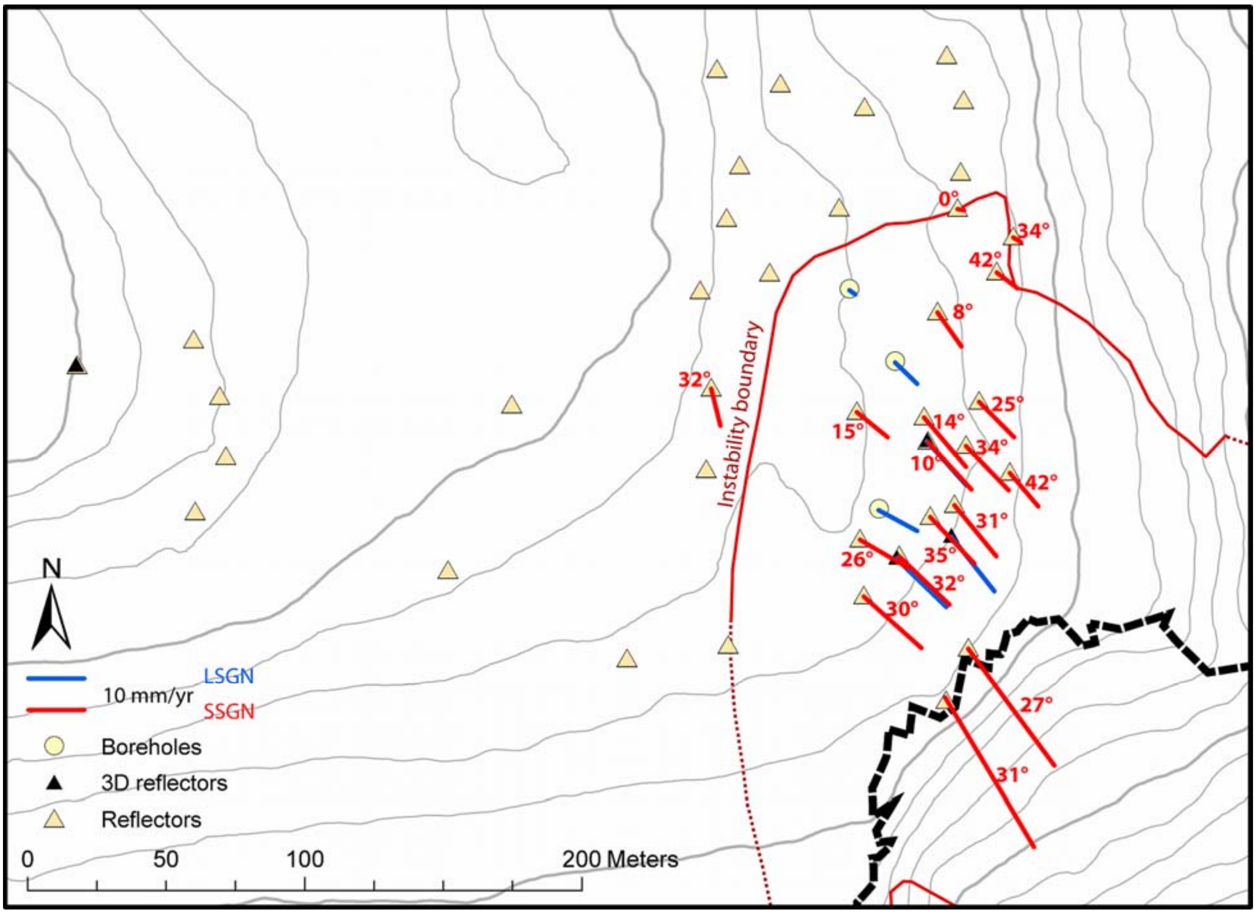

Figure 4.8: Scaled displacement vectors from both the LSGN (blue) and the SSGN (red). Numbers next to each vector indicate the displacement plunge angle. The instability boundary derived previously by Willenberg et al. (2008b) was confirmed by the new measurements. Maximum displacement rates greater than 30 mm/yr were found at the edge of the failure scarp.

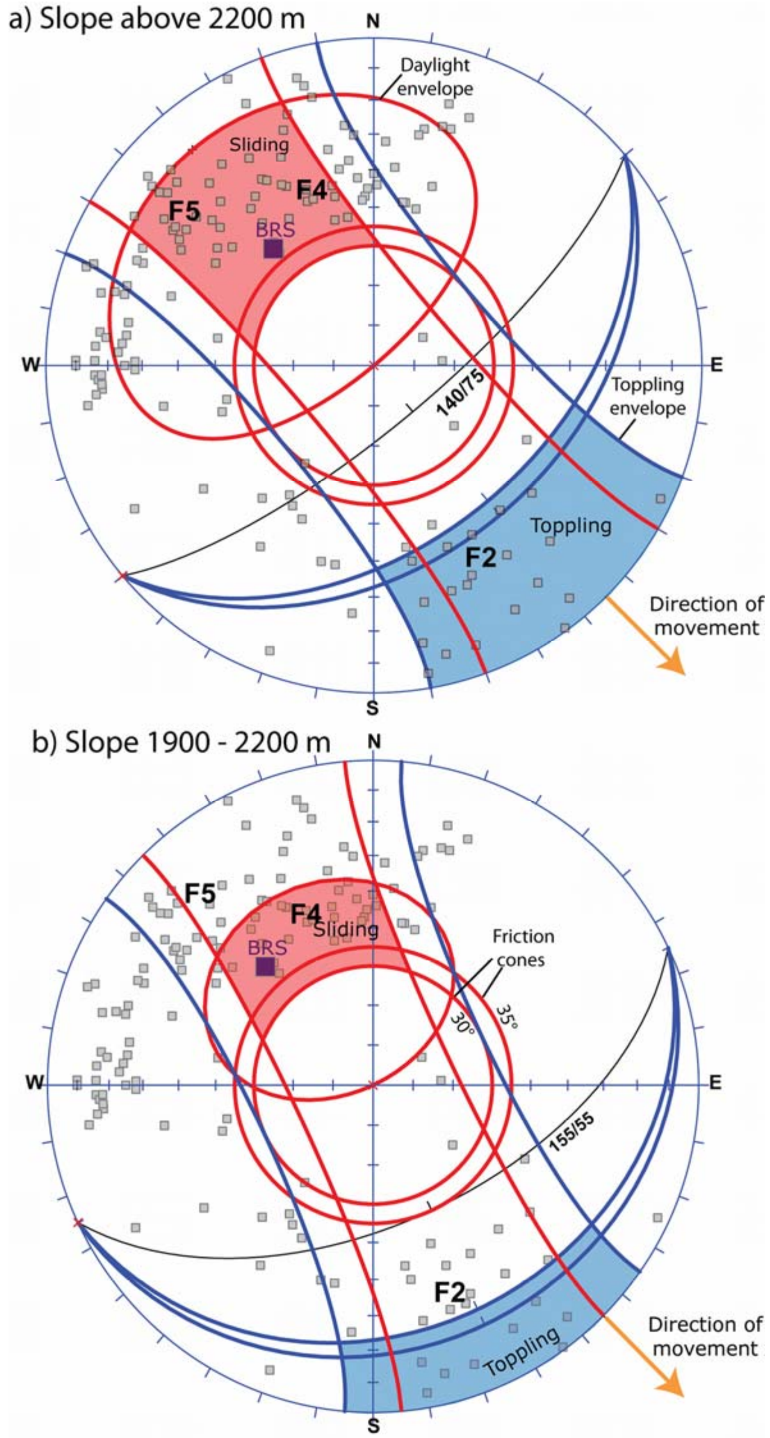

Figure 4.9: Kinematic analysis of structural data (contours indicate the pole density). a) Slope angle of 75° representing the region above 2200 m. b) Slope angle of 55° for regions below 2200 m. For the steeper slope angle of 75°, both sliding and toppling are feasible, however borehole inclinometer data show that toppling is the dominant kinematic mode in this region. Both sliding and toppling become less likely at a slope angle of about 55°. Sliding is only possible along F4 sets and along the basal rupture surface (BRS). The presence of a basal sliding surface was derived from GB-DInSAR data, which implies that sliding is more likely in the lower regions.

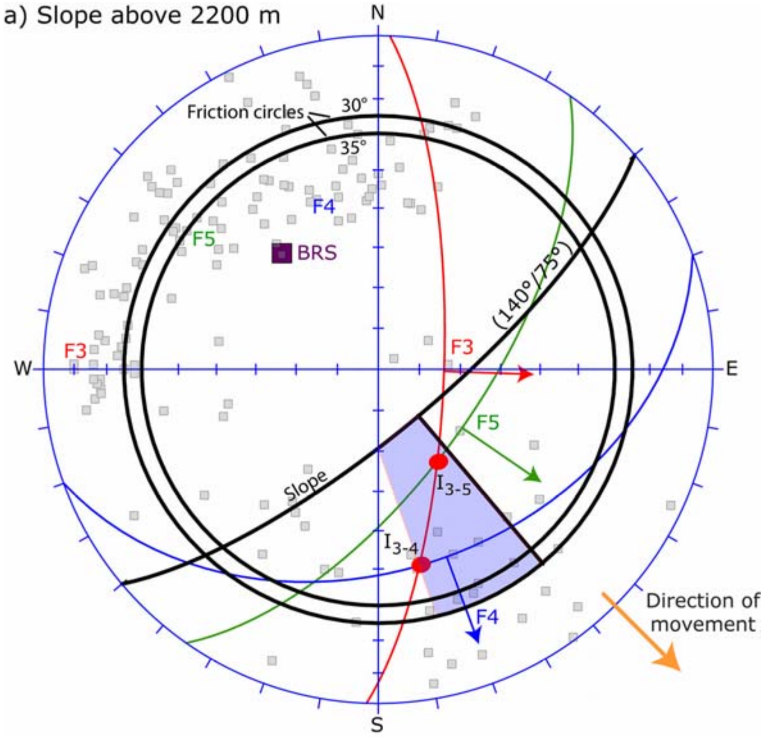

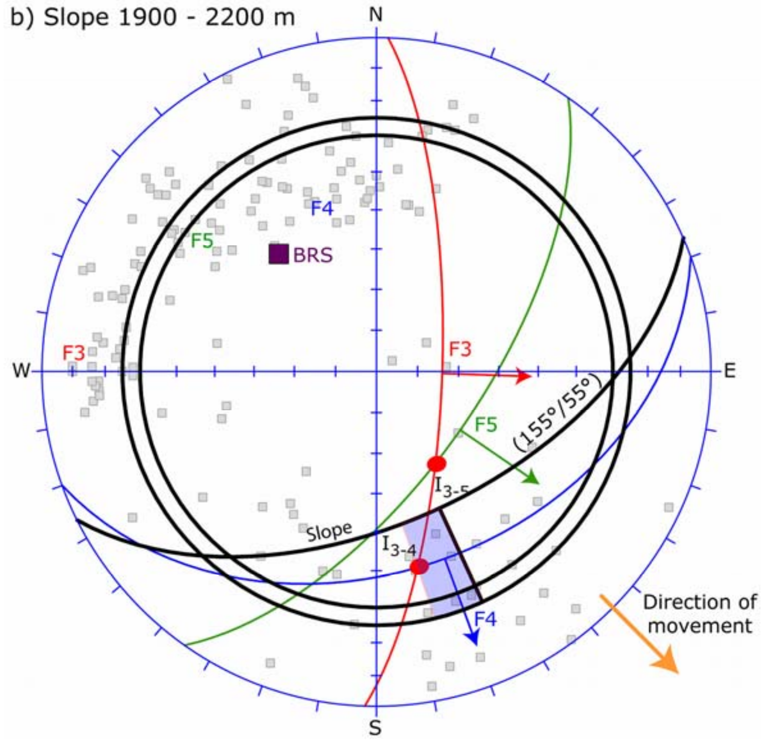

Figure 4.10: Wedge sliding analysis according to Markland (1972) with Hocking's refinement (Hocking 1974), which allows distinguishing planar sliding and wedge sliding. a) For a slope angle of 75° above 2200 m. b) For a slope angle of 55° between 1900 – 2200 m. I3-4 and I3-5 denote the intersection lines of the set F3 and F4 as well as F3 and F5, respectively. For both slope angles, the dip angle of set F4 lies between the slope dip angle and the plunge of the intersection line (shaded area). Thus, planar sliding along F4 is preferred to wedge sliding along I3-4. BRS is the pole of the basal rupture surface. The intersection of F3 and F5 produces wedges that are unrealistic for the current instability.

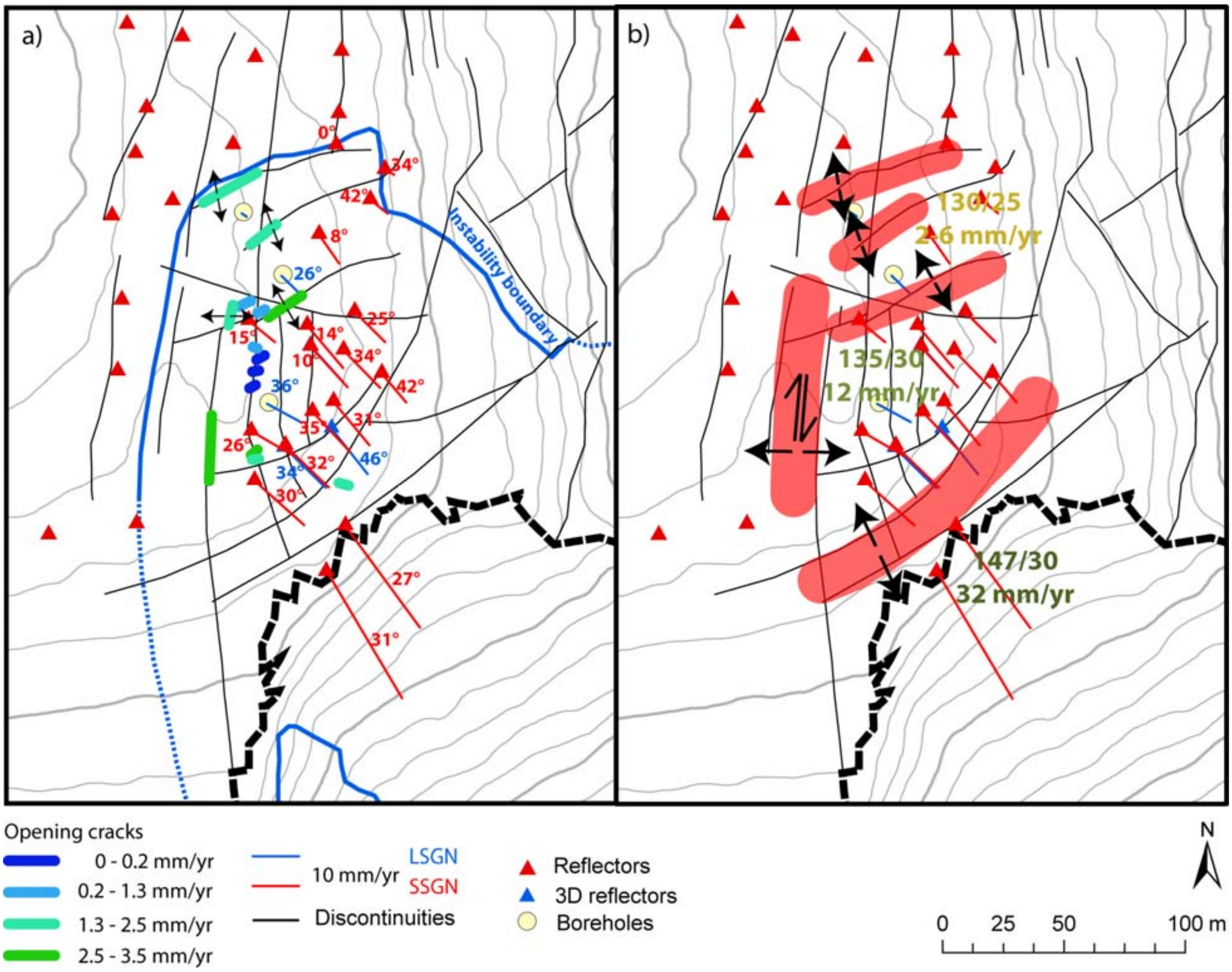

Figure 4.11: a) Results from geodetic measurements overlain on hand-measured crack openings. Relative opening direction was measured for four cracks with benchmark quadrilateral arrays (black arrows). The discontinuity map from Willenberg et al. (2008a) is also included. b) Interpretation of the 3D displacement field. Three compartments are distinguished with different displacement rates bounded by opening cracks or zones of differential displacement. Displacement directions indicate that not only shearing, but also opening occurs along the western boundary, which is the continuation of the lateral release surface.

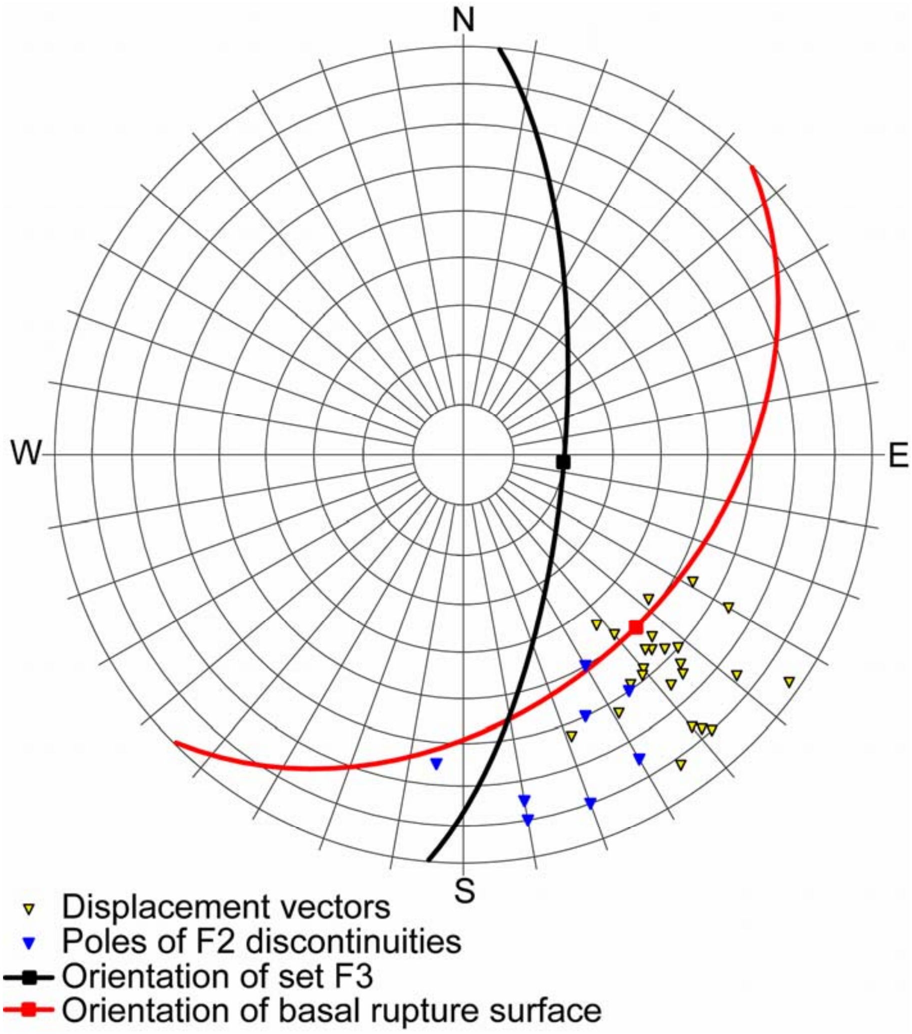

Figure 4.12: Geodetic displacement vectors in stereographic projection. Also shown are poles of the mapped F2 discontinuities at the top of the instability (Figure 4.11), which indicate the displacement direction expected for pure toppling. Similarly, the orientation of the basal rupture surface and the F3 set are given, which shows the expected displacement direction for slip along these structures.

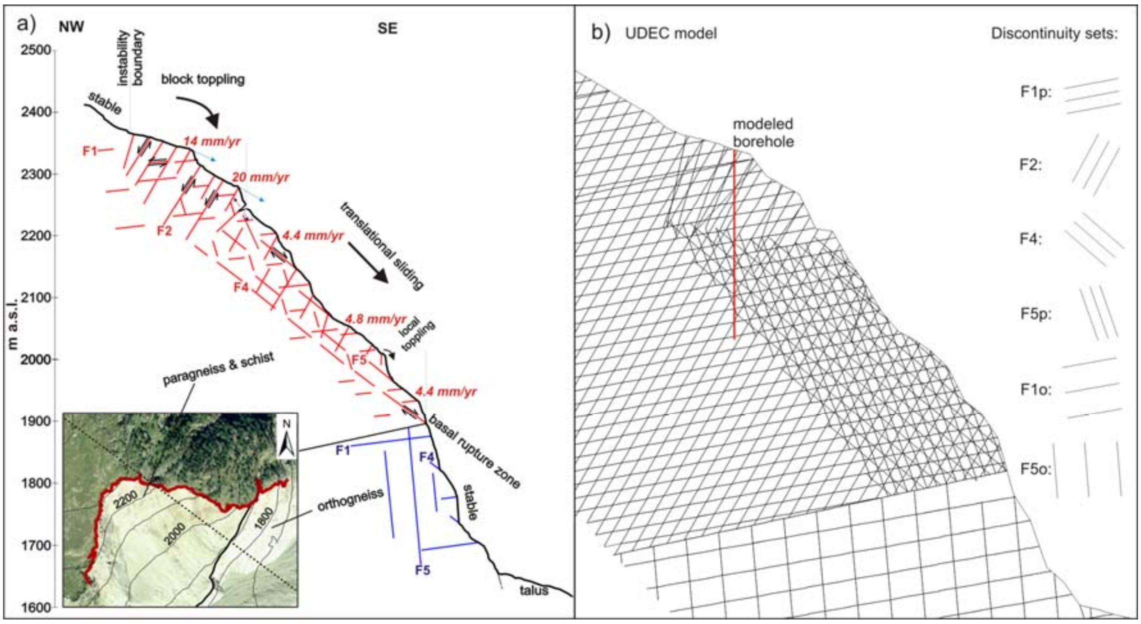

Figure 4.13: a) Conceptual kinematic model derived from combined analysis of LiDAR and photogrammetry data, GB-DInSAR displacement maps, geodetic measurements, and results from former studies presented by Willenberg et al. (2008a/b). F3 discontinuities are not shown since their dip direction deviated more than 30° from the orientation of the profile. b) Geometry of the model implemented in UDEC. Large-scale discontinuities with known location and dip angle from 3D structural analysis (Willenberg et al., 2008a) were explicitly included. All discontinuity sets were created as fully persistent and intact rock bridges were simulated using increased discontinuity strength properties as suggested by Jennings (1970).

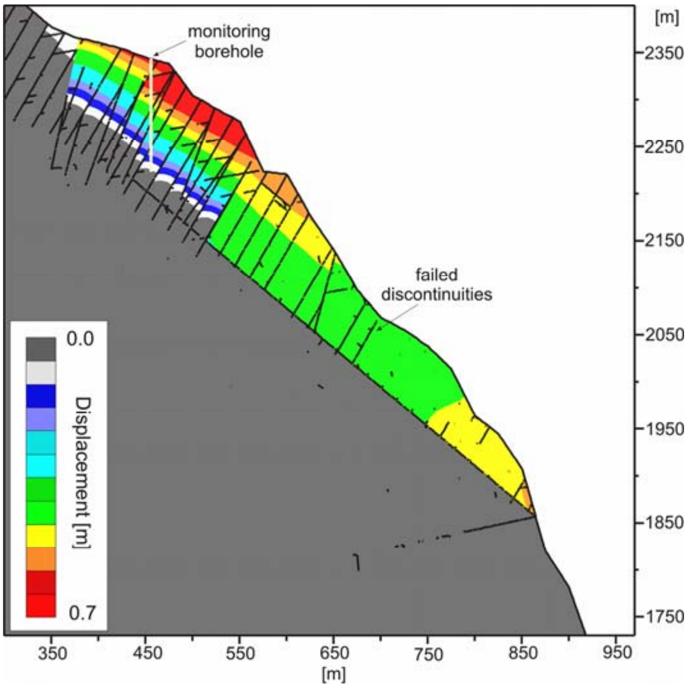

Figure 4.14: Cumulative displacements after reaching force-equilibrium following the 1991 failures. Large-scale discontinuities whose strength has been exceeded are shown in black. A basal rupture surface has formed and movements in the lower areas show translational sliding. After a transition zone, where both toppling and sliding occur, toppling becomes the dominant kinematic mode at the top of the instability. Most F2 discontinuities have failed in this upper region.

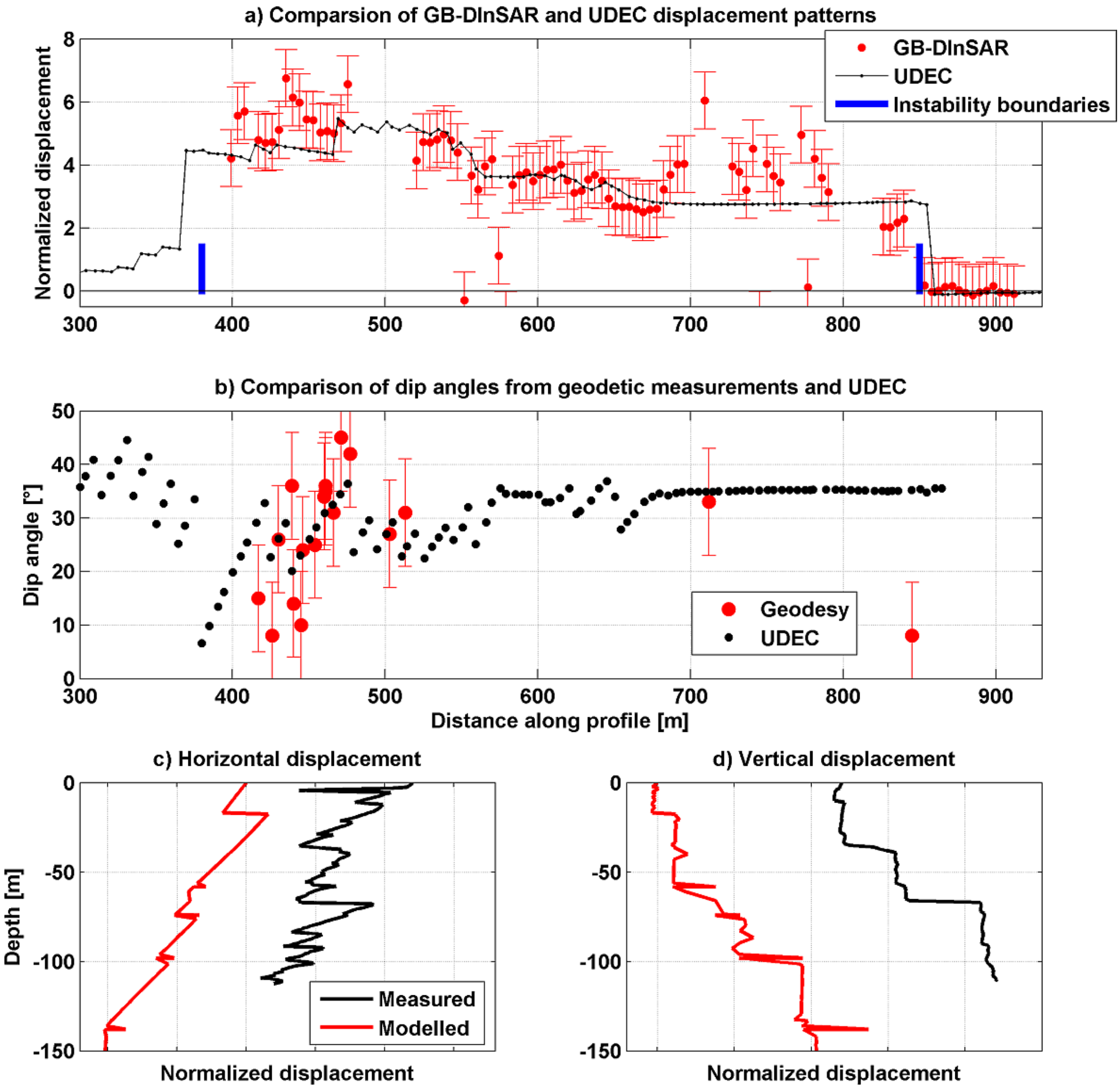

Figure 4.15: a) Comparison of the modeled surface displacements with GB-DInSAR displacements extracted along the modeled profile. The error of GB-DInSAR displacements is 0.9 mm. b) Plunge angles derived from 3D geodetic measurements compared to plunge angles modeled with UDEC. Error bars for geodetic measurements are 10°. c) Inclinometer and d) extensometer surveys in borehole sb120 compared with vertical displacement profiles extracted from the model at the approximate location of the borehole. Note that in all figures displacements were normalized to dimensionless values in order to highlight the internal displacement pattern. The displacement magnitude of the measured values and the model results are not comparable since they cover different time intervals.

PART II

Temporal behavior of the current Randa instability

5. THERMO-MECHANICAL FORCING OF DEEP ROCK SLOPE DEFORMATION – PART I: CONCEPTUAL STUDY OF A SIMPLIFIED SLOPE

Gischig, V., Moore, J.R., Evans, K.F., Amann, F. and Loew, S.

Resubmitted in revised form to *Journal of Geophysical Research*

21 June 2011

Abstract: Thermo-elastic rock slope deformation is often considered to be of relatively minor importance and limited to shallow depths subject to seasonal warming and cooling. In this study, we demonstrate how thermo-mechanical (TM) effects can drive rock slope deformation at greater depths below the annual thermal active layer. Here in Part I of two companion papers, we present 2D numerical models of an elementary slope subject to annual surface temperature cycles. The slope geometry and discontinuity sets are loosely based on the Randa instability considered in detail in Part II. Results show that near-surface thermo-elastic stresses can propagate to depths of 100 m and more as a result of topography and elasticity of the rock mass. Shear dislocation along discontinuities can have both a reversible component controlled by discontinuity compliance, and, provided that the stress state is sufficiently close to the strength limit, an irreversible component (i.e. slip). Induced slip increments are followed by stress redistribution resulting in the propagation of slip fronts. Thus, deformation and progressive rock slope failure can be driven solely by thermo-mechanical forcing. The influence of TM-induced stress changes becomes stronger for increasing numbers of critically stressed discontinuities and is enhanced if failure of discontinuities involves slip-weakening. The net TM effect acts as a meso-scale fatigue process, involving incremental discontinuity slip and hysteresis driven by periodic loading.

5.1 Introduction

Temporal variations in rock slope deformation are often related to changes in water pressure within a rock mass, and many case histories of rock slope failures attest to the strong influence of water. Thermal effects are normally considered to have secondary effect, although Erismann and Abele (2001) suggested that thermo-elastic strains can lead to fracture propagation at shallow depths when conditions are particularly favorable for failure. In some reported instances of slope instabilities, the temporal deformation behavior appears to be controlled by thermal effects. For example, Mufundirwa et al. (2010) suggested that observed permanent fracture displacements are caused by thermal fatigue, Gunzburger et al. (2005) demonstrated that unstable blocks up to a few cubic meters can move incrementally downhill due to cyclic thermo-elastic deformation, and Krähenbühl (2004) observed increased rates of crack opening during times of cold temperatures on unstable slopes along road cuts in Switzerland. These reported thermal effects are, however, limited to shallow depths subject to annual temperature changes, here referred to as the thermal active layer. Temperature changes within this layer directly induce stress changes through thermo-elastic expansion and contraction. Related shallow thermal effects reported in literature refer to freezing of water and ice pressure in fractures. Wegmann and Gudmundsson (1999) measured strains in permafrost rock walls, which could be correlated to formation of ice during subzero temperatures. Matzuoka (2000) reported fracture opening related to ice formation, both during periods of strong cooling in fall and during times of sufficient water availability during snowmelt in spring.

Our study focuses on strictly thermo-mechanical effects in the absence of any fracture infill (such as ice or water). Berger (1975), Harrison (1976), and Harrison and Herbst (1977) demonstrated that thermo-elastic stresses give rise to lateral strains in the presence of lateral temperature variations, material heterogeneities, or topography. Moreover, these authors demonstrated that thermo-elastic induced strains are not only limited to the thermal active layer, but can penetrate to greater depth below the active layer. At the Checkerboard Creek landslide in Canada, seasonal thermal effects were suggested to control slope movements down to depths of 26 m, below the annual active layer (Watson et al., 2004). There, a landslide in gneissic rock is controlled by steeply-dipping discontinuities; displacement rates are observed to be maximum in winter and minimum in summer. Thermal effects were suggested to control the temporal deformation behavior at the site: in winter, as blocks contract during cooling, normal stresses along steeply dipping discontinuities decrease and slip can occur. In summer, thermal expansion results in increased normal stresses, which inhibit slip.

Understanding the physical processes leading to failure of unstable rock slopes is not only crucial for correct interpretation of early-warning monitoring data, but can also provide new insights into the failure mechanisms of brittle rock in natural settings. Deformation histories of instabilities in brittle rock commonly exhibit a quasi-continuous, creep-like pattern. Purely static rock- or fracture-mechanics approaches are not sufficient to understand this behavior, since they do not consider time-dependent processes. However, small temporal changes of stress or strength are able to produce localized brittle damage and slip within a rock mass, which may result in apparent continuous deformation. Such failure processes involve the gradual propagation of new fractures through intact rock bridges, as well as frictional sliding along preexisting discontinuities, and are collectively referred to as progressive failure (Terzaghi, 1962; Erismann and Abele, 2001; Eberhardt et al., 2004). Although the single increments of failure may be small in magnitude, the cumulative effect can lead to catastrophic collapse of an entire rock slope.

Processes leading to stress or strength changes in a rock mass, and thus driving progressive failure, are described as so-called preparatory (Gunzburger et al., 2005) or driving factors. They can be divided into external driving factors (water pressure changes, passing seismic waves, surface temperature variations, freeze/thaw effects, and changes in slope geometry) and internal driving factors (chemical weathering, microscopic damage processes such as fatigue, stress corrosion, or creep). While all these processes may act simultaneously on a rock mass, often one factor will dominate the behavior of a particular slope. Commonly reported cases invoke water pressure changes as the cause of slope deformation or failure (Nishii and Matsuoka, 2010), either as a preparatory factor or ultimate trigger (e.g. Goldau, Switzerland, 1806, Heim (1932); Val Pola, Italy, 1987, Crosta et al., (2004)). Only rarely have thermal effects been recognized as exerting a controlling influence on deep rock slope deformation.

This manuscript is Part I of two companion papers that explore the effects of surface temperature cycles on deep (50 – 100 m) rock slope deformations below the thermal active layer. Here we present conceptual numerical models of a simplified slope which demonstrate how stresses induced by thermo-mechanical (TM) processes contribute to rock slope failure. In Part II (Gischig et al., this issue), we then focus on a case study of the Randa rock slope instability, where up to nine years of monitoring data from both the surface and boreholes suggest that thermal effects control ongoing displacements. As the conceptual models presented in this paper are intended to provide insight into observations made at the Randa instability, they include idealized features adopted from the site, such as failure kinematics and rock mass properties. We begin with a short description of the Randa site, and then present conceptual 2D numerical models of an elementary rock slope geometry subject to thermo-mechanical forcing. After describing the structural elements of the models and the modeling strategy, we investigate their behavior under near-surface, cyclical, thermo-elastic forcing. We compare models whose discontinuities are ascribed three different constitutive properties: purely elastic (no failure); and elastic with a limiting strength set by a Mohr-Coulomb failure criterion both with and without slip-weakening. The effect of prescribed elastic properties and discontinuity strength on TM induced stresses and permanent displacements is examined. Finally, we discuss outcomes of this numerical study in the context of progressive rock slope failure driven by TM forcing.

5.2 The Randa instability

The conceptual study presented here is motivated by observations of seasonally variable deformation rates at the unstable rock slope above the village Randa in southern Switzerland. A detailed description of the instability, including geological setting, failure kinematics, deformation monitoring, etc., is presented in Gischig et al. (this issue). Here we mention only key features that influence the design of our conceptual models.

The current rock slope instability at Randa (Figure 5.1) is the legacy of two catastrophic rockslides in 1991 that released in total ~30 million m^3 of crystalline rock (Schindler et al., 1993). The failure surface forms an 800 m high cliff, consisting of a sub-vertical orthogneiss face below 1900 m a.s.l. overlain by paragneiss and schists reaching to 2300 m a.s.l. (Figure 5.1). Geodetic monitoring initiated after these failures revealed that a sizable rock mass of ~6 million m^3 remains unstable and currently moves at maximum rates of about 30 mm/yr (Sartori et al., 2003; Jaboyedoff et al., 2004; Gischig et al., 2009). Comprehensive analysis of structural data, as well as patterns of displacements and internal deformation, led to the development of a kinematic model of the slope shown in Figure 5.1b (Willenberg et al., 2008a and b; Gischig et al., 2011). The instability was found to be characterized by two main kinematic modes: toppling in the upper portion

(>2150 m) and translational sliding along a basal rupture surface below. Toppling occurs because of the existence of a discontinuity set dipping into the slope at angles of 50 to 80°, and translation sliding is permitted by the presence of a set dipping about 40° out of the slope which also forms a highly persistent basal sliding surface. The kinematic pattern of deformation has been reproduced with 2D numerical models of the slope using realistic discontinuity geometry and constitutive properties (Gischig et al., 2011).

As described in Part II of this work (Gischig et al., this issue), quasi-continuous deformation monitoring both on the surface of and within the toppling rock mass revealed a relatively consistent seasonal deformation trend characterized by higher displacement rates in winter and slower rates in summer. We hypothesize that this temporal behavior is controlled by thermal effects, which we explore both with conceptual models here and Randa-specific models presented in Gischig et al. (this issue).

5.3 Numerical study of thermo-mechanical effects

Factors controlling progressive rock slope deformation driven by thermo-mechanical forcing were first investigated using a simplified numerical model that loosley incorporated key properties of the Randa rock slope instability (i.e. kinematic modes, discontinuity spacing, and rock mass properties). The model used a simplified slope geometry and included two orthogonal discontinuity sets that allowed simulation of two primary kinematic failure modes: sliding and toppling (the main kinematic modes identified at the Randa instability (Gischig et al., 2011)). The aim of this modeling exercise was to understand the details of processes activated within the rock mass due to cyclical TM stresses. We also assessed the magnitude of resulting TM-induced deformation in relation to rock mass properties and discontinuity orientation. Simulations were conducted for three different discontinuity constitutive relations: purely elastic without strength limit, elastic with strength limited by a Mohr-Coulomb criterion both without and with slip-weakening. In the following, we define the term shear dislocation as the in-plane component of the relative displacement vector of two originally neighboring points on opposite sides of a discontinuity. In general, this can include a reversible (elastic) component, termed the compliant response, and an irreversible component if the discontinuity strength is reached, termed slip. Throughout this paper, compression is taken as positive.

5.3.1 Method

Conceptual rock slope models were created using the commercial 2D discontinuum software UDEC (Itasca, 2008), based on the distinct element method (Cundall and Hart, 1992). The method considers an elastic continuum that contains a large number of discontinuities, which represent the medium as an assembly of blocks. The blocks themselves are treated as continuous domains and discretized with a finite difference mesh. They can deform, translate, rotate, and interact with each other. Discontinuities are assigned shear and normal elastic compliances, and strength properties such as friction, cohesion, and tensile strength. Shear failure, which invariably results in irreversible slip, occurs if the shear stress reaches the strength limit as defined by these discontinuity properties. Tensile failure leads to the normal stress at the failed interface being set to zero and opening of the discontinuity. Due to stress redistribution after failure, stresses accumulate at slip fronts. This can lead to additional failure and slip front propagation, until the stress state in the vicinity of the slip front again drops below the strength limit. Due to discretization along the discontinuities in UDEC, no stress singularities occur in the vicinity of the slip front, which is in contrast to basic fracture mechanical theory (Atkinson, 1989). Thus slip front propagation does not infinitely continue, but is able to cease. Different constitutive laws can be implemented governing the evolution of strength with slip. The software is ideal for simulating the behavior of a discontinuous, fractured rock mass. It also includes provision for solving the thermal diffusion equation and implementation of thermo-mechanical coupling.

The conceptual model geometry is shown in Figure 5.2. A 200 m high slope inclined at ~60° was created. This represents a generalized rock slope that may be found in many natural settings. Steep cliffs of more than 800 m height such as those at Randa are typically limited only to high mountain ranges, while 200 m high slopes are more widespread. Two sets of fully-persistent discontinuities with 20 m spacing were included, one dipping 30° out of the slope (Set 1) and one dipping 60° into the slope (Set 2). The two sets thus cut the model into square blocks 20 m on a side. By assigning high strength to one discontinuity set, failure (i.e. first-time slip or opening) becomes possible only along the other set. Allowing slip along Set 1 produces sliding kinematics (right-lateral shear), whereas slip along Set 2 produces toppling kinematics (left-lateral shear). At depth, a mesh size of 5 m was chosen, while a denser mesh of 2 m was used for the uppermost 20 m. Note that all models, also the purely elastic model, include both discontinuity sets. It may seem unnecessary to include both discontinuity sets when slip is inhibited along one (or along both in case of the purely elastic model). This was done for two reasons: (1) This approach has the advantage that the mesh remains consistent throughout. (2) The bulk rock mass elastic properties, which are a function of both blocks elastic properties as well as discontinuity compliance, remain the same regardless of which discontinuity set is activated.

Material properties used in the models are listed in Table 5.1. For intact blocks, i.e. the continuous material between discontinuities, linear elastic behavior was assumed. A Mohr-Coulomb failure criterion was used for discontinuities, which requires that friction, cohesion, and tensile strength be specified. Once shear failure along a discontinuity has occurred (i.e. slip has initiated), the subsequent slip behavior is governed by one of two constitutive laws: non-slip-weakening and slip-weakening. For non-slip-weakening behavior, the friction and cohesion under slip remain constant at the initial failure level while the tensile strength drops to zero. Such discontinuity behavior was applied for simplicity to help interpret the model results. In reality, the frictional strength of discontinuities may decrease after failure and slip. This behavior, here referred to as slip-weakening, is implemented by reducing the value of friction and cohesion immediately after the peak strength is reached. This means that failure (first-time slip) is accompanied by a stress drop. As in the non-slip-weakening models, tensile strength drops to zero after either shear or tensile failure.

For the non-slip-weakening models, the friction angle and cohesion at peak strength were set to 30° and 130 kPa, respectively (e.g. Barton and Choubey, 1976). For the slip-weakening models, the friction angle and cohesion at peak strength were set to 30° and 170 kPa, respectively, and then decreased to 29° and 10 kPa immediately after failure. We change the friction angle as well as the cohesion because this combination of strength parameters happened to produce a particularly large slip event at a chosen monitoring point (i.e. a location where the evolution of the stress components acting on a discontinuity was continuously monitored). The specific locations where such events occurred depended upon the strength values assigned to the slip-weakening model. Keeping the post-failure friction angle at 30° rather than 29° also produced large slip events, but not at the point where the stresses were monitored. In any case, at the normal stress levels appropriate for our models, the discontinuity strength reduction is dominated by a drop in cohesion. For example, at a normal stress of 1 MPa (corresponding to ~38 m overburden), a decrease in the friction angle of 1° reduces shear strength by only 23 kPa, while the specified drop in cohesion amounts to 160 kPa strength reduction. In reality, strength usually decreases progressively with sliding. Thus, we consider the assumed behavior as an end-member description of the true case, which may lie somewhere between non-slip-weakening (no post-peak stress drop) and slip-weakening (sudden stress drop). A friction angle of 36° and cohesion of 7.3 MPa was assigned to the set for which slip was prevented. For the purely elastic models, both discontinuity sets were assigned these high strength values. The normal and shear stiffness of discontinuities were set to 10 and 5 GPa/m, respectively, which ignores any dependence of fracture stiffness on normal stress.

Thermal diffusivity of the medium was set to 1.9E-6 m^2/s, which corresponds to a generalized value for gneiss found in the literature (Clauser and Huegens, 1995; Gueguen and Palciauskas, 1994), and also reproduces rock temperatures recorded at depths of 0 to 4 m at the Randa monitoring site. Although a dependence of thermal diffusivity on both stress and temperature has been reported (Clauser and Huegens, 1995), the value is assumed to remain constant over the region of interest (stresses corresponding to ~0 to 200 m overburden and temperatures between ±15 °C). Similarly, the coefficient of thermal expansion (8E-6 K-1) was taken from literature (Gueguen and Palciauskas, 1994) and assumed to be constant for the entire model.

Roller boundaries were chosen for the sides of the model so that vertical displacement was allowed while horizontal displacement was prohibited. The bottom of the model was fixed allowing no displacement. In the third dimension, plane strain conditions were assumed. Thus, all out-of-plane strain components were zero, while normal stress on this plane was calculated according to the input elastic properties. Boundary conditions for the thermal model assumed a constant temperature of 0 °C at the bottom and zero heat flux at the sides.

The following modeling procedure was applied: First, tectonic stresses were initialized by setting both horizontal stress components (in-plane and out-of-plane) equal to the vertical stress, which corresponds to lithostatic conditions. Then, the elastic stress field due to gravity and model topography was initiated by running the model until force-equilibrium was reached. The strength of all discontinuities was set to sufficiently high values during this phase to prevent failure. Next, the properties of the discontinuity set chosen to be activated were assigned so that failure in either sliding or toppling modes was enabled. After recalculating force equilibrium, some discontinuities had already reached their strength limit. This model then served as the initial state to which surface temperature cycles were applied. An initial temperature of 0 °C (arbitrary) was first set for the entire model. A sinusoidal temperature time history with 30 °C peak-to-peak amplitude and one year period was then applied to the ground surface. Since we only model the transient effect of temperature changes relative to the mean temperature, it is sufficient to set the latter to 0 °C, while ignoring a background geothermal gradient in the slope. The results are not sensitive to the initial temperature condition. The conductive heat equation was solved implicitly, and a thermal time step of 1 day was used to ensure numerical stability. After each thermal time step, the mechanical equations were solved again until a new force-equilibrium state was reached.

5.3.2 Results

5.3.2.1 Elastic model

Figure 5.3a shows the rock slope temperature field after 10 years of applied thermal cycling (see Figure 5.3c for surface temperature). Also shown in the inset of Figure 5.3a is a vertical profile of peak-to-peak temperature variations to 30 m depth after 10 years. The annual thermal wave penetrates to a depth of about 20 m, but has considerable amplitude only in the uppermost several meters. At 20 m depth, for example, annual temperature fluctuations are only about 0.3 °C. The same driving temperature field was applied in all models. Figure 5.3b shows the peak-to-peak amplitude of vertical tilt induced by shallow subsurface thermo-elasticity. Tilt amplitudes are greatest in the thermal active layer of the steep slope face and in the vicinity of sharp breaks in topography. However, regions of constant temperature behind the slope face also undergo annual vertical tilt variations on the order of 5 to 10 µrad. Figure 5.3d shows the y- and z-displacement time series resolved at six different points along the vertical profile shown in Figure 5.3a, ranging from 0 to 100 m depth. It is evident that thermo-elastic displacements are not limited to the comparatively thin thermal active layer, but extend to depths of at least 100 m. The peak-to-peak horizontal displacement amplitude is 1.2 mm at the surface decaying to 0.4 mm at 100 m depth. The vertical displacement amplitude is more than 2 mm at the surface, decaying to 1.0 mm at 20 m, and 0.4 mm at 100 m depth. Such deeply-penetrating disturbances are an effect of topography and elasticity, as described by Harrison and Herbst (1977). The peak-to-peak amplitudes of thermo-elastic stress fluctuations in the plane of the model at the near-surface point in Figure 5.3a (actually at 0.5 m depth) are ~4.2 MPa for σ_{yy} and ~0.0 MPa for σ_{zz}. As the average stress level of σ_{yy} during cycling is about 0.0 MPa, this stress component fluctuates between -2.1 to +2.1 MPa. Similarly, the variation of the out-of-plane stress, σ_{xx}, has a peak-to-peak amplitude of 4.7 MPa, while it is ~0.0 MPa on average during cycling. At 100 m depth, the in-plane stress amplitudes reduce to ~50 kPa for σ_3 (average stress level during cycling: 0.95 MPa) and ~25 kPa for σ_1 (average stress level: 2.41 MPa), and the out-of-plane stress amplitude becomes ~17 kPa (average stress level: 2.21 MPa). All stress components at the surface are more compressive than the ambient level when the applied temperature is above 0 °C. In contrast, below the thermal active layer (i.e. below ~20 m), all stress components are more compressive than their ambient level when the applied surface temperature is below 0 °C. The peak-to-peak amplitudes of induced strain fluctuations at 100 m depth (lowest red point in Figure 5.3a) are about 3.9 µε for e_{zz}, 0.4 µε for e_{yy}, and 3.1 µε for e_{yz} (see Figure 5.3a for coordinate system). It can be seen that the maxima of the annual displacement signals in Figure 5.3d progressively decrease to a stable level during the first few years of thermal cycling. The initial decline reflects the transient effect of suddenly applying a sinusoidal temperature fluctuation to the model, and was found to become negligible after about five cycles. Thereafter, the temperature field and the thermo-elastic displacement fluctuations it drives, reach quasi-static equilibrium.

5.3.2.2 Discontinuum models without slip-weakening

Figure 5.4 shows results from a model that allows sliding without slip-weakening along 30° dipping discontinuities (Set 1). The applied surface temperature history and resulting temperature distribution are the same as in the purely elastic model. Black lines in Figure 5.4a denote portions of the discontinuities that first failed under gravitational loading, prior to thermal cycling. Orange lines denote those that first failed during the initial 5 years of thermal cycling. Blue lines mark those that first failed during the subsequent 15 years of thermal cycling. Most of the discontinuities that failed under gravity alone slipped further during subsequent thermal cycling. It is evident that TM-induced stress cycles resulted in the first-time failure of many discontinuities in the rock mass below the top of the slope, and led to the propagation of failure along discontinuities at greater depth. Most of this failure, however, occurred during the first 5 years of simulation when the transient response of the model was at a maximum. In reality, such deformation might follow a change in the geometry of the scarp due to a major rockfall, when a new rock face is suddenly exhumed and becomes subject to annual temperature cycles.

The three model states presented in Figure 5.4a (gravitational loading alone, after 5 years of TM cycling, after 20 years of TM cycling) illustrate that first-time failure of discontinuity segments always occurs at the edge of sections that have already failed. Thus, progressive failure of the slope occurs through step-wise advancement of slip fronts. Figure 5.4b and c show the history of shear dislocation at two points on the particular Set 1 discontinuity that constitutes the main basal slip surface for the slope (see Points 1 and 2 in Figure 5.4a). Negative values denote right-lateral shear (i.e. movement of the top wall to the right with respect to the bottom). All time series are colored red when the temperature applied at the ground surface is positive and blue otherwise, thus indicating 'summer' and 'winter' conditions. Points 1 and 2 lie along the same discontinuity, with Point 1 being within the thermal active layer about 3 m from the slope surface and Point 2 being about 50 m up dip in a region of constant temperature. Most slip occurs during the first 5 years of thermal cycling after equilibration with gravity as a result of initial penetration of the applied surface temperature boundary condition. The increment of permanent shear dislocation added after each year decays, but remains greater than zero even after five years.

Shear dislocation for the same two points, during the period after quasi-static thermal equilibrium has been achieved (i.e. cycles 6 through 20) is shown in Figure 5.5a and e. The corresponding cross-plots of shear versus normal stress resolved on the discontinuities at the two points are shown in Figure 5.5b and f. Again, negative shear stresses would tend to move the upper block to the right with respect to the lower block in a right-lateral sense. At Point 1, periods of heating drive downward movement of the top block with respect to the bottom by ~1.3 mm, while during periods of cooling (i.e. autumn and winter), the trend reverses (Figure 5.5a). This is also evident in Figure 5.5b, which shows the stress path at this point for years 6 through 20 on a shear versus normal stress cross-plot. The failure envelope used in these simulations is also shown. The sequence of dislocation across the discontinuity during year 10, as well as the stress path involved, is shown in Figure 5.5c and d. Beginning at the end of the period of negative temperatures in cycle 9, the magnitude of the shear stress acting on the discontinuity increases (i.e. becomes more negative - path sector (1)) as the rock warms at the surface until the failure envelope in the negative quadrant is reached. Downward (right-lateral) slip is then initiated, and the path moves along the failure envelope as the magnitude of the shear stress continues to increase (i.e. becoming more negative) and the normal stress increases (sector (2)). When the shear stress trend reverses, the stress path departs from the failure envelope and slip halts. The shear stress then increases (i.e. becomes less negative and eventually positive) producing a small left-lateral compliance-related dislocation across the discontinuity (sector (3)) as temperature again becomes negative. In winter, the stress path is similar but shear stress has the opposite sign, resulting in upslope slip when the stress path reaches the failure envelope in the positive quadrant (sector (4)). It can be seen that downward slip in summer (sector (2)) is not fully recovered in winter (sector (4)), resulting in an incremental permanent dislocation after each cycle that accumulates to ~0.6 mm over 15 years (Figure 5.5a). However, the incremental offset for each cycle clearly diminishes; if it converges to zero for a large number of cycles, progressive slip on this particular discontinuity would cease. Nevertheless, the results serve to demonstrate that thermal cycles can drive progressive failure including slip along discontinuities and propagation of slip fronts.

Similarly at Point 2 (Figure 5.5e), located in the region where temperatures remain constant throughout the year, permanent down-dip slip amounting to ~0.08 mm accumulates between cycles 6 and 20. In this case, the stress path touches the failure envelope in winter, while stress conditions in summer prohibit failure (Figure 5.5f). Thus, discontinuity slip occurs only in winter, while the shear dislocation in summer is purely elastic and recoverable (i.e. governed by shear stiffness) (Figure 5.5g and h). As at Point 1, the irreversible slip increment diminishes with time and may converge to zero after a large number of cycles. It should be noted that this phase (cycles 6 through 20) is not a consequence of the initial thermal-transient phase of the numerical simulation, but rather reflects attainment of equilibrium in the rock mass through TM stress cycling. At both Points 1 and 2, the thermal stress cycles drive irreversible slip because the discontinuity is locally critically stressed, i.e. already close to the failure envelope.

Model results exploring toppling kinematics along discontinuities dipping 60° into the slope (Set 2) are presented in Figure 5.6. Only a small subset of discontinuities have failed due to gravitational loading alone (black lines in Figure 5.6a). Most of these failures occurred at the back of the slope, where tensile stresses are high enough to exceed the tensile strength of discontinuities. Dislocation across these discontinuities includes both an opening and slip component. A notable increase in the extent of failure occurs during the first 5 years of thermal cycling. Most of this additional failure occurs at the crown of the slope but also extends below to greater depths (orange lines in Figure 5.6a). Further downward, additional propagation of the slip front occurs during the following 15 years, although the propagation distance is not large (blue lines in Figure 5.6a). Histories of shear dislocation and the stress paths at two points on a discontinuity that daylights near the crown of the slope are shown in Figure 5.6b-e. Point 1 is close to the ground surface at a depth of ~2 m and within the thermal active layer, while Point 2 is about 80 m down-dip into the rock mass. At Point 1, the shear dislocation across the discontinuity has annual cycle amplitude of ~0.2 mm and a small permanent offset in a left-lateral sense (Figure 5.6b). Examination of the stress path shows that the cycle amplitude is largely controlled by the shear stiffness of the fracture, and that the permanent offset results from the stress path meeting the failure envelope during winter (Figure 5.6c). The stress cycle amplitude is about 1.7 MPa for normal stress and 1.1 MPa for shear stress. Both stress components decrease in absolute value during cooling and increase during warming. After the minimum temperature is reached, the magnitude of shear stress increases faster than the normal stress, and failure occurs during warming (transition from winter to summer). The resulting permanent dislocation accumulates each year and reaches about 1.3 mm over 15 years (positive for left-lateral shear). A slight reduction in the increment of slip added each year occurs for later cycles, but it is uncertain whether this will converge to zero after many cycles. At Point 2, permanent slip occurs exclusively in winter and reaches ~0.5 mm cumulative dislocation over 15 years (Figure 5.6d). Annual stress fluctuations are about 20 kPa (Figure 5.6e). During cooling, shear stress increases until the failure envelope for left-lateral slip is reached. The subsequent increase of normal stress and decrease of shear stress brings stress again below the strength limit. Shear stress further decreases during warming until normal stress also decreases and another cycle begins. Both normal and shear stress levels are lower after each cycle.

The component of permanent shear dislocation along discontinuities added for each cycle generally decreases with time for both sliding and toppling models. This is illustrated both in Figure 5.7 and Figure 5.8. Figure 5.7 compares the absolute displacement magnitude accumulated over the first 5 years of TM cycling with that from the subsequent 15 years for both toppling and sliding. Most displacement accumulates during the first five years as the models adjust to the new thermal boundary conditions (Figure 5.7a and c). However, total displacements are greater for toppling than for sliding. In the time period between 5 and 20 years, induced displacements are smaller and a substantial difference between toppling and sliding models can be observed. For sliding, induced displacements are smaller than for toppling (Figure 5.7b), and are limited to a small area near the crown of the slope. For toppling, induced displacements penetrate to depths of up to 100 m depth (Figure 5.7d). Similarly, Figure 5.8 shows the increment of permanent absolute displacement added each year for a point 40 m below the top of the slope (denoted as 'Point A' in Figure 5.4 and Figure 5.6). Calculations were performed for both sliding and toppling models over a duration of 20 years, and for a range of discontinuity strength properties as shown in the legend of Figure 5.8. For the purely elastic model, discontinuity strength was set to a high value (φ = 36°, c = 7.3 MPa), which inhibits failure in our models. For other models, the friction angle was set to 30° and cohesion varied between 70 and 240 kPa. Recall that the model results shown in Figure 5.4 and Figure 5.6 used a cohesion of 130 kPa. All models show a progressive decrease in the annual displacement rate with an increasing number of cycles. Displacements are greatest during the first 5 years, which reflects the thermal-transient phase at the start of cycling. All but the highest strength models show TM-induced permanent displacement continuing to accrue even after 5 years. The highest permanent displacements are accumulated for models with lowest cohesion (70 kPa). The displacement rates for toppling are generally higher than for sliding with the same strength values. The variation in strength explored over the five models is small and points to high sensitivity of the predicted TM-induced displacement on discontinuity strength.

5.3.2.3 Discontinuum models with slip-weakening

During slip-weakening, the shear stress that a failing discontinuity can support is reduced. Consequently, part of the stress supported by the discontinuity is instantaneously transferred to the surrounding rock mass at failure, thereby promoting subsequent failure of other nearby discontinuities to a greater degree than in models without slip-weakening. Figure 5.9 shows results for a toppling model in which the discontinuity strength exhibits slip-weakening; the simulation time extends to 30 years. The colors used to denote the time at which first failure occurs on the discontinuities are consistent with the color scheme used in previous models (Figure 5.4 and Figure 5.6). However, an additional color, red, is now used to indicate discontinuity segments that first fail during a slip propagation event that occurred after 22 years.

The dislocation behavior of the toppling model is monitored at three points, denoted Point 1, 2 and 3, that lie on the same discontinuity (Figure 5.9a). They illustrate the shear dislocation and stress transfer effects associated with a large slip propagation event. The dislocation histories at the three points are shown in Figure 5.9b. Point 1 lies below the depth to which the slip front extends, and thus shear dislocation oscillates reversibly due to discontinuity compliance. Point 2 lies just beneath the downward extent to which the slip front has extended after 20 years (see inset to Figure 5.9a). This point experiences failure (i.e. first-time slip) after 22 years of thermal cycling. The stress path at Point 2 for the period 13 to 30 years is shown in Figure 5.9c. At 13 years, the shear stress magnitude is about 20 kPa below the failure envelope. TM cycling primarily affects normal stress, which increases during summer and decreases during winter. However, the shear stress magnitude undergoes a slight, irreversible increase with each cycle as a result of accumulating dislocation behind the slip front where failure has already occurred and strength is at residual values. Thus, stress at Point 2 moves progressively closer to the peak strength with each cycle. After the peak strength is reached, shear stress drops by about 200 kPa due to post-failure weakening and slip of about 0.15 mm occurs. Thereafter, the stress remains close to the residual strength envelope and each TM cycle results in a small amount of slip. At Point 1, where stresses lie below both the peak and the residual failure envelopes, the slip event across Point 2 induces an increase in shear stress of ~10 kPa (Figure 5.9d). This produces a small instantaneous shear dislocation (offset in the dislocation time series), which is an elastic (compliant) reaction to stress redistribution. Point 3 is located above Point 2 in the zone that had failed previously under gravitational stress, and thus the discontinuity strength is already at the residual level. Its stress path is shown in Figure 5.9e. The annual cycles of shear dislocation include an irreversible slip component that occurs in winter and results in a long-term slip rate of about 0.02 mm/year. The large slip event at Point 2 transfers shear stress to the region of Point 3, which consequently undergoes greater slip. This additional slip accumulates over two years, because the Point 2 slip event occurred shortly after the annual slip at Point 3 for that year had been completed and the stress state was below and moving away from the failure envelope. The additional shear stress from the event at Point 2 returned the stress state at Point 3 to the failure envelope when it was partly released by slip. The remainder of the additional shear stress was released in the following year as the TM-induced stress again increased. Note that similar slip events also occurred along other discontinuities elsewhere in the model, and they also occurred in other slip-weakening models that used different discontinuity strength properties, albeit at different locations.

5.3.3 Effect of stiffness and strength

The key outcome of the simulations is the demonstration that TM-forcing can drive progressive failure for a physically reasonable set of input parameter values. It is of interest to examine the sensitivity of this result to the values ascribed to the various parameters. These may be grouped into elastic parameters (Young's modulus, Poison's ratio, fracture stiffness's), thermal parameters (thermal diffusivity, thermal expansion coefficient, amplitude of the input temperature history), and geometry (slope height and angle, discontinuity orientation, persistence and spacing). Performing a sound sensitivity analysis for all these parameters would involve extensively mapping the entire parameter space, which is beyond of the scope of our current study given the long computation time required per model (typically up to 50 hours for 20 cycles with a Intel Xeon W5590 3.33 GHz processor). Nevertheless, on basic physical grounds we expect rock mass elasticity and discontinuity strength to play an important role in the progressive failure process. Hence, in the following section we examine the effects of varying these parameters individually. These studies help demonstrate the importance of two requirements that must be met for TM forcing to drive progressive failure: that the bulk stiffness of the rock mass is sufficiently high, and that a substantial fraction of discontinuities in the rock mass are critically-stressed.

The downward extension of significant strain more than 100 m below the thermal active layer (Figure 5.3b) is due to the elastic nature of the medium. Here we demonstrate the dependence of TM-induced stresses at depth on the elastic properties of the medium. In a discontinuous rock mass, the bulk elastic properties are a function of both the elastic properties of intact rock (Young's modulus and Poisson's ratio), and the normal (k_n) and shear (k_s) stiffnesses of the discontinuities. To investigate the dependence of TM-induced stresses on the bulk rock mass moduli, we performed simulations using purely elastic models (including both discontinuity sets) in which the Young's modulus and Poisson's ratio were each individually varied between ±50% of the value given in Table 5.1 (which was used to produce the simulations shown in Figure 5.3). Similarly, the joint stiffness parameters, k_n and k_s, were varied within the range of ±50% of the values in Table 5.1. Both stiffness parameters were changed simultaneously for both discontinuity sets while maintaining a constant ratio (i.e. if we changed k_n from 10 to 5 GPa/m, k_s was reduced from 5 to 2.5 GPa/m). The results of the analyses are presented in Figure 5.10 which shows the relative change in peak-to-peak amplitude of TM-induced fluctuations in maximum principal stress, σ_1, at two points at 40 and 100 m depth (see Figure 5.3) versus the magnitude of parameter change in percent. The reference model corresponds to the one presented in Figure 5.3 using elastic parameters in Table 5.1. In this model the peak-to-peak amplitude of σ_1 cycles is ~50 kPa at 100 m and ~120 kPa at 40 m. The strongest effect on TM-induced stress changes is obtained for variations in the Young's modulus. At both depths, the amplitude of σ_1 changes by 40 to 50 % when the Young's modulus changes by 50%. Changing Poisson's ratio by the same amount results in a 15-20 % change of the σ_1 amplitude at 40 m depth and a similar 15-25% change at 100 m depth. The smallest effect is obtained for changing discontinuity stiffness: at 40 m depth stress amplitudes change by only 5-15 %, while at 100 m depth they change by up to 10-20 %. Note that the dependence of peak-to-peak stress amplitude on the parameter values is slightly non-linear.

As shown in Figure 5.5b,f and Figure 5.6e, slip along a discontinuity is induced by TM cycles if the stress acting on it is already close to the failure envelope (i.e. the discontinuity is critically stressed). For a given slope and discontinuity geometry, the quantity of critically stressed discontinuities within the medium is determined by the strength of the discontinuities relative to the ambient stress level. We conclude that the relative quantity of critically stressed discontinuities is likely to exert first order control on the magnitude of TM-induced progressive failure at depth. The closer the slope is to failure, the stronger the TM-induced permanent displacements. We have examined a series of models with different discontinuity strengths: for sliding models, cohesion was varied between 20 and 500 kPa and tensile strength between 0 and 200 kPa, while for toppling models, cohesion was varied between 10 and 390 kPa and tensile strength between 0 and 140 kPa. The friction angle was held constant at 30° in all models. For each model, the degree of criticality before thermal cycling was computed. The degree of criticality is expressed by the percentage of total discontinuity area in the model that is critically stressed (an out-of-plane dimension of unity is assumed). A discontinuity is considered to be critically stressed if it is within 50 kPa of the strength limit. This implies that an increase in shear stress of that order will most likely result in failure. In Figure 5.11b, we show the TM-induced displacement rate after 10 years at the point 40 m below the crown of the slope (Point A in Figure 5.4 and Figure 5.6) plotted against different degrees of criticality (i.e. different discontinuity strengths). For sliding, the displacement rate increases sharply with increasing criticality. At high criticality (i.e. > 21% or cohesion less than 20 kPa), we found that the sliding slope can fail as a result of TM cycling alone. For toppling, the displacement rates similarly increase until ~14% of discontinuities are critically stressed. Unlike for sliding models, the rates drop abruptly for higher criticality (i.e. for cohesion less than 100 kPa), and remain nearly constant for increasing criticality. This is a result of the self-stabilizing nature of flexural toppling (Nichol et al., 2002), and will be discussed in the following section. Although only cohesion was changed in the presented models, similar results can be expected for changing friction angle: lower friction values result in more discontinuities being critically stressed, which then become susceptible to TM-induced stresses.

5.4 Discussion

Our numerical simulations indicate that the magnitude of TM-induced displacements is generally greater for toppling than for sliding (Figure 5.7 and Figure 5.8). Also, shear dislocation time series and stress paths along discontinuities are different depending on their orientation and location, and are similarly variable along a single discontinuity. Thus, our results demonstrate that the magnitude of TM effects is essentially defined by model geometry and discontinuity orientation. For toppling, the normal stress on discontinuities within the thermal active layer relaxes as the rock cools and contracts during winter, which favors slip (Figure 5.6c,e). The opposite occurs during summer when the rock warms and expands: normal stresses along discontinuities increase inhibiting slip. For sliding (Figure 5.5), the shear stress along a discontinuity daylighting at the slope face increases in summer as the rock expands, and therefore slip is favored in summer. During winter as the rock contracts, the shear stress decreases and at some points even changes sign, as shown in Figure 5.5b. TM-induced stress changes can also be expected to depend on the slope geometry. We conclude that TM effects are related to rock slope kinematics in a complex manner, since kinematics itself is a function of slope geometry, discontinuity orientation and spacing, as well as the elastic properties and strength of both the rock mass and discontinuities (Sjöberg, 2000).

The presented models of sliding and toppling slopes that have a large number of critically stressed discontinuities behave differently (Figure 5.11). For sliding, the TM-induced displacement rate at the monitoring point (Point A) increases dramatically as the percentage of critically stressed discontinuities in the model exceeds 14%, whereas for toppling, the displacement rate is more stable beyond 14%. This difference can be explained by the self-stabilizing effect of flexural toppling. Nichol et al. (2002) demonstrated that slopes undergoing flexural toppling can only deform a limited amount before stabilizing due to kinematic constraints. Toppling can only continue if failure across the rotating slabs (failure of so-called cross joints) is allowed. This latter situation is referred to as block toppling as opposed to flexural toppling (Cruden & Varnes, 1996). Thus, once a flexural toppling slope has accumulated enough slip to self-stabilize, i.e. further failure is inhibited, TM effects cease, except possibly for cyclical, reversible dislocations governed by fracture compliance. Such a self-stabilizing mechanism does not exist for sliding slopes, where slip will continue until catastrophic failure if strength and stress conditions permit. It should be noted that flexural toppling is a somewhat unrealistic kinematic mode in natural rock slopes. In reality, as toppling progresses, elastic bending of the slabs results in tensile stresses developing along the outer side of the slabs. This can be seen in Figure 5.12, which shows the distribution and magnitude of the minimum principal stress, σ_3, where it is tensile (i.e. only tensile stress is shown, compressive stress is masked). Figure 5.12a shows tensile stress that has developed in toppling slabs after gravitational equilibration and 20 years of TM-forcing for the model with relatively low-strength discontinuities (φ= 30°, c = 10 kPa). Tensile stresses of up to 1 MPa develop, of which 0.5 MPa are only due to the thermal cycling (Figure 5.12b). Given the discontinuous nature of an unstable rock mass, situations where there are intact slabs capable of supporting significant tensile stress in flexure are likely to be rare. Thus, even in the absence of cross joints, self-stabilization of flexural toppling is unlikely,

Figure 5.11 clearly shows that TM forcing generally becomes more effective if a greater proportion of discontinuities in the rock mass is critically-stressed. Although the definition of criticality used in our study may not be transferable to all cases of slope stability, it is clear that a necessary condition for TM-induced stresses to produce slip and drive propagation of slip fronts at depth below the thermal active layer is that the stress state along discontinuities is close to their strength limit. In natural settings, such conditions can be expected for slopes that were formed through a preceding failure. The rock mass adjacent to the failed material that forms the new slope may have remained stable throughout preceding failures, but is brought close to failure by the new conditions. Retrogressive type failures, like the current Randa instability, are likely to contain large amounts of critically stressed discontinuities and may thus be prone to progressive failure through TM forcing. In general, TM effects can be significant for other natural slopes whose discontinuity distribution has developed the requisite degree of criticality, either through strength degradation or a change of slope geometry.

The models presented in Figure 5.4a and Figure 5.6a showed that slip front propagation is not exclusively induced by the initial gravitational equilibration of the model or during the thermal-transient phase in the first 5 years, but also occurs later by continued TM-induced forcing. Through incremental slip along critically stressed discontinuities, stress is transferred to the rest of the model and concentrates at slip fronts. TM-induced slip thus drives the propagation of progressive failure. The effect is significant for models without slip-weakening, but is enhanced if slip-weakening is allowed. The results presented in Figure 5.9 illustrate the effects of slip-weakening and the resulting stress redistribution within the surrounding rock mass after discontinuity failure. Models without slip-weakening, such as those shown in Figure 5.4 and Figure 5.6, indicate that TM-induced slip decays during continued cycling and may reach a stable state after some time. However, if failure involves a drop in strength, the resulting stress redistribution is stronger and more abrupt. As a result, TM-induced slip rates can be enhanced after a single slip event before they again decay slowly over time (Point 2 and 3 in Figure 5.9b). Incremental failure of discontinuities involving slip-weakening thus helps maintain TM effects for longer than predicted in the case without slip-weakening. Even when slip-weakening is not as abrupt as in the applied constitutive law, TM-induced strains at depth may be strongly enhanced by slip weakening.

Since TM effects depend on the slope geometry, we can expect that TM-induced strains will also vary for 3D topography. Although our numerical analysis is limited to 2D, we can deduce some implications for 3D from the calculated out-of-plane stress, σ_{xx}. Our models showed that, similar to other stress components, σ_{xx} varies during thermal cycling. Indeed, at the ground surface, the annual amplitude of σ_{xx} is the largest of the three stress components, as out-of-plane strain is inhibited in 2D. Typically, instabilities in natural settings are bounded laterally by discontinuities, so-called lateral release surfaces, which provide a necessary degree of kinematic freedom. Furthermore, 3D kinematic modes often involve wedge sliding, which is sliding on two intersecting discontinuities. In both cases, lateral stresses are important for analysis of slope stability. If discontinuities forming lateral release planes are critically stressed, then TM-induced stress changes on these discontinuities would be expected to drive dislocations. Thus, TM effects in natural slopes are likely to be greater than in our 2D analyses, since they are enhanced through TM-induced slip on lateral release surfaces or wedge planes.

In the modeling sequence used here, sinusoidal temperature cycles were initiated after the rock slope had equilibrated to gravitational loading. After application of this new surface temperature boundary condition, about 5 years were required to establish a new quasi-steady temperature field in the rock mass and accommodate the changing stress conditions resulting from thermo-elastic effects. Considerable TM-induced damage occurred during this thermal-transient phase (Figure 5.4 and Figure 5.8). While this may seem unrealistic for a rock surface subject to temperature fluctuations over hundreds or thousands of years, it is applicable to slopes that have been recently exposed by large failures, such as the 1991 rockslides at Randa. The newly formed cliff surface consists of rock that was previously below the thermal active layer and had been at constant temperature. After exposure, the rock mass had to adapt to the new thermal conditions, and our results suggest the potential for considerable TM-induced damage during the subsequent thermal-transient phase.

As shown in Figure 5.5a-d, the shear dislocation at Point 1 close to the ground surface along the sliding discontinuity changes direction during each cycle. This cyclical shear dislocation is not only a compliant response but involves a component of slip in both directions. Note that upslope slip may be a consequence of simplifications in our models. To our knowledge there are no field observations of such a phenomenon reported in the literature. However, we point out that the behavior may be significant in illustrating hysteresis associated with TM-induced cyclic stress changes: although a small amount of permanent dislocation remains after each full cycle, most of the slip during summer is recovered in winter. Due to frictional slip in both directions, energy will be dissipated during each cycle; even through the dislocation is mostly reversible. Energy loss associated with such bi-directional slip driven by stress cycling can be interpreted as hysteresis. In a natural rock slope, energy dissipated by hysteresis may be readily provided through a loss of potential energy.

5.5 Summary and conclusion

The key outcomes of our conceptual study exploring TM effects on a simplified slope can be summarized as follows:

1. As a result of topography and thermo-elastic strain within near-surface bedrock subject to cyclic temperature changes, seasonal stress changes are induced at depth below the thermal active layer. While stress changes within the active layer are considerable (>1 MPa in our case), TM-induced stress changes at greater depth (up to 100 m) are small in amplitude (on the order of 10 – 100 kPa).
2. Although stress changes at depth are small, they can cause slip along discontinuities provided that the stress state along these is already close to failure. If a sufficient number of discontinuities are critically stressed, TM effects become efficient and can contribute to failure of an unstable rock slope.
3. TM effects depend strongly on the assumed discontinuity strength properties, which determine the number of critically stressed discontinuities within the rock mass. TM effects further rely on the ability of the rock mass to transfer stress fluctuations in the thermal active layer to greater depth, a process that is promoted by a higher elastic modulus of the bulk rock. TM effects vary for different discontinuity orientations and depend on the geometry and kinematic failure mode of an unstable slope. In our models, TM effects were more pronounced for toppling than for sliding.
4. TM effects are enhanced for models including slip-weakening discontinuity constitutive behavior. Slip-weakening after failure results in stress redistribution throughout the rock mass, which alters the distribution of neighboring critically stressed discontinuities that may react to TM effects. Models including slip-weakening also demonstrated that stress redistribution associated with slip front propagation can reactivate decaying TM effects.
5. The net TM effect can be interpreted as a meso-scale fatigue process within the rock mass, which involves incremental slip along critically stressed discontinuities, as well as hysteresis driven by periodic TM loading.

Acknowledgements

We thank William Schulz, Prof. Stephen J. Martel and Prof. Erik Eberhardt for careful reviews that led to an improvement of the manuscript. This project was funded by the Swiss National Science Foundation (Project No. 200020-112073).

Table 5.1: Input parameter values used in the numerical study. Discontinuities for which failure is allowed are termed active and have variable strength. For the other discontinuity set, termed passive, the strength is set high to prevent failure. Thermal diffusivity was estimated from temperature measurements in a shallow borehole and is consistent with values reported in the literature (Clauser and Huegens, 1995). Thermal expansion coefficient was estimated from relevant literature (Gueguen and Palciauskas, 1994).

	Intact rock blocks	
Density, ρ (kg/m^3)	2700	
Young's modulus, E (GPa)	18	
Poisson's ratio, ν	0.2	
	Discontinuities	
	Active	**Passive**
Friction angle, φ	30°	36°
Cohesion, *c* (MPa)	0.13	7.3
Tensile strength, *t* (MPa)	0.01	3.5
Joint normal stiffness, k_n (GPa/m)	10	10
Joint shear stiffness, k_s (GPa/m)	5	5
	Thermal properties	
Thermal diffusivity (m^2/s)	1.9E-6	
Thermal expansion (1/K)	8E-6	

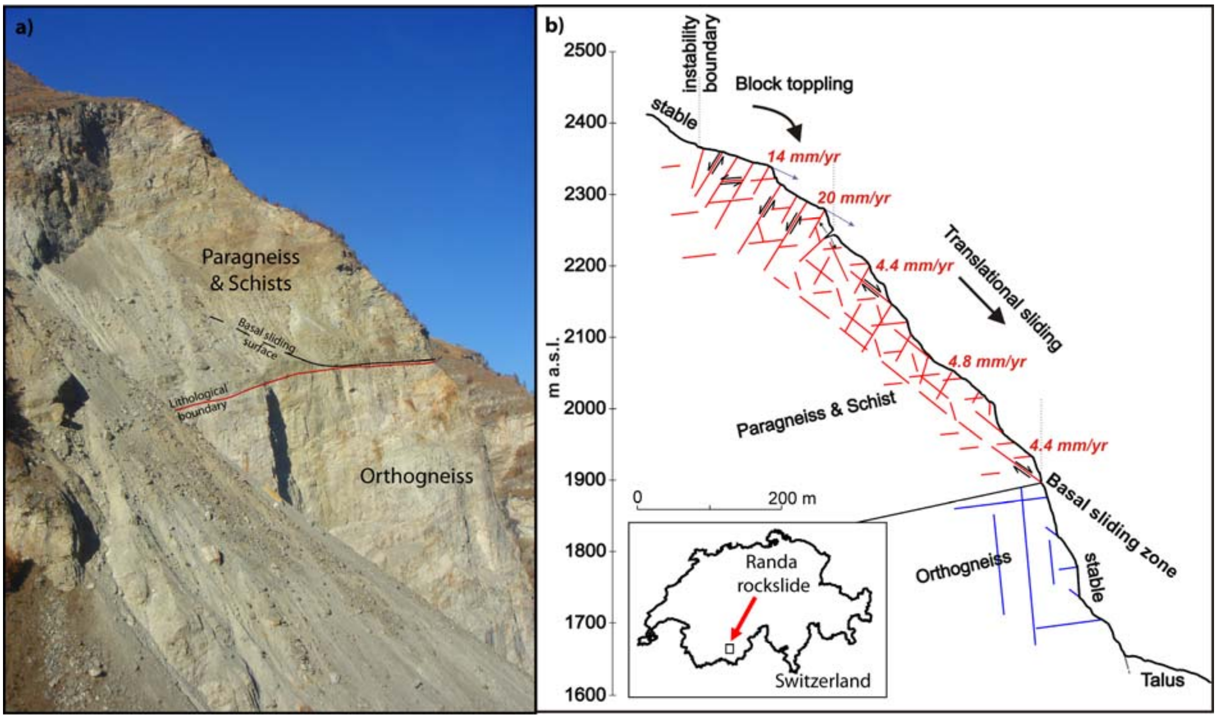

Figure 5.1: a) Photo of the failure surface of the 1991 rockslides above the village Randa, highlighting the two main lithologies (orthogneiss below 1900 m, paragneiss & schists above). b) Cross-section through the current Randa instability showing the conceptual 2D model of the kinematic behavior. The model includes information on internal structure (i.e. discontinuity orientations) and kinematics (i.e. shear sense along discontinuities and internal deformation patterns) as derived and presented by Willenberg et al., (2008a and b) and Gischig et al., (2011). Velocities are absolute displacement rates derived from radar interferometry data (Gischig et al., 2009) and geodetic measurements (Willenberg et al., 2008b).

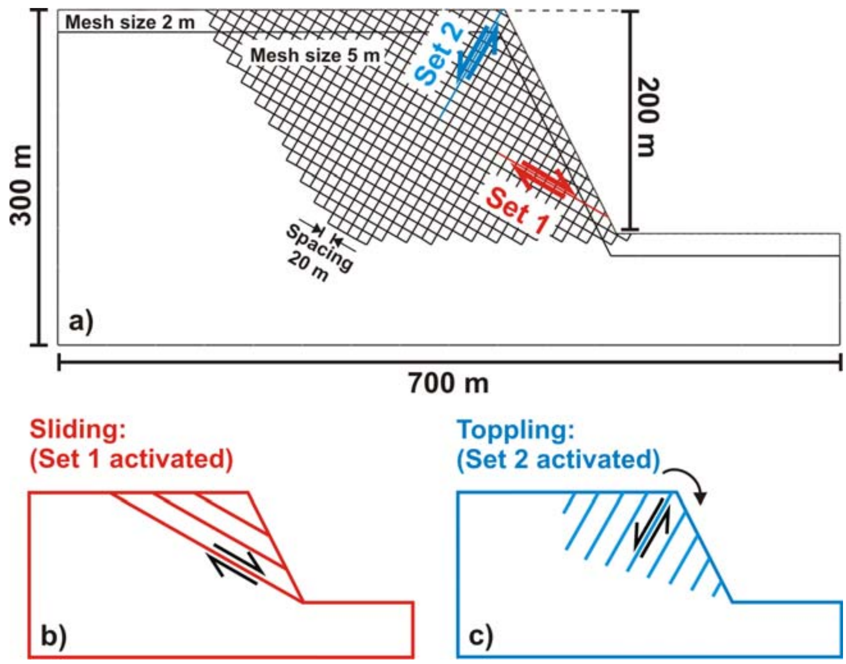

Figure 5.2: a) Model geometry used for the conceptual TM study in UDEC. Two discontinuity sets dipping 30° out of the slope (Set 1) and 60° into the slope (Set 2) were included. The sets were activated by decreasing their respective strength properties; sliding is permitted by activating Set 1, while toppling occurs if Set 2 is activated. b) and c) Sketches illustrating the two kinematic modes investigated.

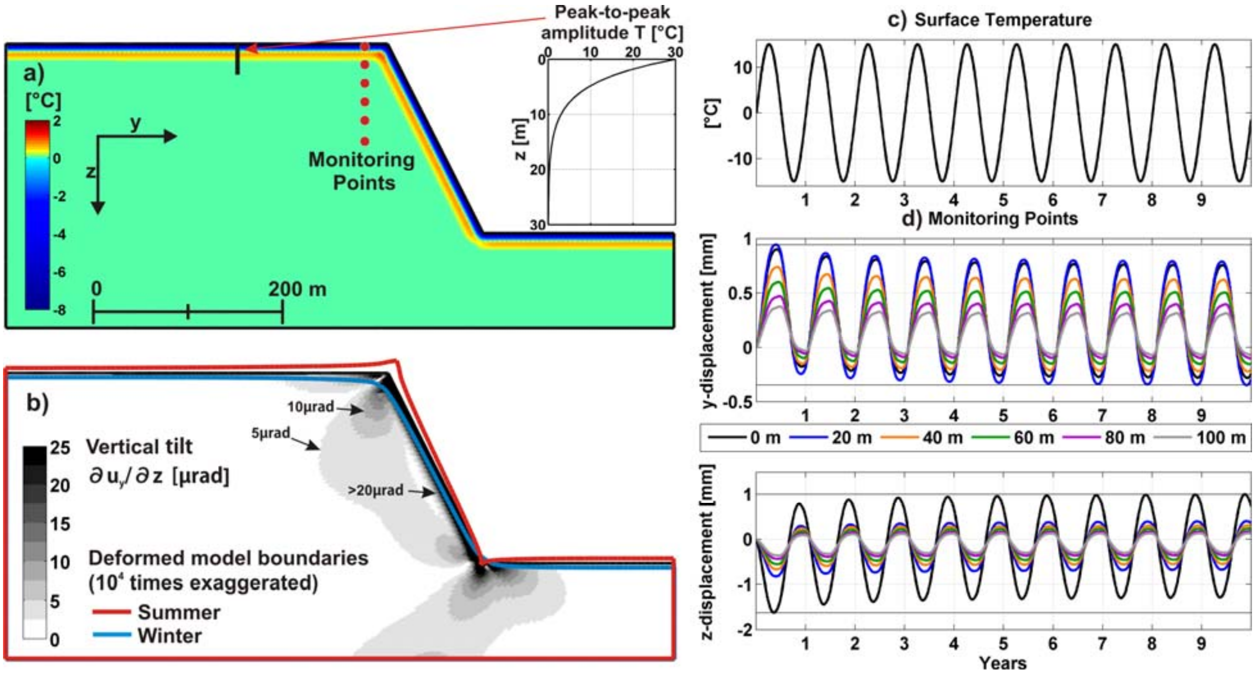

Figure 5.3: a) Temperature field after 10 years of thermal cycling. Monitoring points presented in d) are indicated as red dots. b) Peak-to-peak amplitude of vertical tilt induced by thermo-elastic strain in the shallow subsurface. Also included are the deformed model boundaries for when the temperature at the surface is minimum and maximum, exaggerated by a factor of 104. c) Sinusoidal temperature history with amplitude of 15 °C applied to the surface. d) Displacement time series were extracted for six points from 0 to 100 m depth at a spacing of 20 m, shown by red dots in (a) . The displacement amplitudes decrease with depth, but are not less than 30% of the surface displacement amplitudes for depths as great as 100 m. This reflects thermo-elastic effects in the continuous medium.

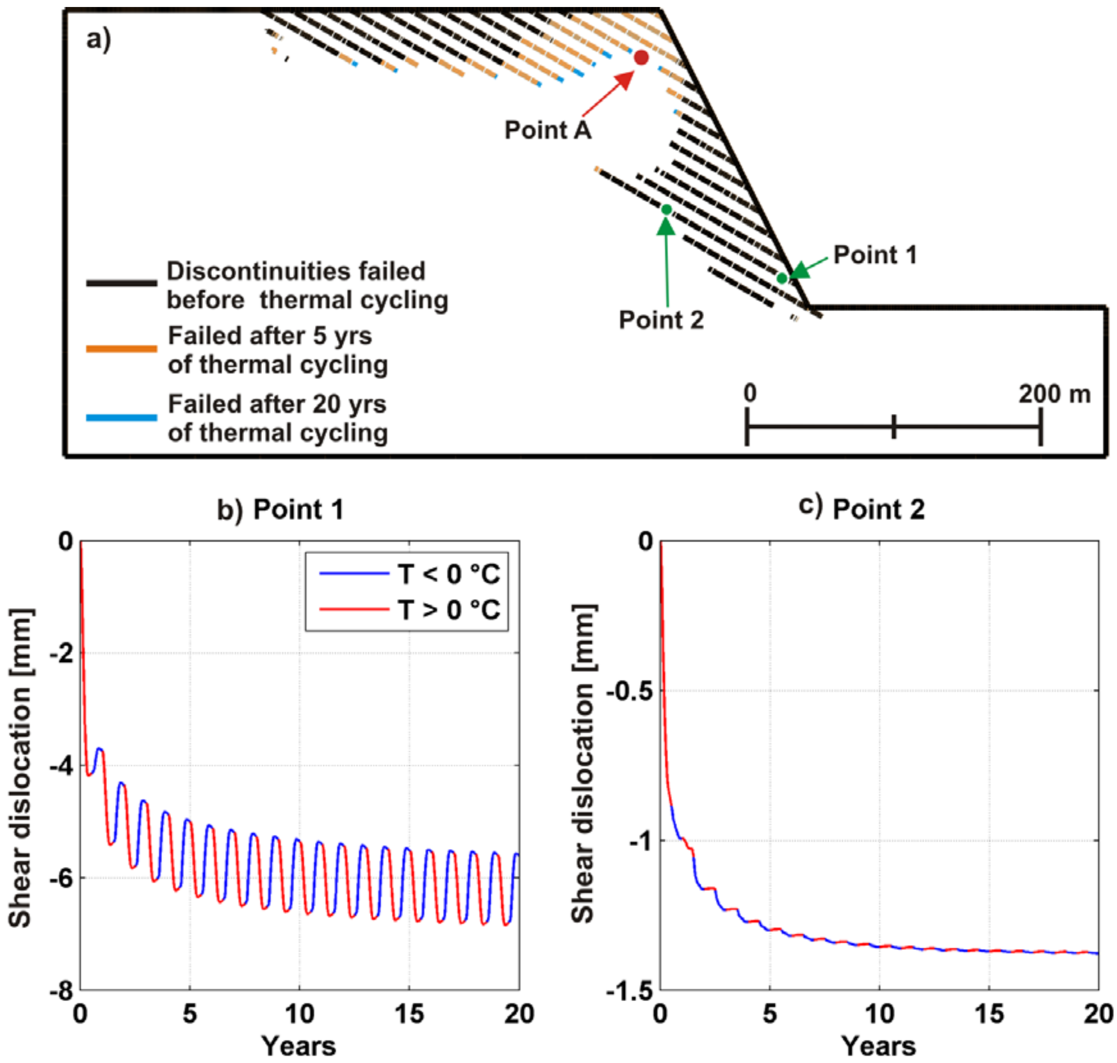

Figure 5.4: a) Sliding model without slip-weakening showing discontinuities that failed before TM cycling (black lines), and after 5 (orange lines) and 20 years (blue lines) of TM cycling. The locations of Points 1 and 2, as well as Point A (used in Figure 5.8 and Figure 5.11) are shown. b) Shear dislocation time series on the sliding discontinuity at Point 1 for 20 years of thermal cycling beginning after gravitational equilibration. The time series is colored red when surface temperatures are above 0 °C and blue otherwise. Negative dislocation corresponds to right-lateral shear. c) Same as in b) but for Point 2.

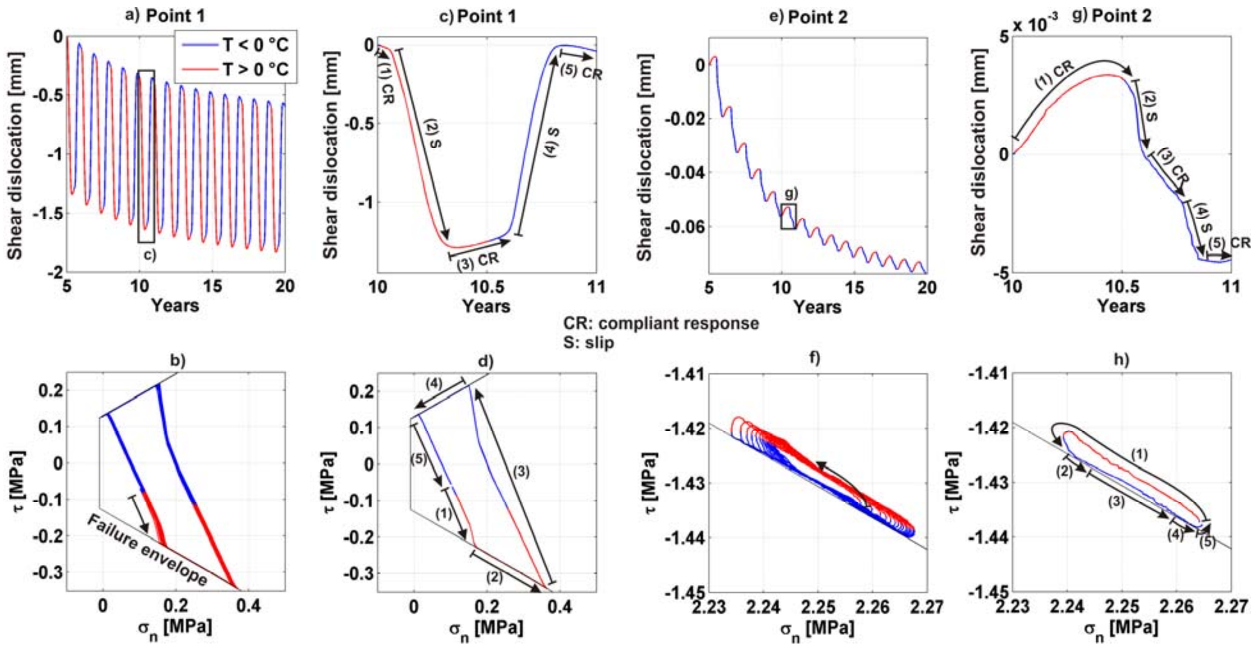

Figure 5.5: a) Shear dislocation at Point 1 in Figure 5.4. b) Stress path at Point 1 in a normal versus shear stress cross plot. Colors correspond to positive or negative temperatures at the ground surface. Note that negative shear stress induces right-lateral shear dislocation. Also included is the failure envelope (both positive and negative quadrant) with tensile strength cut-off for negative normal stresses. c) and d) Details from plots in a) and b) highlighting cycle number 10 of the models. The figures illustrate both reversible (compliant response) and irreversible components (i.e. slip) of a TM cycle at Point 1. e) Shear dislocation of Point 2. f) Stress path at Point 2. g) and h) Details of the plots in e) and f) highlighting cycle number 10.

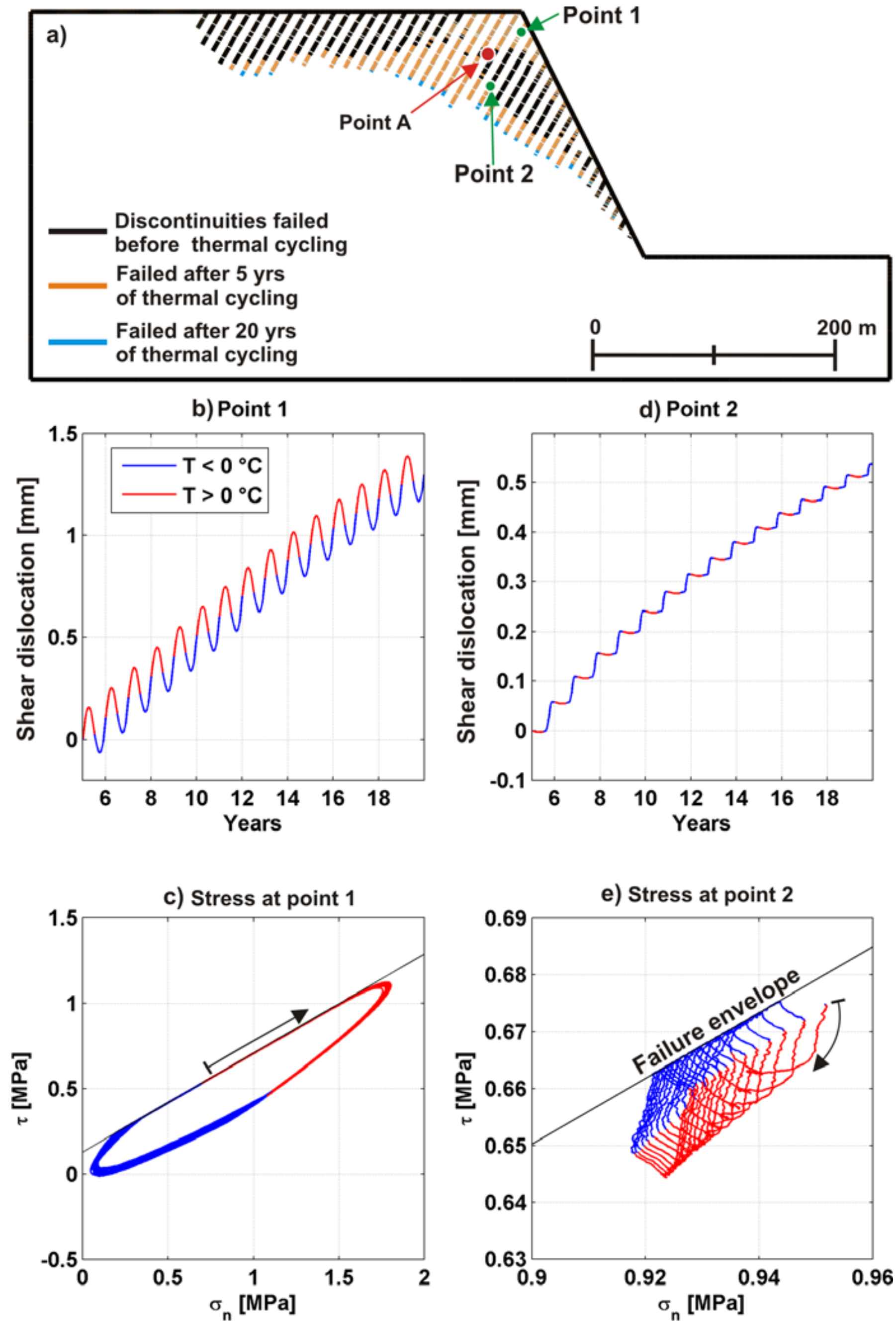

Figure 5.6 a) Results of the toppling model showing failed discontinuities before TM cycling, and after 5 and 20 years of TM cycling. b) Shear dislocation at Point 1 (positive dislocations denote left-lateral shear). c) Stress path at Point 1. d) Shear dislocation at Point 2. e) Stress path at Point 2. The black arrows indicate the sense of rotation of the stress cycle.

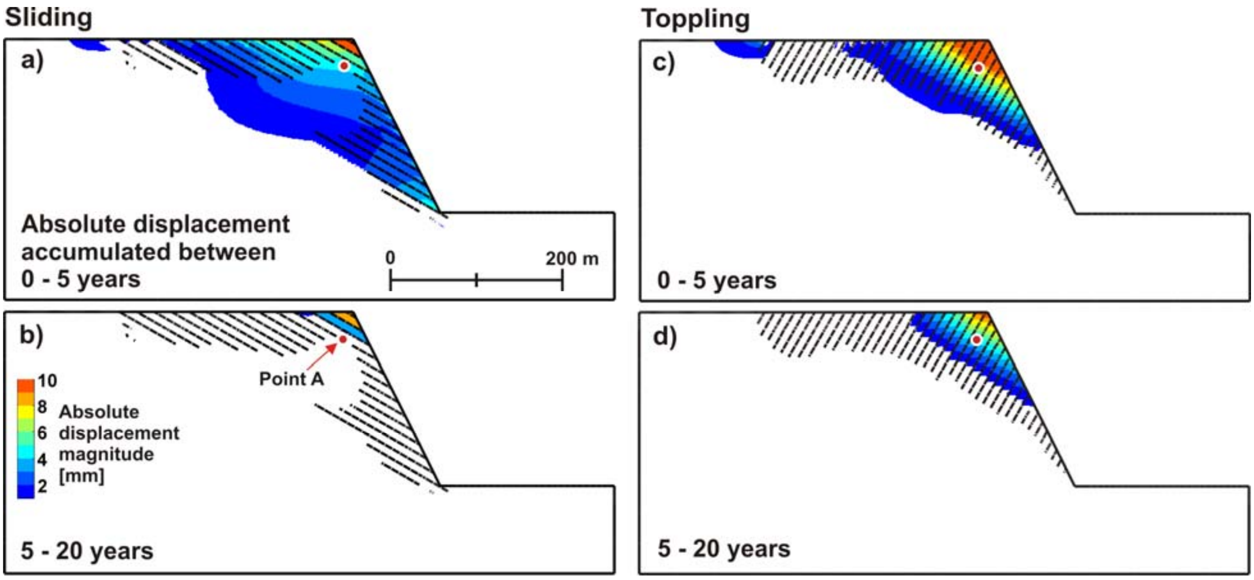

Figure 5.7: Displacement maps showing the absolute displacement magnitude resulting from TM cycling. a) Displacement accumulated between 0 and 5 years for sliding. b) Displacement accumulated between 5 and 20 years for sliding. c) and d) Same as in a) and b) for toppling. Also shown are the discontinuities which have slipped after 5 (a and c) and 20 (b and d) years of TM cycling, respectively.

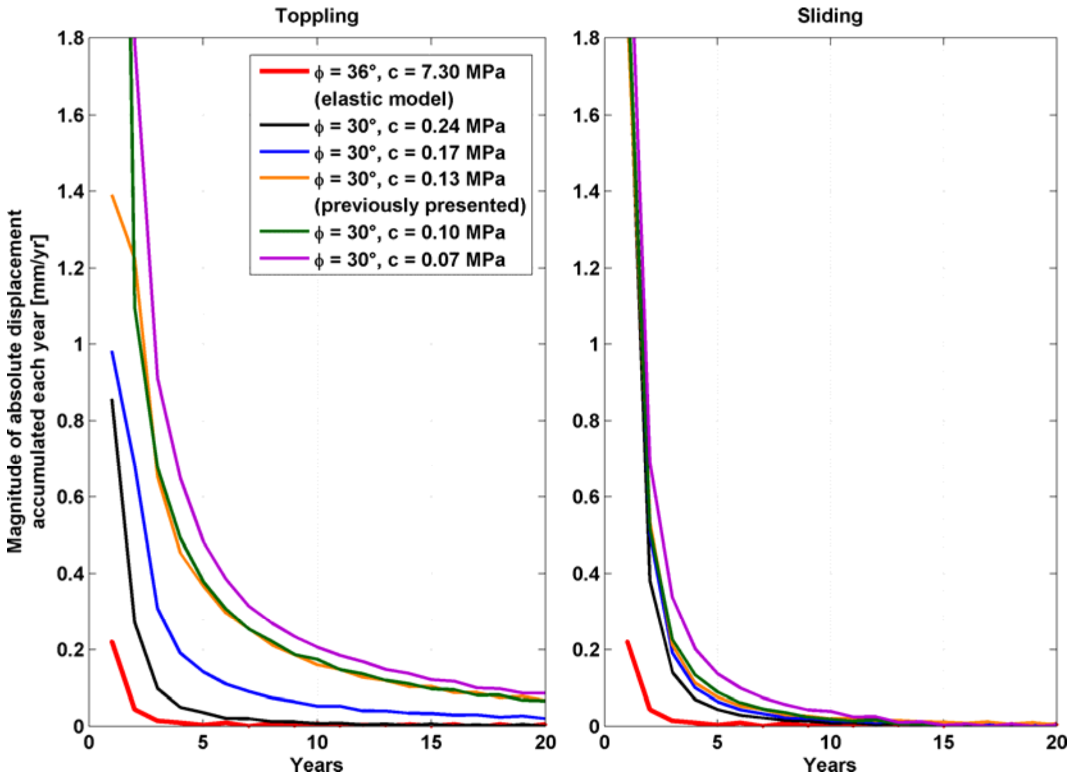

Figure 5.8: Temporal evolution of absolute displacement rate at a monitoring point 40 m below the top of the instability (Point A in Figure 5.4a and Figure 5.6a). Displacement rates are shown for both toppling and sliding kinematics as well as for different strength properties. Rates decay during successive cycling, especially within the first 3 to 5 years. For equal strengths, toppling maintains higher displacement rates after 20 years.

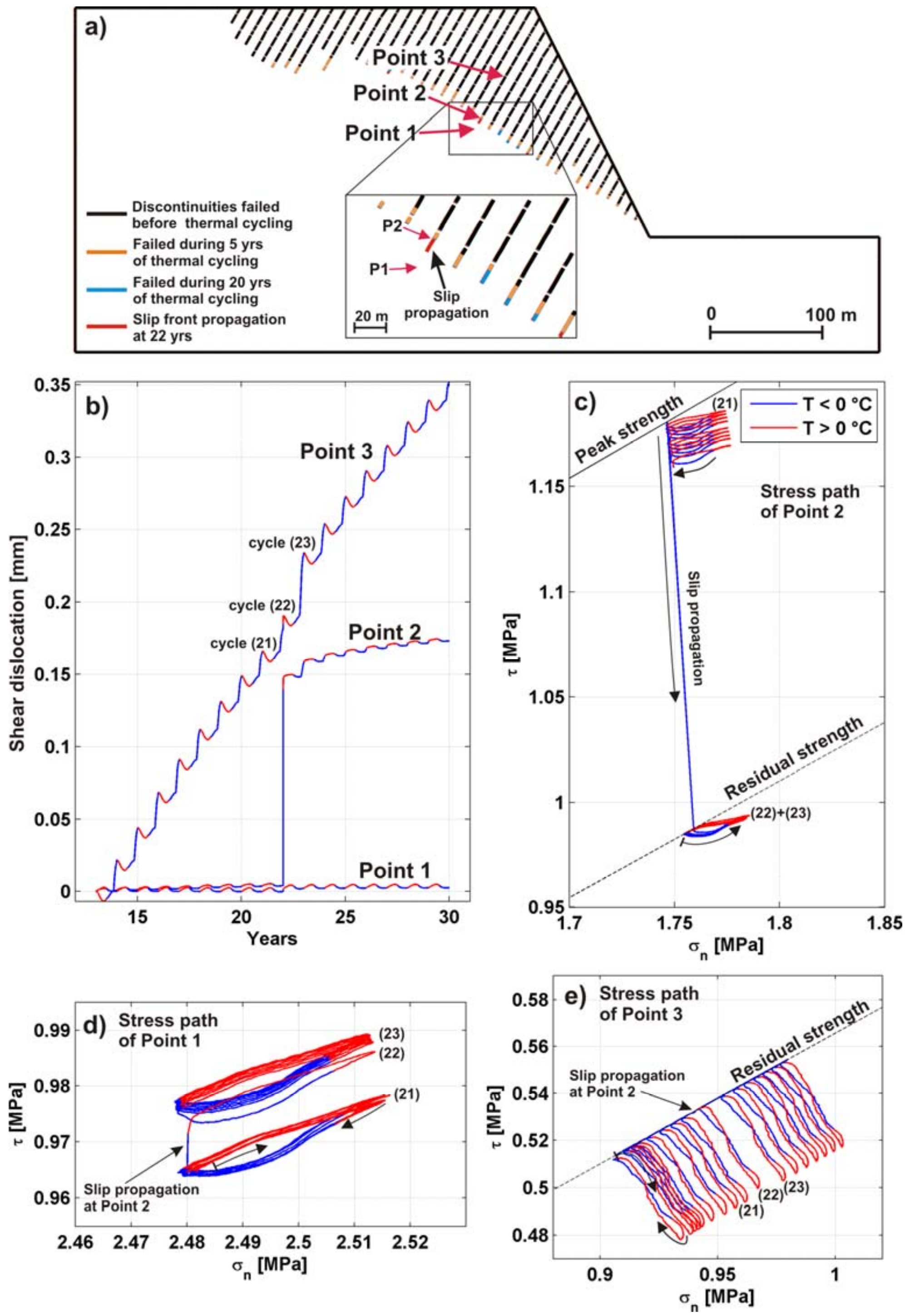

Figure 5.9: a) Model results including slip-weakening discontinuity behavior. After 22 years of TM cycling, the peak strength at Point 2 was reached, which produced an abrupt sliding event with ~0.15 mm slip. Stresses instantaneously dropped to residual strength, which led to stress redistribution within the entire slope and caused propagation of the slip front at other discontinuities (shown in red). b) Dislocation histories at Points 1, 2 and 3. c) Stress path of Point 2 showing the stress drop at 22 years of cycling. d) Stress path of Point 1, which lies below the failure limit. A compliant response is induced through stress redistribution after the slip event at Point 2. e) Stress path of Point 3, which was already at the failure limit through gravitational loading alone. The slip event at Point 2 results in an anomalous step in both shear and normal stress. The cycle numbers (21), (22), and (23) help to track the stress path shortly before and after the slip event.

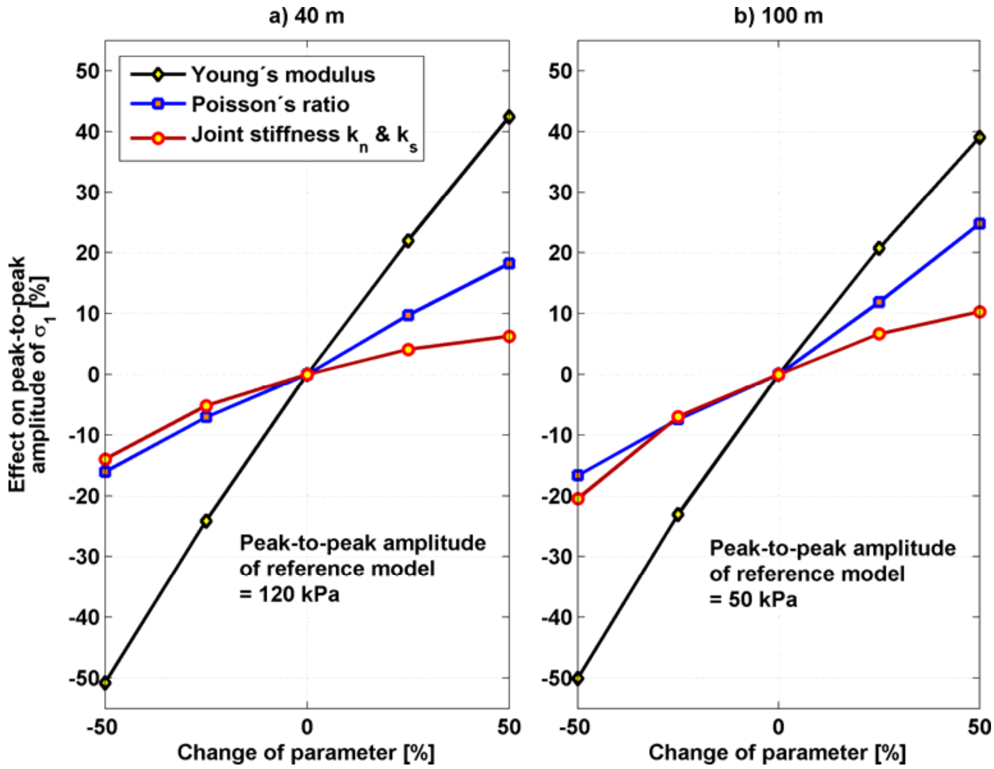

Figure 5.10: a) Effect of varying elastic parameters on the predicted TM-induced stress cycle amplitude at a point at 40 m depth (Point A). The relative change (in percent) of peak-to-peak amplitude of the maximum principal stress component (σ_1) is presented in comparison to a reference model, which is shown in Figure 5.3. Also indicated is the peak-to-peak amplitude of stress fluctuations in the reference model. The values of Young's modulus, Poison's ratio, and joint normal stiffness (k_n) and shear stiffness (k_s) were changed between -50% and +50% of the values given in Table 5.1. The ratio of k_n to k_s was kept constant. Strength parameters were set sufficiently high to avoid failure so the model is purely elastic, as in Figure 5.3. b) Same as in a) for a point at 100 m depth.

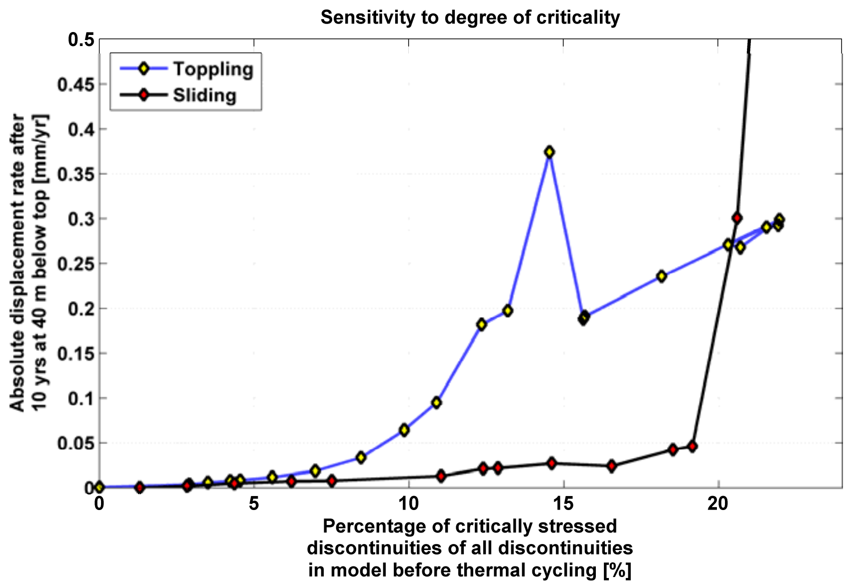

Figure 5.11: TM-induced displacement rates at Point A in Figure 5.4 after 6 years of cycling versus the amount of critically stressed discontinuities in the models. Displacement rates correspond to the absolute displacement accumulated over one year (i.e. during cycle number six).

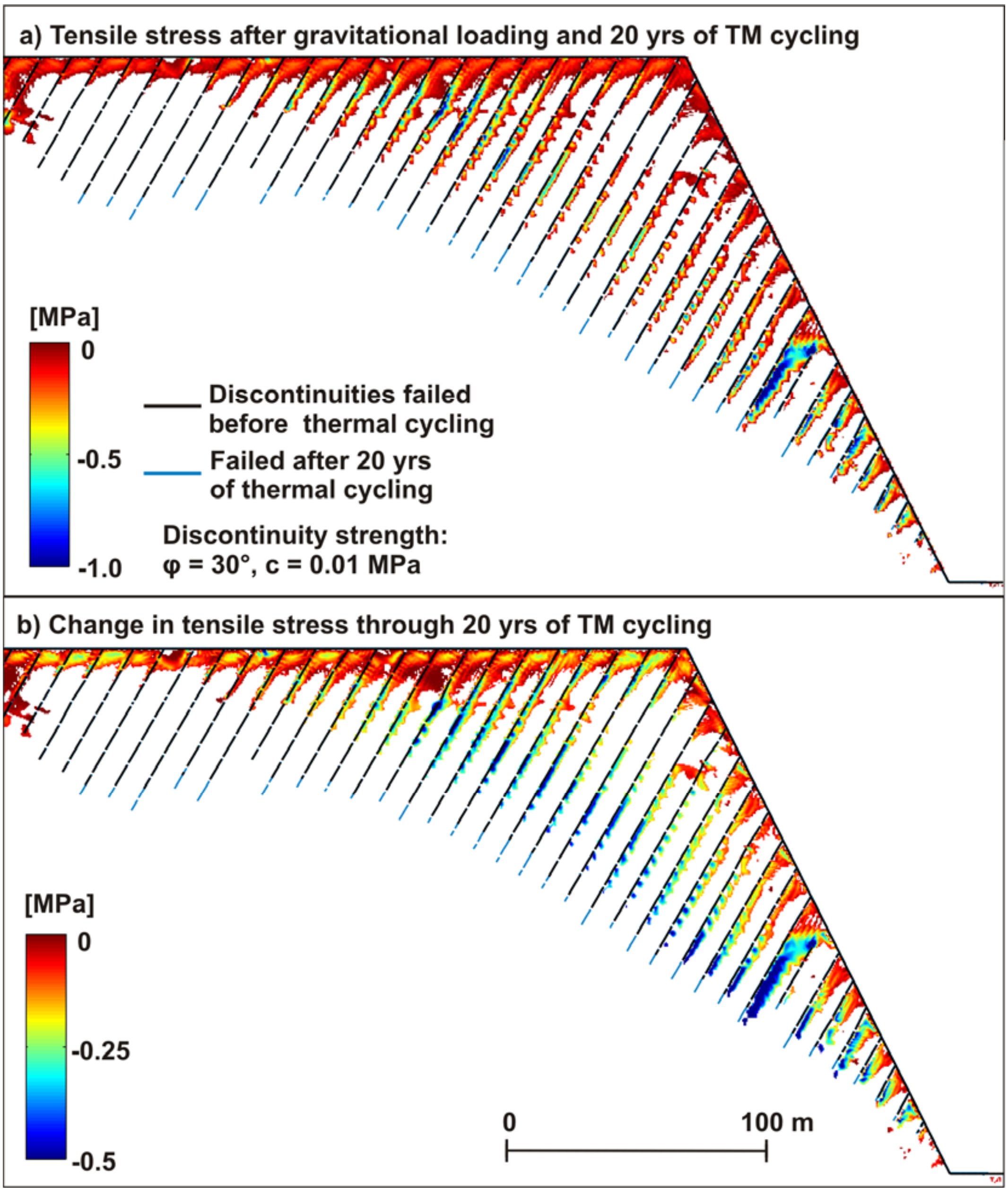

Figure 5.12: a) Maximum tensile stress component (i.e. most negative) developed in toppling slabs in response to gravitational equilibration followed by 20 years of TM cycling for a model with relatively low-strength discontinuities ($\varphi = 30°$, $c = 10$ kPa). Tensile stresses as larger as 1 MPa develop on the upper side of the toppling slabs due to flexure; no compressive stresses are shown. b) Same as in a) but with the gravitational component of the tensile stress removed (i.e. the gravitational stress field was subtracted from that resulting from gravitational loading and 20 years of TM cycling). Twenty years of thermal cycling accounts for 0.5 MPa of the 1.0 MPa stress developed in a).

6. THERMO-MECHANICAL FORCING OF DEEP ROCK SLOPE DEFORMATION – PART II: THE RANDA ROCK SLOPE INSTABILITY

Gischig, V., Moore, J.R., Evans, K.F., Amann, F. and Loew, S.

Submitted to *Journal of Geophysical Research*

25 February 2011

Abstract: Deformation monitoring between 2003 and 2011 at the rock slope instability above Randa (Switzerland) has revealed an intriguing seasonal trend. Relative displacement rates across active fractures increase when near-surface rock temperatures drop in fall and decrease after snowmelt as temperatures rise. This temporal pattern was observed with different monitoring systems at the ground surface and at depths up to 68 m, and represents the global instability behavior. In this paper, the second of two companion pieces, we interpret this seasonal deformation trend as being controlled by thermo-mechanical (TM) effects driven by near-surface temperature cycles. While Part I of this work demonstrated in a conceptual manner how TM effects can drive deep rock slope deformation and progressive failure, we present here in Part II a case study where temperature-controlled deformation trends were observed in a natural setting. A 2D discrete-element numerical model is presented, which allows failure along discontinuities and successfully represents observed kinematics of the Randa instability. Implementing simplified ground surface temperature forcing, model results were able to reproduce the observed deformation pattern, and TM-induced displacement rates and seasonal amplitudes are of the same order of magnitude as measured values. Model results, however, exhibit spatial variation in displacement onset times, while field measurements showed more synchronous change. Additional heat transfer mechanisms, such as crack ventilation, likely create deviations from the purely transient-conductive temperature field modeled. We suggest that TM effects are especially important at Randa due to the absence of significant groundwater within the unstable rock mass.

6.1 Introduction

The role of ambient temperature cycles as a driving mechanism of large rock slope instabilities is often considered negligible. While thermo-elastic stresses in the near-surface thermal active layer have been shown to cause seasonal movement patterns (e.g. Mufundirwa et al., 2010; Gunzburger et al., 2005; Krähenbühl, 2004), only a few cases are reported where thermal effects were conclusively proven to drive deeper instability deformation. One example is the Checkerboard Creek landslide in Canada, for which Watson et al. (2004) demonstrated that thermo-elastic induced stress changes at shallow depth can force deformation at greater depth. Borehole extensometer data from 26 m showed increased displacement rates during cold periods, which were related to thermo-elastic contraction in the upper active layer. The discontinuous nature of the slope instability was suggested to play a key role in allowing these movements.

In Part I of this study (Gischig et al., this issue), we investigated thermo-mechanical (TM) effects on rock slope deformation induced by surface temperature cycles with help of simplified numerical models. The models implemented both purely elastic behavior (no failure) and elastic behavior combined with failure allowed along prescribed discontinuities. This conceptual study aimed to support interpretation of seasonal deformation trends observed in monitoring data from the Randa instability in the southern Swiss Alps. Therefore, the two kinematic failure modes controlling the Randa instability, namely translational sliding and toppling, were investigated. Our models demonstrated that the thermo-elastic reaction of near-surface bedrock subject to temperature cycling induces stress changes at depths below the thermal active layer as a result of strong topography. If discontinuities at depth are critically stressed, these stress changes can induce irreversible slip. Subsequent stress redistribution due to slip along discontinuities leads to increasing stresses at slip fronts and can eventually result in slip front propagation. Thus, TM-induced stress changes can drive progressive failure of an unstable rock slope. The magnitude of the effect largely depends on the elastic properties of the medium, the amount of critically stressed discontinuities within the system, and on the assumed post-failure constitutive behavior of discontinuities (e.g. slip-weakening).

In this paper, we present the case study of the Randa rock slope instability, where up to eight years of monitoring data from both the surface and boreholes suggest that thermal effects control ongoing slope displacements. We first introduce the current Randa instability and summarize results from past investigations at the site. We then describe relevant details of the deployed monitoring system and present data from 2004 – 2011. Deformation time series are interpreted in combination with insights gained from the conceptual study presented in Part I and with the help of site-specific numerical models. In the final section, we discuss the role of TM effects as a driving mechanism of progressive rock slope failure.

6.2 Randa rock slope instability

The current rock slope instability above the village of Randa in the southern Swiss Alps (Figure 6.1) is the legacy of two catastrophic rockslides in 1991 that released in total ~30 million m^3 of crystalline rock (Schindler et al., 1993). About 22.5 million m^3 of orthogneiss that forms the lower part of the present scarp failed in April 1991, followed by retrogressive failure of ~7 million m^3 of the overlying paragneiss and schists in May 1991 (Sartori et al., 2003). The resulting failure surface forms an 800 m high cliff reaching to 2300 m a.s.l., which is composed of a sub-vertical orthogneiss face below 1900 m a.s.l. overlain by paragneiss and schists (Figure 6.1). Geodetic monitoring initiated after these failures revealed that a sizeable rock mass remains unstable and currently moves at a rate of more than 30 mm/yr (Jaboyedoff et al., 2004). The volume of this instability was recently estimated to be ~6 million m^3 (Sartori et al., 2003; Gischig et al., 2009).

In 2000, a collaborative research program was initiated with the goal of understanding the internal structure and kinematics of the unstable rock mass, as well as investigating temporal deformation trends. A comprehensive, multi-component monitoring system was installed, creating a so-called *in situ* laboratory (Figure 6.2a). Monitoring components and data will be described in detail in Section 6.3. Geological, geotechnical, and geophysical investigations were performed to create and constrain 3D geological, structural and kinematic models of the unstable slope (Willenberg et al., 2008a/b). Geological mapping and structural characterization yielded a trace map of large-scale discontinuities, i.e. faults and fracture zones with persistence greater than 15 m. Fracture imaging and radar logs in three boreholes, two of 50 m and one of 120 m depth, combined with surface radar surveys locally extended the mapping of structures to 3D (Heincke et al., 2005, Spillmann et al., 2007a, Willenberg et al., 2008a). Seismic refraction tomography helped delineate a zone of lower rock mass quality in the shallow subsurface (Heincke et al., 2006). Periodic measurement of inclinometer and extensometer casing cemented in the boreholes yielded profiles of differential displacement and rotation. The results showed that slip was localized at highly-persistent, large-scale discontinuities that cut the borehole, and yielded estimates of the dislocation vectors across these discontinuities. Observed deformation patterns were best interpreted as toppling, with sliding along discontinuities dipping into the slope and block rotation in between. Thus, the internal structure and deformation kinematics in the upper part of the instability to a depth of ~120 m were constrained (Figure 6.1b) (Willenberg et al., 2008a/b). It should be noted that no evidence of persistent, down-slope dipping discontinuities was evident from these investigations.

Research activities conducted between 2000 and 2005 were mostly limited to the accessible area at the top of the instability, while information remained sparse for the inaccessible failure surface. This limitation was subsequently alleviated by applying remote-sensing techniques, including ground-based radar interferometry (GB-DInSAR), laser scanning (LiDAR), photogrammetry, and additional geodetic measurements to resolve structures and kinematics in the inaccessible areas. GB-DInSAR displacement maps confirmed the toppling behavior in the uppermost portion of the instability (Gischig et al., 2009). Additionally, the lower boundary of the instability, formed by a persistent basal sliding surface, and a lateral release plane bounding the instability to the south were identified. Structural analysis of LiDAR and orthophoto data helped complete the structural and kinematic models (Gischig et al., 2011). Two kinematic failure modes were shown to control instability movement: toppling occurs in the upper portion above 2150 m, while translational sliding is dominant in the lower portion of the unstable rock mass. This sliding occurs on a set of discontinuities which dip down-slope and could be observed in the scarp, but were seemingly absent in the upper portion of the rock mass investigated in previous phases. 2D numerical models of the discontinuous rock mass presented in the next section confirmed the feasibility of this kinematic model.

6.3 Monitoring system and components

A comprehensive monitoring program was initiated at the Randa rock slope to record temporal trends in instability behavior (Willenberg et al., 2002). An overview of the current monitoring system is shown in Figure 6.2a. Two crack extensometers (labeled Z9 and Z10) measure normal displacement across tension fractures at the ground surface. Three sub-vertical boreholes were drilled to depths of 120 and 50 m (labeled sb120, sb50n, and sb50s). The 50 m holes were equipped with inclinometer casing and the 120 m hole with inclinometer/extensometer casing. Between 2001 and 2008, bi-annual borehole inclinometer and extensometer surveys were performed to detect and measure dislocation along discontinuities at depth (Figure 6.2b). Two in-place inclinometers were installed in borehole sb120 in 2003, spanning active discontinuities that dip into the slope at ~45° and show normal faulting with a minor opening component. These vertical inclinometers measure tilt along two orthogonal axes. Multiplying tilt in radians by the instrument base-length of 1.87 m gives the horizontal component of the dislocation vector of the lower block with respect to the upper block. Pore pressure is measured at the bottom of each borehole with piezometers isolated in slotted increments. Crack extensometers, in-place inclinometers, and piezometers are vibrating-wire (VW) type sensors and include embedded temperature sensors for thermal correction. The latter data provide an approximate record of air temperature around the instruments both at the ground surface as well as in the borehole. However, thermal equilibrium may not always be ensured between the borehole and surrounding rock.

A vertical thermocouple array was installed in shallow bedrock in 2008 to obtain accurate information about near-surface thermal conditions. The array consists of nine sensors distributed in a 4 m deep borehole. The spacing between sensors increases from 20 mm at the surface to 2 m at the bottom of the borehole, providing optimal data coverage where temperature changes are strongest. The sensors were embedded in grout that has a similar thermal conductivity to the surrounding rock. Relevant meteorological parameters at the site, namely air temperature, barometric pressure, relative humidity, and rainfall, have been recorded since 2008. These and the VW sensors are recorded by a Campbell Scientific CR10X data logger. The sampling rate for all sensors was 60 min before 2008, and 30 min afterwards.

A second monitoring system based on fiber optic (FO) strain sensors was installed at the site in 2008 (Moore et al., 2010). This system is able to record measurements with an accuracy of a few microstrain (displacements of micrometers over a 1 m base-length) at a sampling rate of 100 Hz. Two 0.8 m base-length FO extensometers were installed at the ground surface across the opening tension fractures, co-located with VW extensometers. In borehole sb120, six 1.5 m base-length FO axial extensometers were installed across steeply-dipping fractures at three depths to measure the vertical component of dislocation (Figure 6.2b); the instruments were installed in pairs for redundancy. The FO monitoring system thus provides independent and complementary deformation data to that from the VW sensors.

The monitoring systems described above provide information only about relative displacements across active discontinuities. To increase spatial data coverage, a 3D local geodetic network was installed in 2008 and surveyed monthly over the course of one year. This network was tied into the larger, valley-scale geodetic network surveyed since 1995 (Jaboyedoff et al., 2004). The absolute displacement of reflectors in the local network could thus be determined. Distances and angles within the local network of 34 retro-reflectors were measured with a Leica total-station (type TPS1201). In total, 11 surveys were performed at intervals of 30 – 45 days. The network geometry and measurement results are described by Gischig et al., (2011). In addition to the magnitude and direction of displacement vectors, time series absolute displacement data were obtained for all reflector points with resolvable movement.

6.4 Monitoring data

Figure 6.3 presents four years of monitoring data measured prior to 2008. All time series except piezometric pressure were low-pass filtered to remove signals with periods less than 3 days. Figure 6.3a and b show data from the VW extensometers spanning tension fractures Z9 and Z10, together with temperature from their built-in sensors. Measurements show that these two fractures are opening at an average long-term rate of about 2 mm/yr. A considerable annual signal can be seen superimposed on the linear trends, with opening strongly enhanced in winter and reduced after snowmelt so that even some fracture closure occurs in summer. The amplitude of this signal is stronger at fracture Z10, which is snow-free throughout most of the winter. The temperature record at this sensor shows a nearly sinusoidal annual trend, as opposed to the temperature at fracture Z9, which is steady at 0°C when covered by snow. Temperatures fall below zero in autumn and then rebound towards zero when the snowpack is thick enough to insulate the ground from air temperature variations.

Figure 6.3c shows horizontal relative displacement between the ends of the in-place inclinometer at 68 m depth. This is equivalent to the horizontal component of relative displacement across the monitored fracture. Displacement increases in a nearly linear trend at an average rate of about 1.8 mm/yr. However, a slight annual signal is also superimposed with acceleration to rates up to ~2.7 mm/yr in winter and deceleration to ~0.8 mm/yr in summer. This variation becomes more obvious in the de-trended time series shown in Figure 6.3d. Periods when the ground temperature is above or below zero, as inferred from the temperature sensor in extensometer Z10, are shown as red or blue, respectively. The displacement rate increases sharply as soon as the temperature falls below 0 °C and decreases gradually after snowmelt. It should be noted that temperature sensors in the borehole inclinometer show constant temperature throughout the entire measurement period.

Piezometric pressure at the bottom of boreholes sb50s and sb120 is shown in Figure 6.3e. Pressure data from sb50n are not available as the sensor has been malfunctioning since installation. Pressure in borehole sb120 is nearly constant at a value corresponding to the air pressure at the altitude of the sensor, indicating that the water table is below 120 m depth. However, pressure measurements in borehole sb50s indicate the existence of a groundwater table at ~3 m above the sensor (i.e. at 47 m depth). The water column increases to 4 m after the onset of snowmelt, then slowly decays back to 3 m over the course of the year. Borehole sb50s is located only ~50 m distant from the dry borehole sb120. Therefore, it is likely that water in sb50s is part of a localized, perched groundwater body. The onset of snowmelt, indicated by the piezometer record from sb50s does not correlate with the onset of increased deformation rates in inclinometer data, nor does it coincide with the onset time of decreased rates (Figure 6.3d). Snowmelt usually begins around April, whereas the onset of increased movements occurs around November.

With the addition of new FO sensors in 2008 in borehole sb120, the inclinometer previously at 68 m was moved to an active discontinuity at 12 m depth. Data from this instrument since relocation are shown in Figure 6.4a, and with the linear trend removed in Figure 6.4b. Data from the FO extensometer at 38 m depth are also shown on both plots. Although FO and inclinometer sensors measure different relative displacement components across fractures at different depths, the signals mimic each other well showing a maximum displacement rate during winter and a minimum rate in summer.

The vertical temperature profile from the shallow bedrock array during the same time period is presented in Figure 6.4c, where sensor data are presented as a color-coded time series that is a function of both depth and time. Rock surface temperature, measured at the top of the sensor array, as well as ambient air temperature are shown in Figure 6.4d. Temperatures at 4 m depth range between 2.5 °C in April to 10 °C in September. The ground surface temperature rapidly falls to 0 °C after first snowfall, and then slowly decreases to a minimum value of about -0.5 °C in January.

Contemporary inclinometer and temperature data show a similar relationship as observed for the previous inclinometer record from 68 m depth (compare to Figure 6.3). Displacement rates increase when the rock surface rapidly cools at the time of first snowfall and decrease after snowmelt as the rock warms. In fall of 2008 and 2009, the first cooling events correlate with a sudden increase of displacement rate (see blue arrows in Figure 6.4b). They are followed by a short-lived return to summer displacement rates and then gradually increase to higher rates over several weeks. Displacement rates decrease again as soon as the rock surface begins to warm after snowmelt. A sharp decrease to the displacement rates prevailing in summer occurs as soon as the snow has disappeared and rock can efficiently warm (see red arrows in Figure 6.4b). Thus, comparison between rock surface temperature and displacement measured at 12 m depth shows that displacement rates react to temperature changes not only on an annual basis, but also within shorter time intervals. Piezometric pressure data from sb50s (Figure 6.4e) indicate the onset of snowmelt as a sharp increase of water pressure. The record of daily precipitation since June 2009 is also shown in Figure 6.4e. Times of maximum water pressure or heavy rain fall do not correlate with significant acceleration phases in inclinometer data.

Note that in contrast to the sensor position at 68 m, the built-in temperature sensor at 12 m depth measured a slight annual signal of about 0.5 °C amplitude. Calculations attempting to fit temperature data from the 4 m deep rock array using a thermal diffusivity of about 1.9E-6 m^2/s showed that this amplitude is consistent with thermal wave penetration to 12 m depth. However, the direct temperature influence on the instrument is too small to create the observed inclinometer signal.

Data from the FO sensor shows several abrupt steps, which do not correlate with signals from the inclinometer (Figure 6.4b). The largest step occurs in fall 2009 and denotes rapid axial extension of more than 20 μm. Such transient events interrupting the long-term shortening rate are commonly observed on all FO sensors, however, more often in winter when displacement rates are higher. The origin of these events is still unclear, though they have been interpreted to result from intermittent activation and sliding on nearby discontinuities (Moore et al., 2010).

Absolute displacement time histories for several reflectors in the local geodetic network between 2008 and 2009 are shown in Figure 6.5a, and the network geometry is shown in Figure 6.5b. Only points having a complete set of 11 measurements are presented. The measurement standard error is estimated to be ±2.5 mm. The total displacement of these points accumulated during the measurement period is 8 – 12 mm. Displacements between subsequent measurements are too small to be considered significant at the given error margin. The trends, however, are consistent for all points: most of the observed displacement occurs in winter (7 – 10 mm), while displacements in summer cannot be considered significant. Geodetic measurements thus support observations of an annual displacement trend from inclinometer and FO deformation monitoring data.

6.5 Interpretation of monitoring data

In situ monitoring at the Randa rock slope has revealed a clear seasonal pattern of changing deformation rates across active discontinuities at depth. An abrupt change to higher rates occurs around the time of first snowfall as the rock rapidly cools. A decrease of displacement rates occurs after the onset of snowmelt when the rock warms. Significant variations in deformation rate do not correlate with heavy rainfall events or with increased water pressure after snowmelt. Instead, near-surface rock temperatures seem to control the temporal deformation pattern, as measured by independent monitoring techniques at the ground surface and at depth. We conclude that the observed temporal deformation trend is not a local effect but represents the global behavior of the entire monitored rock mass.

Deformation signals related to surface temperature changes have been previously reported and related to thermo-elastic (Wyatt et al., 1988; Bonaccorso et al., 1999) or freezing effects (Wegman & Gudmunsson, 1999; Matsuoka, 2001). Different authors also discuss the role of temperature changes in driving movements of single blocks (Gunzburger et al., 2005) or deformation of shallow instabilities in brittle rock (Krähenbühl, 2004). Vargas et al. (2009) further suggest that strong temperature changes can induce fracture propagation and lead to rockfall, and that thermal cycling can contribute to fatigue at fracture tips. Few studies report such effects at large slope instabilities reaching below the thermal active layer. One notable case is the Checkerboard Creek landslide in Canada described by Watson et al. (2004). Deformation rates at 26 m depth show a seasonal trend comparable to that observed in our monitoring data, with acceleration during winter and deceleration in summer. A rather exotic case is also described by Bonaccorso et al. (2010) for a landslide at a volcanic crater rim subject to heating and cooling through changing fumarole activity. Measured displacement patterns were explained by thermo-elastic contraction and expansion of the entire landslide body, while a portion of the downhill displacement was shown to be irreversible.

In our case at Randa, seasonal opening and closing of surface tension fractures is readily explained by direct thermo-elastic expansion and contraction of near-surface rock blocks. However, seasonal deformation trends at depths where temperatures are essentially constant can only be interpreted in association with induced thermo-mechanical effects, as investigated with conceptual models in Part I of this study (Gischig et al. this issue). These simplified models revealed how surface temperature cycles induce strain and stress signals at depths below the thermal active layer due to thermo-mechanical stress transfer and topography. If a sufficient number of critically stressed discontinuities are present within the rock mass, TM-induced stresses promote slip along discontinuities and lead to failure propagation at slip fronts. We hypothesize that the temporal behavior of the Randa instability can be interpreted within the framework of TM forcing, and here attempt to apply the findings from the conceptual study to the Randa instability. Two hypotheses explaining the observed signals are presented:

- The annual deformation signal is a purely thermo-elastic reaction of the rock mass to shallow temperature changes in the presence of strong topography. Thermo-elastic induced strain signals at depth are superimposed on an ambient, underlying displacement trend driven by some other process, such as stress corrosion. Thermo-elastic induced stress changes at depth are too small to cause failure along discontinuities, but create reversible strain signals modifying the deformation time series.

- Thermo-mechanical induced stress changes at depth, although small in amplitude, are sufficient to promote slip along discontinuities and result in a seasonally variable deformation rate. The effect is irreversible and can be regarded as a mechanism driving time-dependent, progressive rock slope failure.

In the following section we explore both hypotheses through 2D numerical simulations.

6.6 Numerical models

Similar to the conceptual study of TM effects (Gischig et al., this issue), 2D numerical modeling of the Randa instability was performed using the distinct-element software UDEC (Itasca, 2008). Both a purely elastic model and one allowing failure along prescribed discontinuities were calculated. The models were based on results of a previous study at the Randa instability (Gischig et al., 2011), which used analysis of structural data and displacement patterns to create a 2D kinematic model implemented in UDEC. Two kinematic failure modes were identified: toppling at higher altitudes and sliding along a basal rupture surface below. Here we explore the reaction of the Randa instability to seasonal thermal forcing by adopting this kinematic model (including geometry, discontinuity orientations, material and discontinuity properties, and boundary conditions) in a coupled TM mode. The model geometry is presented in Figure 6.6a. As with the conceptual models, zero-displacement boundary conditions were applied at the base, while the sides were horizontally constrained. The mesh size was set to 3 m for the uppermost 20 m of the model, 8 m in deeper portions, and 15 m in the far-field of the region of interest. Implemented rock mass material properties are presented in Table 6.1 and Table 6.2, and are identical to those used in the previous kinematic study (Gischig et al., 2011). Intact rock properties were derived from laboratory tests (Willenberg, 2004), while rock mass properties were estimated using the Geological Strength Index (GSI) approach (Hoek et al., 2002). A Mohr-Coloumb failure criterion including slip-weakening was assigned to the discontinuities. Peak strength values were derived by Gischig et al. (2011) in an attempt to reproduce the observed kinematic behavior at Randa (Table 6.2). Different friction angles, cohesion and tensile strength values were chosen for each of the four discontinuity sets. Thermal diffusivity and the coefficient of thermal expansion were kept the same as in the conceptual models, derived from analysis of *in situ* rock temperatures and literature values (Clauser and Huegens, 1995; Gueguen and Palciauskas, 1994). A sinusoidal temperature time history with a one year period and 20 °C peak-to-peak amplitude was applied to the model surface, as estimated from measured temperature data.

6.6.1 Purely elastic model

Figure 6.6b presents profiles of the peak-to-peak amplitude of thermo-elastic induced horizontal tilt ($\partial u_y/\partial z$) and vertical strain (e_{zz}) predicted by the elastic model at the location of borehole sb120. Also shown are the peak-to-peak amplitudes of horizontal tilt and vertical strain signals measured with in-place inclinometers and FO strain sensors in the same borehole. We note that the predicted thermo-elastic strains and tilts are significantly smaller than the measured signals. Various effects may be included in the model to enhance the magnitude of estimated thermo-elastic strains and tilts at depth, such as lateral temperature variations, material heterogeneities, and 3D topography. However, it is unlikely that including these effects will significantly reduce the observed discrepancy, since the model predictions differ from measured values by several orders of magnitude.

6.6.2 Discontinuum model

The implemented discontinuity distribution is shown in Figure 6.7a, which was based on the geological observations depicted in Figure 6.1b. Block displacements accumulated after 10 years of thermal cycling are also shown in Figure 6.7a. The net displacement at the top of the unstable area is ~100 mm, while only ~5 mm displacement has accumulated at the toe of the instability. Discontinuities that have reached their strength limit solely due to gravitational stress are shown as black lines in Figure 6.7b, whereas those that failed during the subsequent 10 years of TM cycling are indicated as orange lines. Evidently, several additional discontinuities have failed. A number of monitoring locations were chosen in the model to visualize the temporal behavior. These include a tension fracture at the back of the instability (C1), discontinuities at depth that show either toppling or sliding dislocation (D1-3, B1-2, respectively), as well as two points on the ground surface (S1-2).

Figure 6.8a presents the annual temperature cycle applied at the ground surface. Figure 6.8b shows the predicted horizontal relative displacement (analogous to the measured displacement in Figure 6.4a) induced across three neighboring, but different toppling discontinuities: D1, D2, and D3 at 14, 48, and 68 m depth, respectively (Figure 6.7b) (left-lateral shear sense is positive). At all depths, a clear annual trend is visible that is controlled by slip along discontinuities (i.e., not only due to discontinuity compliance). At 14 m depth, the displacement rates changes from negative to positive after the surface temperature has reached a minimum and begins to warm. At 68 m depth, the opposite is observed with an abrupt change to positive displacement rates when the surface temperature is at a maximum and starts cooling. At 48 m, the greatest displacement rates occur predominantly during the negative cycle of surface temperature. TM-induced relative displacements also have consistent long-term rates ranging from 0.2 - 0.8 mm/yr. Although these rates are lower than the 1-2 mm/yr values measured across active discontinuities (Figure 6.4a), they are of a similar order of magnitude. Shear displacements at points B1 and B2 on the basal sliding surface are shown in Figure 6.8c (right-lateral shear sense is negative). An annual variation in relative displacement is present at both locations, superimposed on long-term rates of -0.1 and -0.25 mm/yr at B2 and B1, respectively. For the annual signal, displacement increases and decreases at relatively constant rates with rapid reversals at times when temperature changes from T>0 °C to T<0°C and vice-versa. Thus, the greatest displacement rates (i.e. most negative) along the basal sliding surface occur predominantly in summer, unlike discontinuities at the top of the instability.

Simulated fracture opening at ground surface across the discontinuity that delineates the back of the unstable zone (C1) is shown in Figure 6.8d. The fracture opens at an average rate of about 1.1 mm/yr and exhibits a strong annual signal with amplitude of 1.4 mm, both of which are similar to the ,measured values at tension fractures Z9 and Z10 (see Figure 6.3a). The phase of the predicted annual signal also matches observations, with closure during summer and opening in winter. Time histories of horizontal and vertical absolute displacements predicted by the model at two points on the ground surface (S1, S2) are presented in Figure 6.8e. Long-term displacement rates are consistent at ~6 mm/yr, which is lower than the 14 mm/yr measured at the top of the instability (the absolute maximum of 30 mm/yr being measured at the headscarp). However, these are still within the same order of magnitude, and also well within the error expected for such simulation. The surface monitoring points all show a similar annual signal: for the vertical component displacement rates increase at the beginning of winter, while the horizontal component shows a more gradual rate increase towards the middle of winter. The ratio of vertical to horizontal displacement reveals a plunge angle of about 27°, which matches well with geodetic measurements.

Figure 6.9 shows comparison of measured and modeled annual signals both at the ground surface and at depth. All model results were shifted in time by a constant value which provided best fit between the observed and modeled surface temperatures (Figure 6.9a). Deformation time series were de-trended to highlight annual variations. The amplitude of surface fracture opening matches well between measured data and model results (Figure 6.9b). The measurements, however, lag behind the modeled signal by about 40 days. At depth, the predicted amplitudes of TM-induced signals are of the same order of magnitude as the measured values (Figure 6.9c). Recall that this was not the case for the purely elastic model, where amplitudes were 1 – 2 orders of magnitude below the measured values (Figure 6.6b). Times when displacement rates change in the model vary with depth, and differ by –120 to +40 days from the observed changes. The modeled displacement trend at a surface point matches reasonably well with geodetic measurements (Figure 6.9d), although with a time lag of +90 days. Modeled displacement rates are predominantly higher in winter as observed in all monitoring data.

6.6.3 Discussion of numerical models

Results of discontinuum numerical modeling demonstrate the feasibility of TM effects as a driving mechanism for slope deformation at the Randa instability. Simulated relative and absolute displacement rates are smaller than the measured values but well within the same order of magnitude. Annual variations in displacement rates were induced both at depth and at the ground surface, with modeled amplitudes similar to those measured in the field. Along toppling discontinuities, increased deformation predominantly occurs in early winter and decreases in summer, which is in accordance with monitoring observations. However, predicted times of displacement rate changes did not fully match with field data, which showed a more synchronous behavior across various depths within the toppling rock mass. Model results, on the other hand, exhibited certain spatial variability of displacement onset times. Furthermore, times of increased displacement along the basal sliding surface were found to be opposite of those at the top of the instability. The onset of slip is determined by the time that the stress path touches the failure envelope, which depends on the orientation of discontinuities with respect to the transient stress field. For the basal sliding surface, this occurs in summer, while for the toppling discontinuities slip initiates in early winter. Thus, if TM cycling drives global rock slope failure, times of increased displacement rates are not strictly limited to winter, but higher rates can also occur in summer. The model shows that times when displacement rates change varies spatially and as a function of complex local kinematics.

Assumptions made in the 2D model of the Randa instability include purely conductive heat transport, isotropic and homogenous mechanical and thermal properties, spatially-uniform surface temperature, as well as a strongly simplified applied surface temperature forcing. Deviations from these assumptions may in reality alter the presented results. The surface temperature distribution at Randa is certainly heterogeneous, controlled by both spatially varying insolation due to the changes in aspect and altitude, as well as non-uniform snow cover in winter. While the top of the instability is covered with snow throughout the winter, the steep failure surface is largely snow free and experiences different annual temperature variations. As shown by Berger (1975), lateral temperature variations can also create thermo-elastic strain at depth. Thus, spatially-homogeneous temperature forcing used in our models may underestimate the true thermo-elastic strains. Furthermore, the real temperature field appears to be influenced by advective disturbances, such as temporary inflow of water and ventilation of air in deep fractures (Moore et al., in preparation; Weeks et al., 2001). Given the large portion of voids within the disturbed, unstable rock mass (up to 17% predicted by Heincke et al., 2006) such processes are likely to be abundant at the instability.

Advective thermal disturbances generally have a cooling effect at depth. The resulting contraction affecting discontinuity surfaces may result in reduction of normal stress and thus an enhancement of TM-induced slip. Furthermore, the slope has a strong 3D topography. Since TM effects largely depend on the presence of topography, some error due to our 2D approximation is expected. Anisotropy and heterogeneity of rock properties, in addition to varying surface temperature, are also expected to contribute further heterogeneity of the TM-induced stress field (Harrison, 1976). We believe that simplifications made in our model generally tend to underestimate the efficiency of TM effects. One additional factor not considered in our models, and which may reduce TM-induced strains at depth, is a contrast in compliance between the uppermost meters of the rock mass (where temperatures fluctuate) and the underlying medium. Fracture compliance decreases with normal stress (Zangerl et al., 2008; Goodman et al., 1968). Thus, higher compliance can be expected at shallow depths where normal stresses are small and the rock is more weathered. Such a layer of low compliance near the surface would tend to attenuate strains transmitted downwards.

As shown with conceptual models, TM effects depend strongly on rock mass mechanical properties, such as discontinuity strength and material stiffness. Strength influences the amount of critically stressed discontinuities within the model ready to slip through small stress changes. Elastic properties determine the efficiency of stress transfer to depth. However, changes in these parameters may not only influence TM effects, but can also change the kinematic behavior of the modeled instability (Sjöberg, 2000). In our models of the Randa instability, kinematics involves both sliding and toppling, but the detailed kinematics is complex and also depends on a number of model parameters. Thus, the sensitivity of TM effects to these parameters is strongly non-linear and difficult to quantify. However, results from conceptual models also apply qualitatively to the Randa models. Increasing the elastic modulus (i.e. increasing model stiffness) is expected to enhance TM effects, and changing strength properties to lower values produces more critically stressed discontinuities within the model able to react on TM-induced stresses.

6.7 Discussion

Through both a conceptual study presented in a companion paper, and analysis of monitoring data at the Randa rock slope presented here, we have demonstrated that deep deformation of rock slope instabilities can be driven by irreversible TM effects. Efficient TM forcing of slope failure is promoted by steep topography, stiff rock mass elastic properties, and the presence of critically stressed discontinuities. Reversible thermo-elastic strains extending below the thermal active layer occur wherever competent rock extends to the surface of a slope (Harrison & Herbst, 1977). However, irreversible strains can occur when the slope is already in a near-critical state, i.e. a large number of discontinuities are critically stressed. At the Randa instability this is certainly the case, since the rock mass is currently moving and is therefore expected to contain a large number of critically stressed discontinuities susceptible to small stress changes induced by TM effects.

TM modeling of the Randa study site, allowing slip along discontinuities, was able to reproduce the order of magnitude of measured displacement rates and the amplitude of seasonal variations. However, some aspects of the observed temporal displacement trend could not be reproduced. The measured displacement time series from the ground surface and different depths revealed spatially synchronous changes in the onset of increased displacement rate for all monitoring points. The modeled displacement time series, however, showed substantial phase shift at different locations (Figure 6.9). Such spatial variation in onset times may be understood as a reflection of the model complexity introduced by the composite kinematic behavior. Since monitoring data show no such phase shift, we assume that additional processes, disregarded in our models, may occur at Randa, which help to synchronize the temporal instability behavior. One candidate may be air ventilation in open tension fractures (Moore et al., 2011, in preparation). In contrast to purely conductive heat transfer as assumed in our model, air convection through open fractures is more efficient at communicating surface temperature changes to depth. As soon as ambient air temperature falls below a threshold value and crack convection is allowed, relatively rapid cooling at depth may decrease normal stress along fractures and initiate TM effects. Enhanced TM effects through air ventilation may also partly explain why modeled displacement rates are about half of the observed values. However, neglecting lateral temperature variations through heterogeneous insolation and snow cover, combined with natural material heterogeneities, may also create discrepancies between the modeled and measured displacement rates and trends.

Incremental damage accumulation induced by cyclic loading (in the present case through temperature changes) resembles the process of cyclic fatigue observed in laboratory experiments and described by many authors (e.g. Attewell and Farmer, 1973; Brown and Hudson, 1974; Scholz and Koczynski, 1979). Similar to the laboratory scale, this meso-scale fatigue process involves irreversible slip on pre-existing discontinuities, as well as propagation of fractures by cycling loading. In laboratory experiments, it depends on the maximum applied stress if the sample reaches a quasi-static equilibrium in which it can bear a theoretically infinite number of cycles, or ruptures after a certain amount of cycles (Attewell and Farmer, 1973). Analogous in a rock mass subject to cyclic loading, the degree of criticality dictates whether the rock mass becomes stable in a quasi-static equilibrium, or if it approaches a limit as damage accumulates after which it will fail catastrophically.

Similar to fatigue acting on pre-existing discontinuities, intact rock between fracture tips and at interlocking asperities can be affected by micro-scale damage through stress cycling. The simplified constitutive laws for the discontinuities used in our models dictate that slip occurs only when stress exceeds the specified strength limit. At the micro-scale, however, brittle rock does not only accumulate irreversible damage at rupture, but also at stresses far below the ultimate strength (Bieniawski, 1967). Micro-cracking is commonly thought to initiate at stress levels between 30 – 50% of the unconfined compressive strength (Brace et al., 1966), while coalescence of micro-cracks occurs at about 70 – 90% of the rupture strength (Bieniawski, 1967). Cyclic loading of intact rock at stress levels above the limit required for crack coalescence (e.g. through TM forcing) leads to accumulation of microscopic damage, and to progressive strength degradation (Attewell and Farmer, 1973). Thus, micro-scale cyclic fatigue can additionally contribute to progressive failure of intact rock bridges and interlocking asperities, as also suggested by Vargas et al., (2009). However, at the stress amplitudes and annual period typical for TM effects investigated here (<100 kPa below the active layer), stress corrosion (sometimes referred to as static fatigue) may be equally important and also contribute to progressive failure (Scholz and Koczynski, 1979).

In most case studies reported in literature, water pressure changes due to heavy rainfall or snowmelt influence slope deformation rates to a much greater degree than TM effects, and water pressure variations are now routinely included in slope stability analyses (e.g. Wyllie and Mah, 2004). TM-induced stress changes at depths below the thermal active layer at Randa are estimated to be less than 100 kPa for both shear and normal stress, whereas water pressure heads of only 10 m are sufficient to induce effective stress changes in this range. Given the evidence that TM effects play a predominant role at the Randa instability, the question arises as to why water pressure changes do not affect the deformation rates, as reported at other sites. Pressure data in Figure 6.3 show that the continuous groundwater table is below 120 m depth. Pockets of perched groundwater exist (borehole sb50s), and show maximum pressure changes of about 15 kPa, which are within the range of stress changes expected from TM effects. Water seepage at the 1991 failure surface as observed from field visits and time-lapse photography only occurred within the orthogneiss, whereas no springs occurred in the overlying paragneiss and schists, throughout the year (Alpiger, 2010). It is likely that the unstable rock mass lies entirely above the continuous groundwater table and thus is outside its range of influence. Such groundwater conditions are a consequence of the highly-fractured rock mass and ridge topography of the instability. Water from rainfall and snowmelt drains either as surface run-off or infiltrates rapidly to depths below the unstable volume. We suggest that effects of water pressure are secondary due to the absence of a continuous water table within the unstable rock mass. In contrast to other instabilities controlled by water pressure, TM effects at the Randa instability are not masked by more dominant water pressure effects. Similar hydrogeological conditions may prevail at other sites with strongly fractured slopes, or arid climates. Groundwater conditions within instabilities may also change as damage within the rock mass accumulates. Progressive opening of tension fractures increases hydraulic conductivity of the rock mass and results in lowering of the water table. In consequence, water pressure effects decreases until the rock mass is fully drained (e.g. Amann et al., 2006). Thus, for instabilities initially controlled by water pressure, TM effects may become increasingly important as they approach an advanced stage of progressive failure.

6.8 Summary and conclusion

Through combined analysis of conceptual numerical models (Gischig et al., this issue), deformation monitoring data from the current Randa rock slope instability, as well as site-specific, detailed numerical models, we demonstrate the role of TM effects as an important driving factor of rock slope deformation. The key outcomes of our study are summarized as follows:

- Cyclic thermal expansion and contraction in the shallow subsurface creates stress changes at greater depth (up to 100 m), which can induce slip along discontinuities if these are already close to failure. Subsequent stress redistribution increases stresses at discontinuity slip fronts and can lead to slip front propagation. Thus, TM-induced damage is not limited to shallow bedrock subject to seasonal temperature variations (and the attendant thermo-elastic response), but can penetrate to depths well below the thermal active layer.
- Stress propagation to depth is dependent on the elastic properties of the rock mass, and TM effects become greater for more competent rock. Furthermore, the net TM effect depends on the amount of critically stressed discontinuities within the rock mass, which are sensitive to small stress changes. The closer a slope is to failure, the more efficient TM forcing becomes.
- Discontinuity orientation and location within the rock slope controls the efficiency and onset time of slip induced by TM stress changes. TM effects are thus strongly dependent on rock slope kinematics.
- TM effects are enhanced when discontinuity constitutive behavior includes slip-weakening. Stress redistribution after peak strength failure alters the stress state of surrounding critically stressed

discontinuities, making them more sensitive to TM effects. Including slip-weakening also enhances propagation of discontinuity slip fronts.

- At the current Randa instability, deformation time series data from depths of 12, 38, and 68 m reveal a seasonal deformation trend of increased displacement rates in winter and slower rates in summer. Contrary to most rock slope instabilities, phases of increased displacement rates do not correlate with snowmelt or heavy rainfall, but rather with cooling at the onset of winter.
- Numerical modeling of the Randa instability showed that TM effects are a feasible driving mechanism of slope deformation. Modeled deformation rates match measured values within an order of magnitude, and the amplitudes of annual signals at depth were reproduced well. However, synchronous displacement rate changes observed in field data could only be partly reproduced.
- Due to strong topography and the highly-fractured nature of the rock mass, the groundwater table is low at the Randa instability. We suggest that TM effects are observable because the role of water is minor; TM effects at Randa are not masked by potentially stronger groundwater effects.
- The net TM effect can be interpreted as a meso-scale fatigue process within the rock mass, which involves incremental slip along critically stressed discontinuities, as well as hysteresis driven by periodic TM loading.

Acknowledgements

Geotechnical and borehole monitoring equipment were installed by Stump Foratec AG, who also performed inclinometer and extensometer surveys. Local geodetic measurements were conducted by the group for Geodetic Metrology and Engineering Geodesy at ETH Zurich (Prof. Dr. H. Ingensand). Orthoimages for map views in ArcGIS were prepared by Freddy Xavier Yugsi Molina. This project was funded by the Swiss National Science Foundation (Project No. 200020-112073).

Table 6.1: Intact rock and rock mass properties implemented in UDEC. Intact rock properties (i.e. elastic properties, UCS, friction angle, and cohesion) were estimated from laboratory tests (Willenberg, 2004). Rock mass properties were then determined using the Geological Strength Index (GSI; Hoek et al., 2002)

	Orthogneiss	**Paragneiss**
Intact rock		
Density (kg/m³)	2640	2700
Young's modulus (GPa)	32	21
Poisson's ratio	0.21	0.2
UCS (MPa)	97	69
Rock mass (elastic blocks)		
GSI	75	65
Young's modulus (GPa)	26	14
Thermal properties		
Thermal diffusivity (m²/s)	1.9e-6	1.9e-6
Thermal expansion (1/K)	8e-6	8e-6

Table 6.2: Discontinuity properties for the Mohr-Coulomb constitutive law including slip-weakening used in UDEC. Strength values were derived by Gischig et al. (2011) to reproduce the kinematic behavior of the Randa instability.

	Orthogneiss	**Paragneiss**			
Discontinuities		**F1**	**F2**	**F4**	**F5**
Peak friction angle	46°	31.0°	31.7°	33.6°	35.3°
Peak cohesion (MPa)	8.3	1.2	2.1	4.4	6.5
Peak tensile strength (MPa)	5.2	0.6	1.0	2.1	3.1
Residual friction angle	27°	27°	27°	27°	27°
Residual cohesion (MPa)	0.05	0.02	0.02	0.03	0.03
Residual tensile strength (MPa)	0	0	0	0	0
Joint normal stiffness (GPa/m)	10	10	10	10	10
Joint shear stiffness (GPa/m)	5	5	5	5	5

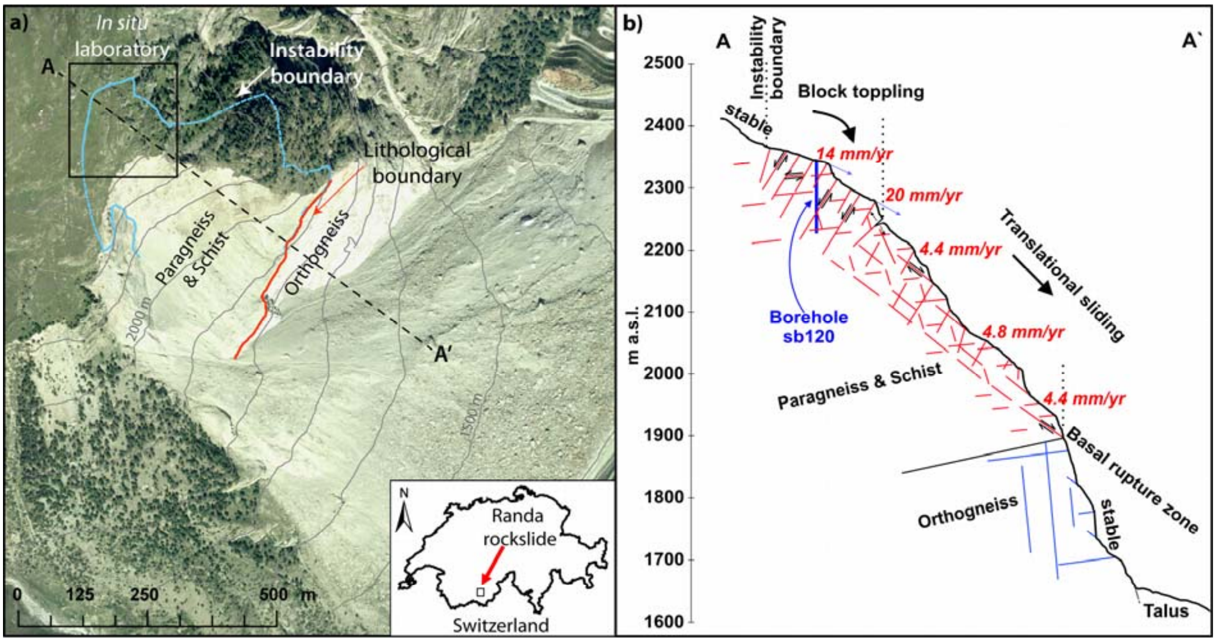

Figure 6.1: a) Overview of the Randa rock slope instability, highlighting the instability boundary. The rectangle delineates the location of the monitoring system presented in Figure 6.2. b) Sketch of structure and kinematics of the current Randa instability along cross-section AA'. The instability is characterized by toppling above 2150 m and translational sliding below along a planar or stepped basal sliding surface. (Willenberg et al., 2008b; Gischig et al., 2011).

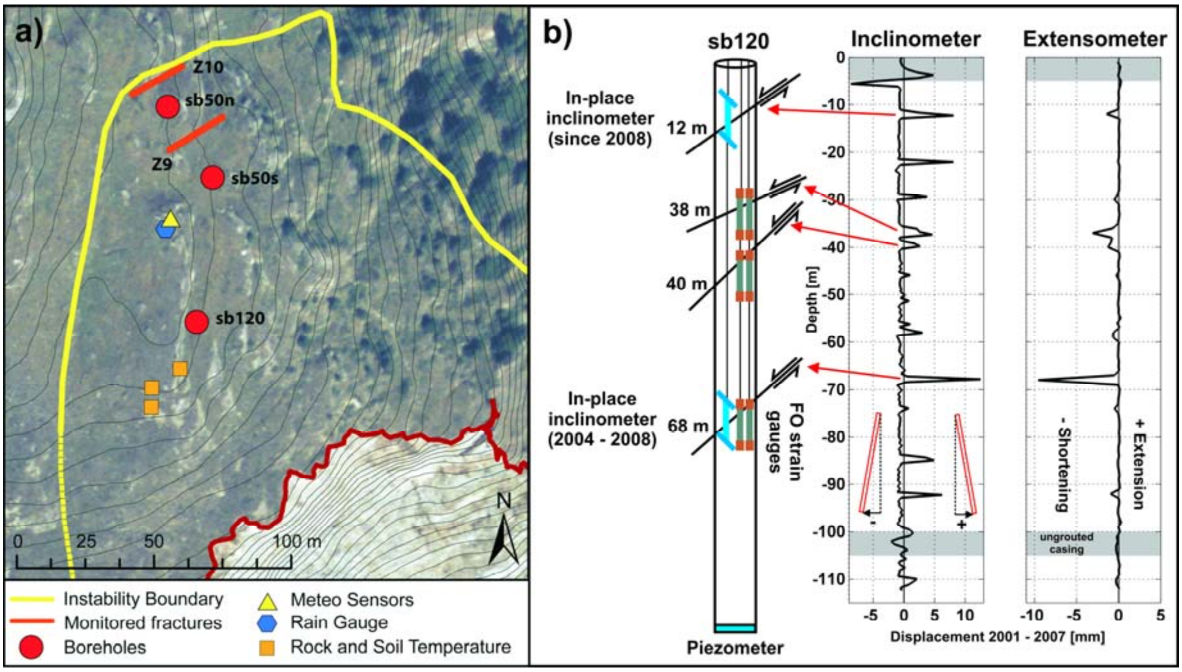

*Figure 6.2: a) Overview of monitoring system at the top of the Randa instability (*in situ *laboratory in Figure 6.1). Boreholes sb120, sb50n, and sb50s extend to depths of 120, 50, and 50 m, respectively. Fractures Z9 and Z10 are active tension cracks monitored with automatic extensometers. b) Sketch of monitoring components within the 120 m deep borehole (sb120). Also shown are data from inclinometer and extensometer surveys showing incremental displacements accumulated between 2000 and 2007. Grey shading indicates sections of the borehole where the inclinometer/extensometer casing is not grouted. Displacements within these sections do not reliably reflect discontinuity dislocation (see Willenberg et al., 2008b, for details).*

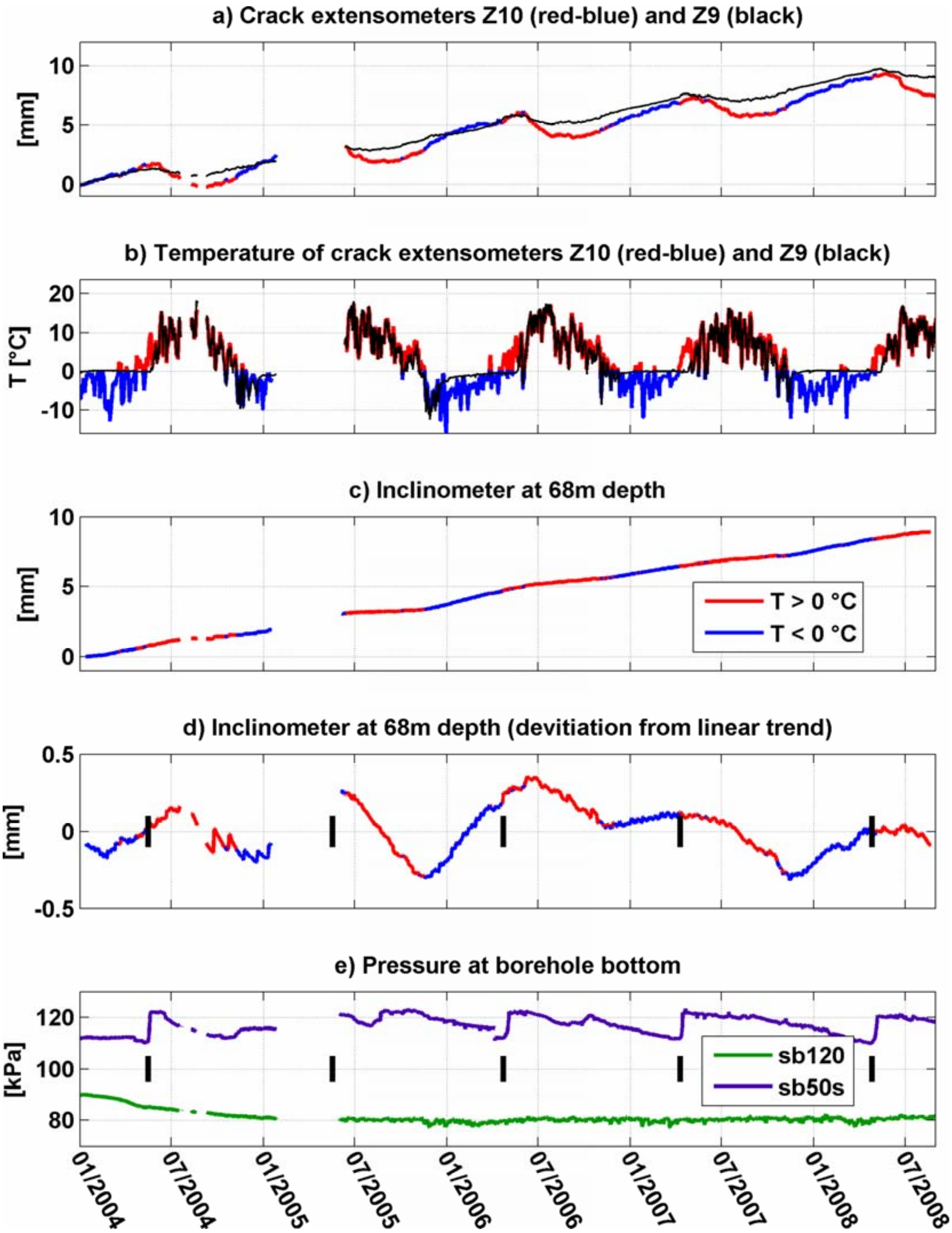

Figure 6.3: a) Crack extensometer data; the record from Z10 is colored according to temperature from its built-in sensor. Red colors are T > 0 °C, blue are T < 0°C. b) Temperature measured at fractures Z10 and Z9. c) Inclinometer data from 68 m depth in borehole sb120 colored according to the temperature at fracture Z10. d) Inclinometer data with linear trend subtracted to emphasize temporal variations in the time series. e) Piezometric pressure from the bottom of borehole sb120 and sb50s. Black bars indicate the onset of snowmelt derived from piezometer data. All data are filtered with a 3 day low-pass filter (except piezometric pressure).

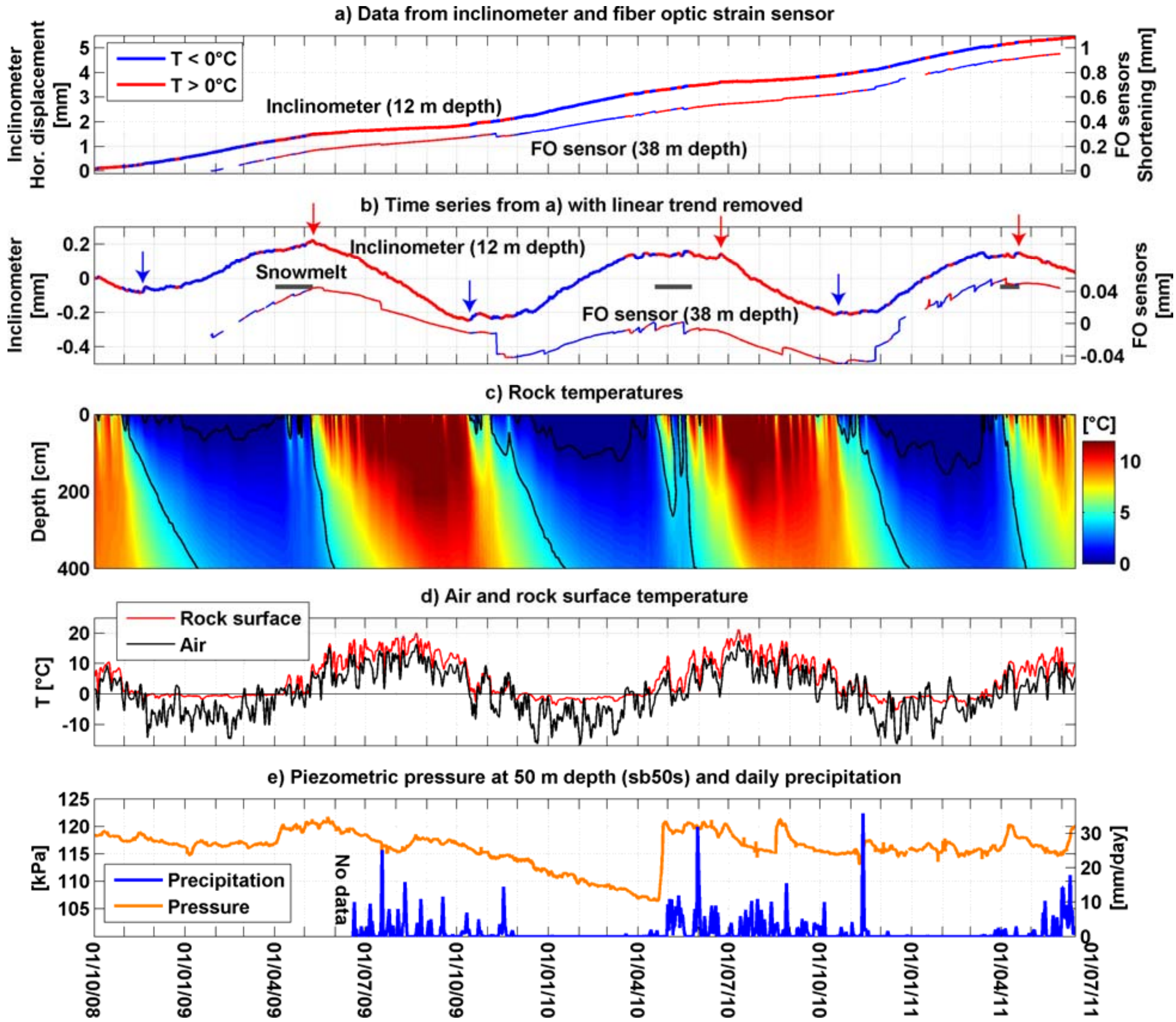

Figure 6.4: a) Inclinometer data from 12 m depth (filtered), and fiber optic data at 38 m depth (unfiltered) in sb120. b) Same as in a) but with linear trend removed. Positive slopes imply a rate increase with respect to the average, negative slopes a rate decrease. c) Color-coded temperature data from all depths of the rock temperature array. Data were interpolated between sensor depths. Also shown are the 0 and 4 °C isotherms. d) Rock surface temperature data from the topmost thermocouple of the rock array, as well as ambient air temperature. All data are filtered with a 3 day low-pass filter. e) Piezometric pressure measured at 50 m depth in borehole sb50s. The sharp pressure increase in spring indicates the onset of snowmelt. Also shown is precipitation since June 2009.

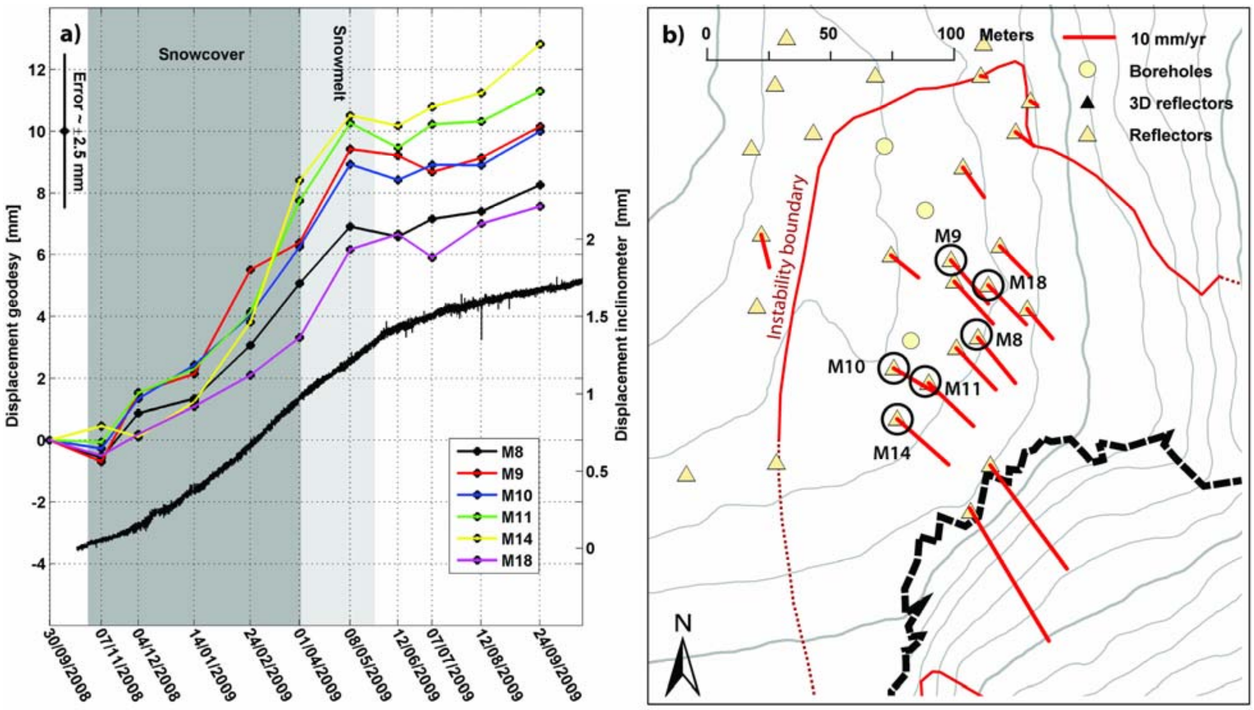

Figure 6.5: a) Time series extracted from 11 geodetic surveys between 2008 and 2009. Measurement error is estimated to be ±2.5 mm. Also included are inclinometer data from 12 m depth for the same time interval. The change in displacement rate is similar for the two complementary measurements. b) Displacement vectors for geodetic points shown on an overview map. The points for which time series data are shown in part a) are indicated with black circles.

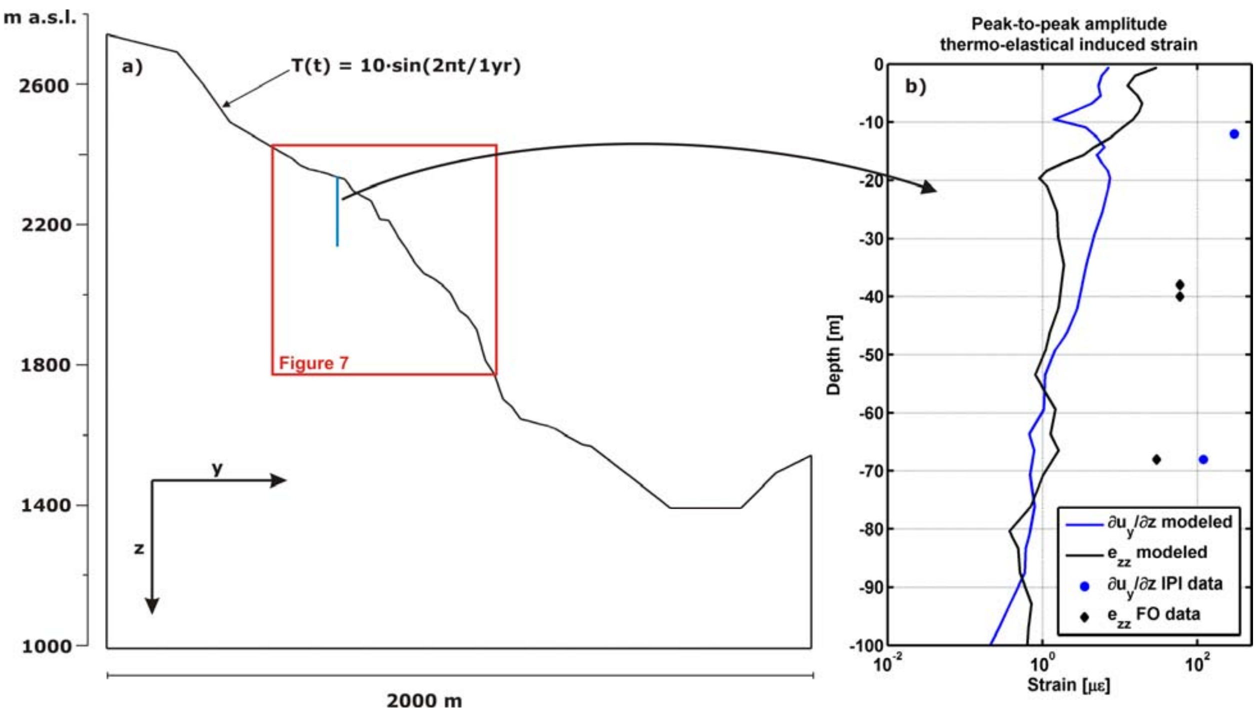

Figure 6.6: a) Model geometry of the Randa rock slope used for both elastic and discontinuum models in UDEC. b) Amplitude of thermo-elastic induced vertical strain and tilt along borehole sb120 for a purely elastic model (solid lines). Modeled amplitudes are 1 – 2 orders of magnitude smaller than the measured signals (points).

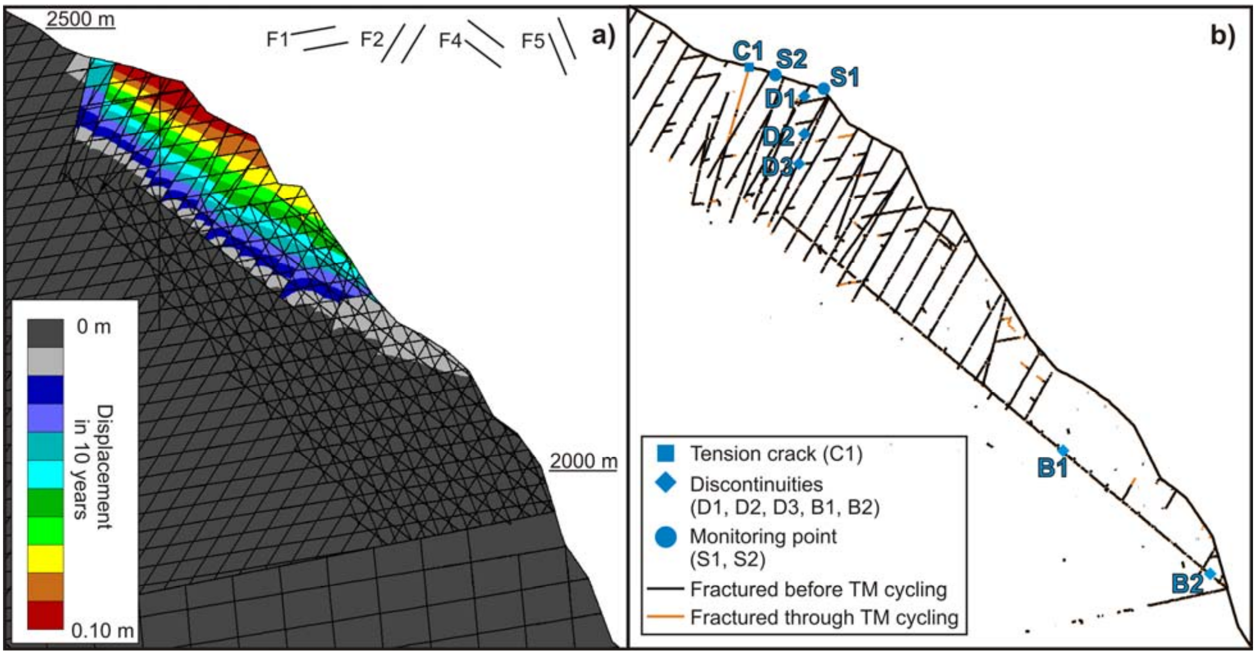

Figure 6.7: a) TM-induced absolute displacements after 10 years of thermal cycling. Also shown are all prescribed discontinuities within the model. Four discontinuity sets (F1, F2, F4, and F5) were included (see Gischig et al., 2011). b) Discontinuities in black have reached their strength limit and slipped prior to TM cycling, while discontinuities in orange failed during the modeled 10 years of TM cycling. Points for which time series results are shown in Figure 6.8 are also indicated.

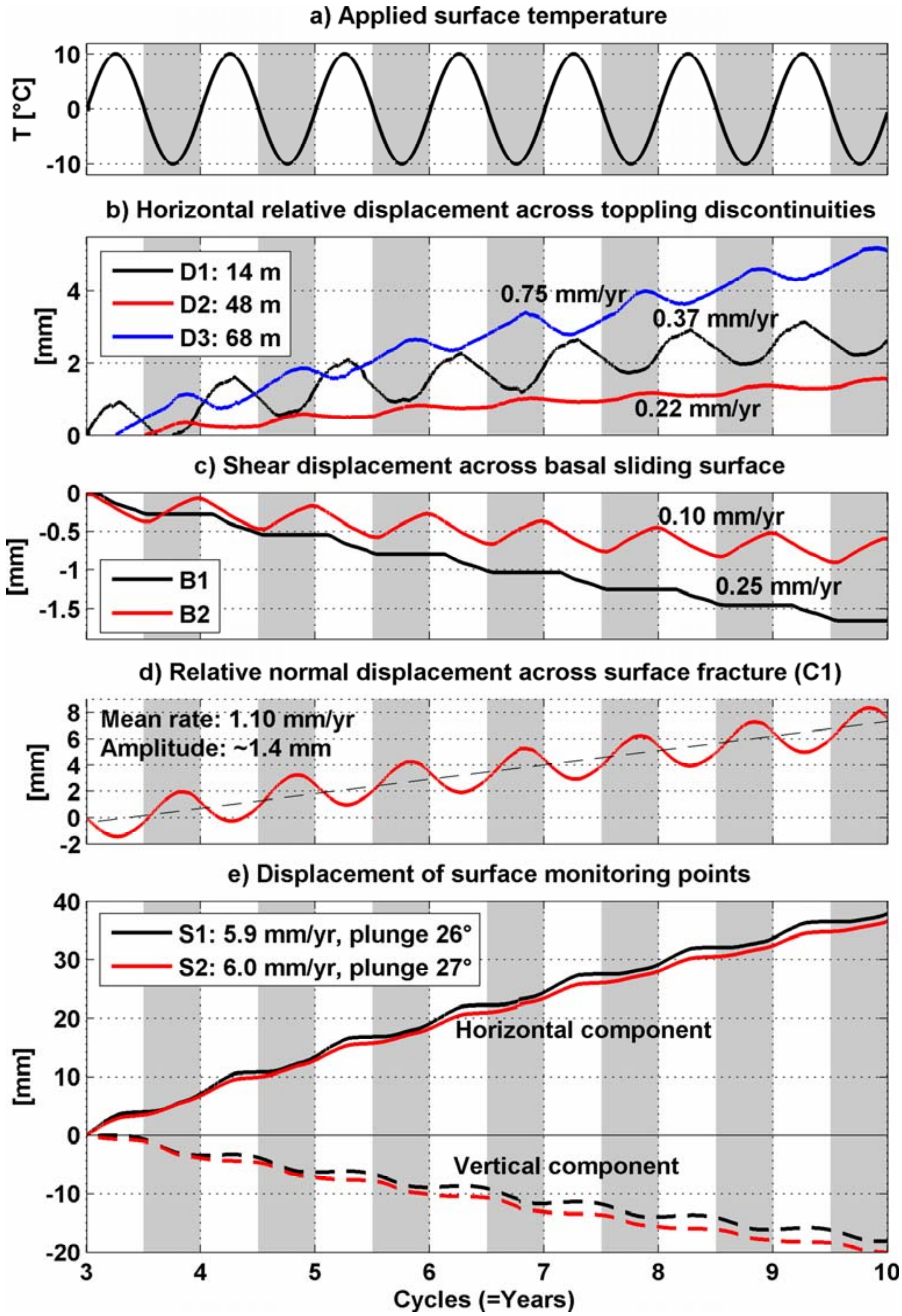

Figure 6.8: a) Temperature time history applied to the model ground surface. b) Time series of horizontal displacements measured across discontinuities at depth (left-lateral shear is positive). Grey shading indicates times when temperatures at the surface are below 0 °C. c) Time series of shear displacement for two points along the basal rupture surface (right-lateral shear is negative). Times of increased deformation occur in summer. d) Simulated fracture opening at a point approximately corresponding to the location of fracture Z10. e) Absolute displacement of two points at the ground surface.

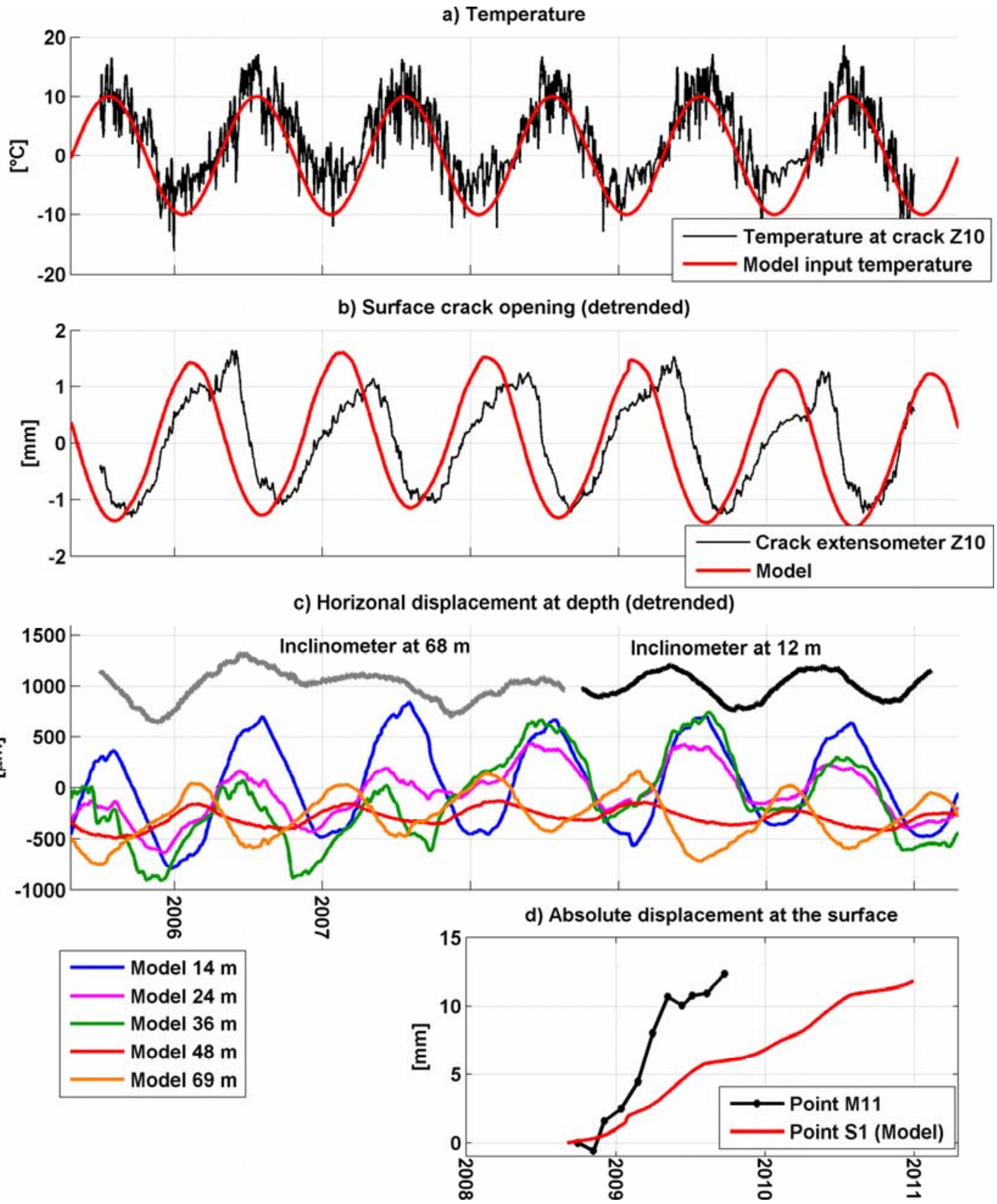

Figure 6.9: Comparison between model results and measured data. a) Temperature measured at fracture Z10 and sinusoidal temperature time history applied as a surface boundary condition in the model. b) Fracture opening at Z10 together with modeled fracture opening; the time series have been de-trended for comparison of amplitudes. Amplitudes match well, but a phase shift of about 40 days between modeled and measured data is observed. c) Inclinometer data from both 12 and 68 m depth, as well as modeled horizontal displacement across toppling discontinuities at various depths (all de-trended). Amplitudes of modeled and measured annual signals are well within the same order of magnitude, but a phase shift varying from -120 to +40 days with respect to measured data can be observed in the model results. d) Measured absolute displacement of geodetic point M11 (see Figure 6.5), and that from a point on the surface of the model (see Figure 6.7b).

7. EFFECTS OF OTHER DRIVING FACTORS: WATER, AIR, ICE, AND EARTH-QUAKES

As demonstrated in Chapter 6, thermo-mechanical (TM) effects alone are sufficient to explain temporal patterns of instability behavior observed in monitoring data from Randa. While often one single forcing factor controls the temporal behavior of an unstable rock slope, other factors can act simultaneously to assist in driving progressive failure. Monitoring data from the Randa instability were therefore also investigated to clarify the role of other possible factors that may contribute to rock slope deformation. We begin by discussing the role of groundwater, which in contrast to many reported landslides appears to be of secondary importance at the Randa instability. We present hydrogeological observations aimed at answering the question of why groundwater pressure only marginally affects the unstable rock mass. We also briefly discuss the role of ice formation within soil-filled fractures, inspired by observations of night-time accelerations in fracture opening rate in late winter. Next we describe air ventilation from steeply-dipping, open tension fractures, which was observed during field visits in winter, and discuss the possible role in contributing to TM effects. Finally, we present results from integrated investigations aimed at understand the seismic response of the Randa rock slope.

7.1 Groundwater

7.1.1 Introduction

As presented in Chapter 6, groundwater does not or only marginally influence deformation rates at the Randa instability, which is in opposite to most cases of instability reported in literature (e.g. Bonzanigo et al., 2007). This is illustrated again in Figure 7.1, which compares displacements recorded by the in-place inclinometer at 12 and 68 m depth with rainfall, snowmelt, and pressure changes in borehole sb50s. The data demonstrate that increased pressure after snowmelt or heavy rainfall does not induce temporary displacement rate increases. Water pressure in sb50s is at a maximum in March/April, while the largest change in displacement rate occurs in October/November, which corresponds to a time lag of more than half a year. Also shorter-term displacement rate increases (i.e. within days/weeks) do not correlate with rainfall events or snowmelt. Time lags between the occurence of water pressure maxima and displacement rate increases have been reported for many landslides (e.g. Weidner, 2000). At the Randa instability, however, a time lag of half a year seems unrealistic, while a correlation to temperature is obvious (Figure 6.4).

Hydrogeological investigations were conducted within the framework of a BSc thesis (Alpiger, 2010) and are summarized here. They help understanding the local hydrogeological situation at the Randa site, and clarify why groundwater pressure effects are of secondary importance at this particular instability. First, the spatial and temporal occurrence of groundwater seepages from the 1991 failure surface was described with help of time-lapse photographs. The time-lapse camera is installed on the opposite valley flank at the benchmark originally dedicated for GB-DInSAR measurements (see Chapter 3), and takes an image of the 1991 failure surface every 3 hours. Second, during field investigations shortly after snowmelt (June 2010) and in summer (July 2010), springs were mapped and characterized by their electric conductivity (EC). Locations of springs helped delineate an approximate spring-line and construct a conceptual model of the hydrogeological situation at the Randa instability.

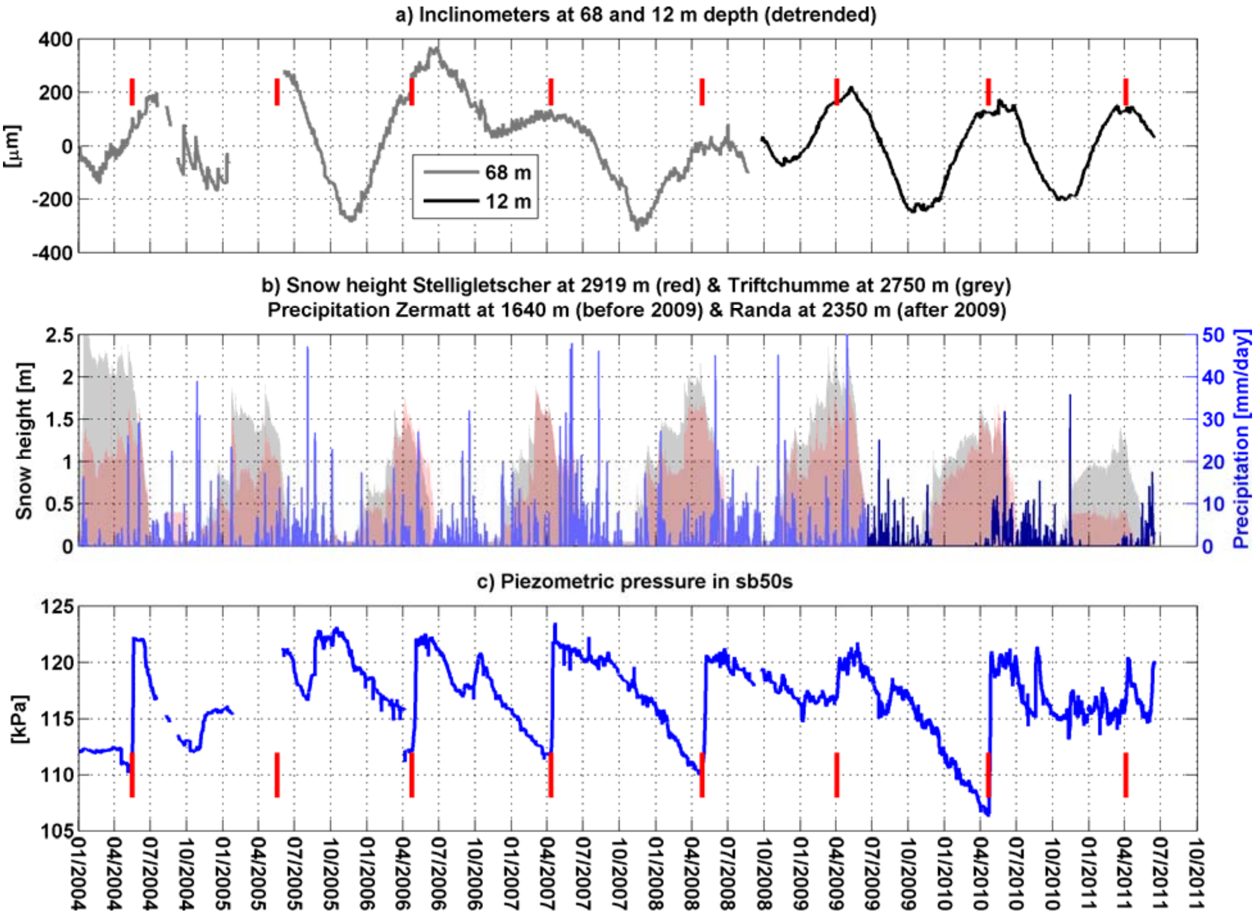

Figure 7.1: a) Displacements measured by inclinometers at two different depths, with linear trend removed to highlight deviations from background displacement rates. Red bars indicate onset of snowmelt as derived from groundwater pressure data shown in c). b) Snow height at two SLF stations around the Randa instability (9 km to the south and 6 km to the north; SLF-Data © 2011, SLF), as well as precipitation. Before summer 2009, precipitation data were not recorded at the in situ *laboratory, and precipitation from the station at Zermatt is shown (source MeteoSwiss). c) Piezometric pressure recorded at 50 m depth in borehole sb50s. Displacement rate changes do not correlate with heavy rainfall events or snowmelt associated with water pressure increases in sb50s.*

7.1.2 Results

Analysis of time-lapse photos of the 1991 failure scarp revealed the spatial and temporal occurrence of groundwater seepages (Figure 7.2). During days of rainfall and strong snowmelt, groundwater seepage is obscured by surface runoff and difficult to locate. Further, it was not always possible to deduce from the images whether springs originate from shallow groundwater within surficial debris cover or from the deep groundwater body in the rock mass. Figure 7.2 shows only seepages that are thought to reliably originate from within the rock mass. The following general pattern could be derived from observations: During the entire observation period between January and November 2010, no water seepage was observed within the paragneiss and schist units above about 1900 m, i.e. also not from the unstable rock mass. Springs only occurs within the orthogneiss, mostly along faults belonging to F1 set, i.e. foliation-parallel structures. The strongest outflow rates are observed at the boundary between the orthogneiss unit and the paragneiss and schist unit, which coincides with the trace of the basal rupture plane of the instability (springs A and B). In winter, neither seepage nor icicles were observable from the orthogneiss.

Water outflow occurs predominantly in spring after snowmelt. Especially at the lithology boundary at springs A and B, outflow rates increase strongly between 13 April and 10 June and cease again until they disappear on 29 June. All springs shown in Figure 7.2 are active during this time. The piezometric pressure in borehole sb50s increases to a maximum between 21 – 26 April and decays after 29 June (inset in Figure 7.2). During summer, most springs disappear and only a few damp spots remain, which show trickling water after rainfall events (e.g. at the bottom of the orthogneiss as well as at the lithological boundary). Springs A and B become active again after a few days of rainfall in August, and, at the same time, water pressure in sb50s increases. A strong temporal correlation is evident between water pressure changes in borehole sb50s and the springs at the base of the instability.

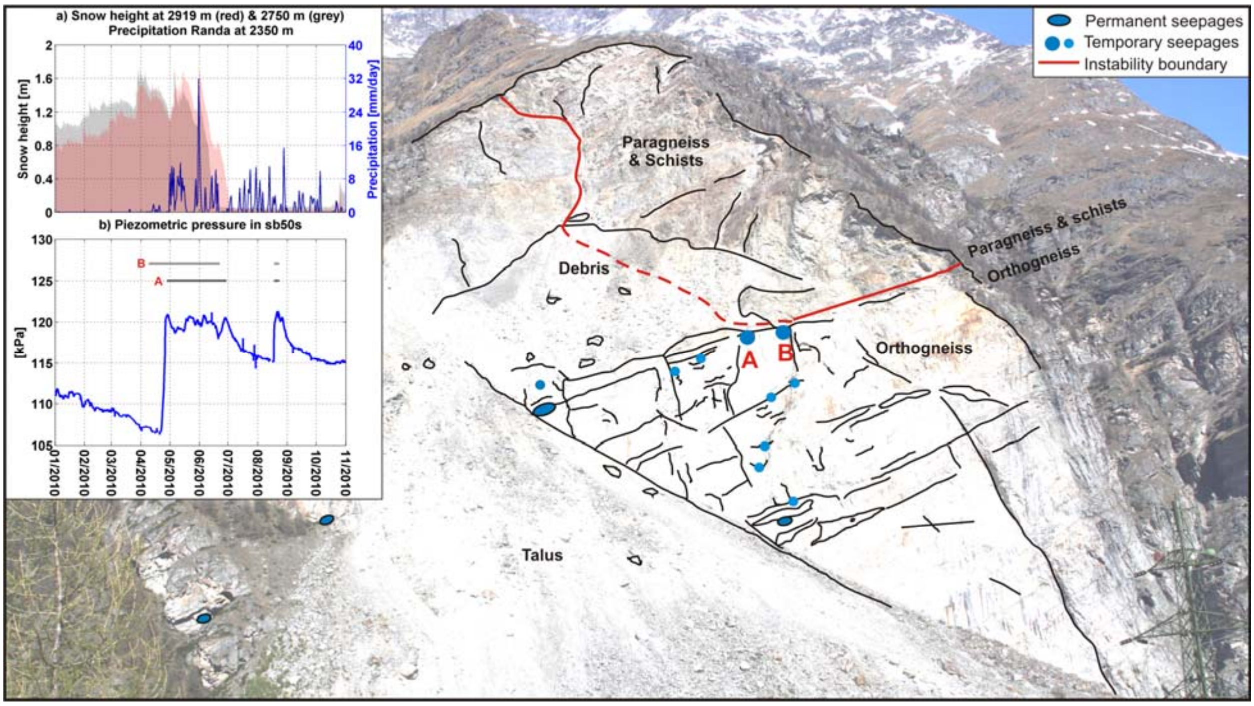

Figure 7.2: Springs identified from time-lapse photographs of the 1991 failure surface at Randa. The inset figure shows a period when springs A and B were active, and correlation with water pressure, snow height (SLF-Data © 2011, SLF) and rainfall data.

Figure 7.3 shows springs in map view identified during field visits between 9 June and 12 July 2010. It further includes the locations of the seepages observed with time-lapse imagery. EC could be measured for most spring waters. This value indicates whether the water originates from the shallow subsurface with short residence times or from deep persistent groundwater bodies with long residence times. Typically, snowmelt in the area has EC values of less than 15 µS/cm. Water outflow with low EC values of 20 – 25 µS/cm were found at 2500 m, which likely originates from snowmelt that has infiltrated only into shallow ground. At about the same altitude to the south, a small stream starts that remains active until fall. The stream flows along a gully formed by a highly persistent fracture zone (F3 set). EC was measured near the top of stream at two different times and once along a profile between 1900 and 2150 m. At 2500 m, EC increased from 50 to 80 µS/cm over 14 days. EC also increases from 65 to 90 µS/cm with decreasing altitude between 2150 and 1900 m. These measurements suggest that the water is a mixture of snowmelt and groundwater seepage along the fracture zones. Additional springs were found at five locations below 1700 m, which exhibit EC values between 180 and 450 µS/cm. Such values are high for seepage from crystalline rock and indicate long subsurface residence times (Richter, 1989). Similar values were reported by

Girod (1999) from the bypass tunnel below the rockslide. In their study, water seepage from the paragneiss to the south of the river Bisbach had EC values between 180 and 280 µS/cm (overburden above tunnel ~450 m), whereas from the orthogneiss the values ranged between 250 and 400 µS/cm (overburden ~900 m). The springs measured below 1700 m are thus interpreted to be seepage of deep groundwater. A spring line representing the intersection of the deep groundwater table with the topography was interpolated from mapped springs.

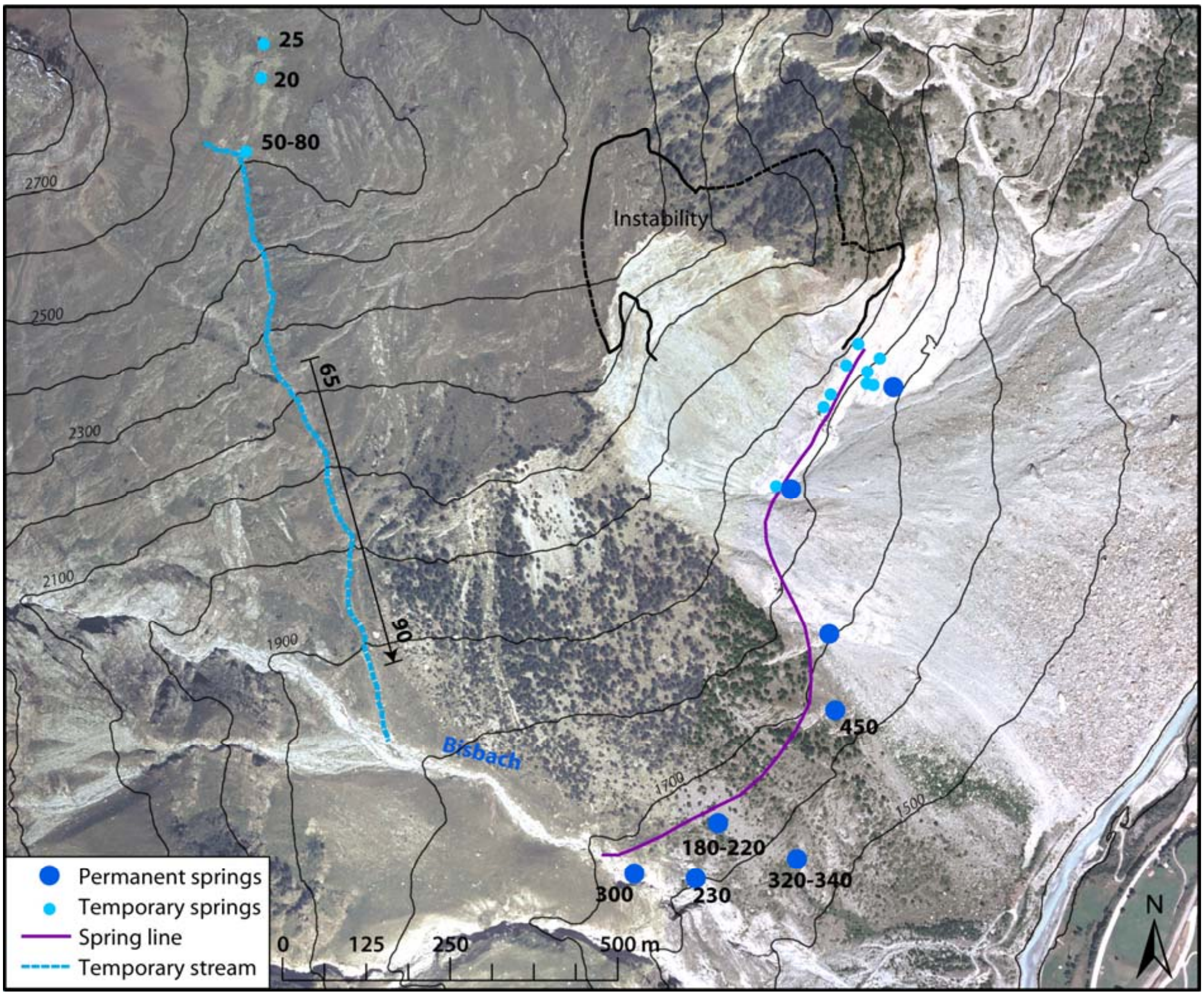

Figure 7.3: Springs identified on photographs and during field visits between June and July 2010. Also indicated is the electric conductivity (in µS/cm) for the springs that could be measured. If several measurements were carried out, the range of values is given. For the small stream, which almost completely dries during summer, a profile of electrical conductivity values was measured between 1900 and 2150 m.

7.1.3 Interpretation

Hydrogeological investigations in the area around the Randa instability revealed that groundwater seepage from deep perennial water bodies occurs mostly within the orthogneiss units in the bottom half of the slope. No springs could be identified within the currently unstable rock mass. After snowmelt, water outflow from the 1991 failure surface intensifies, and two major springs appear temporarily at the lithological contact between orthogneiss and paragneiss. The locations of these springs also coincide with the trace of the instability's basal rupture surface. The times of occurrence correlate well with times of maximum water pressure observed in borehole sb50s, which may point to a high hydraulic conductivity of the fractured rock mass. Figure 7.4 summarizes the hydrogeological observations in a simple sketch. It assumes a contrast in hydraulic conductivity between the underlying orthogneiss and more heavily fractured paragneiss and schists of the instability. Groundwater is 'dammed' behind the orthogneiss, which has low conductivity and whose boundary to the paragneiss dips into the slope. Within the more conductive unstable rock mass, the groundwater table is low and is limited to a few pockets of perched water. During summer and winter, when the groundwater table lowers within the orthogneiss, little seepage occurs and partly evaporates at the rock face. During snowmelt, both perched groundwater and deep groundwater recharge until the latter overflows at the lithological boundary. Only during this time does the groundwater table reach, or at least approach, the unstable rock mass at the basal rupture surface. Such hydrogeological conditions are also in accordance with the borehole measurements, which show dry conditions in two boreholes to a depth of 120 m. The conceptual model provides an explanation as to why snowmelt and heavy rainfall are not followed by accelerated rock mass deformation: since the rock mass is highly fractured and nearly drained, water pressure cannot build up and affect stress conditions on fractures within the instability.

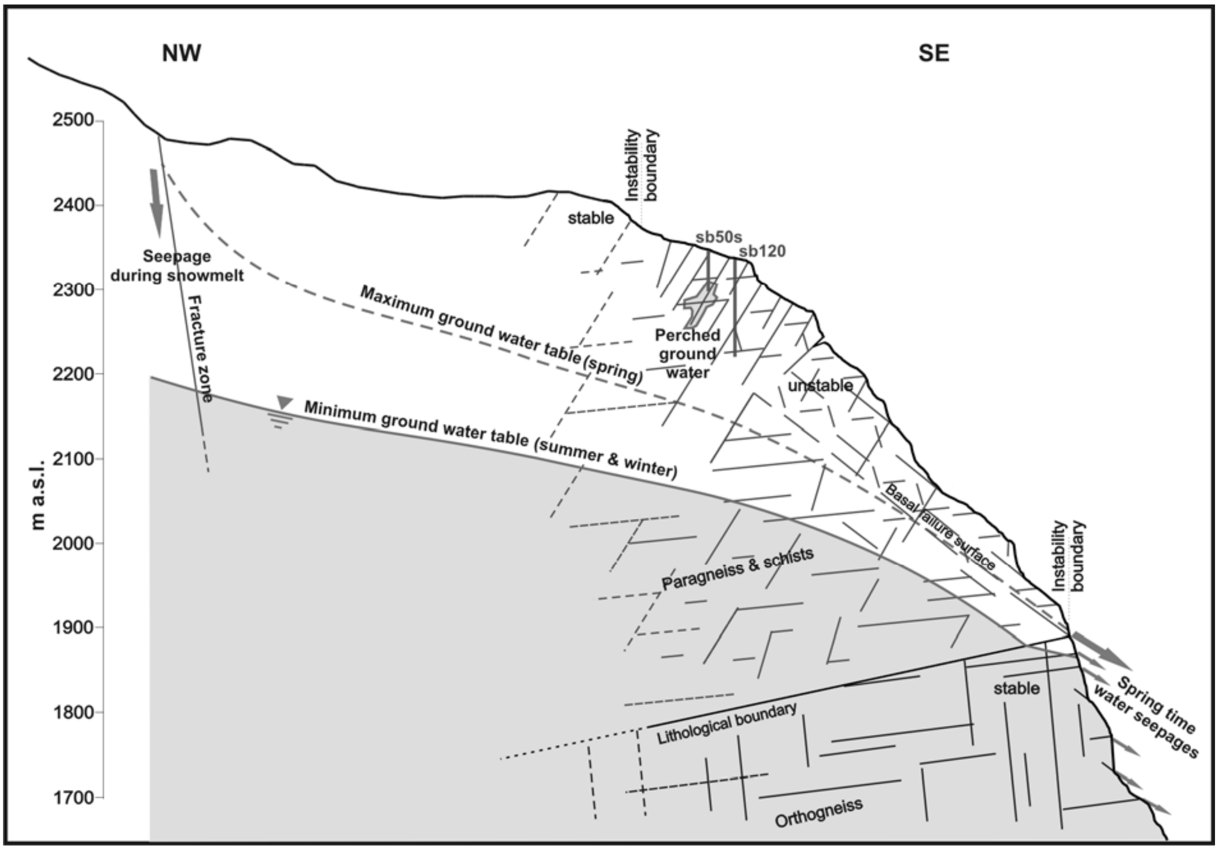

Figure 7.4: Conceptual overview on the hydrogeological situation of the Randa instability as interpreted from borehole pressure data, and observations from time-lapse imagery and field investigations.

7.1.4 The role of ice formation in fractures

While borehole displacement data did not show any rate increases during snowmelt (Figure 7.1), unique spring time accelerations were observed across tension fracture Z9 (Figure 7.5a). However, the onset of these rate increases occurs some days to weeks before the piezometric pressure in sb50s increases (Figure 7.6). We argue that they indicate freezing effects, and are not caused by increased groundwater pressure.

In winter, fracture Z9 is buried below 1 – 2 m of snow as it lies in a local depression. Temperature at the fracture is strongly negative in fall, then tends towards zero during winter, but always stays slightly below zero. Short-term (e.g. daily) fluctuations are absent in the temperature record. Spring time rate increases occur notably during periods when temperatures above the snow cover (here taken from fracture Z10) become positive and snowmelt intensifies (Figure 7.5b). The behavior is repeated every year around the same time in spring. Data from the FO sensor across fracture Z9 show that during these periods of increased opening rates, a daily signal occurs marked by increased opening rates at night and lower (sometimes zero) opening rates during the day (Figure 7.7; Moore et al., 2010). The daily signal is not related to temperature fluctuations at the sensor, as the temperature remains constant during this time.

Accelerated fracture opening during snowmelt, both on the daily basis as well as over several days, is interpreted to result from freezing of water within the soil-filled fracture, instead of a groundwater-related effect. Fracture Z9 has a thick infilling of soil originating from collapsed regolith material. Temperatures at the fracture below the snowpack are slightly below 0 °C during snowmelt. Meltwater infiltrating through the snowpack to the soil infill can freeze and lead to expansion of the saturated material creating pressure on the fracture walls. Daily rate fluctuations can be similarly explained: during the day, meltwater infiltrates into the fracture void space and subsequently freezes at night as soon as the input of meltwater (and the heat it carries) ceases. The recordings show similar behavior as described by Matzuoka (2001b), who reported spring time fracture opening related to freezing of meltwater and induced pressure on fracture walls.

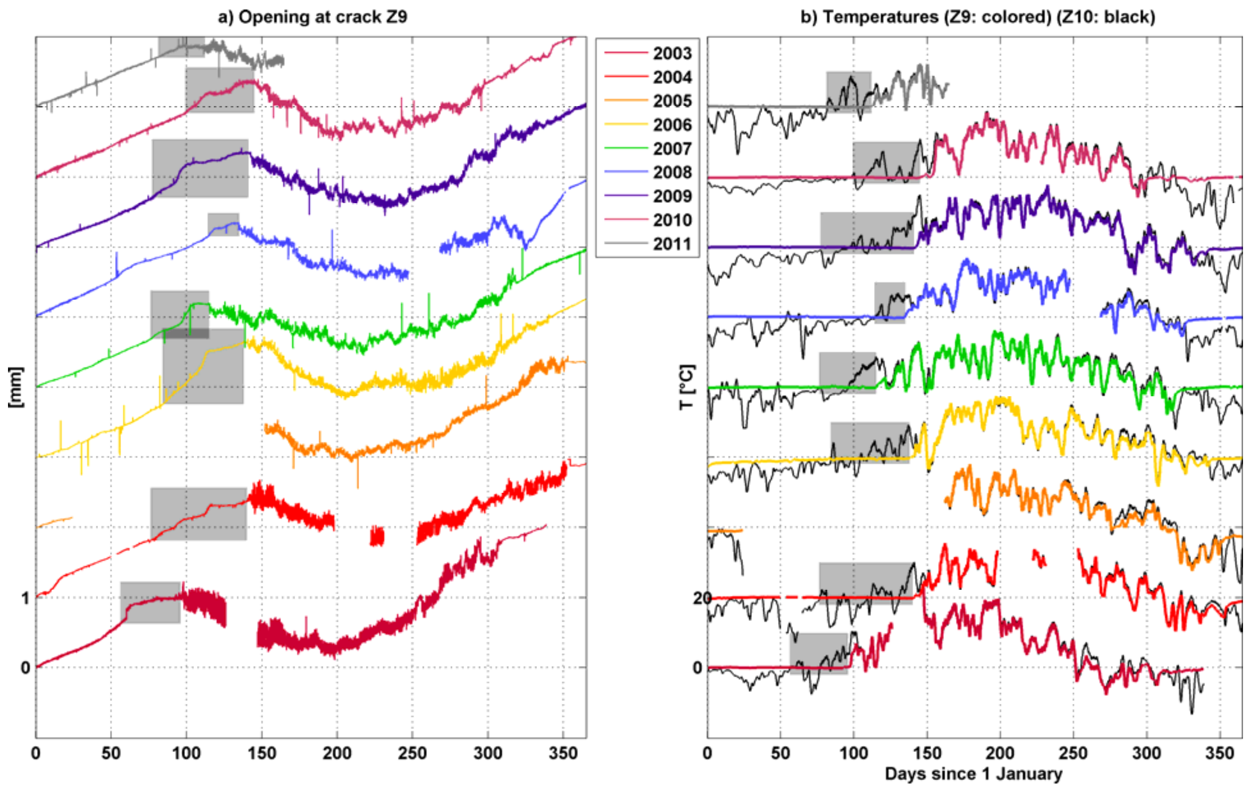

Figure 7.5: a) Fracture opening at fracture Z9 for each year since 2003. They gray shaded area highlights periods of increased opening rates in spring. b) Temperature measured at fractures Z9 (colored) and Z10 (black). Data from Z10 represent temperature above the snow cover and indicate when snowmelt occurs. Gray shading corresponds to time periods highlighted in a). Increased opening rates occur when temperatures above the snowpack allow snowmelt, but remain <0 °C below the snowpack at Z9.

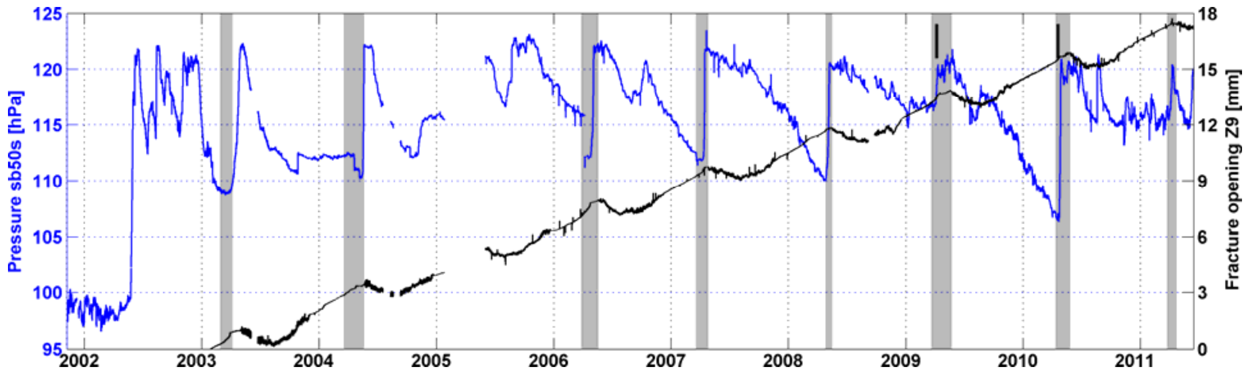

Figure 7.6: Pressure plotted against fracture opening at Z9. The periods of increased opening rates as presented in Figure 7.5 are highlighted with grey shadings. Pressure increases usually occur after the onset of rate increases. Black bars in 2009 and 2010 indicate the time periods shown in Figure 7.7.

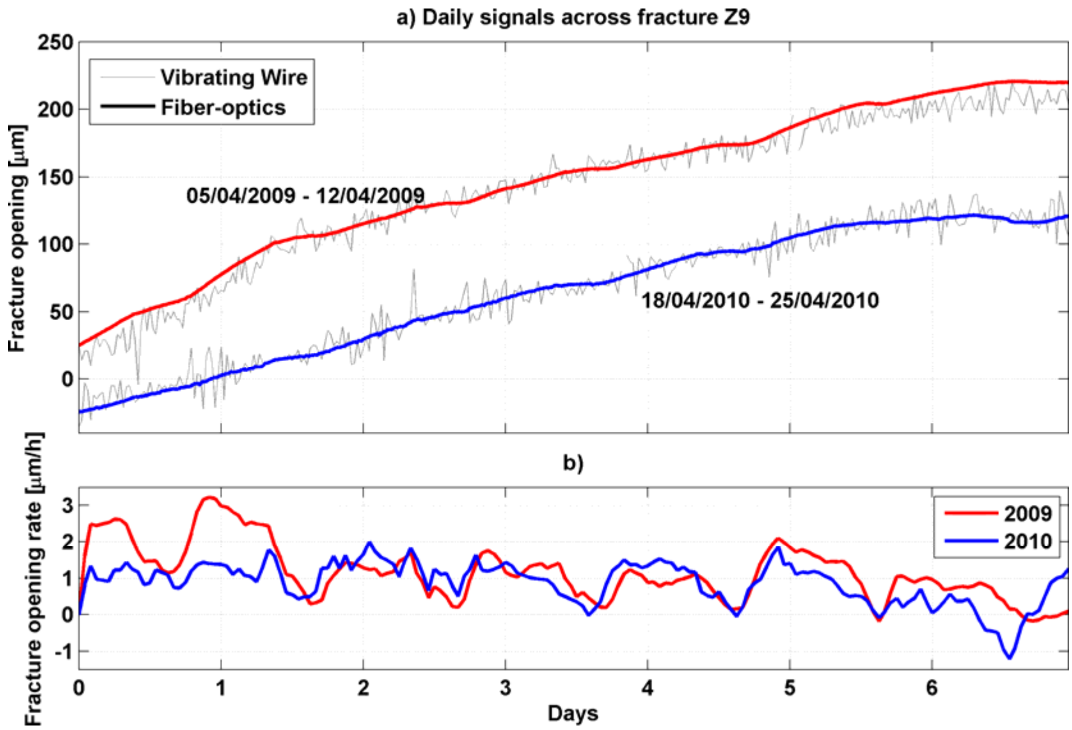

Figure 7.7: a) One week displacement time series from 5 April 2009 and 15 April 2010 showing a clear daily signal in the fiber-optic strain data (red and blue thick line). Also shown is the vibrating wire crack extensometer data (thin grey line), for which the noise levels is not sufficient to resolve the daily signals. b) Displacement rates derived from the time series in a). The time period is characterized by increased rates at night and lower rates during the day. (Figure adapted from Moore et al., 2010)

Matzuoka (2001a) distinguishes two main processes involved in freezing-induced fracturing in rock or soil. The first process, referred to as *ice segregation*, describes the formation of ice lenses in a porous material due to the transport of water from partially or fully saturated regions to a freezing front. The gradual formation of ice lenses can result in large heaving pressures and stress at fracture tips, and may induce fracturing of the medium especially if tensile strength is low. The theoretical model by Walder & Hallet (1985) suggests that fracture growth primarily occurs between -15 and -4 °C; below -15 °C water migration is inhibited, and above -4 °C not enough pressure can build for fracturing to occur. Ice segregation is most efficient for slow freezing of a medium with high internal surface area (high porosity), i.e. if sufficient time is available for water migration and capillary suctions aid transport. Fracturing through ice segregation thus mainly occurs in saturated soils.

The other ice-related fracturing process is simply a consequence of the 9% *volumetric expansion* as water freezes in fractures. Matzuoka & Murton (2008) point out that volumetric expansion can only result in fracturing when the fractures are water-saturated and freeze from all directions. They also note that hydraulic fracturing may occur if water cannot escape during freezing, and significant pressure builds up in the unfrozen water. Water pressures measured in the field at 2 m depth reached values up to 400 kPa in such conditions (Dyke, 1984). Davidson and Nye (1985) measured stresses in an idealized fracture in the laboratory (i.e. a slot in photo-elastic material) subject to rapid freezing from the top surface, and report pressures of 1.1 MPa generated below the freezing front. They note that in most cases, ice does not extrude from the fracture. Matsuoka (2001b) describes observations of so-called frost wedging in crack extensometer data measured across surface fractures in the Japanese Alps. These data were characterized by anomalous opening periods in fall and spring when temperatures fell below 0 °C. He states that in fall, fracture widening depends on the availability of water and the freezing intensity, while in spring widening was controlled by refreezing of infiltrating meltwater. Similarly Wegmann and Gudmundson (1999) suggested that volumetric expansion of freezing water induced extension across fractures, which is negatively correlated with subzero temperatures.

At the Randa instability, we consider only volumetric expansion of water within fractures as a feasible ice weathering process, as the necessary conditions for ice segregation (namely high internal surface area and water saturation), are not met within the fractured, generally dry crystalline rock mass. Although displacement data from fracture Z9 constitute the only available suggestion of freezing-related fracture displacements, it is certainly possible that similar processes also occur elsewhere at the Randa instability. However, as will be shown in Section 7.2, most fractures at the top of the instability show temperatures elevated above 0 °C during the winter because of air ventilation, rather than subzero temperatures which would promote freezing. Thus, freezing within fractures may only occur in fractures that do not participate in ventilation, such as those daylighting on the 1991 failure surface. Here, the rock is not insulated by snow cover and exposed to temperatures far below 0 °C in winter. From data measured at the snow-free rock face, the penetration depth of subzero temperatures was estimated with a finite difference model solving the 1D heat diffusion equation (2.1) and using the thermal diffusivity value derived in section 2.3.7 (1.9E-6 m^2/s). It was found that subzero temperatures can penetrate to a depth of about 3 m in a snow-free rock face. In comparison, if covered by a ~0.5 m thick snowpack, subzero temperatures penetrate to only about 1.2 m in rock, and to about 0.4 m in soil. Thus, the temperature regime would allow freezing in fractures to a depth of about 3 m at the 1991 failure surface. However, as shown by several authors (e.g. Matzoka, 2001b; Matzuoka and Murton, 2008), the availability of water is critical for freezing in fractures to become an important factor. As shown earlier, saturated fractures are not expected within the 1991 failure surface. Furthermore, observations from fracture Z9 show that freezing effects predominantly occur in spring, when meltwater is available. Hence, we acknowledge that freezing effects can occur and support TM forcing in winter, but we conclude that their relative importance is minor at the Randa instability.

7.2 Enhanced TM effects through fracture ventilation

7.2.1 Introduction

During winter field visits between 2008 and 2010, open holes were observed in the snowpack exhausting warm, moist air. Such air vents had diameters on the order of 0.1 – 1 m, were surrounded by large hoar crystals, and consistently lay above steeply-dipping active tension fractures. Various investigations were carried out to help understand the origin and mechanism of air circulation through these fractures, and the role in disturbing the otherwise conductive temperature field. In January 2010, the spatial distribution of air vents was mapped, and further visualized with thermal imagery. Three stand-alone temperature sensors (UTL dataloggers) were installed at depths of 0.5, 1.5 and 2.5 m within one tension fracture where a large ventilation hole was observed during all field visits. Borehole temperature profiles were performed in summer 2010 to describe the conductive temperature field and detect any potential deviations. A detailed description and discussion of the relevant phenomena is given by Moore et al. (2011). Here we give a summary and discuss the possible role of air ventilation in enhancing TM effects by altering the temperature field of the unstable rock mass.

7.2.2 Warm air vents

The mapped locations of air vents are shown in Figure 7.8 along with the traces of known discontinuities. Temperatures of exhausted air were measured with a lab thermometer and are also included. Air vents align primarily along actively opening, steeply-dipping tension fractures. Temperatures range from 1 to 4 °C, which is roughly the temperature of rock at depths of 10 – 100 m. Note that ambient air temperature on that particular day ranged from -8 to -2 °C, and temperature of the rock surface below the snowpack was -2 °C.

Thermal images (Figure 7.8c) visualize the occurrence of warm air vents through increased temperatures around the holes. Note that apparent temperature changes in the image can also arise from spatially varying radiation properties (i.e. thermal emissivity) of different surfaces. Rock surfaces show higher temperature, partly due to a real temperature difference, but partly also due to a contrast in emissivity. On the snow surface however, temperature variations in the image can be considered reliable, while the absolute temperature values have an error up to 5 °C. Air vents are indicated with arrows in Figure 7.8c. Swaths of increased temperature on the snow surface near the air vents indicate the ambient wind direction. Snow with increased temperature is limited to the surrounding areas of the holes and does not occur along the entire tension fracture. Thus, warm air does not penetrate the snow cover and ventilation is concentrated at open holes.

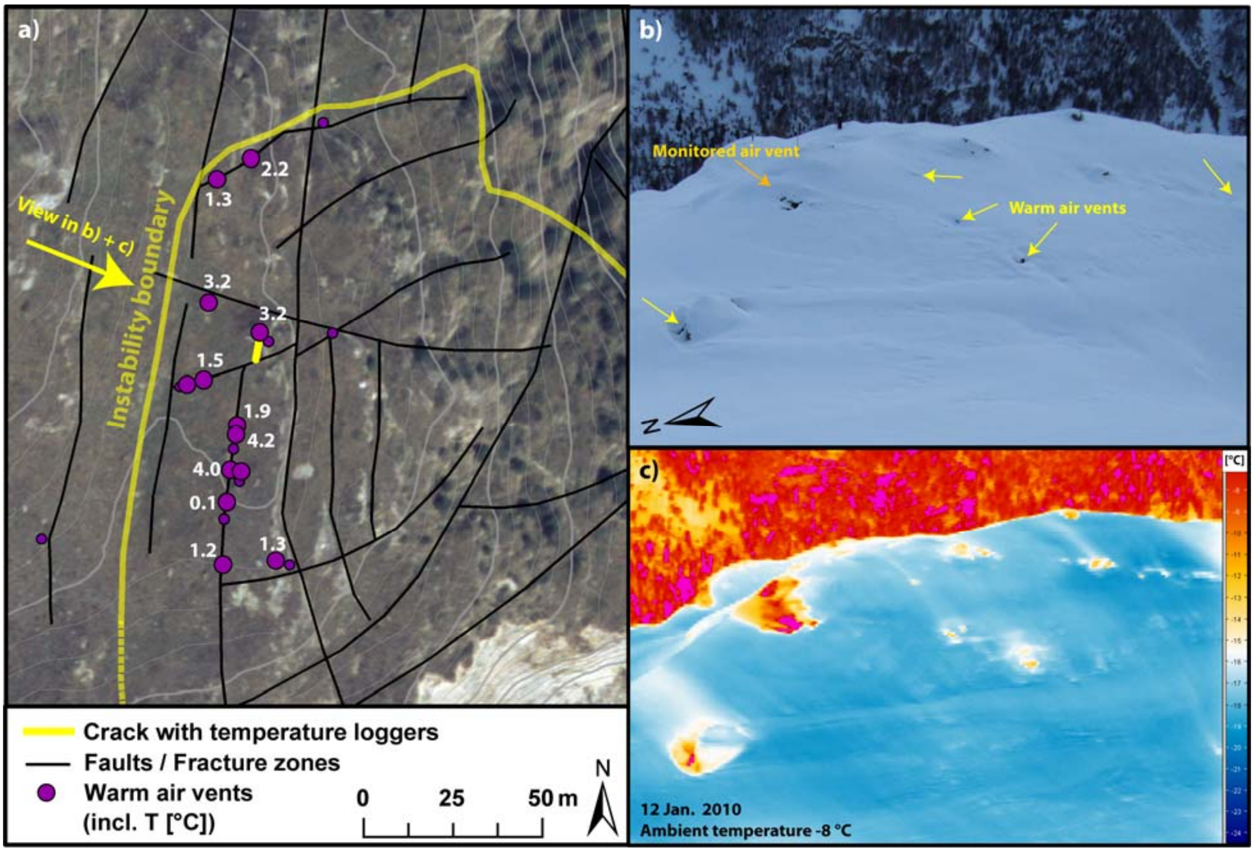

Figure 7.8: a) Map of warm air vents. b) Photograph of air vents. c) Thermal image of the scene in b).

7.2.3 Fracture air temperature

Temperature time series recorded within the tension fracture below the largest air vent at depths of 0.5, 1.5, and 2.5 m are presented in Figure 7.9a along with ambient air temperature. The time series exhibit clearly distinguishable summer and winter regimes. In summer, fracture temperatures mimic daily air temperature cycles, and are predictable for diffusive heat transfer in air (Figure 7.9d). The highest temperature and strongest daily variation is measured at the shallowest sensor, and both temperature and amplitude decay with depth. In winter, temperatures are steady regardless of air temperature fluctuations, although the air around the sensors is connected to free air (Figure 7.9c). They show a slow decrease over the season from about 3 to 2 °C. Occasionally steady temperatures are interrupted during warm periods or times of strong wind. The slow temperature decrease likely results form cooling of rock at depth, which transfers heat to the circulating air. Also in winter, the shallowest sensor usually records the highest temperature. This is expected as more buoyant warm rises up through the fracture and collects below the snowpack before it is exhausted through air vents.

Figure 7.9b shows the Rayleigh number R, which predicts when temperature conditions favor free convection within a single fracture. The value is the ratio of buoyant forces to the product of thermal diffusivity and viscosity of air (Nield, 1982; Weisbrod and Draglia, 2006):

$$R = \frac{\Delta\rho g k L}{\alpha\eta} \tag{7.1}$$

where $\Delta\rho$ is the temperature-related density contrast between air within and outside of the fracture, k the fracture permeability, L the characteristic length, α the thermal diffusivity of air, and η the dynamic viscosity. Fracture permeability is calculated from the cubic law $k = (2b)^2/12$, where b is the average fracture width. Unstable buoyancy conditions favoring convection are predicted when R is greater than $4\pi^2$ or ~40. In our case, we calculated R from air temperature and an assumed steady temperature of 3 °C at a depth within the rock mass. L was set to 30 m, and a fracture width b of 10 mm yielded k = 3E-5 m^2. We used a thermal expansion coefficient of 3.6E-3 1/K, thermal diffusivity of α = 2E-5 m^2/s and viscosity $\eta \approx$ 1.7E-5 m^2/s.

The presented Rayleigh number time series correlates well with the observed fracture ventilation pattern. During convective conditions, fracture temperatures stabilize at ~2 - 3 °C (Figure 7.9c), while during conductive conditions fracture temperatures follow air temperature (Figure 7.9d). On the seasonal time scale, convection is pervasive throughout winter, while in spring and fall alternating convection and conduction conditions occur due to periodic warm and cool periods. Each significant atmospheric warming brings predicted onset of conductive heat transfer, and fracture air temperatures begin to mimic the outside air temperature until successive cooling again brings on convection and fracture venting. In summer, conductive conditions prevail, and fracture air temperatures gradually rise with significant daily variations.

Air circulation in deep, open fractures may disturb the purely conductive temperature field of the rock slope. Convective venting of air during winter would act to cool the deep subsurface as it gives up heat to the colder incoming air, while warming the near-surface active layer as air rises in the fractures. This will be explored in the next section.

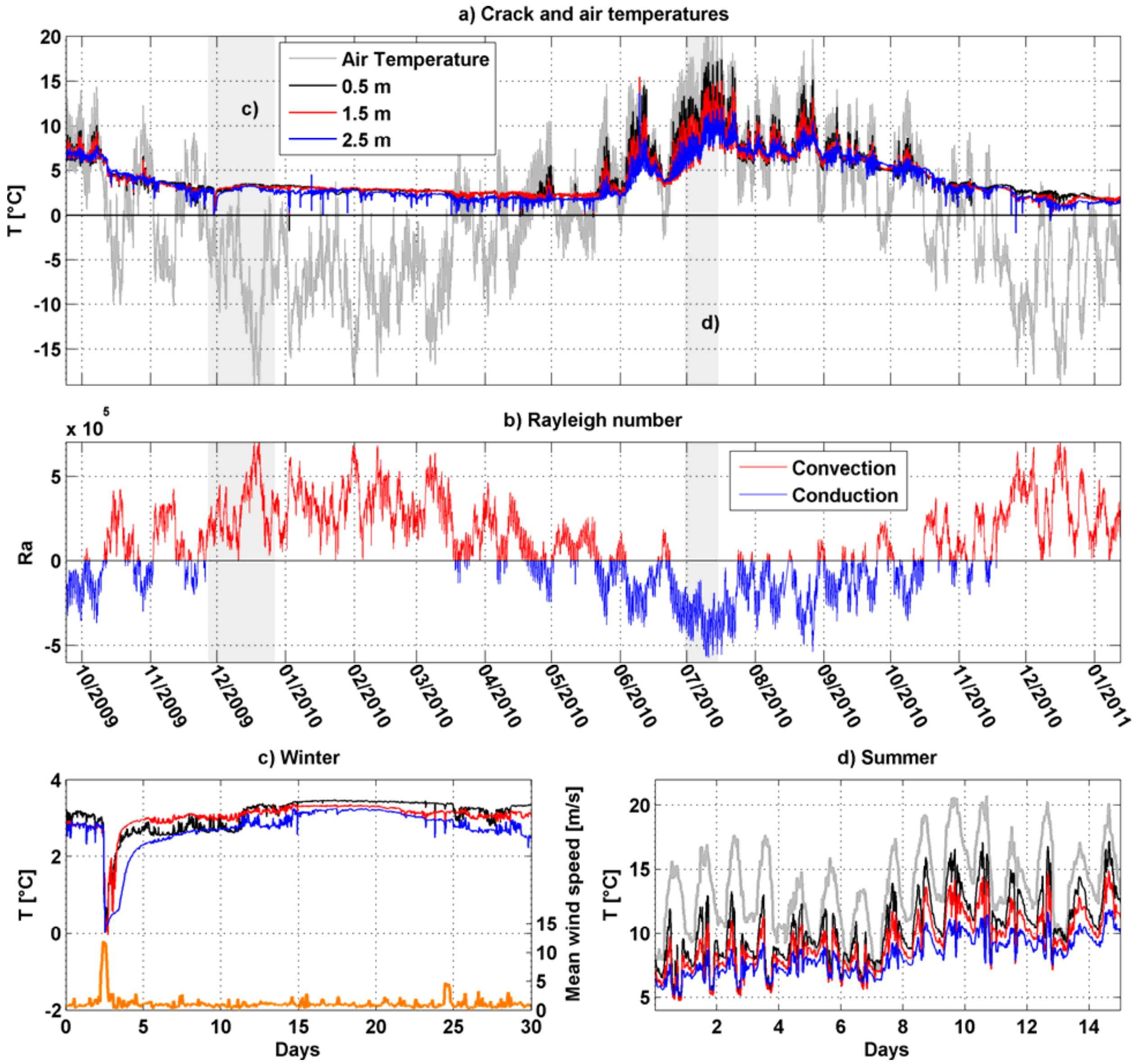

Figure 7.9: a) Fracture air temperature at depths of 0.5, 1.5, and 2.5 m, as well as ambient air temperature. b) Rayleigh number calculated from air temperature and assuming a steady deep fracture temperature of 3 °C. c) Fracture temperatures measured in winter when convection conditions prevail. Steady temperatures around 3 °C are disturbed by high wind events (Wind data taken from Zermatt). d) Fracture temperature in summer, when heat conduction is dominant. Fracture air temperatures follow air temperature.

7.2.4 Borehole temperatures

Inspired by the observation of air convection in deep tension fractures, possible disturbances to the otherwise assumed conductive temperature field were explored. First, the conductive temperatures field was modeled in 2D and 3D including true topography. Conductive temperatures were then compared with temperature logs measured in August 2010 in sb50s and sb50n. In borehole sb50s, only the section between 34 and 44 m depth could be logged since water quickly leaked from the hole at a zone at 34 m depth. In borehole sb50n, temperatures could be measured between 15 and 35 m depth. In addition temperature sensors (Keller druck DCX-22) were suspended at different depth during periods of weeks to months, to verify the temporal stability of the temperature field at depth (see Moore et al., 2011 for details).

7.2.4.1 Conductive temperature field

The conductive temperature field was modeled with the commercial finite element software COMSOL Multiphysics. We computed isotropic and anisotropic 2D models, as well as a 3D model for comparison. The following input parameters were required: (1) the geothermal heat flux (lower boundary condition), (2) effective thermal diffusivity of the medium, and (3) the ground surface temperature distribution (upper boundary condition). Zero heat flux boundaries were chose for the side boundaries. The following parameters were used in our models (see also Table 7.1):

- The geothermal heat flux was estimated to be 75 mWm^{-2} from values reported for the Swiss Alps in the literature (Rybach and Pfister, 1994; Noetzli et al., 2007).
- Thermal diffusivity (α) can be calculated as $\alpha = \lambda/C$, where λ is thermal conductivity and C is the volumetric heat capacity. General values for rocks are $\lambda \sim 3$ W $m^{-1}K^{-1}$ and C ~ 2E6 J $m^{-3}K^{-1}$, giving a typical diffusivity of $\alpha \sim$ 1.5E-6 m^2s^{-1} (Gueguen and Palciauskas, 1994). The thermal diffusivity of intact Randa paragneiss was estimate earlier to ~2.0E-6 m^2s^{-1}, which is comparable to the generalized value above. Heat conduction properties of the rock mass implemented in COMSOL were λ= 1.5 W $m^{-1}K^{-1}$ and C = 1.9E6 J m-$^{3}K^{-1}$, yielding diffusivity α = 7.7E-7 m^2s^{-1}. These values were found to provide best fit between measured and modeled temperature profiles. The implemented diffusivity, however, differs substantially from our calculated value; a factor of 2.5 lower. This difference is likely caused by the strongly-fractured rock mass within the instability, which creates lower effective diffusivity than for intact rock (up to 17% air-filled void space was predicted from geophysical measurements in the upper meters; Heincke et al., 2006). For the anisotropic model the thermal conductivity parallel to foliation was increased to 2.25 W $m^{-1}K^{-1}$, while perpendicular to foliation the value was kept as for the isotropic case (anisotropy ratio = 1.5; Goy et al., 1996).
- To determine the ground surface temperature distribution, two parameters are needed: (a) the mean ground surface temperature (MGST) at a known elevation, and (b) the variation of MGST with altitude. MGST at the monitored slope is highly heterogeneous depending on aspect, ground cover and shading, and for this exercise we need both a spatial and temporal mean. We compared local MAAT values with measured temperatures from *in situ* sensors, and assume that MGST is typically ~1 °C greater than the mean annual air temperature (MAAT; Goy et al., 1996) and less than measured temperatures at depth. The MGST at the shallow rock borehole is not representative because of the south-facing aspect. Rather, mean temperatures recorded by crack extensometers provide the best estimate of MGST, despite these sensors not directly measuring the ground temperature (they are covered and lie a few mm above rock). MGST at 2360 m was thus estimated to be approximately 2.6 °C. Rybach and Pfister (1994) review collected data from Switzerland regarding variation of MGST with altitude, and report an average value of -5 °C km^{-1}. This is consistent with the local air temperature lapse rate, which we measured to be -5 C km^{-1} between the town of Randa and the monitored area (930 m difference).

Table 7.1: Model parameters used to calculate the 2D conductive temperature field.

Thermal conductivity (λ)	1.5 W $m^{-1}K^{-1}$
Volumetric heat capacity (C)	1.9E6 J $m^{-3}K^{-1}$
Thermal diffusivity (α)	7.7E-7 $m^2 s^{-1}$
Conductivity anisotropy ratio	1.5
MGST at 2360 m	2.6 °C
Variation of MGST with elevation	-5 °C km^{-1}
Geothermal heat flux	75 mW m^{-2}
Annual temperature cycle amplitude	10 °C

The modeled steady-state conductive temperature field for the complete mountain profile above Randa is shown in Figure 7.10a, while a detail of the monitored area is shown in Figure 7.10b. The modeled temperature distribution is similar to other reported cases for Alpine rock slopes (e.g. Noetzli et al., 2007), and the 0 °C isotherm is located at an altitude of 2880 m, consistent with the modeled permafrost distribution (BAFU, 2006). Figure 7.10c shows modeled steady temperatures along a simulated borehole through the center of the monitored area compared with measured values. Good fit could be achieved between the 2D isotropic model and the temperature data from logs in the two 50 m deep boreholes. Notable deviations are also evident, especially in borehole sb50n where the temperature log shows a cooling trend around 30 m depth. Temperatures measured at the base of the boreholes with the thermistors included in the VW piezometers could not be matched precisely with the model fitting the borehole temperature logs. This may be due to: a) lack of calibration between the different sensor types (it is not possible to access the bottom-hole sensors), or b) localized disturbances to the temperature field, as in sb50n. The same model parameters used to provide best match with temperatures in the upper ~100 m of the rock mass were used throughout the entire model, as no data are available regarding the variation of rock mass thermal properties with depth, and since we are primarily interested in the near-surface zone.

Figure 7.10c also compares isotropic and anisotropic as well as 2D and 3D models against measured temperatures along a simulated borehole. The effect of implementing anisotropic thermal conductivity was found to be relatively small in our conduction model, only a slight deviation from the isotropic case can be observed (~0.5 °C at 100 m). We cannot say which model is more accurate, so for simplicity retain isotropic heat transfer properties throughout the following discussion. For the 3D model, we kept the surface temperature (only a function of altitude), boundary conditions and the thermal properties the same as in the isotropic 2D models. Thus, the model only explores the effect of geometry, ignoring the influence of aspect which is potentially large but poorly constrained. The resulting steady-state conductive temperature field is represented in a profile along the simulated borehole in Figure 7.10c, and compared to the 2D cases of isotropic and anisotropic heat transfer properties. Results demonstrate a significant influence of 3D geometry, where the rock mass at depth is cooled by ~1 °C at 100 m compared to the 2D isotropic case. Heat transfer is more efficient in strong 3D topography as a point in the interior of the body has an overall shorter average distance to the ground surface (Noetzli et al., 2007).

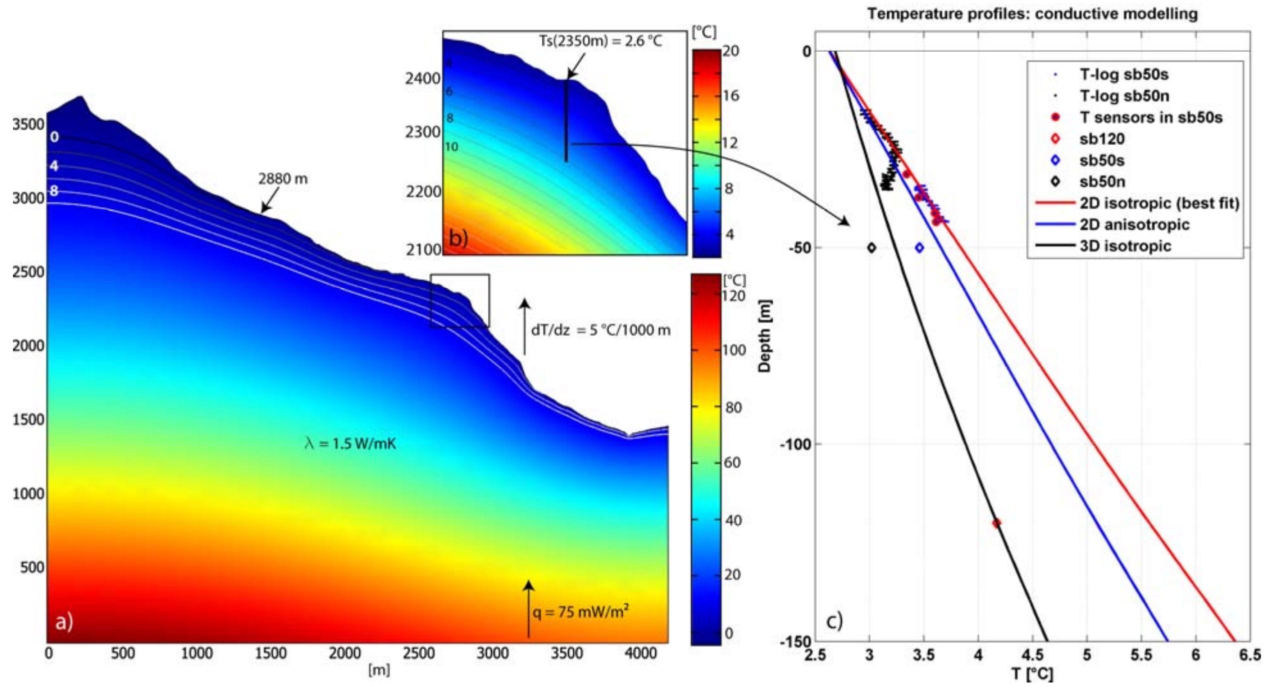

Figure 7.10: a) Modeled steady-state conductive temperature field for the complete mountain profile, showing implemented thermal diffusivity and boundary conditions and select isotherms. b) Detail of the monitored area showing simulated borehole where temperature profiles are extracted and compared against measured values. The MAGT at 2350 m is also shown. c) Model results and measured temperature values along a simulated borehole in the center of the monitored area. Shown are the best-fit results assuming 2D isotropic heat transfer, results of 2D anisotropic simulation (anisotropy ratio = 1.5), and the effect of implementing the true 3D geometry of the rock slope.

Transient effects and annual thermal active layer dynamics at the site was modeled by superimposing a sinusoidal temperature history with 10 °C amplitude and one year period to the surface temperature distribution used before. Transient ground temperature profiles representing winter (1 January), spring (1 April), summer (1 July), and fall (1 October) conditions are shown in Figure 7.11a, and together with measured borehole temperature data in Figure 7.11b. Thermal wave propagation in the annual active layer modifies temperatures up to 15 m depth, where the annual variation falls below 0.1 °C (10% of the surface amplitude). In summer, the warming front propagates downward, heating the bedrock at shallow depths, while the deeper portion of the active layer is still below the mean temperature due to the previous winter cooling.

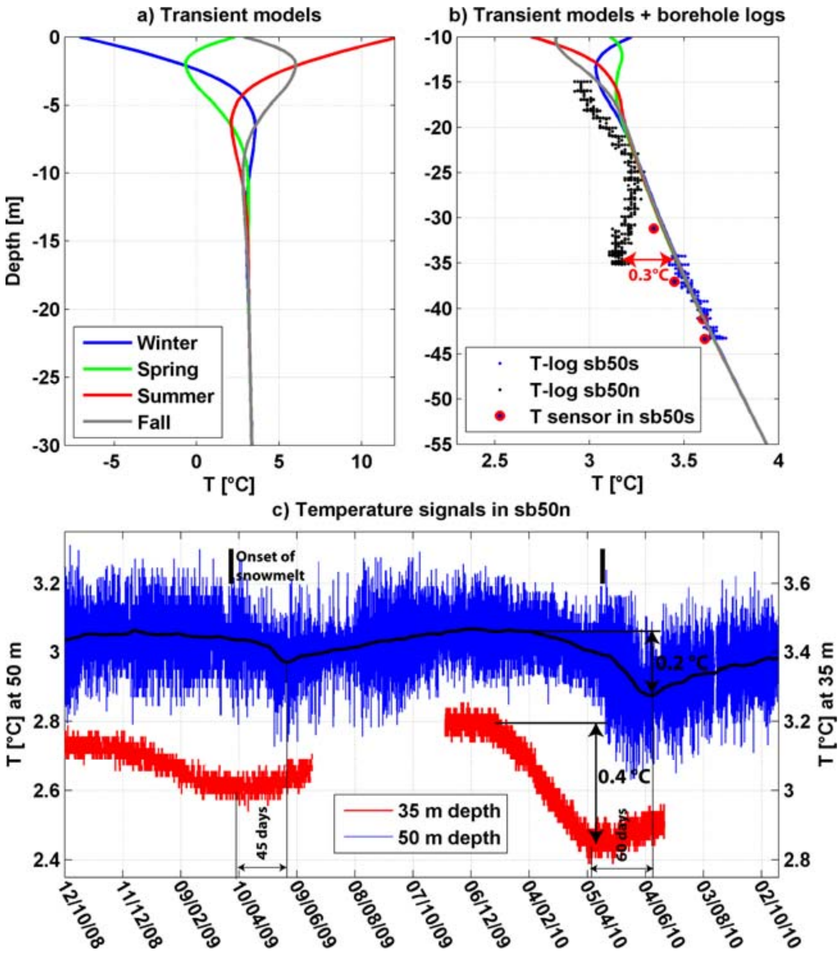

Figure 7.11: a) Seasonal temperature profiles from transient conductive models created by applying a sinusoidal temperature wave with an annual period at the ground surface. b) Transient temperature profiles from 10 – 55 m depth including temperatures measured during borehole logging and short term temperature monitoring in sb50s. c) Temperature time series from sb50n measured by the vibrating wire sensor at 50 m depth and a portable sensor at 35 m depth. Both time series show small annual changes in temperature.

7.2.4.2 Convective disturbances of the temperature field

Figure 7.11b highlights observed deviations in the borehole temperature data that can not be explained by either steady or transient heat conduction models. The temperature profile in sb50s is linear and predictable for a purely conductive temperature field. In this borehole at 50 m depth, long-term temperature time series showed constant temperature of 3.47 °C over the last 10 years. Short-term monitoring (of a few weeks) in 2009 and 2010 at various depths between 31 and 43 m also showed constant temperatures. In contrast, the measured temperature profile in sb50n (about 50 m north from sb50s) deviates from the modeled conductive temperature field by about 0.3 °C at 35 m depth. Temperatures first increase with depth as expected for conductive conditions to a depth of about 25 m, but then decrease again to about 3.15 °C at 35 m depth. Temperatures measured at 50 m are about 3.05 °C (as opposed to 3.47 °C in sb50s), and exhibit a small seasonal variation (Figure 7.11c). The peak-to-peak amplitude is about 0.2 °C and the minimum temperature occurs in spring. To verify these seasonal variations, a temperature datalogger (Keller druck DCX-22), was suspended in water at 35 m depth. Seasonal temperature changes (0.4 °C in 2010) were also measured at this depth, however, with a time shift to earlier times compared to the sensor at 50 m. The temperature decrease initiated in early January and the minimum value occurred about 1 - 2 months earlier than at 50 m depth.

Possible origins of observed deviations from the predicted conductive temperature field may be caused by either air or water flow in deep through-going fractures. While the two boreholes sb50n and sb120 are dry throughout the year, a rapid change in pressure head of about 1 m in spring was measured in sb50s. Temperatures, however, remain constant at that depth, and thus infiltrating water does not significantly disturb the deep temperature measured in this borehole. Similarly, seasonal signals in sb50n do not match the expected temperature variation caused by infiltrating water. The temperature decrease occurs in early January when barely any snowmelt has yet occurred. The temperature minimum at 50 m depth occurs in spring and may be related to snowmelt. However, at 35 m depth, the minimum is reached much earlier and temperatures have already begun to increase during snowmelt. Although we do not discard the possibility of infiltrating meltwater depressing temperature within the rock mass, we consider it more likely that the temperature disturbances observed in borehole sb50s are primarily caused by fracture air ventilation in winter.

7.2.5 Discussion of air ventilation processes

Observations of warm air ventilation from deep tension fractures indicate that winter-time convection cells within open fractures may be an important mechanism for transporting heat, both sensible and latent, out of the rock mass. Similar observations have been made in the Negev desert by Weisbrod et al. (2009), who describe the process of both heat and vapor transport from open fractures to free air at night and during winter when air temperatures favor convection. In this case, local convection cells are contained entirely within the fracture. Other cases have also been reported in literature where air ventilation is an important heat transport mechanism, e.g. in boreholes piercing strong topography (Weeks, 2001), or in highly-permeable blocky talus slopes (Delaloye and Lambiel, 2005; Philips et al, 2009). However, these latter ventilation processes differ from the fracture convection mechanism described by Weisbrod et al. (2009) and thought to explain our observations, since they include convection cells half within the permeable medium and half in the surrounding atmosphere. Buoyant warm air within the rock mass rises up into the atmosphere, and the resulting pressure difference forces air to invade the rock mass at lower elevations. The same ventilation effects are also reported from mines or embankments in permafrost (Goering and Kumar, 1996; Lai et al., 2004). The process relies on topography and is referred to as either 'topographic' or 'chimney effect'. It cannot be excluded in our case that similar effects also drive ventilation within the Randa instability, given the strong topography and the highly-fractured rock mass. However, as the model of local fracture convection cells contained entirely within a fracture can fully explain the observed temperature patterns, we consider fracture convection more plausible. Numerical modeling may provide useful insights into the feasibility of both described mechanisms.

Observed air ventilation at the Randa instability demonstrates the relevance of convective disturbances on temperatures at depth. The subsurface temperature field of alpine rock slopes is a key open question in permafrost research (Gruber and Haeberli, 2007). Often, conductive temperature models are used to approximate near-surface thermal conditions (Noetzli et al., 2007), while in a real rock mass the temperature field is frequently modified by air or water flow through discontinuities. Philips et al. (2009) demonstrated that air ventilation can strongly influence the occurrence of ice through the transport of both sensible and latent heat, even though measured temperature deviations are small in magnitude.

7.2.6 Implications for TM effects

As described in Chapter 6, rock slope deformation at the Randa instability appears to be controlled by TM-induced stresses. Previously, it was mentioned that fracture ventilation may enhance TM effects and play a role in synchronizing displacement rate changes at different depths. Here, the possible effect of convective air flow on the temporal deformation behavior is further discussed. The tensile fractures that are observed at the top of the instabilities are likely to have strongly irregular surfaces at depth (Willenberg et al., 2008a; Heincke et al., 2006a). Dislocation across these fractures includes both an opening and a shear component as they dislocate in toppling mode. Thus, a considerable number of interlocking asperities that are critically stressed may exist at depth. Although temperature changes along fractures at depth are small, even slight cooling could assist in releasing normal stress across these interlocking asperities and enhancing slip during winter. Further, temperature changes along fracture walls and related thermo-elastic reactions can result in stress changes being transferred to regions in the rock mass where temperatures remain constant. The mechanism is the same as the one suggested in Chapters 5 and 6, where near-surface temperature changes were shown to result in stress changes at greater depth due to 2D (or 3D) topography. Thus, stress changes induced by temperature changes along fracture walls would be superimposed to the ones from the near-surface temperature changes. An essential difference to TM-induced stress changes in a purely conductive temperature field is that a faster response can be expected from ventilation effects, especially for ventilation-induced normal stress release across interlocking asperities. Ventilation is related to a convective process that can quickly penetrate to greater depth, while conductive heat transport is relatively slow and limited to shallow depths.

In Figure 7.12a, the Rayleigh number time series is shown along with de-trended data from the in-place inclinometer at 12 m depth in borehole sb120. The low-pass filtered inclinometer data are colored according to the Rayleigh number indicating if convection conditions (red) or conduction conditions (blue) prevail. Good correlation can be seen between the onset or end of convection and the change in displacement rates (Figure 7.12b). In spring (May/June), for example, displacement rates abruptly change to slower rates as soon as convection stops. Similarly in fall (October/November), displacement rates increase as soon as convection starts. Extended time periods both in spring and fall have strongly fluctuating displacement rates associated with alternating convective and conductive conditions. During summer, several short-term accelerations correlate with short predicted convection time intervals.

While a variation of displacement rate with temperature, recorded at locations where temperatures remain constant, can be explained by TM effects, the observed short response time of displacement rates to air temperature changes is remarkable. From conductive TM effects alone one would rather expect delayed changes in displacement rates with variable onset times at different depths. Site-specific TM modeling in Chapter 6 could not reproduce the onset times of displacement rate changes as observed in the monitoring data. Instead, a significant phase lag of the displacement signals at different locations was predicted, which does not correspond to the nearly synchronous behavior of measured displacement time series at various depths. Therefore, we suggest that nearly immediate effects of short-term temperature changes on displacement rates could be explained by the additional aid of ventilation related TM effects. Air ventilation, characterized by the sharp transitions between convective and non-convective regimes, may be a possible cause for the short response times and the synchronous onset of displacement rate changes at depth.

Ventilation may also play a role in other slope instabilities. Krähenbühl (2004) reports three cases in Graubünden where instability deformations appeared to be mainly driven by near-surface temperature cycles. Displacement rates across fractures down to depths of 10 m were maximum in winter and stagnant or reversed in summer. Anchor forces also increased in winter, and stabilized or decreased in summer. Common to all sites was that the onset to increased displacement rates or anchor forces occurred as soon as mean daily air temperatures fell below 10 °C (around November). If this temperature is the threshold temperature for the onset of air convection, then fracture ventilation may play an additional important role in defining the onset of increased movements.

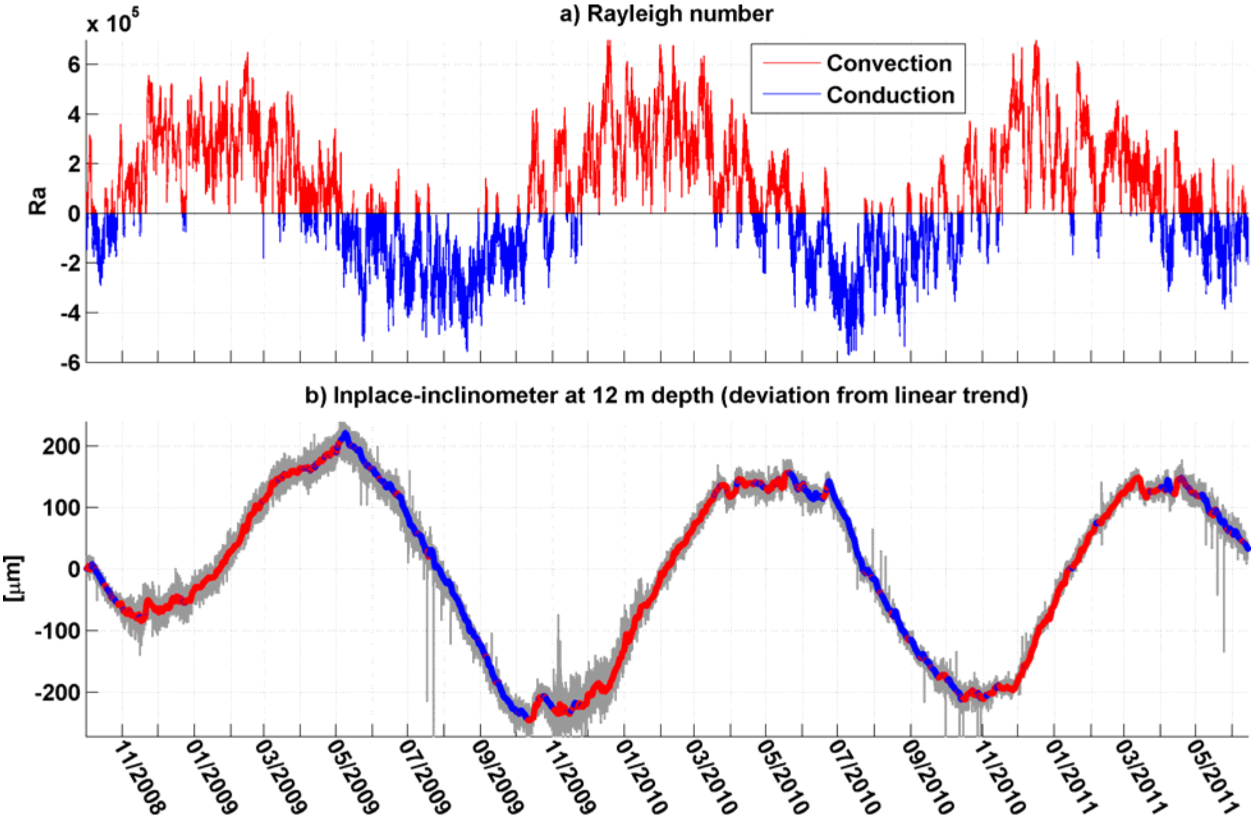

Figure 7.12: a) Rayleigh number time series. b) In-place inclinometer at 12 m depth with linear trend removed. Both unfiltered data and 3-days low-pass filtered time series are shown. Filtered data are colored according to the Rayleigh number.

7.3 Earthquake forcing

7.3.1 Introduction

In the Canton Valais, earthquakes with magnitude 6 or larger occur about every 100 years, and are commonly accompanied by rockslides and widespread rock falls. The earthquake hazard of the region is the highest in the Swiss Alps and is rated as moderate hazard on a global scale (Giardini et al., 1999). During the 1855 earthquake centered near Visp (M = 6.4), a large amount of rockfalls were reported in the Matter Valley by historical accounts (Fritsche et al. 2006). Similarly, the most recent major earthquake (Sierre 1946, M_w = 6.1) triggered several small rockfalls and landslides and one large rock avalanche (Rawilhorn, ~4-5-million m^3; Fritsche et al., 2009).

Earthquake-induced slope processes in Valais are studied within the framework of the project COGEAR (COupled seismogenic GEohazards in Alpine Regions, funded by the ETH competence center CCES). A major focus is the Randa instability, which became the subject of numerous seismic investigations (Burjanek et al., 2010). Also part of the study was the installation of the fiber-optic strain system dedicated to record dynamic and permanent strain resulting from regional earthquakes (Moore et al., 2010). In May 2010, a small earthquake (M_w = 3.4) occurred roughly 5 km north from Randa and at a focal depth of ~5 km. The radiated seismic waves triggered the fiber-optic system, which recorded continuous displacement data across the two monitored surface tension fractures. Here, we summarize the outcomes of seismic investigations conducted since 2007 in cooperation with the Swiss Seismological Service (SED), and present deformation data recorded during the May 2010 earthquake. We then present results from a numerical study attempting to understand and reproduce some aspects of the observed seismic response of the Randa instability.

7.3.2 Seismic investigations

Different seismological investigations were performed at Randa between 2008 and 2010 focusing on the seismic response of the instability to ambient vibrations and nearby earthquakes. Seismic surveys and data processing were performed by the SED (esp. Jan Burjanek), these included:

- Ambient vibration array measurements were performed in June 2008, originally aimed at determining shear-wave velocity profiles within and outside of the unstable rock mass. In the end it was not possible to extract velocity profiles, however the data could be explored in terms of amplification and polarization of the wave field in the vicinity of the unstable slope. Site-to-reference spectral ratios were extracted, comparing spectral amplification within the instability to a reference station on nearby stable ground. Furthermore, wave field polarization as a function of frequency could be deduced from recordings within the instability.
- Two semi-permanent 5s seismometers were installed in summer 2009, one with the instability and one on adjacent stable rock. Site-to-reference spectral rations were calculated between these two stations from seven regional earthquake recordings.
- Triggered seismic data from 80 regional earthquakes were recorded by a micro-seismic array of nine 3-component-geophones between 2002 and 2004 (see Spillmann et al., 2007). These data

were reprocessed with special focus on spectral amplification and polarization within the unstable rock mass.

Ambient vibration array measurements were presented by Burjanek et al. (2010) and partly reproduced in Figure 7.13a and b. Spectral analysis with reference to a station within the stable area showed that strong amplification occurs within the instability. The boundary of the area with strong amplification coincides precisely with the boundary of the instability. Figure 7.13a and b show spectral amplification for 3 Hz (amplification factor ~5) and for 5 Hz (amplification factor >10) energy, respectively. Strong amplification was also assumed for 15 Hz (amplification factor ~30) energy. Similarly, polarization analysis of ambient noise at stations within the instability revealed that the preferential polarization is sub-horizontal and oriented parallel to the direction of maximum instability displacement. At some stations, the polarization direction deviated for two frequency bands of 2-10 Hz and 10-30 Hz. The orientations of the higher frequency band then coincided with the opening direction of nearby tension fractures. These measurements suggest that the wave field within the unstable rock mass appears to be dominated by normal mode vibration of individual blocks, superimposed on that of the larger instability.

Analysis of seven small regional earthquakes recorded with the two continuously operating stations (RAND1 and RAND2) showed complementary and supporting results to previous ambient noise measurements (thick black line in Figure 7.13d). Amplifications within the instability reached factors of up to 7 for a frequency band centered around 3 Hz (Figure 7.13d-e), and another local spectral peak was identified at 28 Hz. Reprocessing data recorded on the seismic array by Spillmann et al. (2007) for 80 small regional earthquakes again showed complementary results: site-to-reference amplification factors of up to 5 at a frequency of 3 Hz (Figure 7.13c), and strong polarization of the wave field in the direction of instability deformation (roughly 135° azimuth).

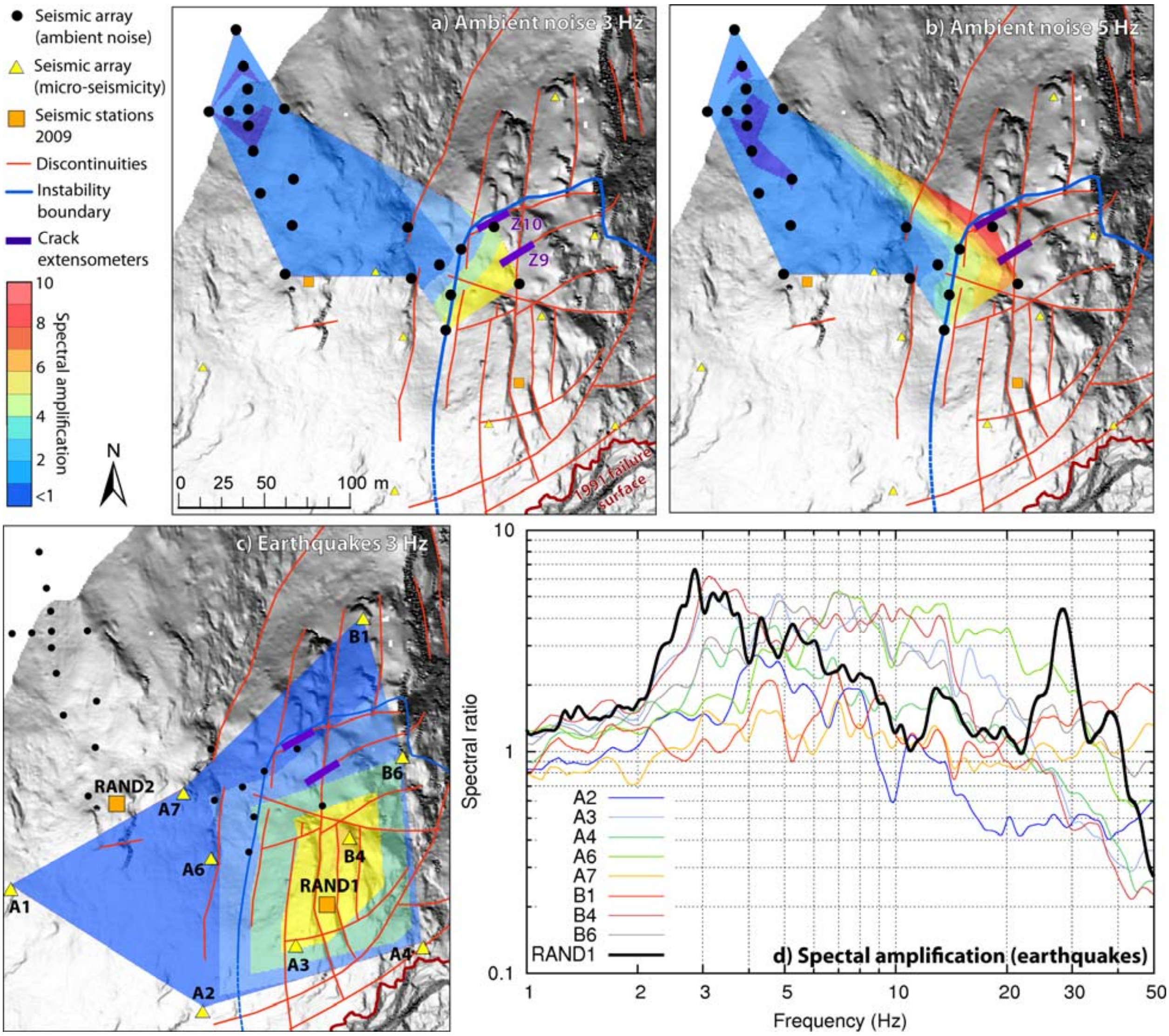

Figure 7.13: a) Layout of ambient noise measurements performed in June 2008, and a map of site-to-reference spectral amplification ratios at 3 Hz in the direction of polarization corresponding to the main direction of movement. b) Map of site-to-reference spectral amplification ratio at 5 Hz into the main direction of movement. c) Overview of micro-seismic array active between 2002 and 2004 (stations labeled A# and B#; Spillmann et al., 2007), and the two semi-permanent seismometers (RAND1 and RAND2) that were operational in summer 2009. Also included is the map of the site-to-reference spectral amplification at 3 Hz for the seismic array. d) Site-to-reference spectral ratios (amplification with respect to a station on stable ground). The reference station for the micro-seismic array is not shown; station RAND2 served as a reference for RAND1.

7.3.3 Dynamic strain from FO sensors

Fiber-optic strain sensors were installed in a borehole at three depths and at the surface across two tension fractures (see Section 2.3.9). The sensors measure strain at high resolution (~ 1 $\mu\varepsilon$) at a sampling rate of 100 Hz. The system is operated both in averaging mode and in triggered mode. When the triggering threshold is exceeded, 100 Hz data are recorded for 30 s (5 s pre-tigger, 25 s post-trigger) on all sensors, even if only one sensor met the triggering criterion.

On 15 May 2010, an earthquake of M_w = 3.4 occurred about 5 km north of Randa at a focal depth of 5 km. The earthquake was able to trigger the fiber-optic system at Randa. Data from the two surface strain gauges (Z9 and Z10) are presented in Figure 7.14, along with ground motion recorded at the nearest seismic station'Embd'from the SED. Note that the time axes do not represent absolute time, since the time base of the fiber-optic system is not synchronized with the Swiss seismic network; time series were simply shifted for optimal display. Also note that only a qualitative comparison of the signals is possible, since the FO sensors measure changes in fracture aperture and seismometers measure ground velocity. The amplitude of fracture displacement reached a peak value of around 50 µm. The permanent offset after the earthquake was less than 3 µm and should not be regarded as significant. Also presented in Figure 7.14 are the spectra for both the fiber-optic recordings and seismograms. The seismograms contain energy between 1 and 8 Hz, as well as two higher frequency peaks at 14 and 17 Hz. FO recordings show more distinct peaks at 3 and 5 Hz. Narrow band-pass filtering of the FO signals revealed that the 3 Hz signals at both tension fractures are in-phase, while the 5 Hz signals are out of phase. The FO signals exhibit longer duration than the seismic signals and more monochromatic compared to the seismograms. It is notable that borehole recordings not show any signals emerging above the noise level. One reason for this may be different orientations of the borehole sensors and surface sensors with respect to the wave field. More feasible, however, seems that measured signals are caused by a rock mass response limited to the near-surface, while deeper fractures remained locked during the transient event.

After the earthquake, the in-place inclinometer at 12 m depth showed a permanent offset of about 30 µm (recall the sampling rate of this instrument is 30 min). It is not clear, however, if this represents real deformation of the rock mass or is just an effect of shaking and readjustment of the sensors within the inclinometer casing. Inclinometer data often exhibit such steps, which cannot conclusively be assigned to real deformation events.

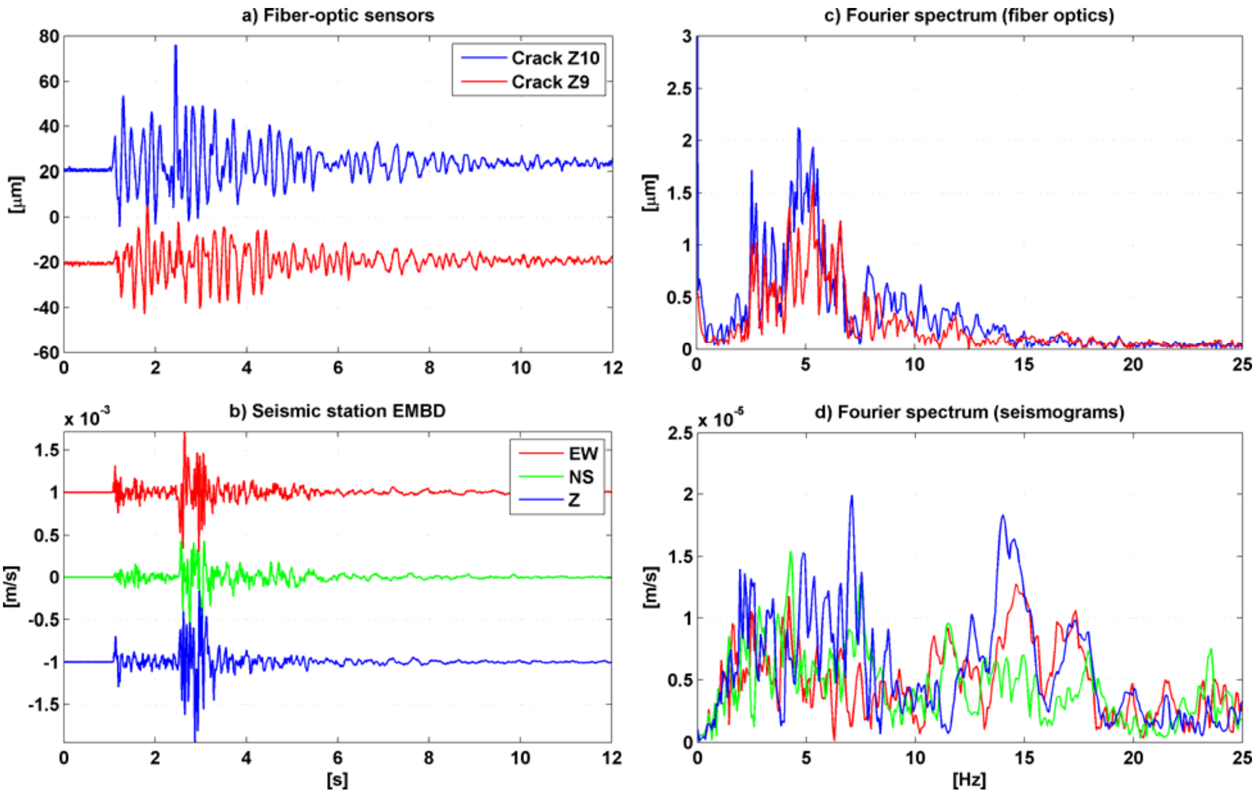

Figure 7.14: Data from the 15th May 2010 earthquake (source time: 05:09 UTC). a) Fiber-optic data from sensors spanning two surface tension fractures. b) Seismic data from station Embd. c) Spectra of fiber-optic data. Clearly visible are peaks at 3 Hz and ~5 Hz. d) Spectra of seismic data recorded at station Embd.

7.3.4 Interpretation

Both the seismic amplification characteristics and the dynamic signal from FO sensors are interpreted as effects of normal mode vibration of the unstable rock mass and individual blocks within it (Figure 7.15). The 5 Hz component of the FO signal, which is out of phase between the two sensors, may reflect normal mode motion of the block between the two fractures. The in-phase signal of 3 Hz, on the other hand, may reflect the normal mode motion of the entire unstable rock mass, which results in simultaneous opening and closing of all tension fractures within the instability. Similar interpretations can be deduced from amplification characteristics. Amplification at 3 Hz with polarization in the main direction of movement was found to occur at most station within the instability. Deviations from the main polarization direction occur at higher frequencies, at which the amplification pattern is more heterogeneous among different stations. Both polarization and normal mode vibration requires sufficient kinematic freedom of blocks, which is provided by open tension fractures at the ground surface. At depth, however, fractures are more confined and opening and closing is inhibited, so that normal mode vibrations are not detectable.

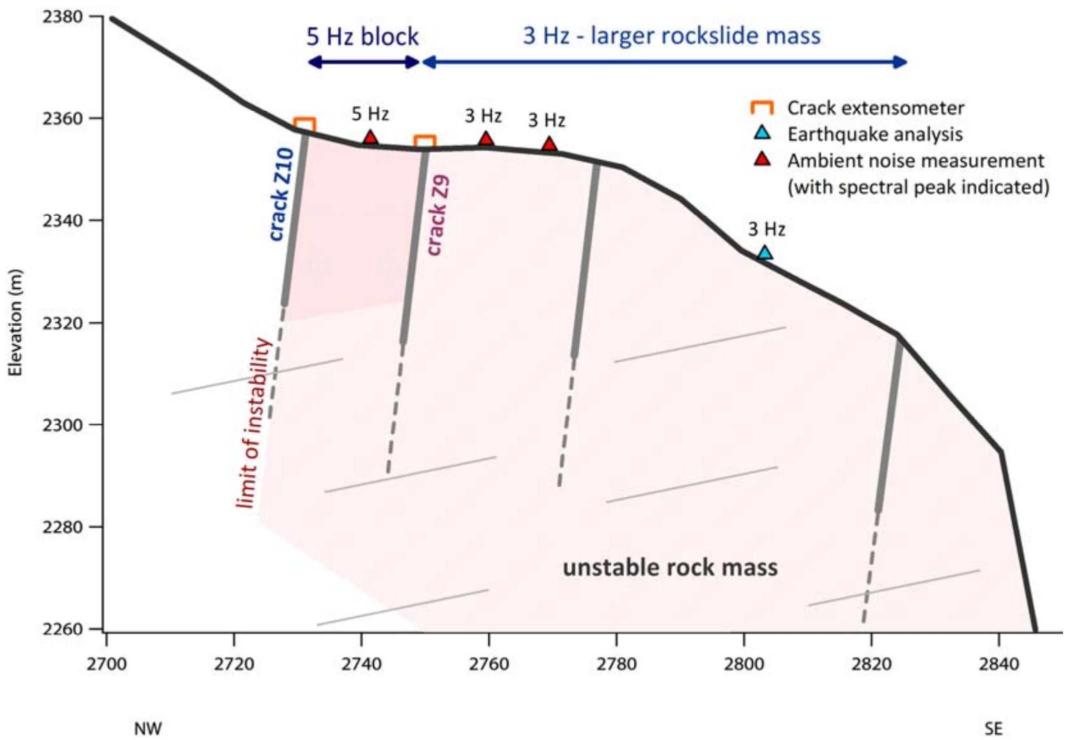

Figure 7.15: Schematic model summarizing the seismic response of the Randa instability.

Normal modes vibration of an unstable rock column (21000 m^3) was also described by Levy et al. (2010). They report resonance frequencies of about 3.6 Hz progressively decreasing as a result of rock bridge failure prior to collapse. Changes in resonant frequency were correlated with temperature, rainfall and freezing events. Detailed analysis was possible due to the simplified geometry of the rock column, which is only separated from the stable rock mass by a single tension fracture. While their study supports the suggested model of block vibration, the more complex geometry at Randa is expected to result in a complex seismic response.

7.3.5 Numerical simulation

In an attempt to understand the seismic response of the Randa rockslide, in particular during the May 2010 earthquake, a numerical study was performed with UDEC (Itasca, 2008). Several studies on rock slope response to dynamic loading have been previously preformed in UDEC, which demonstrated the capability of the code to simulate simple cases of slope response to earthquakes. For example, Zhao et al. (2008) verified the performance of dynamic analysis in UDEC with a generic study on wave transmission across discontinuities. Kveldsvik et al. (2009) and Bhasin and Kaynia (2004) perform seismic hazard analyses for two rockslides in Norway. Liu et al. (2004) simulated the response of a rock slope to nearby blasting. The advantage of UDEC compared to other numerical codes is the possibility to model the reaction of a discontinuous rather than continuous rock mass. The medium is represented as an assemblage of elastic blocks. The blocks can be thought to be connected by elastic springs, which can fail if they are assigned a failure criterion (e.g. Mohr-Coulomb). The springs represent normal and shear stiffness's of discontinuities.

Our numerical study takes advantage of the previously-constructed 2D kinematic model of the Randa instability. Discontinuities within this model are based on real observations of discontinuity sets, as well as of individual discontinuities relevant for deformation (presented in Chapter 4). At this stage, we focus only on the elastic response of the unstable rock mass and do not assign a failure criterion to the discontinuities. We attempt to model normal mode block vibrations at the surface by including highly-compliant discontinuities representing steeply-dipping tension fractures. They create a high degree of kinematic freedom, which was assumed for blocks limited by open fractures. In order to keep modeling and interpretation as simple as possible, we limit ourselves only to discontinuities that were mapped as open tension fractures at the top of the instability.

7.3.5.1 Model setup

Figure 7.16 shows the model geometry and boundary conditions. The geometry was adopted from the model presented previously in Chapter 4. For simplicity, however, only discontinuities corresponding to observed tension fractures were included. Further, discontinuities were restricted to the unstable area, which allows a clearer distinction between the seismic response of the stable and the unstable area. The model width was enlarged to minimize boundary effects on the wave field.

The lateral boundaries were changed to viscous boundaries, which absorb the incoming seismic waves. Wave absorption, however, is only perfect for waves at an incidence angle of 90°, while for lower incidence angles reflections and wave conversions occur. To maintain stresses at the boundaries, a so-called free-field boundary must be combined with the viscous boundary conditions. This is a 1D chain of nodes that exert supporting stress on the viscous boundaries. Thus, the model cannot be initiated with roller boundaries, as was done in Chapter 4. Instead, elastic model initiation has to be computed with stress boundary conditions. The stress field simulated in the model presented in Chapter 4 can thus not be reproduced, which has no implications for model results as long as purely elastic properties are applied and no failure is allowed. Velocity boundaries were chosen for the bottom model boundary at -500 m a.s.l. By assigning a velocity time history corresponding to the seismograms recorded at the station 'Embd' (Figure 7.14b), a vertically-propagating shear wave simulating the May 2010 earthquake is induced. The EW- and the Z-component of the seismograms was used as horizontal and vertical velocity history, respectively. We acknowledge that these time series do not correspond to the true incoming wave of the earthquake at that depth, and various effects are not accounted for, such as the radiation pattern from the source, path effects that are different for the Randa site and the station 'Embd', as well as surface effects at the instrument site. Thus, only amplitude and frequency content can be modeled reliably, but realistic waveforms cannot be reproduced.

The mesh size of the model was set to maximum 15 m. Wavelengths larger than 200 m should be reasonably represented, while wavelengths shorter than 40 m result in aliasing. Therefore, at minimum seismic velocities of 2000 m/s, only frequencies of less than 10 Hz are reliable, while frequencies >50 Hz are aliased. The input seismogram was thus filtered with a 15 Hz low-pass filter. Rayleigh damping ensuring numerical stability was set to 0.1 %.

Elastic properties of blocks and discontinuities are shown in Figure 7.16. The chosen properties correspond to seismic velocities of Vp = 3460 m/s and Vs = 2100 m/s, which are in accordance with the results of Heincke et al. (2006). They deduced P-wave velocities from 3D seismic refraction tomography, which gave about 2700 - 3800 m/s for the rock mass outside the instability and strongly heterogeneous velocities within the unstable rock mass in the range 1500 – 2700 m/s. Seismic velocities within the unstable (discontinuous) rock mass are a function of both elastic properties of the blocks and the discontinuity shear and normal stiffness, and cannot be calculated analytically. However, they are expected to be lower than within the continuous medium. The stiffness parameters used in our model were chosen such that all discontinuities simulating tension fractures (set F2) have a very low stiffness of 0.1 GPa/m. For all other discontinuities very high values (100 GPa/m) were chosen, suppressing any response to incident waves (Figure 7.12).

Prior to introducing a wave at the bottom model boundary, a force-equilibrium state was calculated to initiate gravitational forces. In UDEC this is accomplished by running the simulation until the ratio of unbalanced forces to the maximum force in the model falls below a certain threshold (in our case 5E-6). As observed from the results of dynamic models, the remaining small unbalanced forces within the model still induce measureable displacements, which exceed the amplitude of the wave field. The displacement series are characterized by very low frequency (~0.15 Hz) oscillation, which possibly represent the normal mode of the entire model. To eliminate such erroneous displacements, a model without an induced wave was computed for the same time span as the dynamic model. The 'zero-wave' model was than subtracted from the model from the dynamic model.

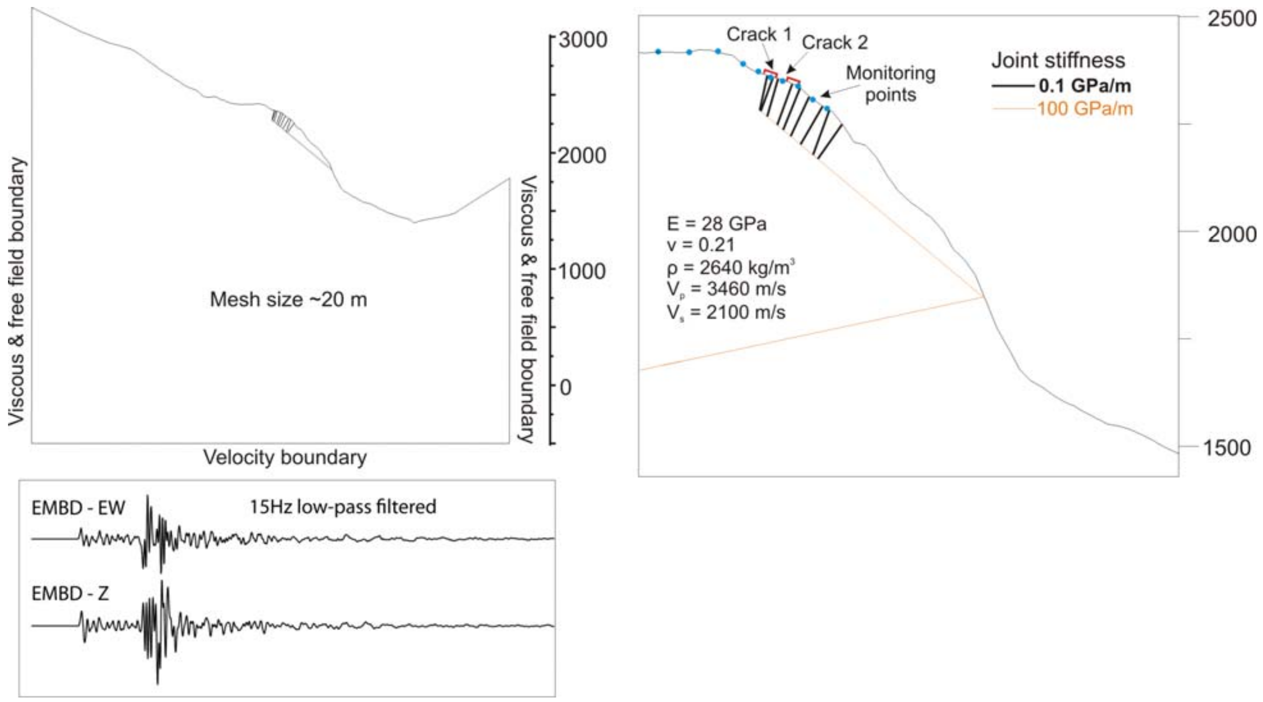

Figure 7.16: Model geometry, boundary conditions, input motion, and material properties of the dynamic model simulation of the Randa rock slope.

7.3.5.2 Dynamic model results

Figure 7.17a shows two modeled seismograms (horizontal component) from within and outside of the unstable rock mass. Also shown is the horizontal component of the input seismogram. The modeled seismograms from within the instability exhibit high frequency noise, which likely originates from the discontinuity contacts. Modeled time series were thus filtered with a 30 Hz low-pass filter. The seismogram from outside the instability shows observable P- and S-wave arrivals. The amplitude is larger than that of the input seismogram, due to the effect of the free surface. The seismogram from within the instability shows much higher amplitudes compared to that from outside the instability. Also shown in Figure 7.17b are the spectra of the input wave, and both spectra from outside and inside the instability. The spectral amplitudes from outside the instability are enhanced compared to the input spectrum, both through the free-surface effect and the long coda of the signal. However, we also recognize strong amplification of the signal within the instability compared to adjacent stable ground.

Figure 7.18a compares smoothed average spectra for five stations located both outside and inside the instability. Also shown is the ratio of these two mean spectra, which represents the modeled amplification within the instability compared to the stable area (Figure 7.18b). Amplification is greater than 1 throughout the entire frequency band and reaches values between 4 and 8 for distinct frequencies (e.g. 2-3, 4.9, 8 and 10 Hz). These results are also compared to a model where discontinuity stiffness for all discontinuities was set to very high values of 100 GPa/m in order to prevent dynamic displacements across discontinuities. For the latter ‘stiff’ model, spectral amplitudes from both outside and inside the instability are similar (Figure 7.18c). The amplification reaches maximum values of 1.5, but mostly varies around unity (Figure 7.18d).

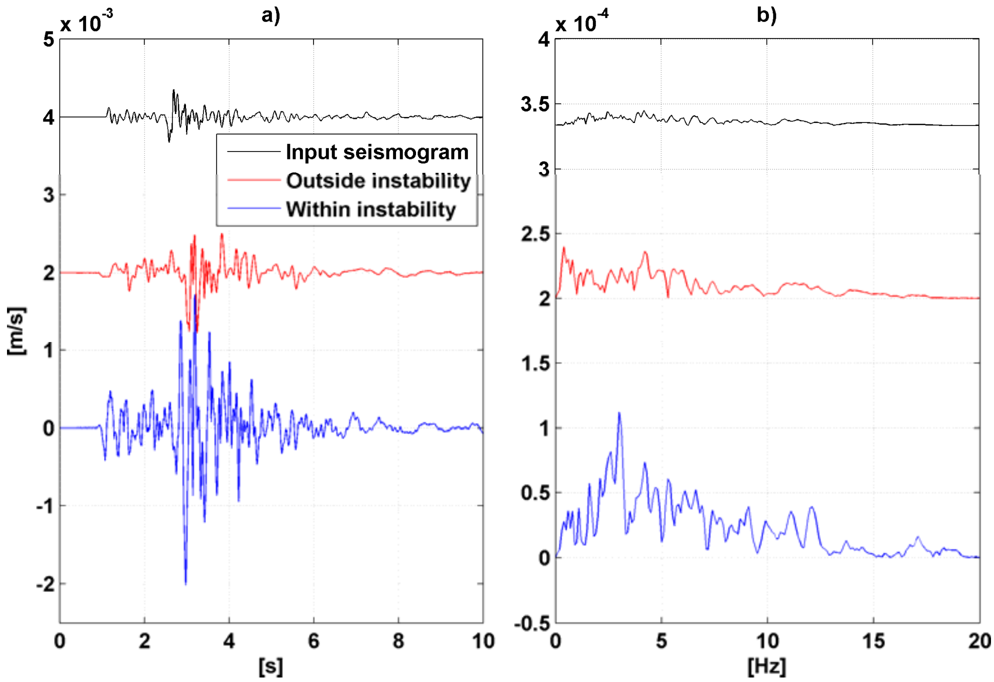

Figure 7.17: a) Input seismogram and modeled seismograms outside and within the unstable rock mass, extracted at the ground surface. Modeled seismograms were filtered with a 30 Hz low-pass filter. b) Spectra of the seismograms in a).

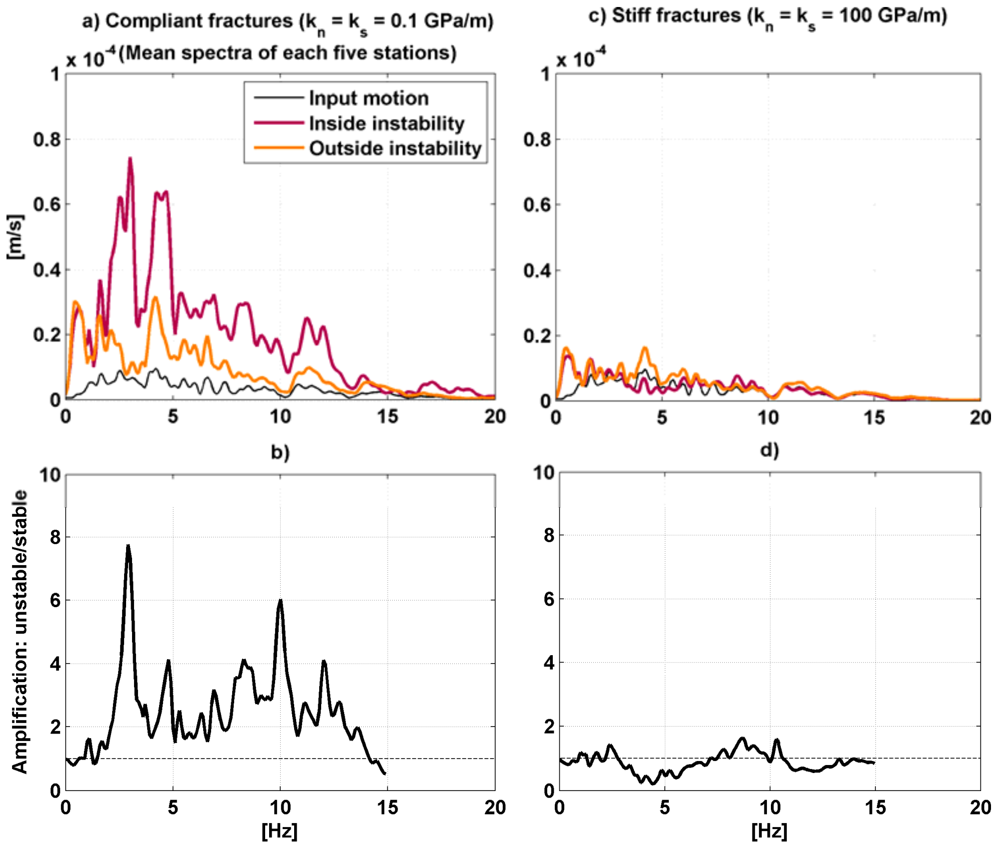

Figure 7.18: a) Mean spectra of five stations within and outside of the instability. b) The ratio of the two mean spectra shows the amplification of the instability with respect to adjacent stable ground. c) and d) Same as in a and b) for a model where all discontinuities are made very stiff to suppress their effect (normal and shear stiffness = 100 GPa/m).

Figure 7.19a and b show the measured and modeled relative displacement signals extracted across two fractures near the back of the instability (Figure 7.16). Also shown are the corresponding spectra (Figure 7.19c and d). The waveforms exhibit similar characteristics as the modeled seismograms in Figure 7.17. While the amplitudes are captured well, the waveforms deviate from the measured signals. The modeled signals exhibit a long coda with low frequencies probably produced by eigenmode vibration of the entire model geometry. The modeled spectra show greater amplitudes than the measured signals due to the long coda, however, similar to spectra of the measured signals, the modeled spectrum exhibits peaks at 2 - 3 Hz, 4.9 Hz, as well as a few smaller peaks between 5 – 15 Hz. Applying a narrow band-pass filter to these frequency ranges revealed that the two modeled fractures are nearly in-phase at 2 - 3 Hz and out-of-phase at 4.9 Hz and for higher frequencies. Thus, the model was able to reproduce measured fracture displacement signals in terms of amplitude and distinct frequency peaks; simply by setting discontinuity stiffness's to low values blocks are allowed to move in their normal modes. For higher stiffness values (i.e. 1 GPa/m), fracture displacement signals were orders of magnitude smaller than observed.

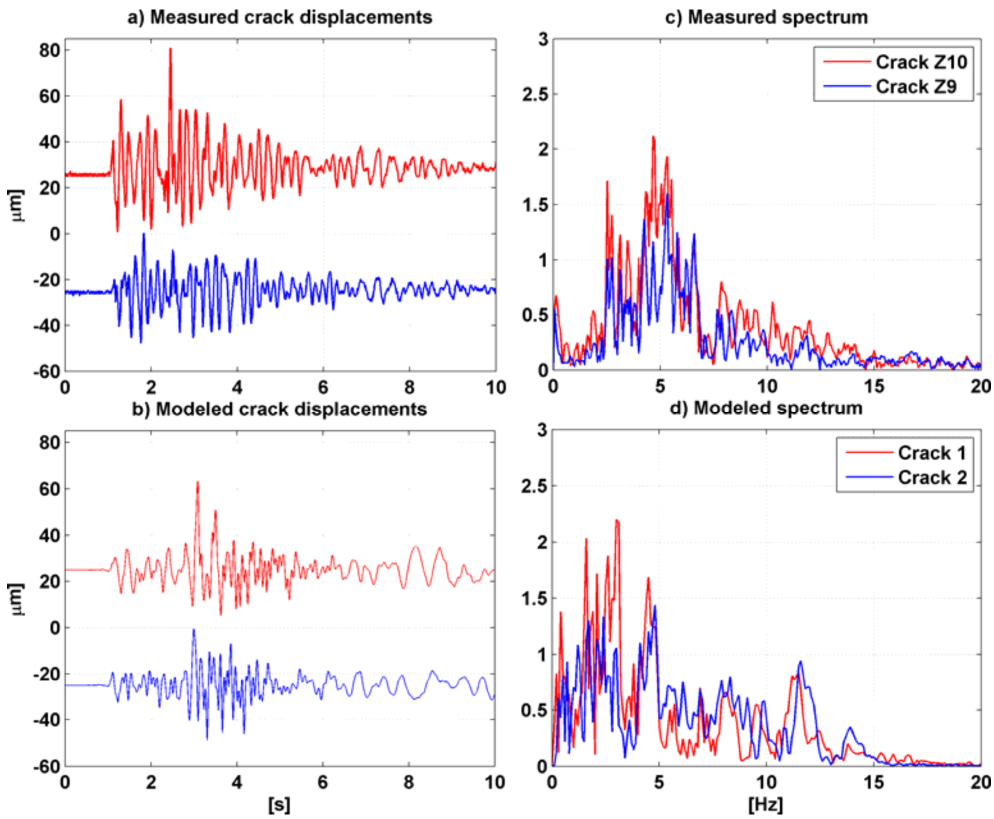

Figure 7.19:a) Fracture displacement signals measured with FO strain sensors. b) Modeled displacements across fractures, as shown in Figure 7.16. c) Spectrum of measured fracture displacements. d) Spectrum of modeled fracture displacements.

Normal and shear stress time series were extracted at two points along discontinuities at 15 m and 85 m depth in the model. Peak-to-peak stress amplitudes were found to be about 4 – 7 kPa at 15 m depth and about 3 – 4 kPa at the point at 85 m. This stress level did not change remarkably for models with higher stiffness values (e.g. 1 GPa/m). For comparison, we also calculated models with input motions from five other earthquakes with larger moment magnitudes. The events are listed in Table 7.2. For each event, recordings from the station nearest to the epicenter were chosen (distances varied between 4 and 12 km). Hypocentral depths range from 5 – 15 km, similar to those expected in the study area. Similar to aforementioned models the recordings were used as input motion at the base of the model. The induced stresses are listed in Table 7.2, representing the order of magnitude of the peak-to-peak amplitude of shear and normal stress at the aforementioned points in model. For most events, induced stresses were higher at the surface than at depth. We acknowledge that the computed stresses are only rough order-of-magnitude estimates, since hypocentral distances, instrument site responses, radiation patterns, etc. vary between all events. Also, for strong events the effect of surface waves may be considerably larger. Although a systematic comparison requires more events to be examined, the values still reveal the stress level expected from a nearby earthquake of a certain magnitude, which is a useful scoping calculation. Also shown in Table 7.2 are ranges of peak-to-peak fracture displacement amplitude expected for tension fractures at the top of the instability.

Table 7.2: Earthquakes used for computing induced stresses in the UDEC model. St. Niklaus (CH), Bormio (IT), Lac Vert (CH/FR), Anza (USA), Aquila (IT). Sources of data are ECOS (Earthquake catalogue of Switzerland), NGA database of the Pacific Earthquake Engineering Research Center. Data from the Aquila earthquake was provided by Jan Burjanek; source unknown. For each event, the signals of the closest seismic station were used. Thus, the indicated epicentral distance corresponds to the distance from the source to the nearest seismic station.

Event	Magnitude (Mw)	Depth [km]	Epicentral distance [km]	Induced stress [kPa]	Estimated fracture displacement [mm]
St. Niklaus (15/05/2010)	3.4	5	5	< 10	0.06 – 0.10
Bormio (06/04/2000)	4.1	15	10	< 20	0.06 – 0.09
Lac Vert (08/09/2005)	4.7	6	4	< 300	1.0 – 1.2
Anza (31/10/2001)	4.9	15	12	< 700	2.1 – 3.9
Anza (25/02/1980)	5.2	13.6	7.5	< 800	3.3 – 4.8
Aquila (06/04/2009)	6.3	8.8	4.4	< 5000	23 – 35

7.3.6 Conclusion

Investigations at the Randa rock slope instability revealed a number of interesting features regarding seismic response of the unstable rock mass. From analysis of ambient noise recordings and signals of nearby earthquakes, it was found that the accessible part of the Randa instability exhibits strong amplification at frequencies of 3 and 5 Hz. Ambient noise characteristics further showed that amplification is polarized in the direction parallel to the main direction of movement. Such seismic response indicates that rock slope instabilities can exhibit much greater amplification than topographic amplification alone, as typically assumed. Amplification factors reach up to a factor of 10 for the frequencies range between 1 – 10 Hz, but preferably occur at distinct frequencies. These likely correspond to resonant frequencies of blocks and are expression of their normal mode vibration with sufficient kinematic freedom.

Fracture displacements recorded by FO strain sensors during the May 2010 earthquake again showed spectral peaks at around 3 and 5 Hz. These data reflect opening and closing of open tensions fractures due to normal mode vibration of the blocks adjacent to the fractures. The data also proved the capability of the FO system to capture co-seismic deformation during small earthquakes.

Dynamic numerical simulations in UDEC were able to reproduce basics of the observed rock mass response to a nearby earthquake. By modeling the purely elastic response to the May 2010 earthquake, amplification characteristics within the instability, as well as dynamic fracture displacements could be reproduced. Modeled spectral amplification factors were on the same order of magnitude as the measured ones. Amplitude and frequency content of the fracture displacements were also reasonably reproduced. Similar to the recorded fracture displacements, modeled signals were in-phase at lower frequency peaks and out-of-phase at higher frequencies. Key to the model results was the choice of low normal and shear stiffness values for the discontinuity set forming opening tension fractures. Thus, the blocks are only weakly connected and have kinematic freedom to move. The model confirmed that the dynamic rock mass response is set by normal mode vibration of individual blocks that are coupled to each other by highly compliant tension fractures.

7.3.7 Suggestion for further dynamic UDEC modeling

Numerical models presented in this chapter test the capabilities of UDEC in dynamic modeling of the Randa instability, and are a first attempt to model its seismic response. As further numerical investigations go beyond the scope of this PhD thesis, some experience gained and outstanding issues for further modeling are summarized here:

- Model results strongly depend on fracture stiffness. Currently only a constant value of 0.1 GPa/m is used along the entire discontinuity length disregarding changing normal stress. Fracture stiffness in literature is generally higher than the value used and is dependent on normal stress along the discontinuity (Zangerl et al., 2008). For granitic rock, characteristic stiffness values of 25 – 110 (1/mm) are realistic, which corresponds to normal stiffness of about 6 – 30 GPa/m for 10 m overburden (normal stress of 0.27 MPa). However, the value used here may be justified for tension fractures that are open down to depths of >80 m. Nevertheless, stress-dependent stiffness values should be used for more realistic modeling of block vibration.
- Investigating amplification for one real earthquake represents a specialized single case study, and may not allow for general conclusions. Different results could be encountered if the response to a wide range of earthquakes is modeled and analyzed jointly. An easier strategy was applied by Levy et al. (2010), who instead of modeling real earthquake signals, used white noise as the input motion.
- Including brittle-plastic behavior along discontinuities could allow for analyzing failure resulting from nearby earthquake of different magnitudes. Such analysis, however, strongly depends on the stress and failure state of the instability prior to earthquake loading. Thus, stress boundary conditions influence the results and need to be considered carefully. The kinematic model as presented in Chapter 4 included roller side boundaries. Changing to stress boundary conditions requires recalibration of the model first towards appropriate kinematics and displacement patterns.
- The input motion is simply the recorded seismogram of the station nearest to the epicenter and at a similar distance as the Randa instability. It does not accurately represent ground motion at the bottom model boundary. More accurate input motion should be corrected for effects of the

site surface, source-site path and the radiation pattern of the source. Such corrections are complex and can only be performed if properties of the station site, seismic velocity model, as well as source location and moment tensor are known accurately.

7.4 Comparison of different driving factors

Investigation of several driving factors at the Randa instability allows qualitative comparison of the different effects. For each mechanism relevant to deformation of the instability, an order of magnitude estimate of the stresses involved was obtained. The main outcomes are summarized here in a comparative manner:

- *TM effects:* Numerical models in Chapter 5 demonstrated that stresses induced along discontinuities by near-surface thermo-elastic strains are >1 MPa within the thermal active layer. Below, at depths of constant temperature, induced stress changes are on the order of 10 – 100 kPa. Both shear and normal stresses change in a complex manner depending on topography, location of the discontinuity within the rock mass, discontinuity orientation, elastic properties, etc.
- *Air ventilation:* Observation of open air vents in the snowpack revealed that the conductive temperature field of the rock mass is disturbed by air ventilation in deep tension fractures. Thus, normal stress across critically stressed asperities at depth of ventilated fractures may be released through thermal contraction of the fracture walls. Similar to TM effects described in the previous item and Chapter 5, stresses induced by temperature changes along fracture walls by may also be transferred to regions of constant temperature.
- *Groundwater:* Changes in water pressure at the Randa instability were measured to be around 10 – 20 kPa. The measurements, however, are limited to a pocket of presumably perched groundwater, while most of the unstable rock mass is likely to be drained. Observations of springs revealed that the groundwater table may reach the basal sliding surface in spring and after heavy rainfall, and might locally affect the stability (e.g. induce slip along the basal sliding surface close to where it is daylighting), However, large groundwater pressures affecting the entire stability, especially in higher portions of the instability, are unlikely. Generally groundwater pressure changes affect normal stresses within the rock mass; normal stress changes of 10 kPa, 100 kPa, or 1 MPa correspond to water pressure heads of 1 m, 10 m, or 100 m respectively. Thus, even if the groundwater table did change by 100 m, stress changes would be similar to those expected for annual TM cycling. However, groundwater related stress changes would affect a much larger volume of rock compared to TM-induced stress changes, which are greatest in the near surface and decay with depth.
- *Ice formation in fractures:* In our case, very little can be deduced about the stresses involved during freezing of saturated soil infill in tension fractures. Values found in literature suggest tensile stresses on the order of 100 kPa – 1 MPa (Davidson and Nye, 1985; Matzuoka and Murton, 2008). They are limited to fractures where water is available and conditions are favorable for freezing-induced stresses. Furthermore, freezing can only occur in the near-surface where subzero temperature can penetrate (1 – 3 m in our case). We note that such stresses can also be transmitted to depth, similar to TM stress changes.

- *Seismicity:* Stresses induced by nearby earthquakes were estimated for different events with help of numerical models. Results show that stresses induced by a Mw = 3.4 earthquake at about 5 km distance are below 10 kPa, but can reach up to 5 MPa for a M = 6.3 event. Compared to other forcing factors mentioned above, such earthquake related stress changes affect the entire rock mass, while others are limited to particular range of influence. Stress changes will be somewhat higher close to the surface due to surface waves. Further, such stress changes are characterized by very high loading rates as they act within the frequency range of 0.1 – 10 Hz. Thus, they are difficult to compare to induced stress changes acting on time scales of days to years.

As shown in Chapter 6, TM effects alone can sufficiently explain observed temporal displacement trends at the Randa instability, and thus are likely to be the dominant driving factor of ongoing deformation. The phenomenon may be enhanced through air ventilation within deep tension fractures. Freezing water within soil-filled fractures, on the other hand, is assessed to be of minor importance. Effects of groundwater pressure are also secondary. However, we emphasize that discontinuities at depth are already critically stressed and allow slip through TM-induced stress cycles, which are comparably small in amplitude (10 – 100 kPa below 20 m). Hence, if significant groundwater pressure could build up within the unstable rock mass, it may adversely affect stability. It is uncertain, however, if this may actually happen during a particularly heavy rainstorm occurring around the time of snowmelt, given that the rock mass is strongly fractured and highly permeable. Similarly, we expect that permanent slip will be induced by a nearby earthquake (at <15 km distance). Stress changes comparable to TM-induced stresses at depth may occur for earthquakes stronger than M = 4 – 4.5. A nearby earthquake of M = 6.5 is likely to result in significant permanent deformation. However, it is unclear if comparison to other forcing factors is valid, since the loading rates are widely different for transient earthquake shaking and annual TM cycles.

8. CONCLUSIONS

8.1 Summary

Building from results of former studies at the Randa rockslide (i.e. Willenberg, 2004; Heincke, 2005; Spillmann; 2006), this thesis contributed to advancing knowledge of the internal structure, kinematics, and failure mechanisms at the current Randa instability. Open questions were successfully addressed regarding the lower extent of the instability, structures visible on the inaccessible 1991 failure surface, and mechanisms driving the temporal displacement behavior. Major outcomes of this work are summarized as follows:

8.1.1 Structure and kinematics of the Randa instability

- Analysis of GB-DInSAR displacement maps revealed the presence and location of both a basal sliding surface and lateral release plane bounding the current instability. The basal sliding surface daylights at the contact between the orthogneiss and paragneiss units. The lateral release surface bounding the current instability to the south corresponds to the continuation of the lateral release plane of the May 1991 failure. Using these identified boundaries, the unstable rock mass was accurately delineated and its approximate volume estimated to be 5 – 6 million m^3. Displacement maps further indicated that two kinematic modes may be active within the instability, toppling in the upper area (> 2150 m) and translational sliding below. Combined analyses demonstrated the potential of radar interferometry to not simply detect landslide movement, but also to characterize the displacement field and deduce possible failure kinematics.
- Combined helicopter-based LiDAR and photogrammetry revealed detailed structural information from the inaccessible 1991 failure surfaces, and gave important new insights into mechanisms acting during the 1991 failures. While shearing on sliding surfaces was dominant in the lower portions of the paragneiss unit, a combination of shearing and breaking of rock bridges prevailed in the middle portion of the scarp. With increasing altitude, fractured rock bridges became more evident indicating a transition to a predominantly tensile regime. Analysis of discontinuities delineated from LiDAR and photogrammetry using ArcGIS allowed extending the 3D structural model from the top of the instability to the lower inaccessible area. Six discontinuity sets were distinguished, which in part confirmed sets identified in previous studies, but additionally include the down-dipping sets necessary to allow translational sliding.
- Stereographic analysis of the identified discontinuity sets confirmed the two predominant kinematic modes at the current instability: toppling in the upper portion (>2150 m) and translational sliding below. In combination with displacement data from new geodetic measurements at the top of the instability, new insights into 3D kinematics were obtained. In particular, it was shown that wedge sliding involving the lateral release plane is not feasible due to geometrical constraints and since dislocation across this discontinuity exhibits a significant opening component.
- The suggested kinematics of the entire unstable rock mass was further explored with numerical modeling in UDEC. It was possible to construct a model that reproduced the observed displacement patterns both at depth (in borehole sb120) as well as at the surface. This model was the foundation for subsequent analyses exploring the temporal behavior of the instability.

- The present study of rock slope kinematics at the Randa instability demonstrated the value of using complementary technologies, such as geophysical imaging, geological and geotechnical investigations, remote sensing, and numerical modeling in a comprehensive manner. Combination of different analysis techniques, each with its particular advantages, proved to be powerful for resolving spatial behavior of an unstable rock mass.

8.1.2 Temporal behavior of the Randa instability

- The automatic monitoring system operational at the top of the instability before 2008 included surface crack extensometers, as well as piezometric pressure sensors and in-place inclinometers in boreholes. In summer 2008, the system was upgraded with rock temperature sensors, meteorological sensors, and a high-resolution dynamic strain monitoring system based on fiber optic sensor technology. Further, additional local geodetic surveys were performed monthly over one year. These data served as solid basis to analyze the temporal behavior of ongoing deformations at Randa.
- Comprehensive analysis of monitoring data revealed that instability deformation reacts primarily to temperature changes rather than to changes of groundwater pressure. Displacement rates increase as soon as temperatures drop in fall and are at a minimum in summer. Annual rate variations were measured both at the surface and at various depths to 68 m where temperatures are constant throughout the year. The observed behavior is unexpected compared to most cases of landslides reported in literature, where displacement rates usually increase after snowmelt or heavy rainfall. It was hypothesized that cyclic thermo-elastic strains at shallow depth drive the observed temporal trend of the entire instability.
- A numerical study exploring thermo-mechanical coupling in a simplified slope explored the effect of annual temperature cycles on slope deformation. The models allowed slip along prescribed discontinuities creating the two kinematic modes observed at the Randa instability: toppling and sliding. Due to topography and elasticity of the rock mass, thermally-induced strain is not limited to shallow depths where temperatures vary (i.e. the thermal active layer), but also occurs at greater depth. Induced stress changes at depth down to 100 m, although small in amplitude (~10 – 100 kPa), are able to induce slip along discontinuities if these are close to their failure limit, and can thus also lead to propagation of slip fronts. The mechanism, referred to as the thermo-mechanical effect, depends on rock mass stiffness, discontinuity strength and post-peak behavior (i.e. slip weakening). Model results showed that thermo-mechanical forcing can drive progressive failure, even at depths below the thermal active layer.
- Thermo-mechanical models using the Randa-specific geometry and properties derived from kinematic analysis were able to reasonably reproduce observed displacement rates and magnitudes of annual variation. The observed synchronous change in displacement rates recorded at various depths and at the surface was not successfully reproduced. It was suggested that additional effects (e.g. fracture air ventilation) may contribute to thermo-mechanical forcing.
- Observations of open holes in the snowpack exhausting warm air in winter indicated that the deep conductive temperature field may be disturbed by buoyancy-driven convective air ventilation. Fracture air temperatures measured down to a depth of 2.5 m confirmed that air convection

occurs throughout winter when ambient air temperatures are negative, while heat diffusion prevails in summer. The resulting thermo-elastic reaction of the rock mass at depth could contribute to thermo-mechanical forcing. As the onset of convection in winter is rather abrupt and occurs simultaneously at all depths affected, it may explain the synchronous nature of thermo-mechanical induced deformation observed at depth. Freezing-related fracture displacement was also postulated but is assumed to be only a localized effect, unlikely to influence temporal behavior of the entire instability.

- Measurements of the seismic response at the Randa instability revealed ground motion amplification factors of 5-10 within the unstable rock mass, preferentially at distinct frequencies of 3 and 5 Hz. Strong polarization of the wave field was also identified, oriented in the direction of instability movement. Dynamic fracture opening recorded during a nearby earthquake (M_w = 3.4) with fiber optic strain sensors at the surface similarly showed two frequency peaks at 3 and 5 Hz, and a maximum peak-to-peak amplitude of about 60 µm. Dynamic numerical modeling was able to reproduce fundamentals of the observed seismic response simply by allowing normal mode vibration of blocks bounded by compliant fractures. Amplification within the unstable rock mass is much larger than expected for topographic amplification alone, and was shown to be caused by steeply-dipping compliant fractures, which are common in rock slope instabilities.

8.2 Outlook

Together with previous studies at the Randa instability (e.g. Phase I and II of this project, Willenberg, 2004; Heincke, 2005; Spillmann, 2006; studies by other groups e.g., Sartori et al., 2003; Jaboyedoff et al., 2004), the presented work achieves thorough understanding of the currently unstable rock mass. Open questions and aspects that have not been completely addressed include hydrogeology in the vicinity of the Randa instability, the reaction of the rock mass to a nearby major (M_w>6) earthquake, displacement thresholds and criteria indicating impending failure, and run-out analysis for future catastrophic failure. More detailed explanation is given in the follow sections.

8.2.1 Hydrogeology

Large uncertainties remain concerning the hydrogeological setting in the vicinity of the Randa instability. Hydrogeological investigations in the area were initiated (Alpiger, 2010), but span only a short time period of a few months and do not allow any final conclusions on the temporal evolution of the groundwater table. Although the groundwater table does not appear to affect the currently unstable rock mass, understanding its temporal behavior would be valuable with regards to the steep rock slopes north of Randa in the Matter valley, which may react on groundwater pressure. While a detailed structural and kinematic analysis of the over-steepened valley flanks north of Randa is available (Yugsi Molina, 2010), little is known regarding temporal behavior and driving factors of these potentially unstable slopes. A more thorough knowledge of the hydrogeological conditions within these slopes would help assess the role of groundwater as a destabilizing factor for other nearby instabilities, such as the Medji rockslide in 2003 (Yugsi Molina, 2010; Ladner et al., 2003). In general, hydrogeological characterization of rock masses in steep terrain is a difficult but feasible task (Thoeny, 2009). Mapping of spring lines, characterization of springs, installation of weirs to automatically record the temporal evolution of electric conductivity and flow rates, etc. could yield new insights into the spatial distribution and seasonal evolution of groundwater conditions. Hydraulic modeling in UDEC calibrated from observations at Randa may additionally help obtain new conceptual insights into groundwater conditions in steep competent rock slopes.

8.2.2 Seismic response

Insights into the seismic response of the Randa instability have been obtained through collaboration with the CCES project COGEAR. As earthquake forcing is a major contributor to rock slope failure in Valais (Fritsche et al., 2006, 2009), it is certainly relevant to explore the reaction of the Randa instability to an M=6 event. Numerical modeling, however, has so far been limited to purely elastic material and discontinuity behavior, which did not allow for prediction of permanent deformation induced by earthquakes. Applying seismic loading to the kinematic model derived in Chapter 4, which allows failure along discontinuities, would help obtaining insight into the reaction of the rock mass to nearby earthquakes. Different scenarios regarding magnitude and epicentral distance could be constructed, yielding a kind of probabilistic fragility analysis for the rock slope. However, this requires the model to be well calibrated and stresses prior to seismic loading to be equilibrated; difficulties regarding these issues were mentioned in Section 7.3.7.

8.2.3 Failure prediction: thresholds and scenarios

The unstable rock mass at Randa constitutes a significant threat for both the village and the valley infrastructure, and therefore investigation of future failure scenarios is of high practical relevance. To date, it is not entirely conclusive whether current movements might eventually cease, or accelerate until catastrophic failure. However, this work has identified a large amount of critically stressed discontinuity area within the rock mass, which suggests that future catastrophic failure may be likely.

Using long-term monitoring for early warning purposes requires estimating displacement or velocity thresholds above which failure is expected. To date, such thresholds cannot be derived from theoretical models and rely on experience gained from similar failures. In case of the second rockslide at Randa in May 1991, monitoring data including geodetic reflectors and fracture opening rates was available before the event and revealed the maximum displacement the failing rock mass could support. A geodetic point at about 60 m distance from the April 1991 failure showed an exponential increase of displacement, until a maximum cumulative value of about 1.7 m when the second failure occurred. At the same time, fractures at the top of the instability opened about 200 – 300 mm between the two failures. Since the rock type of the current instability is the same as that which failed in May 1991, these maximum displacement values may also be representative for future failures, and could be regarded as preliminary failure thresholds. In 2003, another major rockslide occurred north of Randa above St. Niklaus (called the Medji rockslide) in the same orthogneiss material as the April 1991 failures (Ladner et al., 2004). Maximum displacement of about 1.6 m was reached shortly before failure, while a transition from linear to exponential displacement trends occurred after about 1.2 m. Fracture opening began to increase exponentially after about 300 mm and reached a maximum of about 750 mm. Careful assessment of displacement or velocity thresholds would not only be useful for predicting future failures at Randa, but is also an open question in landslide research. Further case studies of instabilities, for which displacement data are available until shortly before ultimate failure, may yield additional insight into characteristic failure thresholds.

The time of catastrophic failure is normally predicted using the inverse velocity method (Voight, 1989), which is based on a power-law description of the displacement rate prior to failure. Application of this method was successful for predicting the failure at Medji in 2003 (Ladner et al., 2004) and Val d'Infern (Krähenbühl, 2006). Commonly, prediction becomes more accurate as failure approaches. Often within a week before failure (however not in all cases) , it is possible to predict the time of failure with an accuracy of less than a day. For instabilities that have been slowly moving over a long time, like the Randa instability, accurate failure prediction is unrealistic. However, periodic inspection of displacement data from ongoing monitoring can reveal anomalous changes in the expected trend, which may indicate when the rock mass prepares for failure. Such long-term observation requires both maintenance and continuation of the monitoring system. It is also necessary to define criteria that reveal when deviations from the expected trend are statistically significant and indicate real changes in the temporal behavior, rather than just short-term excursions. For this purpose, the displacement behavior must be described with a function that fits previous recorded data – preferably one with some physical meaning – as well as a statistical measure describing the uncertainty (Norvik et al., 2010).

Often the idealized displacement behavior of a landslide is thought to be best described by a creep curve (Crosta and Agliardi, 2003), which includes primary creep (relaxation phase), secondary creep (linear regime), and tertiary creep (exponentially increasing displacement). Rarely, however, is an entire deformation history of a landslide available; beginning with the relaxation phase after a preceding failure until the final acceleration phase. Displacement data from between the two 1991 Randa failure resemble a typical creep curve (Schindler et al., 1993; Ischi, 1991), and could offer an occasion to study the behavior of the deforming rock mass until failure. In addition, data since the May 1991 failure offer the chance to study at least the relaxation phase and the onset of the linear phase. Jaboyedoff et al. (2004) found a power-law with superimposed sinusoidal annual variation to be the best fit to the first 7 years of geodetic displacement data after the 1991 failures:

$$\Delta d = 0.438 \cdot t^{0.72} + 2 \cdot \sin(2\pi t / 365) \tag{8.1}$$

Another possible function could be the S-shaped curve, suggested by Xiao et al. (2009) to describe the damage behavior of laboratory samples during fatigue tests, which strongly resembles the previously mentioned creep curve:

$$\Delta d = \alpha \left(\frac{\beta}{\beta - t} - 1 \right)^{\frac{1}{p}} \tag{8.2}$$

where Δd is displacement and α, β and p are constants described in more detail by Xiao et al. (2009). Figure 8.1a shows displacement data from monitoring Point 114 (see Figure 2.2b) with fitted S-shaped curve (Eq. 8.2). Best-fit parameter values are α = 615, β = 84.1, and p = 1.5, which fit the data with a mean residual of 2.5 mm. If a sinusoidal function with amplitude 2.1 mm and a phase offset of 26 days with respect to January 1 is superimposed on the S-shaped curve, the mean error reduces to 1.9 mm. Figure 8.1b shows a number of S-shaped curves, with the parameter β varied between 40 – 100, which also fit the geodetic data well. Also shown are two arbitrarily chosen failure thresholds, 1000 mm and 1700 mm. The results illustrate strong variability of solutions obtained through curve fitting. However, as time passes and additional displacement data become available, the temporal evolution can be described with increasing accuracy and any deviations assessed more reliably.

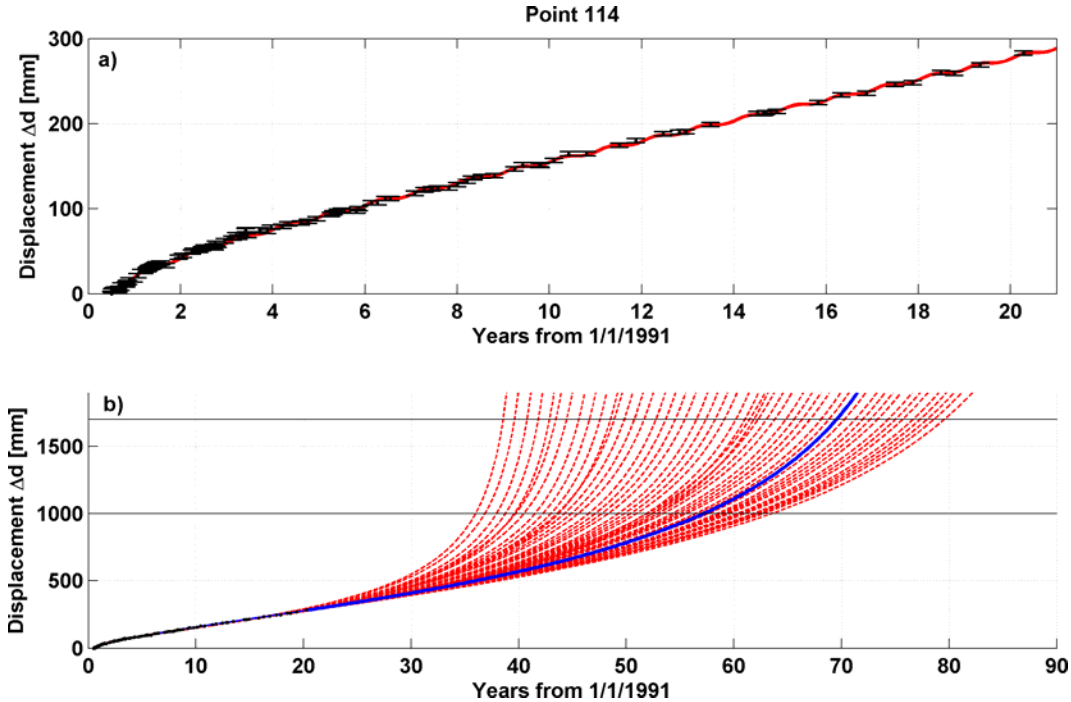

Figure 8.1: a) Geodetic data from monitoring Point 114 (see Figure 2.2b). Error bars are 2.5 mm. Data were fitted with an S-shaped creep curve using α = 615, β = 84.1, and p = 1.5 (Equation 8.2; Xiao et al., 2009) with a superimposed sinusoidal wave of one year period, 2.1 mm amplitude and a phase offset of 26 days with respect to January 1. The mean residual is 1.9 mm. b) A range best-fit curves for β varying between 40 and 100. The curves all fit the data reasonably well, but provide strongly varying predictions. Two failure thresholds of 1000 mm and 1700 mm are also shown. The blue curve is fits the data best and corresponds to the curve in a). Note the relaxation time after the 1991 failures; the linear regime is reached after about 3 years. Similar 'relaxation times' are predicted for TM induced displacements rates after temperature cycling is applied initially (see Chapter 5).

Regarding future rockslides, it is crucial to develop scenarios of the mode in which failure occurs. Questions to address include the total volume involved (which may be greater or smaller than the currently deforming rock mass), as well as the number events and their individual volumes. The volume of single rockslides in part controls the run-out distance and is thus essential information for hazard analysis. As both rockslides in 1991 were multi-stage events themselves, future failure may likely take place in a similar manner. The precise volume distribution of the 1991 events is not known in detail. The Swiss seismological service recorded a total of 10 triggered seismic events representing individual failures in 1991, seven on 18 April, one on 22 April, and two on 9 May. Unfortunately it is not possible to derive volume estimates from these seismograms (personal communication F. Dammeier, 2011). The empirical relationship between volume and Fahrböschung (Scheidegger, 1973) indicates that the volumes of individual events should not have exceeded 0.7 million m^3 for the rockslide on 18 April 1991 and 0.45 million m^3 for those on 9 May 1991. Future failure modes may also be derived with help of UDEC or 3DEC numerical models. Additionally, the fate of the slope after a future failure may be explored. As previous failures and the current instability belong to a retrogressive sequence of failures, it seems feasible that a new rock mass may again become unstable behind the current instability after a future event. Prediction of future instability extents may be assisted by numerical simulation.

8.2.4 Run-out analysis

Having derived possible volumes of individual failures in the past, scenarios of future run-out distances could be constructed. For the case of the current Randa instability, one can benefit from the possibility to calibrate run-out analyses using the 1991 failure events. Both empirical and numerical methods could be utilized. Simple empirical approaches include the previously mentioned relationship by Scheidegger (1973), or that by Hungr and Evans (1988) who suggested a Fahrböschungs angle of 27° for volumes less than 150'000 m^3. However, given the narrow valley width in the region, these methods may be strongly limited due to the non-linear run-out path and the possibility for run-up on the opposite valley flank. Instead, it is suggested to use more sophisticated tools such as numerical methods accounting for 3D topography, which may give more realistic run-out estimates. Numerical codes such as DAN-3D (Hungr and McDougall, 2009) or RAMMS (Christen et al., 2010) have proven to yield good results for 3D run-out analysis.

9. APPENDIX

9.1 Complete GB-DInSAR datasets

In the following section, the complete GB-DInSAR dataset obtained at the Randa instability is shown, in both 3D view (Figure 9.1), and in map view (Figure 9.2 and Figure 9.3): A subset of these images was presented in Chapter 3.

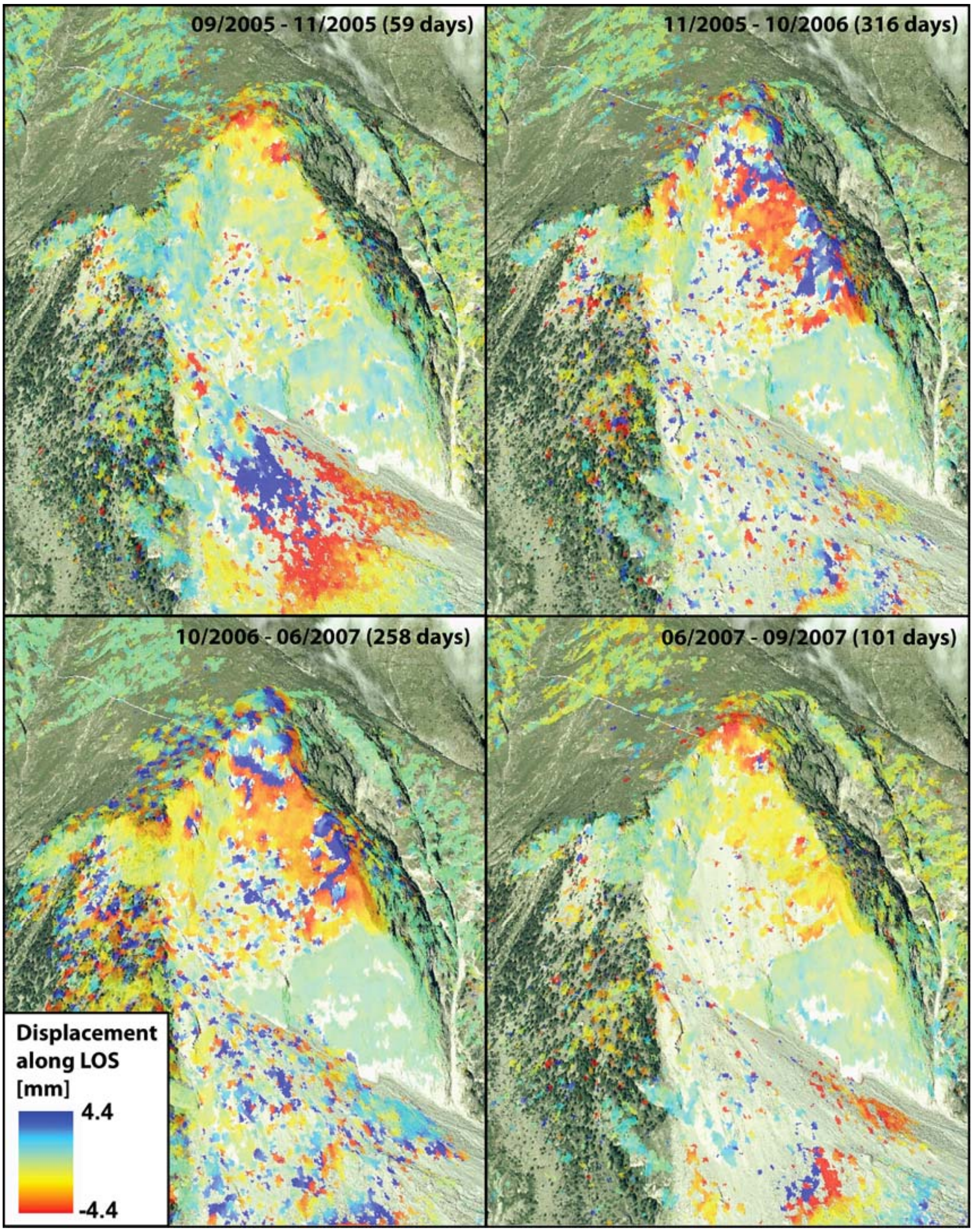

Figure 9.1: 3D scenes of GB-DInSAR displacement data as visualized from about 2000 m at the location of the radar base station.

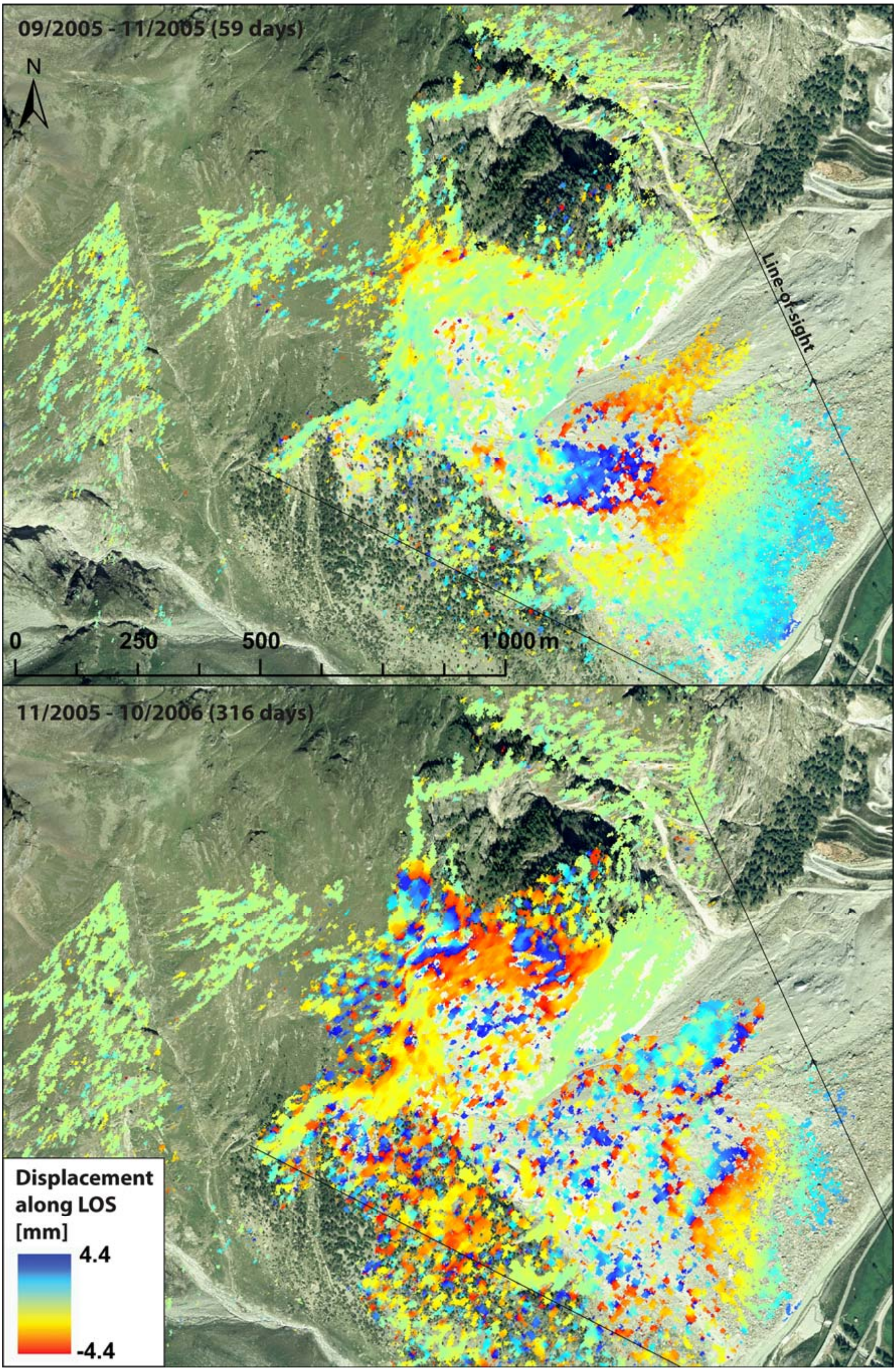

Figure 9.2: GB-DInSAR maps representing displacement between two subsequent time intervals. Also shown is the line-of-sight.

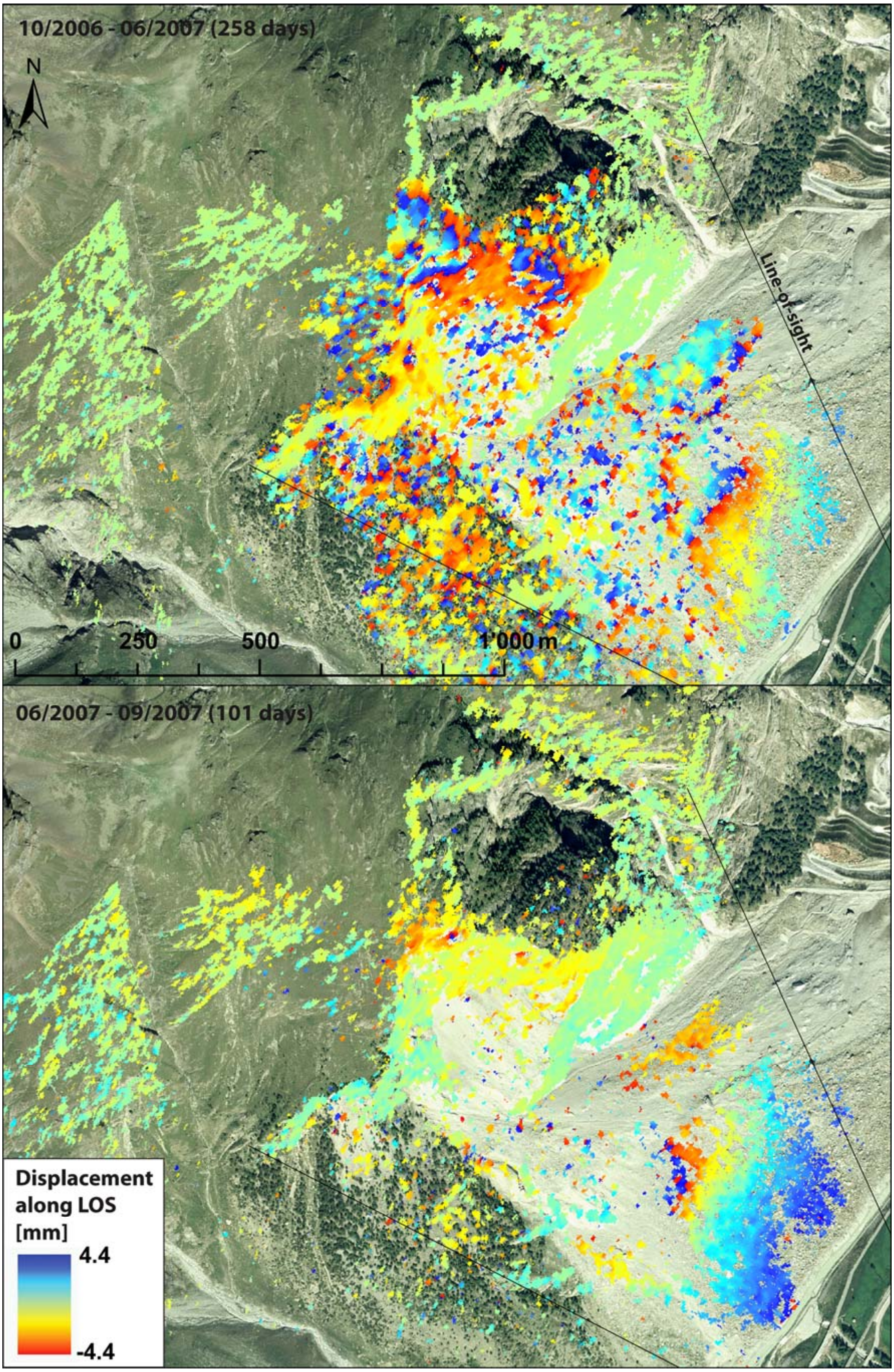

Figure 9.3: GB-DInSAR maps representing displacement between two subsequent time intervals.

9.2 Dependence of thermo-mechanical effects on the factor of safety

As shown in Chapter 5, TM induced stresses at depth can cause slip along discontinuities if their respective stress state is already close to the failure envelope, i.e. the discontinuity is critically stressed. Figure 5.10b illustrated that the amount of critically stressed discontinuities within the model set first order control on the magnitude of TM effects at depth. The closer the slope is to failure, the stronger the TM induced permanent displacements. It is suggested here that the amount of critically stressed discontinuity area can be expressed by the factor of safety (FOS), which is a widely used measure of instability in rock mechanics and engineering (Wyllie and Mah, 2004). For each of the models with varying strength parameters presented in Figure 5.10b, the FOS is calculated to explore its influence on TM effects.

Generally, the FOS is defined as the ratio of stabilizing or resisting forces (e.g. frictional strength, cohesion, etc.) to driving forces (e.g. gravitational stress). Stability is provided when the FOS is greater than one. For the case of a rigid block sliding on a frictional plane, calculation of the FOS is trivial. The diving force is the slope-parallel component of the gravitational force acting on the block, while the resisting force is the frictional force counteracting the gravitational force. In a complex numerical model with several discontinuities, the FOS cannot be calculated analytically. An iterative procedure to estimate the FOS was suggested by Dawson and Roth (1999). In the first step, a model with assumed strength parameters is calculated until force-equilibrium. All strength properties are then reduced by a factor and force-equilibrium is again calculated. This procedure is repeated for increasing factors until force-equilibrium cannot be attained, i.e. an unstable state is reached. This limiting factor is then the model FOS.

For the simplified conceptual models allowing toppling or sliding, only the role of strength properties of the relevant discontinuity set has been investigated. Thus, only these properties were changed iteratively in the FOS analysis while all other strength properties remained constant. For each of the models, the degree of criticality – expressed by the percentage of critically stressed areas to the area of all discontinuities in the model – has also been calculated. Recall that a discontinuity is termed critically stressed if it is <50 kPa below the shear strength. Figure 9.4a shows correlation between the FOS and the percentage of critically stressed discontinuities within the model. Although the relation ship is not linear, it indicates that FOS is a good measure for the amount of critically stressed discontinuity area within the slopes. Figure 9.4b shows the TM induced displacement rate after 10 years at a point at 40 m depth below the top of the slope (see Point A in Figure 5.4a) against the amount of critically stress discontinuity area. Note that the Figure is essentially the same as Figure 5.11 with axes exchanged. Figure 9.4c shows the TM induced displacement rate as a function of the FOS. For both sliding and toppling, the displacement rate is greater than zero for FOS larger than about 1.25 to 1.3. For FOS ranging from 1.08 to 1.25, displacement rate increases for lower FOS and the increase is comparable for both sliding and toppling. Below a FOS of 1.08, the behavior of sliding and toppling slopes diverge. For sliding, the rate increases dramatically for higher criticality, which implies that the slope can easily fail as a result of TM cycling (or other forcing). For toppling, displacement rates begin to fall. This behavior was discussed in Section 5.4 and is related to the self-stabilization nature of flexural toppling (Nichol et al., 2002). The dependence of TM effects on FOS in our conceptual model (Figure 9.4) highlights that TM effects are only significant at low FOS. It may be concluded that slopes showing a clear reaction to TM effects are at low stability. For the case of the Randa instability, this outcome implies a likely FOS value less than 1.25.

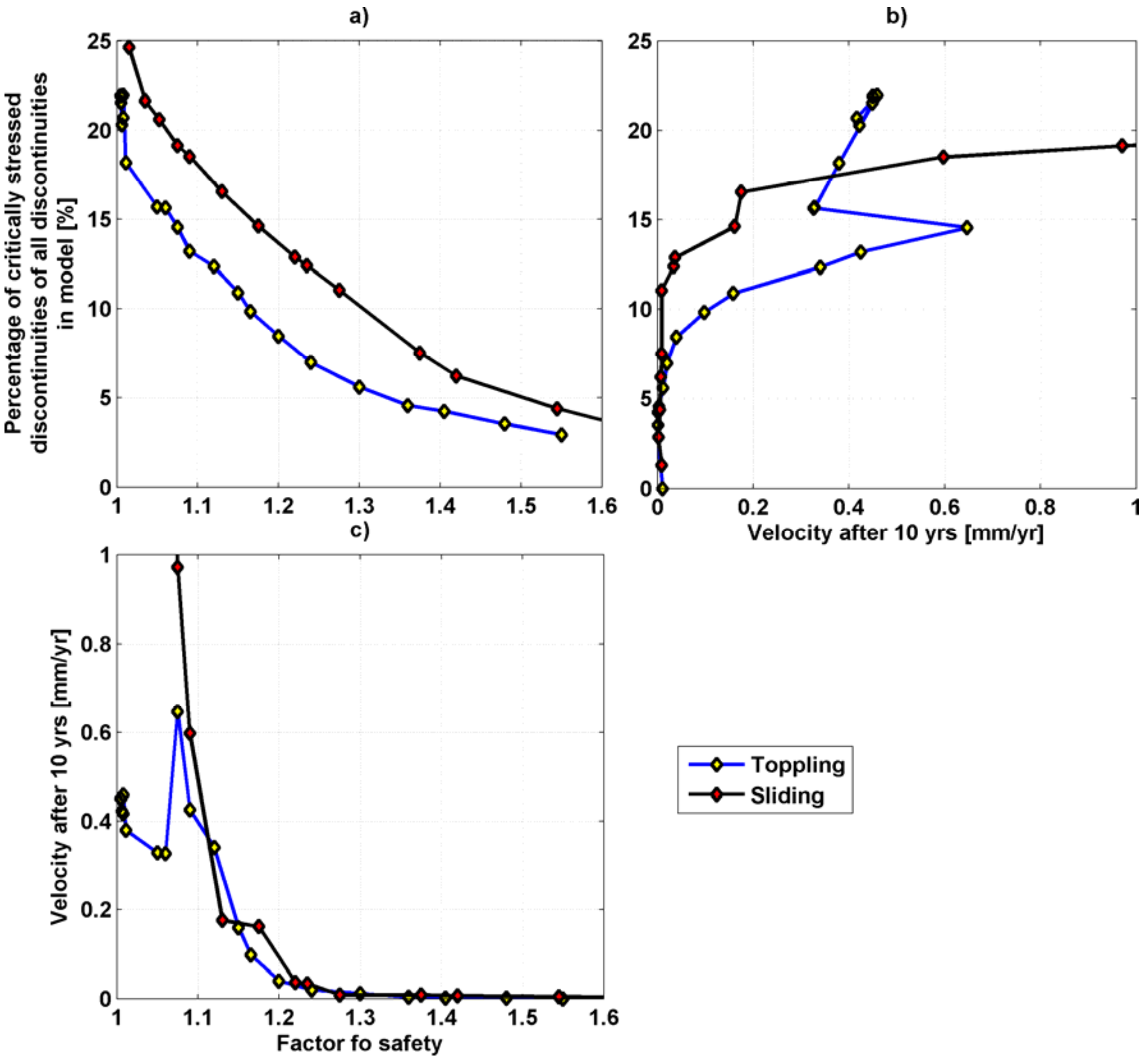

Figure 9.4: a) Relationship between factor of safety and the amount of critically stress discontinuities in the model. b) TM induced displacement rates after 10 years at a monitoring at 40 m depth (Point A in Figure 5.4a) as a function of critically stress discontinuity area. c) TM induced displacement rates as a function of factor of safety. TM effects increase for lower stability since a greater number of critically stress discontinuities are susceptible to induced stress changes.

10. REFERENCES

Alpiger, A., 2010. Hydrogeology of the rock slope instability at Randa (Switzerland). BSc Thesis, ETH Zurich, Switzerland, 44 pp.

Amann, F., 2006. Grosshangbewegungen Cuolm Da Vi (Graubünden, Schweiz), Geologisch-geotechnische Befunde und numerische Untersuchungen zur Klärung des Phänomens, Friedrich-Alexander-Universität, Erlangen-Nürnberg.

Amann, F., Donatsch, G., Bonanomi, Y. and Moser, M., 2006. Kinematik und Bewegungsmechansimus der tiefgründigen Instabilität Cuolm Da Vi (Graubünden, Schweiz). Bulletin für angewandte Geologie, 11(2): 117-132.

Anderson, R.S., 1998. Near-Surface Thermal Profile in Alpine Bedrock: Implications for the Frost Weathering of Rock. Arctic and Alpine Research, 30(4): 362-372.

Atkinson, B. K. (1989), Fracture mechanics of rock, Academic press limited, London.

Attewell, P.B. and Farmer, I.W., 1973. Fatigue behavior of rock. Int. J. Rock Mech. Min. Sci., 10: 1-9.

BAFU, 2006. Übersicht über die potenzielle Permafrostverbreitung in der Schweiz, Bern.

Barton, N., and V. Choubey (1976), The shear strength of rock joints in theory and practice, Rock Mechanics, 10, 1-54.

Berger, J., 1975. A Note on Thermoelastic Strains and Tilts. Journal of Geophysical Research, 80(2): 274-277.

Bhasin, R. and Kaynia, A.M., 2004. Static and dynamic simulation of a 700-m high rock slope in western Norway. Engineering Geology, 71: 213-226.

Bieniawski, Z.T., 1967. Mechanism of brittle fracture of rock, Part I - Theory of the fracture process. Int. J. Rock Mech. Min. Sci., 4: 395-406.

Bjerrum, L., 1967. Progressive failure in slopes of overconsolidated plastic clay and clay shales. Journal of Soil Mech Foundat Div ASCE, 93(SM5): 1-49.

Björck, A., 1996. Generlized least squared problems, Numerical methods for least squared problems. SIAM, pp. 184-187.

Bonaccorso, A., Bonforte, A. and Gambino, S., 2010. Thermal expansion-contraction and slope instability of a fumarole field inferred from geodetic measurements at Vulcano. Bull Volcanol, 72: 791-801.

Bonaccorso, A., Falzone, G. and Gambino, S., 1999. An investigation into shallow borehole tiltmeters. Geophysical Research Letters, 26(11): 1637-1640.

Bonzanigo, L., Eberhardt, E. and Loew, S., 2007. Long-term investigation of a deep-seated creeping landslide in crystalline rock. Part I. Geological and hydromechanical factors ontrolling the Campo Vallemaggia landslide Canadian Geotechnical Journal, 44(10): 1157-1180.

Brace, W.F., Paulding, B.W.J. and Scholz, C.H., 1966. Dilatancy in the fracture of crystalline rock. Journal of Geophysical Research, 71(16): 3939-3953.

Brown, E.T. and Hudson, J.A., 1974. Fatigue failure characteristics of some models of jointed rock. Earthquake Engineering and Structural Dynamics, 2: 379-386.

Buckley, J.S., Vallet, J., Braathen, A. and Wheeler, W., 2008. Oblique helicopter-based laser scanning for digital terrain modelling and visualisation of geological outcrops. The International Archives of the Photogrammetry, Remote Sensing and Spatial Information Sciences, XXXVII(B4): 493-498.

Burjánek, J., Gassner-Stamm, G., Poggi, V., Moore, J.R. and Fäh, D., 2010. Ambient vibration analysis of an unstable mountain slope. Geophysical Journal International, 180: 820-828.

Cai, M., Kaiser, P.K., Uno, H., Tasaka, Y. and Minami, M., 2004. Estimation of rock mass deformation modulus and strength of jointed hard rock masses using the GSI system. International Journal of Rock Mechanics and Mining Sciences, 41: 3-19.

CampbellScientific, 2008. AM16/32B Relay Analogue Multiplexer. Campbell Scientific.

Christen, M., Kowalski, J. and Bartelt, P., 2010. RAMMS: Numerical simulation of dense snow avalanches in three-dimensional terrain. Cold Regions Science and Technology, 63: 1-14.

Clauser, C. and Huegens, E., 1995. Thermal Conductivity of Rocks and Minerals. Rock Physics and Phase Relations, AGU: 105-126

Colesanti, C. and Wasowski, J., 2006. Investigating landslide with space-borne synthetic aperture radar (SAR) interferometry. Engineering Geology, 88: 173-199.

Crosta, G.B. and Agliardi, F., 2003. Failure forecast for large rock slides by surface displacement measurements. Can Geotech Journal, 40: 176-190.

Crosta, G.B., Chen, H. and Lee, C.F., 2004. Replay of the 1987 Val Pola Landslide, Italian Alps. Geomorphology, 60: 127-146.

Cruden, D.M. and Varnes, D.J., 1996. Landslide types and processes. In: A.K. Turner and R.L. Schuster (Editors), Landslides: Investigation and Mitigation. Transportation Research Board, Special Report 247 National Research Council, Washington DC, pp. 36-75.

Cundall, P.A. and Hart, R.D., 1992. Numerical modelling of discontinua. Engineering Computations, 9(2): 101-113.

Davidson, G.P. and Nye, J.F., 1985. A photoelastic study of ice pressure in rock cracks. Cold Regions Science and Technology, 11: 141-153.

Dawson, E.M. and Roth, W.H., 1999. Slope Stability Analysis with FLAC, International FLAC Symposium on Numerical Modeling in Geomechanics, Minneapolis, Minnesota. Rotterdam: A. A. Balkema, pp. 3-9.

Delaloye, R. and Lambiel, C., 2005. Evidences of winter ascending air circulation throughout talus slopes and rock glaciers situated in the lower belt of alping discontinuous permafrost. Norwegian Journal of Geography, 59: 194-2003.

Dyke, L.D., 1984. Frost heaving of bedrock in permafrost regions. Bulletin of the Association of Engineering Geology, 21: 389-405.

Eberhardt, E., Stead, D. and Coggan, J.S., 2004. Numerical analysis of initiation and progressive failure in natural rock slopes - the 1991 Randa rockslide. International Journal of Rock Mechanics and Mining Sciences, 41(1): 69-87.

Eberhardt, E., Thuro, K. and Luginbuehl, M., 2005. Slope instability mechanisms in dipping interbedded conglomerates and weathered marls - the 1999 Rufi landslide, Switzerland. Engineering Geology, 77: 35-56.

Eisbacher, G.H. and Clague, J.J., 1984. Destructive mass movements in high mountains: hazard and management. Ottawa: Canadian Government Publishing Center.

Eisenbeiss, H., 2008. The autonomous mini helicopter: A powerful platfrom for mobile mapping. The International Archives of the Photogrammetry, Remote Sensing and Spatial Information Sciences., 37(B1): 977-981.

Eisenbeiss, H., 2009. UAV Photogrammetry. PhD Thesis, ETH Zürich, 201 pp.

Erismann, T.H. and Abele, G., 2001. Dynamics of rockslides and rockfalls. Springer-Verlag Berlin Heidelberg.

Evans, S.G., Clague, J.J., Woodsworth, G.J. and Hungr, O., 1989. The Pandemonium Creek rock avalanche, British Columbia. Can Geotech Journal, 26: 427-446.

Fortuny, J. and Sieber, A.J., 1994. Fast Algorithm for a Near-Field Synthetic Aperture Radar Processor. IEEE Transactions on Antennas and Propagation, 42(10): 1458-1460.

Fritsche, S. and Fäh, D., 2009. The 1946 magnitude 6.1 earthquake in the Valais: site-effects as contributor to the damage. Swiss Journal of Geosciences, 102: 423-429.

Fritsche, S., Fäh, D., Gisler, M. and Giardini, D., 2006. Reconstructing the damage field of teh 1855 earthquake in Switzerland: historical investigations on a well-documented event. Geophysical Journal International, 166: 719-731.

Giardini, D., Grünthal, G., Shedlock, K.M. and Zhang, P., 1999. The GSHAP Global Seismic Hazards Map. Annali di Geofisica, 42(6): 1225-1230.

Girod, F., 1999. Altération météorique de roche granitique en milieu alpin: le cas de l'orthogneiss associé à l'éboulement de Randa (Mattertal, Valais, Suisse). PhD Thesis, Université de Lausanne, Lausanne.

Gischig, V., Amann, F., Moore, J.R., Loew, S., Eisenbeiss, H. and Stempfhuber, W., 2011. Composite rock slope kinematics at the current Randa instability, Switzerland, based on remote sensing and numerical modeling. Engineering Geology, 118: 37-53.

Gischig, V., Loew, S., Kos, A., Moore, J.R., Raetzo, H. and Lemy, F., 2009. Identification of active release planes using ground-based differential InSAR at the Randa rock slope instability, Switzerland. Natural Hazards and Earth System Sciences, 9(1-12).

Gischig, V., Moore, J.R., Evans, K.F., Amann, F. and Loew, S., this issue-a. Thermo-mechanical forcing of deep rock slope deformation - Part I: conceptual study of a simplified slope. submitted to Journal of Geophysical Research.

Gischig, V., Moore, J.R., Evans, K.F., Amann, F. and Loew, S., this issue-b. Thermo-mechanical forcing of deep rock slope deformation - Part II: the Randa rock slope instability. submitted to Journal of Geophysical Research.

Goering, D.J. and Kumar, P., 1996. Winter-time convection in open-graded embankments. Cold Regions Science and Technology, 24: 57-74.

Goodman, R.E., 1989. Introduction to rock mechanics. John Wiley & Sons.

Goodman, R.E. and Bray, J.W., 1976. Toppling of rock slopes, Specialty Conference on Rock Engineering for Foundations and Slopes, American Society of Civil Engineering, Boulder, pp. 201-234.

Goodman, R.E. and Kieffer, D.S., 2000. Behavior of rock in slopes. Journal of Geotechnical and Geoenvironmental Engineering, 126(8): 675-684.

Goodman, R.E., Taylor, R. and Brekke, T., 1968. A model for the mechanics of jointed rock. Journal of Soil Mehcnaics & Foundations Div ASCE, 94(SM3): 637-659.

Goy, L., Fabre, D. and Menard, G., 1996. Modelling of rock temperatures for deep alpine tunnel projects. Rock Mechanics and Rock Engineering, 29(1): 1-18.

Gruber, S. and Haeberli, W., 2007. Permafrost in deep bedrock slopes and its temperature-related destabilization following climate change. Journal of Geophysical Research, 112: F02S18.

Gruner, U., 2001. Felssturzgefahr Chapf - Üssri Urweid (Gemeinde Innertkirchen): Angaben zur Geologie und zu den Bewegungen. . Bern, Kellerhaus + Haefeli AG: 6 pp.

Gueguen, Y. and Palciauskas, V., 1994. Introduction to the physics of rocks. Princeton University Press, Princeton, NJ.

Gunzburger, Y., Merrien-Soukatchoff, V. and Guglielmi, Y., 2005. Influence fo daily surface temperature fluctuations on rock slope stability: case study of the Rocher de Valabres slope (France). International Journal of Rock Mechanics and Mining Sciences, 42: 331-349.

Haefeli, R., 1967. Zum progressiven Bruch in Schnee, Boden, Fels und Eis. Felsmechanik und Ingenieurgeologie: 17-37.

Hall, K., 1997. Rock Temperatures and Implications for Cold Region Weathering. I: New Data from Viking Valley, Alexander Island, Antarctica. Permafrost and Periglacial Processes, 8: 69-90.

Hancox, G.T., Cox, S., Turnbull, I.M. and Crozier, M.J., 2003. Reconnaissance studies of landslides and other ground damage caused by the Mw 7.2 Fiordland earthquake of 22 August 2003, GNS, New Zealand.

Harrison, J.C., 1976. Cavity and Topographic Effects in Tilt and Strain Measurements. Journal of Geophysical Research, 81(2): 319-328.

Harrison, J.C. and Herbst, K., 1977. Thermoelastic strains and tilts revisited Geophysical Research Letters, 4(11): 535-537.

Heim, A., 1932. Bergsturz und Menschenleben. Zurich: Fretz and Wasmuth Verlag: 218 pp.

Heincke, B., 2005. Determination of 3-D fracture distribution on an unstable mountain slope using georadar and tomographic seismic refraction techniques. PhD Thesis, ETH Zurich, 168 pp.

Heincke, B., Green, A.G., van der Kruk, J. and Horstmeyer, H., 2005. Acquisition and processing strategies for 3D georadar surveying a region characterized by rugged topography. Geophysics, 70(6): K53-K61.

Heincke, B., Green, A.G., van der Kruk, J. and Willenberg, H., 2006a. Semblance-based topographic migration (SBTM): a method for identifying fracture zones in 3-D georadar data. Near Surface Geophysics, 4: 79-88.

Heincke, B., Maurer, H., Green, A.G., Willenberg, H., Spillmann, T. and Burlini, L., 2006b. Characterizing an unstable mountain slope using shallow 2D and 3D seismic tomography. Geophysics, 71(6): B241-B256.

Heynen, M., 2009. The influence of topographic amplification and local site conditions on the seismic stability of rock slopes (Seetalhorn, VS). MSc Thesis, ETH Zurich.

Hocking, G., 1974. A method for distinguishing between single and double plane sliding of tetrahedal wedges Int. J. Rock Mech. Min. Sci. & Geomech. Abstr., 13: 225-226.

Hoek, E., Carranza-Torres, C. and Corkum, B., 2002. Hoek-Brown failure criterion - 2002 edition, NARMS-TAC Conference, Toronto, pp. 267-273.

Hungr, O. and Evans, S.G., 1988. Engineering evaluation of fragmental rockfall hazards. In: Bonnard (Editor), 5th International Symposium on Landslides. Balkema, Lausanne.

Hungr, O. and McDougall, S., 2009. Two numerical models for landslide dynamic analysis. Computers and Geosciences, 35: 978-922.

Hunziker, M., 2011. Rawilhorn slide - in preparation. MSc Thesis, ETH Zurich.

Husen, S., Kissling, E., Deichmann, N., Wiemer, S., Giardini, D. and Baer, M., 2003. Probabilistic earthquake location in complex three-dimensional velocity models: Application to Switzerland. Journal of Geophysical Research, 108(B2): 2077.

Ischi, H., Keusen, H.R. and Scheller, E., 1991. Randa, Kt. Wallis, Bergsturz Grossgufer vom April/Mai 1991 - Zusammenfassender Bericht über die Aktivitäten der Geotest AG, Geotest AG, Martigny.

Itasca, 2008a. 3DEC Version 4.1, 3-Dimensional Distince Element Code, Itasca Consulting Group Inc.

Itasca, 2008b. UDEC Version 4.0 Universal Distinct Element Code. Itasca Consulting Group, Inc.

Jaboyedoff, M., Baillifard, F., Bardou, E. and Girod, F., 2004b. The effect of weathering on Alpine rock instability. Quarterly Journal of Engineering Geology and Hydrogeology,, 37: 95-103.

Jaboyedoff, M., Ornstein, P. and Rouiller, J.D., 2004. Design of a geodetic database and associated tools for monitoring rock-slope movements: the example of the top of Randa rockfall scar. Natural Hazards and Earth System Sciences, 4: 187-196.

Jaboyedoff, M., Ornstein, P. and Rouiller, J.D., 2004a. Design of a geodetic database and associated tools for monitoring rock-slope movements: the example of the top of Randa rockfall scar. Natural Hazards and Earth System Sciences, 4: 187-196.

Jennings, J.E., 1970. A mathematical theory for the calculation of the stability of open cast mines, Symp. on the Theoretical Background to the Planning of Open Pit Mines, Johannesburg.

Jing, L. and Stephansson, O., 2007. The basics of fracture system characterization - field mapping and stochastic simulations, Fundamentals of Discrete Element Methods for Rock Engineering: Theory and Applications, pp. 147-177.

Kamai, T., Weisbrod, N. and Draglia, M.I., 2009. Impact of ambient temperature on evaporation from surface-exposed fractures. Water Resources Research, 45.

Kastrup, U., Zoback, M.L., Deichmann, N., Evans, K.F., Giardini, D. and Micheal, A., J, 2004. Stress field variations in the Swiss Alps and the northern Alpine foreland derived from inversion of fault plane solutions. Journal of Geophysical Research, 109.

Krähenbühl, R., 2004. Temperatur und Kluftwasser als Ursachen von Felssturz. Bulletin für angewandte Geologie, 9(1): 19-35.

Krähenbühl, R., 2006. Der Felssturz der sich auf die Stunde genau ankündigte. Bulletin für angewandte Geologie, 11(1): 49-63.

Kulhawy, F.H., Beech, J.F. and Trautman, C.H., 1989. Influence of geologic development on horizontal stresses in soil, Foundation Engineering Congress ASCE Evanston, Illinois, pp. 43-47.

Kveldsvik, V., Einstein, H.H., Nilsen, B. and Blikra, L.H., 2008. Numerical analysis of the 650,000 m2 Aknes rock rlope based on measured displacements and geotechnical data. Rock Mechanics and Rock Engineering: 689-728.

Kveldsvik, V., Kaynia, A.M., Nadim, F., Bhasin, R., Nilsen, B. and Einstein, H.H., 2009. Dynamic distinct-element analysis of the 800 m high Aknes rock slope. Internation Journal of Rock Mechanics & Mining Sciences, 46: 686-698.

Ladner, F., Rovina, H., Pointner, E., Dräyer, B. and Sambeth, U., 2004. Ein angekündigter Felssturz. Geologische Überwachung und Instrumentierung des Felssturzes "Medji" bei St.Niklaus (Wallis). tec 21, 130(27/28): 10-14.

Lay, Y., Wang, Q., Niu, F. and Zhang, K., 2004. Three-dimensional nonlinear analysis for temperature characteristic of ventilated embankment in permafrost regions. Cold Regions Science and Technology, 38.

Lee, J.-S., Hoppel, K.W., Mango, S.A. and Miller, A.R., 1994. Intensity and Phase Statistic of Multilook polarimetric and Interferometric SAR Imagery. IEEE Transactions on Geoscience and Remote Sensing, 31(5): 1017-1028.

Lemy, F. and Hadjigeorgiou, J., 2003. Discontinuity trace map construction using photographs of rock exposures. Internation Journal of Rock Mechanics & Mining Sciences, 40.

Leroueil, S., 2001. Natural slopes and cuts: movements and failure mechanisms. Géotechnique, 51(3): 197-243.

Leva, D., Rivolta, C., Rossetti, I.B., Kuzuoka, S. and Mizuno, T., 2005. Using a ground based interferometric synthetic aperture radar(GBInSAR) sensor to monitor a landslide in Japan. IEEE.

Lévy, C., L, B., Jongmans, D., Mourot, P. and Hantz, D., 2010. Dynamic response of the Chamousset rock column (Western Alps, France). Journal of Geophysical Research, 1115: 1-13.

Lingua, A., Piatti, D. and Rinaudo, F., 2008. Remote monitoring of a landslide using an integration of GB-InSAR and LiDAR techniques. The Internarional Archives of the Photogrammetry, Remote Sensing and Spatial Information Sciences, XXXVII(B1): 361-366.

Liu, Y.Q., Li, H.B., Zhang, J., Li, J.R. and Zhou, Q.C., 2004. UDEC simulation for dynamic response of a rock slope subject to explosions. Internation Journal of Rock Mechanics & Mining Sciences, 41(3).

Loew, S., Willenberg, H., Spillmann, T., Heincke, B., Maurer, H., Eberhardt, E. and Evans, K.F., 2007. Structure and kinematics of a large complex rockslide as determined from integrated geological and geophysical investigations (Randa, Switzerland). In: V.R. Schaefer, R.L. Schuster and A.K. Turner (Editors), 1st North American Landslide Conference Association of Environmental and Engineering Geologists, Vail, CO, pp. 11.

Lorig, L. and Varona, P., 2000. Practical slope-stability analysis using finite-difference codes. In: W.A. Hustrulid, M.K. McCarter and D.J.A. Van Zyl (Editors), Stability in surface mining, pp. 115-124.

Markland, J.T., 1972. A useful technique for estimating the stability of rock slopes when rigid wedge sliding type of failure is expected. Imperial College Rock Mechanics Reseach Report No. 19: 10pp.

Massey, C., McSaveney, M., Palmer, N., Manville, V. and Hancox, G.T., 2010. The Young River landslide, 11th IAEG Congress, Auckland, New Zealand.

Matsuoka, N., 2001a. Direct observation of frost wedging in alpine bedrock. Earth Surface Processes and Landforms, 26: 601-614.

Matsuoka, N., 2001b. Microgelivation versus Macrogelivation: Towards Bridging the Gap between Laboratory and Field Frost Weathering. Permafrost and Periglacial Processes, 12: 299-313.

Matsuoka, N. and Murton, J., 2008. Frost Weathering: Recent Advances and Future Directions. Permafrost and Periglacial Processes, 19: 195-210.

Metternicht, G., Hurni, L. and Gogu, R., 2005. Remote sensing of landslides: An analysis of the potential contribution to geo-spatial systems for hazard assessment in mountainous environments. Remote Sensing of Environment, 98(2-3): 284-303.

Mikkelsen, P.E., 2003. Advances in Inclinometer Data Analysis, Field Measurements in Geomechanics, Oslo, Norway.

Moore, J.R., Gischig, V., Button, E. and Loew, S., 2010. Rockslide deformation monitoring with fiber optic strain sensors. Natural Hazards and Earth System Sciences, 10: 191-201.

Moore, J. R., Gischig, V., Burjanek, J. Loew, S., Faeh, D. (2011): Dynamic response of a large unstable rock mass (Randa, Switzerland), submitted to Bulletin of the Seismological Society of America.

Moore, J. R., Gischig V., Katterbach, M., Loew, S. (2011): Air circulation in deep cracks and the temperature field of an alpine rock slope, submitted to Earth Surface Processes and Landforms.

Mufundirwa, A., Yoshiaki, F., Kodama, N. and Kodoma, J.-i., 2011. Analysis of natural rock slope deformation under temperature variations: A case from a cool temperate region in Japan. Cold Regions Science and Technology, 65: 488-500.

Nichol, S.L., Hungr, O. and Evans, S.G., 2002. Large-scale brittle and ductile toppling of rock slopes. Can Geotech Journal, 39: 773-788.

Nield, D.A., 1982. Onset of convection in a porous layer saturated by an ideal gas. J. Heat Mass Transfer, 25: 1605-1606.

Niemeier, W., 2002. Ausgleichsrechnung. de Gruyter, 407 pp.

Nishii, R. and Matsuoka, N., 2010. Monitoring rapid head scarp movement in an alpine rockslide. Engineering Geology, 115: 49-57.

Noetzli, J., Gruber, S., Kohl, T., Salzmann, N. and Haeberli, W., 2007. Three-dimensional distribution and evolution of permafrost temperatures in idealized high-mountain topography. Journal of Geophysical Research, 112.

Norvik, T., Blikra, L.H., Nyrnes, E. and Derron, M.H., 2010. Statistical analysis of seasonal displacements at the Nordnes rockslide, northern Norway. Engineering Geology, 114: 228-237.

Oppikofer, T., Jaboyedoff, M., Blikra, L.H., Derron, M.H. and Metzger, R., 2009. Characterization and monitoring of the Aknes rockslide using terrestrial laser scanning. Natural Hazards and Earth System Sciences, 9: 1003-1019.

Oppikofer, T., Jaboyedoff, M. and Keusen, H.R., 2008. Collapse of the eastern Eiger flank in the Swiss Alps. Nature Geosciences, 1: 531-535.

Oppikofer, T., Jaboyedoff, M., Pedrazzini, A., Derron, M.H. and Blikra, L.H., 2011. Detailed DEM analysis of a rockslide scar to characterize the basal sliding surface of active rockslides. Journal of Geophysical Research, in press.

Osmundsen, P.T., Henderson, I., Lauknes, T.R., Larsen, Y., Redfield, T.F. and Dehls, J., 2009. Active normal fault control on landscape and rock-slope failure in nothern Norway. Geology, 37: 135-138.

Philips, M., Zenklusen Mutter, E., Kern-Luetschg, M. and Lehning, M., 2009. Rapid degradation of ice in a ventilated talus slope: Flüela Pass, Swiss Apls. Permafrost and Periglacial Processes, 20: 1-14.

Plafker, G., Ericksen, G.E. and Fernandes, C.J., 1971. Geological aspects of the May 31, 1970, Peru earthquake. Bulletin of the Seismological Society of America, 61(3): 543-578.

Priest, S.D., 1993. Discontinuity analysis for rock engineering. Chapman & Hall, London.

Redfield, T.F., Hermanns, R.L., Oppikofer, T. and others, 2011. Analysis of the 2007 earthquake-induced Punta Cola rockslide and tsunami, Aysén Fjord, Patagonia, Chile, 5th International Conference on Earthquake Geotechnical Engineering, Santiago, Chile.

Richter, D., 1989. Ingenieur- und Hydrogeology. de Gruyter, Berlin New York, 605 pp.

Rybach, L. and Pfister, M., 1994. Temperature predictions and predictive temperatures in deep tunnels. Rock Mechanics and Rock Engineering, 27(2).

Sartori, M., Baillifard, F., Jaboyedoff, M. and Rouiller, J.D., 2003. Kinematics of the 1991 Randa rockslides (Valais, Switzerland). Natural Hazards and Earth System Sciences, 3: 423-433.

Scheidegger, A.E., 1973. On the prediction of the reach and velocity of catastrophic landslides. Rock Mechanics, 5: 231-236.

Schindler, C., Cuénod, Y., Eisenlohr, T. and Joris, C.L., 1993. Die Ereignisse vom 18. April und 9. Mai 1991 bei Randa (VS): ein atypischer Bergsturz in Raten. Eclogae Geologicae Helvetiae, 86(3): 643-665

Scholz, C.H. and Hickman, S.H., 1983. Hysteresis in the closure of a nominally flat crack. Journal of Geophysical Research, 88(B8): 6501-6504.

Scholz, C.H. and Koczynski, T.A., 1979. Dilantancy Anisotropy and the Response of Rock to Large Cycling Loads. Journal of Geophysical Research, 84(B10): 5525-5534.

Singhroy, V., 1995. SAR intergrated techniques for geohazard assessment. Advances in Space Research, 15(11): 67-78.

Sitar, N., MacLaughlin, M.M. and Doolin, D.M., 2005. Influence of Kinematics on Landslide Mobility and Failure Mode. Journal of Geotechnical and Geoenvironmental Engineering, 131(6): 716-728.

Sjöberg, J., 2000. Failure mechanisms for high slopes in hard rock. In: W.A. Hustrulid, M.K. McCarter and D.J.A. Van Zyl (Editors), Stability in surface mining, pp. 71-80.

Skaloud, J., Vallet, J., Keller, K., Veyssiere, G. and Kölbl, O., 2005. HELIMAP: Rapid Large Scale Mapping Using Handheld LiDAR/CCD/GPS/INS Sensors on Helicopters ION GNSS Congress, Long Beach.

Spillmann, T., 2007. Borehole radar experiments and microseismic monitoring on the unstable Randa rockslide (Switzerland). PhD Thesis, ETH Zurich, 221 pp.

Spillmann, T., Maurer, H., Green, A.G., Heincke, B., Willenberg, H. and Husen, S., 2007a. Microseismic investigation of an unstable mountain slope in the Swiss Alps. Journal of Geophysical Research, 112(B07301).

Spillmann, T., Maurer, H., Green, A.G., Heincke, B., Willenberg, H. and Husen, S., 2007a. Microseismic investigation of an unstable mountain slope in the Swiss Alps. Journal of Geophysical Research, 112(B07301).

Spillmann, T., Maurer, H., Willenberg, H., Evans, K.F., Heincke, B. and Green, A.G., 2007b. Characterization of an unstable rock mass based on borehole logs and diverse borehole radar data. Journal of Applied Geophysics, 61(1): 16-38.

Spillmann, T., Maurer, H., Willenberg, H., Evans, K.F., Heincke, B. and Green, A.G., 2007b. Characterization of an unstable rock mass based on borehole logs and diverse borehole radar data. Journal of Applied Geophysics, 61(1): 16-38.

Starfield, A.M. and Cundall, P.A., 1988. Towards a methodology for rock mechanics modelling. International Journal of Rock Mechanics Mining Sciences and Geomechanics, 25(3): 99-106.

Strozzi, T., Delaloye, R., Kääb, A., Ambrosi, C., Perruchoud, E. and Wegmüller, U., 2010. Combined observations of rock mass movements using satellite SAR interferometry, differential GPS, airborne digital photogrammetry, and airborne photography interpretation. Journal of Geophysical Research, 115: 1-11.

Sturzenegger, M. and Stead, D., 2009. Close-range terrestrial digital photogrammetry and terrestrial laser scanning for discontinuity characterization on rock cuts. Engineering Geology, 106: 163-182.

Swisstopo, 2009. LTOP / LTOPWIN Pre-analysis and adjustment software Swisstopo, Bern.

Tarchi, D., Casagli, N., Fanti, R., Leva, D., Luzi, G., Pasuto, A., Pieraccini, M. and Silvano, S., 2003a. Landslide monitoring by using ground-based SAR interferometry: an example of application to the Tessina landslide in Italy. Engineering Geology, 68(15-30).

Tarchi, D., Casagli, N., Moretti, S., Leva, D. and Sieber, A.J., 2003b. Monitoring landslide displacements by using ground-based synthetic aperture radar interferometry: Application to the Ruinon landslide in the Italian Alps. Journal of Geophysical Research, 108(B8): 2387.

Terzaghi, K., 1962. Stability of steep slopes on hard unweathered rock Géotechnique, 12: 251-270.

Thoeny, R., 2008. Dynamic fluid electic conductivity logging for identification and characterization of preferential groundwater flow in the Åknes rockslide (Norway). MSc Thesis, ETH Zurich, 119 pp.

Thuro, K., Berner, C. and Eberhardt, E., 2005. Der Bergsturz von Goldau 1806 - Versagensmechanismen in wechsellagernden Konglomeraten und Mergeln. In: M. Moser (Editor), 15. Tagung Ingenieurgeologie, Erlangen.

Tran, N.H., 2007. Fracture orientation characterization: minimizing statistical modelling errors. Computational Statistics & Data Analysis, 51: 3187-3196.

Vallet, J., 2007. GPS-IMU and Lidar integration to aerial photogrammetry: Development and practical experiences with Helimap System®. Vorträge Dreiländertagung 27. Wissenschaftlich-Technische Jahrestagung der DGPF, 19-21 June.

Vallet, J. and Skaloud, J., 2004. Development and experiences with a fully-digital handheld mapping system operated from a helicopter. The International Archives of the Photogrammetry, Remote Sensing and Spatial Information Sciences, 35(B).

Vargas, E.A.J., Chavez, E., Gusmão, L. and Amaral, C., 2009. Is thermal fatigue a possible mechanism for failures of some rock slopes in Rio de Janeiro, Brazil?, 43rd US Rock Mechanics Symposium and 4th U.S.-Canada Rock Mechanics Symposium, Asheville, NC.

Voight, B., 1989. Relation to describe rate-dependent material failure. Science, 243(4888): 200-203.

Walder, J. and Hallet, B., 1985. A theoretical model of the fracture of rock during freezing. Geological Society of America Bulletin, 96: 336-346.

Watson, A.D., Moore, D.P. and W, S.T., 2004. Temperature influence on rock slope movements at Checkerboard Creek. Landslides: Evaluation and Stabilization, Proceedings of the Ninth International Symposium on Landslides.: 1293-1298.

Weeks, E.P., 2001. Effect of topography on gas flow in unsaturated fracture rock: Concepts and observations. In: D.D. Evans and T.C. Nicholson (Editors), Flow transport Through unsaturated fractured rock, Geophys. Monogr. Ser. Rasmussen Eds., pp. 53-59.

Wegmann, M. and Gudmundsson, G.H., 1999 Thermally induced temporal strain variations in rock walls observed at subzero temperatures. In: K. Hutter, Y. Wang and H. Beer (Editors), VI. International Symposium on Thermal Engineering and Sciences for Cold Regions, Lecture Notes in Physics. Springer Verlag, pp. 511-518.

Weidner, S., 2000. Kinematik und Mechanismus tiefgreifender alpiner Hangdeformationen unter besonderer Berücksichtigung der hydrogeologischen Verhältnisse. PhD Thesis, Friedrich-Alexander-Universität, Erlangen-Nürnberg.

Weisbrod, N. and Draglia, M.I., 2006. Potential impact of convective fracture venting on salt-crust buildup and ground-water salinization in arid environments. Journal of Arid Environments, 65: 386-399.

Werner, C., Strozzi, T., Wiesmann, A. and Wegmüller, U., 2008. Gamma's portable radar interferometer. 13th FIG Symposium on Deformation and Analysis, Lisbon: 1-10.

Willenberg, H., 2004. Geologic and kinematic model of a complex landslide in crystalline rock (Randa, Switzerland), Doctoral Thesis, ETH Zürich, 184 pp.

Willenberg, H., Evans, K.F., Eberhardt, E., Spillmann, T. and Loew, S., 2008b. Internal structure and deformation of an unstable crystalline rock mass above Randa (Switzerland): Part II - Three-dimensional deformation patterns. Engineering Geology, 101: 15-32.

Willenberg, H., Ladner, F., Spillmann, T., Simon, L., Sambeth, U., Evans, K.F. and Eberhardt, E., 2002. Aufbau eines Multi-Parameter Überwachungssystems für Felsrutschungen. Felsbau, 20(3): 1-8.

Willenberg, H., Loew, S., Eberhardt, E., Evans, K.F., Spillmann, T., Heincke, B., Maurer, H. and Green, A.G., 2008a. Internal structure and deformation of an unstable crystalline rock mass above Randa (Switzerland): Part I- Internal structure from integrated geological and geophysical investigations. Engineering Geology, 101: 1-14.

Wyatt, F.K., Morrissey, S.-T. and Agnew, D.C., 1988. Shallow Borehole Tilt: A Reprise. Journal of Geophysical Research, 93(B8): 9197-9201.

Wyllie, D.C. and Mah, C.W., 2004. Rock slope engineering - Civil and mining (4th edition). Spon Press, New York.

Xiao, J.-Q., Ding, D.-X., Xu, G. and Jiang, F.-L., 2009. Inverted S-shaped model for nonlinear fatigue in rock. Internation Journal of Rock Mechanics & Mining Sciences, 46: 643-548.

Yin, Y., Wang, F. and Sun, P., 2009. Landslide hazards triggered by the 2008 Wenchuan earthquake, Sichuan, China. Landslides, 6: 139-151.

Yugsi Molina, F.X., 2010. Structural evolution of slope instabilities in massive crystalline rocks (Matter Valley, Switzerland). PhD Thesis, ETH Zurich.

Zangerl, C., Evans, K.F., Eberhardt, E. and Loew, S., 2008. Normal stiffness of fractures in granitic rock: A compilation of laboratory and in-situ experiments. internation Journal of Rock Mechanics & Mining Sciences, 45: 1500-1507.

Zhao, X.B., Zhao, J., Cai, J.G. and Hefny, A.M., 2008. UDEC modelling on wave propagation across fractured rock masses. Computers and Geosciences, 35: 97-104.

Acknowledgements

I would like to thank Prof. Simon Löw for giving me the opportunity to work on this interesting PhD project and for his encouraging support during the last four years. Special gratitude goes to Jeff Moore, who started in the Randa-related part of the project COGEAR at about the same time when I started my PhD thesis. Thanks, Jeff, for the great collaboration, all fruitful discussions, your supportive way, and the good times we had on the field. All this largely defined the success of this work. Similarly, I thank Florian Amann for this help with various rockslide related and other problems, and for all encouragement and motivation. I also express special gratitude to Keith F. Evans for sharing lots of ideas as well as helpful and illuminating discussions. Gratitude further goes to Prof. Erik Eberhardt for acting as the external co-referee, and for reviewing and commenting on the entire thesis manuscript. Special thanks also go to Reto Seifert for his skillful technical support. Thanks also to Kerry Leith for installing one of the time-lapse cameras he had developed at Randa.

This thesis also benefited from the collaboration with various people within and outside of ETH: Ellegi Srl (Carlo Rivolta) performed the GB-DInSAR surveys and gave useful information on the data. Martin Volken and Klaus Aufdenblatten (Aufdenblatten Geomatik AG, Zermatt) provided geodetic data from Randa and the Matter Valley. Helimap SA (Julien Vallet) conducted the LiDAR and photogrammetry survey. The group for photogrammetry and remote sensing (Henri Eisenbeiss, David Novák) processed the LiDAR and photogrammetry data and skillfully addressed special requirements from the data. Members and students of the group for geodetic meteorology and engineering geodesy (Werner Stempfhuber, Stephan Schütz, Thomas Pfarrwalder, Sebastian Büttler, David Elsig, Sandra Zeder) helped planning geodetic measurements, conducted the surveys in the field and did the final data processing. Ulrich Sambeth from Stump Foratec AG helped planning the borehole installation of fiber-optic sensors and Manuel Wolfensberger assisted with reconfiguration of the datalogger. Luca Manetti (Smartec SA) helped planning and installing fiber-optic system.

I would also like to thank the entire Engineering Geology group for creating a pleasant working environment. Especially all other PhD students (Freddy Xavier Yugsi Molina, Reto Thoeny, Martin Ziegler, Kerry Leith, Franziska Dammeier, Jürgen Hansmann, Olivier Masset), who share the same joy and suffering involved in accomplishing a PhD thesis. Special reference goes to Freddy, with whom I spend a lot of good time sharing the office and who remained (literally) irreplaceable after he has left for Norway.

Special gratitude goes to my family, especially to my parents Rosmarie and Othmar, who have always supported my work. They also contributed to this thesis by being great hosts whenever I worked in the field. Finally, my greatest thanks go to my (future) wife Patrizia Salzmann for her constant support and her love.

Curriculum Vitae

Personal

Name:	Valentin Samuel Gischig
Date of birth:	25 January 1982
Place of birth:	Visp (VS), Switzerland
Nationality:	Switzerland

Education

10/2007 – 05/2011:	PhD studies in Engineering Geology, Department of Earth Sciences, ETH Zurich.
10/2002 – 03/2007:	Diploma studies, Department of Earth Sciences, ETH Zurich. Major: seismology; minors: geodynamics, applied geophysics and glaciology.
08/1997 – 06/2002:	Matura diploma at Kollegium Spiritus Sanctus, Brig (VS).

Work experience

04/2007 – 09/2007:	Seismologist at Geoscience Australia, Canberra. Contributions in the development of the Australian Tsunami Warning System.
07/2005 – 08/2005:	Student assistant to the hazard and risk group of the Swiss seismological service, ETH Zurich. Maintenance of a seismic array in Sion (VS).
03/2004:	Practical training in the office of the geological consulting company \`Odilo Schmid & Partner AG´, Brig (VS).

Publications

Gischig, V., Moore, J. R., Evans, K. F., Amann, F., Loew, S. (2011): Thermo-mechanical forcing of deep rock slope deformation – Part I: conceptual study of a simplified slope, *submitted to Journal for Geophysical Research*.

Gischig, V., Moore, J. R., Evans, K. F., Amann, F., Loew, S. (2011): Thermo-mechanical forcing of deep rock slope deformation – Part II: the Randa rock slope instability, *submitted to Journal for Geophysical Research*.

Moore, J. R., Gischig, V., Burjanek, J. Loew, S., Faeh, D. (2011): Dynamic response of a large unstable rock mass (Randa, Switzerland), *submitted to Bulletin of the Seismological Society of America*.

Moore, J. R., Gischig V., Katterbach, M., Loew, S. (2011): Air circulation in deep cracks and the temperature field of an alpine rock slope, *submitted to Earth Surface Processes and Landforms*.

Amann, F., Button, E. A., Evans, K. F., Gischig, V. S., Blümel, M. (2011): Experimental study of the brittle behavior of clayshale in short-term unconfined compression, *Rock Mechanics and Rock Engineering,* doi: 10.1007/s00603-011-0156-3.

Loew, S., Gischig, V., Willenberg, H., Alpiger, A., Moore, J.R, (2011): Randa: Kinematics and driving mechanisms of a large complex rockslide as determined from comprehensive field and modeling investigations. In: Clague, J.J., Stead, D.: Landslides: Types, Mechanisms and Modeling. *In preparation.*

Gischig, V., Amann, F., Moore, J. R., Loew, S., Eisenbeiss, H., Stempfhuber, W. (2011): Composite rock slope kinematics at the current Randa instability, Switzerland, based on remote sensing and numerical modeling, *Engineering Geology,* doi: 10.1016/j.enggeo. 2010.11.006.

Gischig, V, Moore, J.R., Evans, K. F., Loew, S. (2010) Seasonal changes of rock mass deformation rate due to thermal effects at the Randa rock slope instability, Switzerland. In: *Proceedings of the 11th IAEG conference 2010, Auckland, New Zealand (peer-reviewed)*

Moore, J.R., Gischig, V., Button, E., Loew, S. (2010): Rockslide Monitoring With Fiber Optic Strain Sensors, *Natural Hazards and Earth System Sciences,* 10, 191–201.

Gischig, V., Loew, S., Kos, A., Moore, J.R., Raetzo, H., and Lemy, F. (2009): Identification of active release planes using ground-based differential InSAR at the Randa rock slope instability, Switzerland, *Natural Hazards and Earth System Sciences,* 9, 2027-2038.

Gischig, V., (2007): Seismic Investigations on Gornergletscher, *Diploma thesis*, Institute of Geophysics and VAW, ETH Zurich.

Plus 11 conference contributions out of which 6 as first author.